frontiers | Research Topics

Digital rock physics and machine learning

Edited by
Mingliang Liu, Fernando Bordignon, Leandro Passos De Figueiredo,
Yuqi Wu and Luanxiao Zhao

Published in
Frontiers in Earth Science

ISSN 1664-8714
ISBN 978-2-8325-2214-1
DOI 10.3389/978-2-8325-2214-1

About Frontiers

Frontiers is more than just an open access publisher of scholarly articles: it is a pioneering approach to the world of academia, radically improving the way scholarly research is managed. The grand vision of Frontiers is a world where all people have an equal opportunity to seek, share and generate knowledge. Frontiers provides immediate and permanent online open access to all its publications, but this alone is not enough to realize our grand goals.

Frontiers journal series

The Frontiers journal series is a multi-tier and interdisciplinary set of open-access, online journals, promising a paradigm shift from the current review, selection and dissemination processes in academic publishing. All Frontiers journals are driven by researchers for researchers; therefore, they constitute a service to the scholarly community. At the same time, the *Frontiers journal series* operates on a revolutionary invention, the tiered publishing system, initially addressing specific communities of scholars, and gradually climbing up to broader public understanding, thus serving the interests of the lay society, too.

Dedication to quality

Each Frontiers article is a landmark of the highest quality, thanks to genuinely collaborative interactions between authors and review editors, who include some of the world's best academicians. Research must be certified by peers before entering a stream of knowledge that may eventually reach the public - and shape society; therefore, Frontiers only applies the most rigorous and unbiased reviews. Frontiers revolutionizes research publishing by freely delivering the most outstanding research, evaluated with no bias from both the academic and social point of view. By applying the most advanced information technologies, Frontiers is catapulting scholarly publishing into a new generation.

What are Frontiers Research Topics?

Frontiers Research Topics are very popular trademarks of the *Frontiers journals series*: they are collections of at least ten articles, all centered on a particular subject. With their unique mix of varied contributions from Original Research to Review Articles, Frontiers Research Topics unify the most influential researchers, the latest key findings and historical advances in a hot research area.

Find out more on how to host your own Frontiers Research Topic or contribute to one as an author by contacting the Frontiers editorial office: frontiersin.org/about/contact

Digital rock physics and machine learning

Topic editors
Mingliang Liu — Stanford University, United States
Fernando Bordignon — LTrace, Brazil
Leandro Passos De Figueiredo — LTrace Geophysical Solutions, Brazil
Yuqi Wu — China University of Petroleum (East China), China
Luanxiao Zhao — Tongji University, China

Citation
Liu, M., Bordignon, F., De Figueiredo, L. P., Wu, Y., Zhao, L., eds. (2023). *Digital rock physics and machine learning*. Lausanne: Frontiers Media SA.
doi: 10.3389/978-2-8325-2214-1

Table of contents

frontiers | Frontiers in Earth Science

ORIGINAL RESEARCH
published: 21 June 2022
doi: 10.3389/feart.2022.932929

Rock Physical Modeling of Tight Sandstones Based on Digital Rocks and Reservoir Porosity Prediction From Seismic Data

Wei Guo[1,2], Chunmei Dong[1,2]*, Chengyan Lin[1,2], Yuqi Wu[1,2]*, Xianguo Zhang[1,2] and Jinshuai Liu[1,2]

[1]*Shandong Provincial Key Laboratory of Reservoir Geology, China University of Petroleum (East China), Qingdao, China,*
[2]*Shandong Provincial Key Laboratory of Deep Oil & Gas, China University of Petroleum (East China), Qingdao, China*

Edited by:
Nibir Mandal,
Jadavpur University, India

Reviewed by:
Xinpeng Pan,
Central South University, China
Huaizhen Chen,
Tongji University, China
Junxin Guo,
Southern University of Science and Technology, China

***Correspondence:**
Chunmei Dong
172418378@qq.com
Yuqi Wu
wuyuqi150348@163.com

Specialty section:
This article was submitted to Solid Earth Geophysics, a section of the journal Frontiers in Earth Science

Received: *30 April 2022*
Accepted: *16 May 2022*
Published: *21 June 2022*

Citation:
Guo W, Dong C, Lin C, Wu Y, Zhang X and Liu J (2022) Rock Physical Modeling of Tight Sandstones Based on Digital Rocks and Reservoir Porosity Prediction From Seismic Data. Front. Earth Sci. 10:932929. doi: 10.3389/feart.2022.932929

Digital rock physics (DRP) has become an important tool to analyze the characteristics of pore structures and minerals and reveal the relationships between microscopic structures and the physical properties of reservoirs. However, it is greatly difficult to upscale the rock physical parameters, such as P-wave velocity, S-wave velocity, and elastic moduli, from DRP to large-scale boreholes and reservoirs. On the other hand, theoretical rock physical modeling can establish the internal relationship between the elastic properties and physical parameters of tight sandstones, which provides a theoretical basis for seismic inversion and seismic forward modeling. Therefore, the combination of digital rock physics and rock physical modeling can guide the identification and evaluation of the gas reservoir's "sweet spot." In this study, the CT images are used to analyze the mineral and pore characteristics. After that, the V-R-H model is used to calculate the equivalent elastic moduli of rocks containing only the mineral matrix, and then, the differential equivalent medium (DEM) model is used to obtain the elastic moduli of dry rocks containing minerals and pores. Subsequently, the homogeneous saturation model is used to fill the fluids in the pores and the Gassmann equation is used to calculate the equivalent elastic moduli of the saturated rock of tight sandstones. Rock physical modeling is calibrated, and the reliability of the rock physical model is verified by comparing those with the logging data. Afterward, the empirical relationship of rock porosity established from CT images and rock elastic moduli is obtained, and then, the elastic parameters obtained by seismic data inversion are converted into porosity parameters by using this empirical relationship. Finally, the porosity prediction of large-scale reservoirs in the study area is realized to figure out the distribution of gas reservoirs with high porosity. The results show that the H3b and H3c sections of the study area exhibit higher porosity than H3a. For the H3b reservoir, the northeast and middle areas of the gas field are potential targets since their porosity is larger than that of others, from 10% to 20%. Because of the effects of the provenance from the east direction, the southeast region of the H3c reservoir exhibits higher porosity than others.

Keywords: digital rock, CT scan, rock physical model, porosity inversion, seismic data

1 INTRODUCTION

Digital rock physics (DRP) is an important platform for the characterization of pore systems and minerals and numerical simulations of rock physics which can involve solid mechanics, acoustics, electricity, fluid mechanics, and fluid–solid coupling numerical simulation (Lin et al., 2018; Wu et al., 2018). Compared with the rock physics experiments, DRP, as a numerical simulation method, is cheap and effective to obtain the various rock properties (Yang et al., 2021; Golparvar et al., 2018). At present, 3D digital rocks have been used to evaluate the porosity and analyze the pore radius and connectivity (Anselmetti et al., 1998; Jadoon et al., 2016; Wu et al., 2019a), elastic moduli (Hossain et al., 2019; Miao et al., 2015), permeability (Wu et al., 2019b; Nie et al., 2016), and electrical properties. It is important to construct accurate digital rocks for the simulation of rock physical properties (Wei et al., 2018; Wu et al., 2020a). Digital rocks can be constructed by computed tomography (CT) experiments and stochastic modeling methods, such as multiple-point statistics and simulated annealing (Laird and Putnam, 1951). Among them, X-ray CT is the most widely used physical experiment method to construct 3D digital rocks (Wu et al., 2018). CT scanning is a non-destructive imaging method and can be used to obtain the internal spatial structure of rocks without any damage because it directly scans the core sample to obtain the required 2D gray slice data and then generates the 3D digital model of the core samples through mathematical transformation and image processing methods (Zhu et al., 2019; Nie 2014; Wu et al., 2019c). The acquired CT images usually contain mineral information since different minerals exhibit different gray values on CT images (Wu et al., 2020b; Wang et al., 2021). For example, Ma et al. (2019) obtained the relevant information and distribution characteristics of various components of pyrite rocks, namely, minerals, matrix, and pores, by using CT images. Mao et al. (2022) realized the spatial distribution characteristics of different minerals in granite through the segmentation threshold of the CT gray image.

Rock physics is a bridge to connect the elastic properties of subsurface rocks with the physical properties of reservoirs and is the basis of reservoir prediction. Quantitative characterization of the relationship between elastic parameters such as rock bulk modulus and shear modulus, and physical parameters such as porosity, shale content, and water saturation play an important role in the field of geophysical research. It provides a reasonable rock physical model for seismic forward modeling and seismic inversion interpretation, thereby reducing the ambiguity of seismic interpretation (Mavko et al., 2009; Ba et al., 2017; Liu and Grana, 2018). Traditionally, rock physics studies are based on physical laboratory tests. However, because of the limitation of sample preparation and testing methods, the traditional rock physics research methods cannot fully meet the actual needs of oil and gas reservoir prediction. With the development of computer technology and the application of X-ray CT scanning technology in rock physics experiments, digital rock physics technology provides a new technical means for rock physics research (Zhao et al., 2016; Yin et al., 2015; Jian et al., 2020). Wang (2006) calculated the compressional and S-wave velocities of the formation in this area by selecting the differential equivalent medium model. In the process of calculation, the error between the observed P-wave velocity and the calculated P-wave velocity of the actual formation was minimized through continuous iterative processing (Hilpert and Miller, 2001), the elastic modulus parameters of the formation rock were obtained, and the relationship between the elastic modulus parameters and the P-wave and S-wave velocities was analyzed (Saenger and Bohlen., 2004). Shao (2009) obtained multiple mineral components through conventional logging data and obtained the equivalent elastic modulus of the formation by using the average mineral formula. Taking the P-wave velocity as the constraint condition, the S-wave velocity of the formation is calculated according to the model (Deng, 2009). The comparison between the calculated results and the measured results shows that the average relative error is about 5%, which indicates that the model has good adaptability in the study area (Zong et al., 2015). In the same year, Deng (2009) tested the P-wave and S-wave velocities of sandstone samples under simulated reservoir conditions. The adaptability of the contact cementation model to the sandstone samples in this area was analyzed and discussed (Zhao et al., 2016). Zhou (2010) sorted out the rock physics parameters obtained from the conversion of rock physics experimental data and conventional logging data and predicted the S-wave velocity of the study area by using the model, which is highly consistent with the actual S-wave velocity. It is proven that this method can effectively solve the problem of S-wave velocity prediction in the area lacking S-wave logging data (Zhu et al., 2017). Zhang et al. (2019) and Zhang et al. (2020a) pointed out that the reservoir can be better described based on the rock physical modeling of two-phase media, and the concept of critical porosity can also be used to establish the empirical relationship between the grain matrix and dry rock, providing parameters for fluid identification.

In this study, the 3D image analysis of micro-CT samples about tight sandstone is carried out to obtain information on the pore structure, mineral composition, and particle size distribution, and the rock physical model is established using these data. Tight sandstone rock physical modeling is mainly composed of a boundary average model, inclusion model, fluid replacement model, and so on. The equivalent elastic modulus of the rock mineral matrix is calculated by using the boundary average model of the V-R-H model, the dry rock matrix modulus is calculated by using the differential equivalent medium DEM model, then the pore is filled with fluid through the uniform saturation model, and the equivalent elastic modulus of saturated rock is calculated by using the Gassmann equation. This method can be used to estimate the equivalent modulus of saturated rock in a tight sandstone medium. Finally, the reliability of the rock physical model is verified, the empirical formula of porosity is established through the petrophysical relationship, and the prediction of porosity with seismic data is realized.

2 GEOLOGICAL SETTING

This study takes an offshore gas field in eastern China as the study area. The gas field is mainly structural oil and gas reservoirs with thick sandstone, but the physical properties of the reservoirs are generally tight and change rapidly, and the “sweet spot” of the

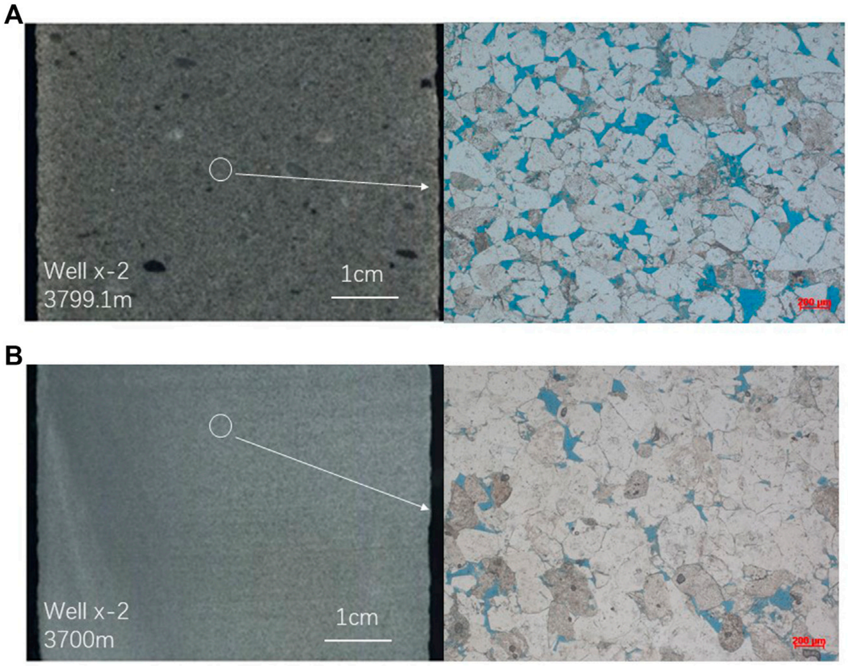

FIGURE 1 | Core image and pore structure slice of the tight sandstone reservoir. **(A)** "Sweet spot" reservoir and **(B)** "non-sweet spot" reservoir.

reservoir plays an important role in controlling oil and gas productivity. The target interval in the study area is mainly the braided delta sedimentary system under the background of a shore-shallow lake, which mainly developed an underwater distributary channel, and sandstone is well developed with large thickness and wide distribution. There are three types of reservoirs, namely, medium-low porosity and medium–low-permeability reservoirs, extra-low-porosity and extra-low-permeability reservoirs, and medium-porosity and medium–high-permeability reservoirs locally. The oil and gas reservoirs in the study area are mainly controlled by structures, such as anticlinal gas reservoirs. The study area is dominated by sandstone with medium grain size. The lithology developed in the study area includes mudstone, siltstone, fine sandstone, medium-fine sandstone, coarse sandstone, argillaceous sandstone, and glutenite. The color of the sandstone is grayish-white, with fine grain size and medium sorting. The pore types in the study area mainly include residual intergranular pores, intergranular dissolved pores, intragranular dissolved pores, and moldic pores. The intergranular dissolved pore is the most common pore type in the reservoir of the study area.

The physical properties of tight sandstone reservoirs are generally poor, and the coexistence of medium-low porosity and medium–low-permeability reservoirs and ultra-low-porosity and ultra-low-permeability reservoirs reflects strong reservoir heterogeneity (Radlinski et al., 2004; Hu et al., 2012; Bordignon et al., 2019; Liu and Mukerji, 2022). It is necessary to build a rock physical model of tight sandstone under heterogeneous conditions. With the increase of the burial depth, the tight sandstone in the middle and deep layers tends to be densified due to strong compaction and cementation. However, because of the influence of heterogeneity, high-quality reservoirs with good porosity and permeability characteristics will appear in local areas, namely, "sweet spots" (Bloch et al., 2002; Mavko et al., 2009).

To carry out rock physical modeling of heterogeneous tight sandstone reservoirs, it is necessary to analyze the structural characteristics of the "sweet spot" reservoir, including rock mineral composition and pore structures. During the process of sedimentation and diagenesis, rocks have experienced tectonism, sedimentation, diagenesis environments, and their matching process in time and space. For example, **Figure 1** shows the core photos and casting thin sections of the "sweet spot" reservoir and the "non-sweet spot" reservoir. The "sweet spot" reservoir is different from the "non-sweet spot" reservoir in terms of rock mineral grain size, pore type, structure, etc., and the "sweet spot" reservoir exhibits coarser grain size and higher porosity.

3 DATA AND METHODS

The research process adopted in this study is shown in **Figure 2**. First, the mineral composition and corresponding volume ratio of rocks in the study area are obtained through digital core analysis and then the rock physical model is established with these data as the input data. The equivalent elastic modulus of the rock mineral matrix is calculated by the boundary average model of the V-R-H model, and the dry rock skeleton containing minerals and pore modulus is calculated by the differential equivalent medium DEM

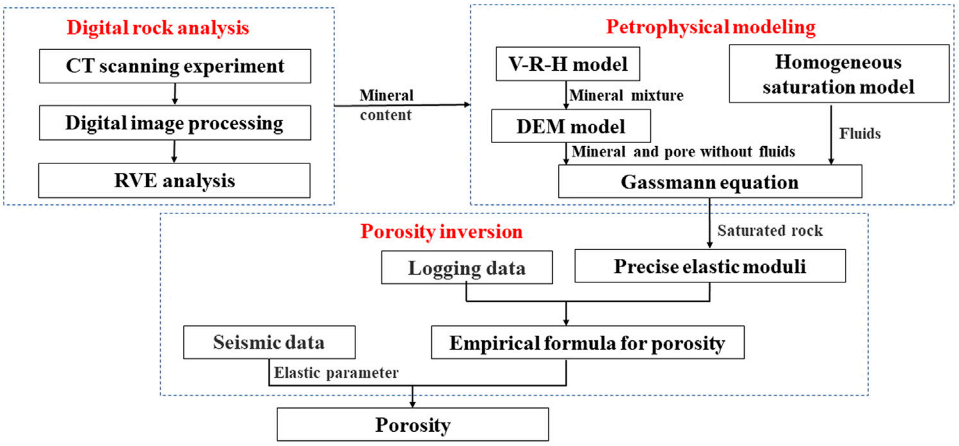

FIGURE 2 | Flow chart of porosity prediction based on seismic data by rock physical modeling.

model. Then the equivalent elastic modulus of saturated rock is calculated by the Gassmann equation with the homogeneous saturated model filled with fluid in the pores, to realize the estimation of the equivalent modulus of saturated tight sandstone and establish the rock physical model of tight sandstone digital rock. The rock physical model is calibrated and its reliability is verified through logging data, then the empirical relationship of the rock porosity established from CT images and rock elastic moduli is obtained, and the porosity parameters can be predicted from seismic data by using this empirical relationship.

3.1 Digital Rock Physics Methods

The construction of 3D digital rocks containing the real pore structure of complex reservoir rocks is the first step of DRP (Markus et al., 2001). The projection data obtained by X-ray CT scanning is used to reconstruct the 3D gray image of the core through the filtering (convolution) back-projection technique. The gray value of the image reflects the density of different parts of the rock slice (Das et al., 2017; Liu et al., 2022). The whiter the image (larger gray value), the higher the density, and the darker the image (smaller gray value), the lower the density. The gray value reflects the degree of X-ray absorption attenuation of the material. How to accurately divide the boundary between the skeleton and the pore is the key to calculating core porosity, pore structure parameters, and rock physical properties by using digital rock.

The modeling process of the X-ray CT scanning method can be summarized into three main steps, namely, CT scanning experiment, digital image processing, and RVE analysis.

CT scanning uses the X-ray CT scanning technique, which has the advantages of high imaging resolution, large scanning area, and no damage to the scanned sample. During the experiment, when the X-ray passes through the scanned rock sample, part of the energy of the X-ray will be absorbed by the rock sample and the energy and intensity of the X-ray will be weakened. This process can be expressed by Beer's law as follows (Wildenschild and Sheppard, 2013; de Figueiredo et al., 2019):

$$I = I_0 e^{-\int \mu(s)ds}. \tag{1}$$

In the formula, I_0 is the intensity of the incident light, $\mu(s)$ is the path of the ray, and s is the local ray attenuation index. By transforming **Eq. 1**, the linear attenuation coefficient of each voxel point can be obtained.

$$\int \mu(s)ds = -\ln\left(\frac{I}{I_0}\right). \tag{2}$$

In general, I and I_0 are easily obtained in the formula, so that the linear attenuation factor μ can be calculated. This factor depends on the density of the scanned material, we can separate the components of different densities in the tested sample according to this technique. At present, there are many methods to convert the linear attenuation coefficient into an image. One of the most common methods is called filtered back-projection. It convolves the linear data obtained at each angle with a specific filter and then back-projects it at the same angle to obtain the image. The next step is image processing after obtaining the X-ray CT scan image (Wildenschild and Sheppard, 2013).

Image processing mainly includes the following processes: cropping, denoising, threshold segmentation, and REV (representative elementary volume) judgment. When the sample is cut, try to select the middle part of the scanned sample rather than the edges and corners. The purpose of denoising is to improve the signal-to-noise ratio of the image. There are many denoising algorithms, such as median filtering, non-local means filtering, sigma filtering, Nagao filtering, SNN filtering, majority filtering, recursive exponential filtering, bilateral filtering, and box filtering. The purpose of threshold segmentation is to identify and separate the object of study (such as the pore or oil phase) from the image. Based on the distribution characteristics of the gray value histogram, the relevant personnel then observe and judge by naked eyes and experience. This research object can be separated. The REV judgment is to

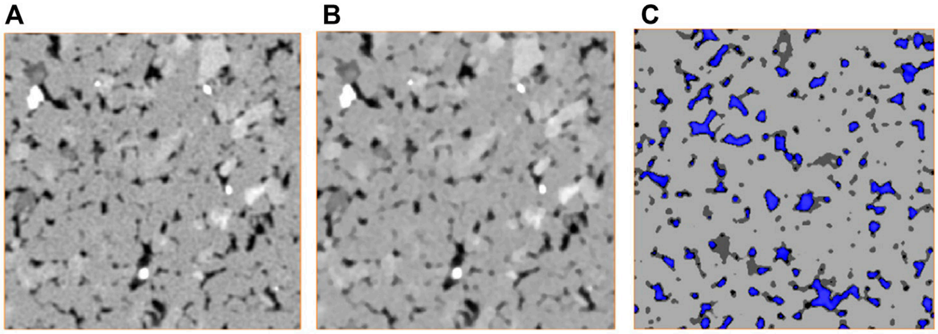

FIGURE 3 | CT images before and after processing. **(A)** Original CT image; **(B)** CT image after filter; and **(C)** image after thresholding segmentation.

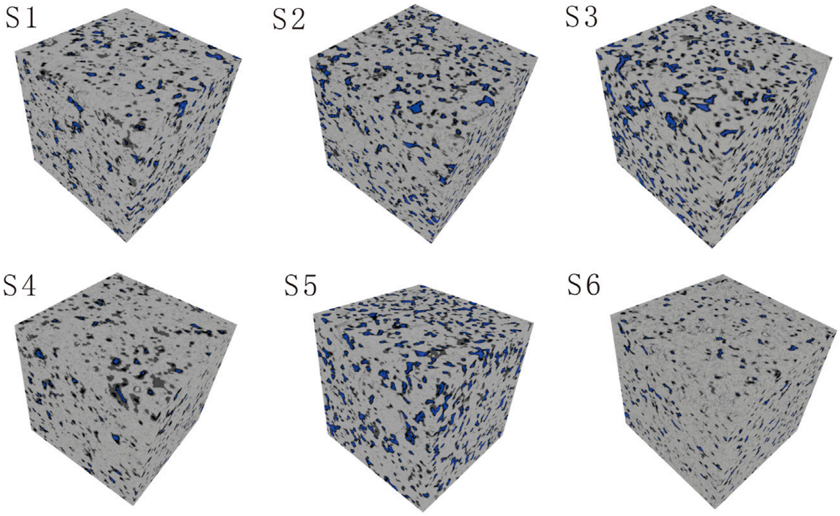

FIGURE 4 | Constructed digital rocks using CT.

determine if the cropped area is greater than the minimum volume representing the rock. For images with poor image quality, the process will also include morphological operations such as dilation, erosion, opening and closing, and removal of small objects. These image processing processes can be done based on software or programs such as ImageJ, Fiji, Matlab, PerGeos/Avizo, etc. Andrä et al. (2013) systematically discussed the issues that should be paid attention to during image processing.

In this study, six low-permeability sandstone reservoir samples with different depths are selected as the research objects, which are sequentially numbered as S1, S2, S3, S4, S5, and S6. They come from the third and fourth members of the Huagang Formation of the X-2 well in the Xihu Sag of the study area, and all of them belong to tight sandstone natural gas reservoirs. The sampling depths of samples S1–S6 are 3736.6 m, 3785 m, 3818.9 m, 3714.5 m, 3373.1 m, and 4008.3 m, respectively, the resolutions are 14.6 μm, 14.1 μm, 13.6 μm, 12.9 μm, 13.0 μm 8 μm, and 10.7 μm, respectively, and the sample size is 300 × 300 × 300. All the samples are from the sandstone deposited in a braided river delta, the lithology is fine sand-medium sandstone, and the clastic components are mainly quartz, feldspar, and clay.

After the CT scan data volume is obtained, the original CT images containing gray information are cropped, denoised, and segmented and the REV is judged by using the image processing technique. During the process of threshold segmentation, pores and different minerals are separated according to different gray values. **Figure 3** shows the image processing process of sample S2. In the original CT image, a smaller gray value corresponds to the pore and a smaller gray value is quartz, which is the main component of the rock. A larger gray value corresponds to feldspar, and the maximum gray value is clay. Therefore, CT images can be used to segment different mineral components.

After selecting the REV of each sample and completing the image processing mentioned previously, the REV images of six samples can be constructed, as shown in **Figure 4**. It can be seen from the external and internal views of the six samples that there are more tiny pores in samples S2, S3, and S5, fewer pores in samples S1, S4, and S6, and the similarity between samples S2, S3, and S5 are higher.

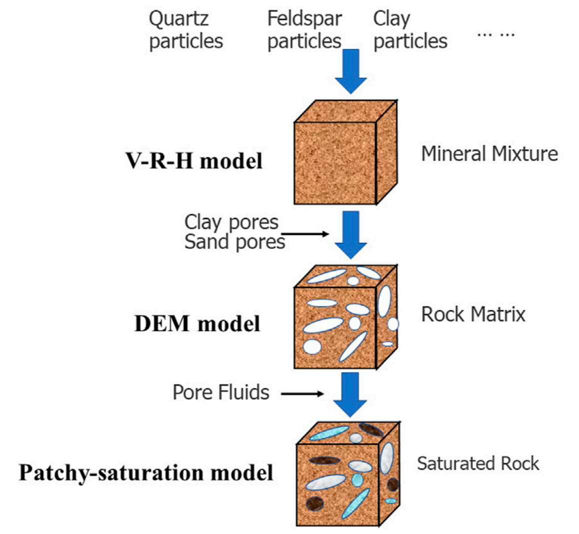

FIGURE 5 | Flow chart of rock physical modeling of tight sandstone.

3.2 Rock Physical Model of Heterogeneous Tight Sandstones

The heterogeneous tight sandstone reservoir has medium–low porosity and medium–low permeability. (Cai et al., 2014; Avseth et al., 2014; Dutta et al., 2012) proposed a rock physical modeling method for medium–low-permeability tight rocks by analyzing the lithofacies type and burial history, that is, the CCT contact model is used to calculate the low porosity section (35%), while the HS upper limit is used to calculate the medium-porosity section (10%–35%) (He, 2017; Tang, 2011; Pan et al., 2019). In this study, considering the pore type and structure in the middle-low porosity and middle–low-permeability section, the DEM model and Gassmann equation, which are suitable for rock physical modeling of relatively high porosity, are used to calculate the equivalent rock physical model (Yin et al., 2017; Antariksa et al., 2022; Fawad and Mondol, 2022; Guo et al., 2016).

Tight sandstone rock physical modeling is mainly composed of a boundary average model, inclusion model, fluid replacement model, and so on (**Figure 5**). The boundary average model is used to calculate the equivalent elastic modulus of the rock mineral matrix, the inclusion model is used to calculate the dry rock matrix modulus, and the fluid replacement model is used to fill the fluid in the pores and calculate the equivalent elastic modulus of the saturated rock. In this way, the equivalent modulus of saturated rock in a tight sandstone medium can be estimated.

3.2.1 Boundary Average Model

The boundary average model calculates the elastic modulus (generally refers to the bulk modulus and shear modulus) of the rock matrix of mixed minerals by calculating the upper and lower limits of the physical properties of the rock matrix. The Voigt-Reuss-Hill average is chosen as the boundary average model in this study. The boundary average model generally does not take into account the geometric structure of mineral components and other factors.

The Voigt-Reuss-Hill (VRH) average is the average of the Voigt and Reuss models (Voigt, 1907; Reuss, 1929). The Voigt model is the upper limit of the equivalent elastic modulus of rock K_v, μ_v, which assumes that the mineral particles are evenly arranged along the direction of the force; the Reuss model is the lower limit of the equivalent elastic modulus of rock K_R, μ_R, which assumes that the rock mineral grains are arranged in layers perpendicular to the stress direction. The rock matrix of tight sandstone is mainly composed of rigid particles and clay, and the rigid particles are mainly quartz and feldspar. The elastic modulus of the rock matrix of a tight sandstone reservoir is calculated by the VRH average K_m, μ_m:

$$\begin{cases} K_v = V_q K_q + V_{clay} K_{clay} \\ \mu_v = V_q \mu_q + V_{clay} \mu_{clay} \end{cases}, \tag{3}$$

$$\begin{cases} \dfrac{1}{K_R} = \dfrac{V_q}{K_q} + \dfrac{V_{clay}}{K_{clay}} \\ \dfrac{1}{\mu_R} = \dfrac{V_q}{\mu_q} + \dfrac{V_{clay}}{\mu_{clay}} \end{cases}. \tag{4}$$

In the formula, K_v, μ_v is the Voigt upper limit of the elastic modulus of the mixed mineral; K_R, μ_R is the Reuss lower limit of the elastic modulus of the mixed mineral; V_q, V_{clay} is the rigid particle content and clay content of the reservoir; K_{clay}, μ_{clay} is the modulus of elasticity of the clay; and K_q, μ_q is the elastic modulus of the rigid particle.

Averaging the two models, the elastic modulus of the rock matrix K_m, μ_m is obtained as

$$\begin{cases} K_m = \dfrac{K_v + K_R}{2} \\ \mu_m = \dfrac{\mu_v + \mu_R}{2} \end{cases}. \tag{5}$$

3.2.2 Inclusion Model

The inclusion model can be used to estimate the equivalent elastic modulus of rock with solid or fluid inclusions. Many different types of inclusion models have been developed according to the differences in rock physics characteristics of specific study areas, such as the differential equivalent medium (DEM) (Bandyopadhyay, 2009), Kuster–Toksoz (KT) model (Kuster and Toksöz, 1974), Kachanov model, Mori–Tanaka model, linear slip model, etc. The fluid inclusion can be represented as the rock pore space, and the pore can be equivalent to an ellipsoid, which can be used to analyze the influence of the rock internal pore structure on rock properties.

The differential equivalent medium model (DEM) assumes that inclusions in rocks are isolated from each other and do not interact with each other. The DEM model divides the inclusions into infinitesimal parts, each part is then added to the background phase step by step, and the equivalent modulus is affected by the addition order of the inclusions. It should be noted that the order of soft and hard pore addition of dry rock has little effect on the final equivalent modulus results. The equivalent bulk modulus of

TABLE 1 | P and Q coefficients of different shapes.

Shape	$\mathbf{P^{mi}}$	$\mathbf{Q^{mi}}$
Globe	$\frac{K_m+4/3\mu_m}{K_l+4/3\mu_m}$	$\frac{\mu_m+\xi_m}{\mu_l+\xi_m}$
Acicular	$\frac{K_m+\mu_m+1/3\mu_l}{K_l+\mu_m+1/3\mu_l}$	$\frac{1}{5}\left(\frac{4\mu_m}{\mu_m+\mu_i}+2\frac{\mu_m+\gamma_m}{\mu_i+\gamma_m}+\frac{K_i+4/3\mu_m}{K_i+\mu_m+1/3\mu_i}\right)$
Discal	$\frac{K_m+4/3\mu_l}{K_l+4/3\mu_l}$	$\frac{\mu_m+\xi_l}{\mu_l+\xi_l}$
Crevice	$\frac{K_m+4/3\mu_l}{K_l+4/3\mu_l+\pi\alpha\beta_m}$	$\frac{1}{5}\left(1+\frac{8\mu_m}{4\mu_i+\pi\alpha(\mu_m+2\beta_m)}+2\frac{K_i+2/3(\mu_i+\mu_m)}{K_i+4/3\mu_i+\pi\alpha\beta_m}\right)$

In the table, $\beta_m=\mu_m\frac{3K_m+\mu_m}{3K_m+4\mu_m}$, $\gamma_m=\mu_m\frac{3K_m+\mu_m}{3K_m+7\mu_m}$, $\zeta_m=\frac{\mu_m}{6}\frac{9K_m+8\mu_m}{K_m+2\mu_m}$.

the DEM model $K_{\overline{DEM}}^{*}$ and shear modulus $\mu_{\overline{DEM}}^{*}$ can be expressed as

$$\begin{cases} (1-y)\dfrac{d}{dy}\left[K_{DEM}^{*}(y)\right]=\left(K_2-K_{DEM}^{*}\right)P^{(*2)}(y) \\ (1-y)\dfrac{d}{dy}\left[\mu_{DEM}^{*}(y)\right]=\left(\mu_2-\mu_{DEM}^{*}\right)Q^{(*2)}(y) \end{cases}, \tag{6}$$

where the initial condition is $K_{DEM}^{*}(0)=K_1$ and $\mu_{DEM}^{*}(0)=\mu_1$. y is the percentage of inclusion and P and Q are the polarization factors related to the inclusion modulus and shape, whose values are shown in **Table 1**.

3.2.3 Uniform Saturation Model

For different types of "sweet spot" reservoirs, the plaque-saturated model (**Eqs 7–9**) is used to calculate the elastic modulus of the mixed fluid.

$$\frac{1}{K_{fl1}}=\frac{S_0}{K_0}+\frac{S_g}{K_g}+\frac{S_w}{K_w}, \tag{7}$$

$$K_{fl2}=K_0S_0+K_gS_g+K_wS_w, \tag{8}$$

$$K_{fl}=\frac{K_{fl1}+K_{fl2}}{2}. \tag{9}$$

In the formula, K_0, K_g, and K_w are the bulk moduli of oil, gas, and water, respectively. S_0, S_g , and S_w are the saturations of oil, gas, and water respectively, and $S_0+S_g+S_w=1$.

3.2.4 Fluid-Filled Model

The equivalent elastic modulus of saturated rock for different types of "sweet spot" reservoirs is calculated using the Gassmann formula (Shi, 2009) and the elastic modulus of saturated rock is used to calculate the compressional and S-wave velocities of tight sandstone reservoirs as follows:

$$V_p=\sqrt{\frac{(K+4/3\mu)}{\rho}}=\sqrt{\frac{M}{\rho}}, \tag{10}$$

$$V_s=\sqrt{\frac{\mu}{\rho}}. \tag{11}$$

Here, V_p, V_s, and ρ are the P-wave velocity, S-wave velocity, and the density of saturated rock; K and μ are the bulk and shear moduli of the saturated rock.

According to the pore structure characteristics of different types of "sweet spot" reservoirs, the new rock physical model constructs the rock physical models of different types of "sweet spot" reservoirs, which can be well applied to tight sandstone reservoirs with large changes in porosity and permeability.

4 RESULTS

Pore refers to the basic reservoir space of fluid in rocks, and pore structure refers to the type, size, distribution, and connectivity of pores in rocks. The determination of pore structure parameters is the basis of calculating the equivalent elastic modulus of the tight sandstone skeleton.

The pore geometry in the tight sandstone is diverse and the pore structure is complex. It can be observed from the digital rock constructed by CT that the rocks in the study area mainly include primary intergranular pores, intragranular dissolution pores, and moldic pores. The pore structure of tight sandstone reservoirs is greatly affected by compaction, and the amount of primary pores is the key factor to determine the quality of the reservoir. Rock grain size, quartz content, and clay content are the main factors affecting the pore structure parameters. The larger the grain size is, the larger the primary pore will be, so that the residual intergranular pore and intergranular dissolution pore are larger under the same burial process and diagenesis. Quartz is the most important rigid mineral in clastic rocks which determines the ability of rocks to resist compaction, that is, the preservation of pores. Rock cuttings mainly composed of quartz also have strong compressibility. The clay content is mainly related to the irreducible water saturation, which is the key factor affecting the seepage. In the theory of rock physical modeling of tight sandstone, the primary intergranular pore has a large pore size and good connectivity. The intragranular dissolution pores are the dissolution pores of feldspar and rock debris, with small grain size and poor connectivity. The diameter of the casting mold hole is larger, but the connectivity is poor. The reservoir of the H3 member of the granite formation in the study area has many primary pores, large porosity, and relatively uniform pore fluid distribution.

The heterogeneity of the tight sandstone reservoir is the difference in porosity and permeability caused by the grain size of rock minerals and pore structure types between different formations. Therefore, according to the geological characteristics of the study area, using porosity as the division standard of natural gas "sweet spot," aiming at the characteristics of medium–low-porosity and medium–low-permeability natural gas reservoirs, the rock physical model of heterogeneous tight sandstone is established. Based on the aforementioned reservoir characteristics, the basic idea of rock physics modeling is to use the effective medium theory to add flat pores (small pore aspect ratio) and more circular pores (large pore aspect ratio) based on isotropic background media and calculate the dry rock stiffness coefficient matrix. The elastic parameters of fluid-saturated rocks are estimated according to the isotropic replacement method. According to the digital rock analysis, the minerals of the tight sandstone reservoir in the study area mainly include quartz,

TABLE 2 | Basic information of the six samples used in this study.

Serial number	Quartz/%	Feldspar/%	Clay/%	Porosity/%	Measured porosity/%	Error
S1	66	27	7	9.63	9.75	−1.23%
S2	70	24	6	12.34	12.52	−1.44%
S3	72	21	7	14.36	14.53	−1.17%
S4	66	27	7	8.56	8.44	1.42%
S5	69	26	5	14.27	14.15	0.85%
S6	70	25	5	6.81	6.92	−1.3%

TABLE 3 | Parameters of the mineral constituent and fluid of the model.

Composition	Bulk modulus (Gpa)	Shear modulus (Gpa)	Density (g/m^3)
Quartz	48	43	2.65
Feldspar	41	18	2.62
Clay	21	7	2.46
Formation water	2.58	0	1.03
Gas	8 × 10^{-4}	0	6.5 × 10^{-4}

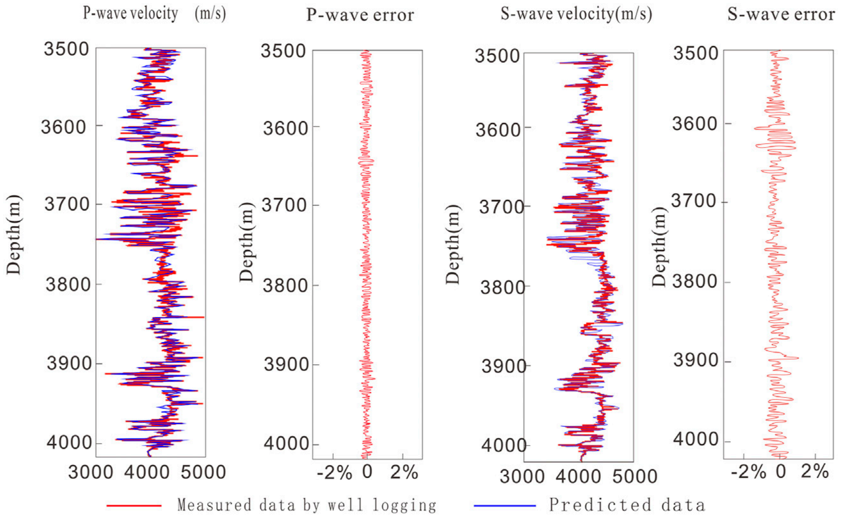

FIGURE 6 | Reconstruction results and errors of P-wave and S-wave velocities based on the rock physical model.

feldspar, shale, and debris, among which quartz is the main component with high content. Because of the deep burial depth and complex diagenesis of the heterogeneous tight sandstone reservoir, the “sweet spot” reservoir has the petrological characteristics of coarse grain size, high quartz content, and low clay content. The grain size of rock minerals affects the pore structure of rocks, so the grain size difference is regarded as the difference in the pore structure of rocks.

The results of the digital rock (**Table 2**) show that the volume fraction of the rigid grains is about 70% for quartz, about 25% for feldspar, and about 5% for clay. Because the density of quartz and feldspar is not very different, it is difficult to distinguish and compare digital rock. However, the difference in elastic physical parameters between quartz and feldspar is not particularly large. Therefore, the influence on the accuracy of the rock physical model results is within an acceptable range. The pore types of tight sandstone reservoirs are divided into connected pores and unconnected pores, and a porosity of 12% is defined as the “sweet spot” of tight sandstone reservoirs. These input parameters (**Table 3**) can be used as the input data of the rock physical model. A rock physical model of heterogeneous tight sandstone is established and a series of analyses are carried out.

5 DISCUSSION

5.1 Rock Physical Model Validation

According to the experimental data of rock physics in the actual work area, the reliability of the rock physics model is verified. **Figure 6** shows the comparison between the P-wave and S-wave

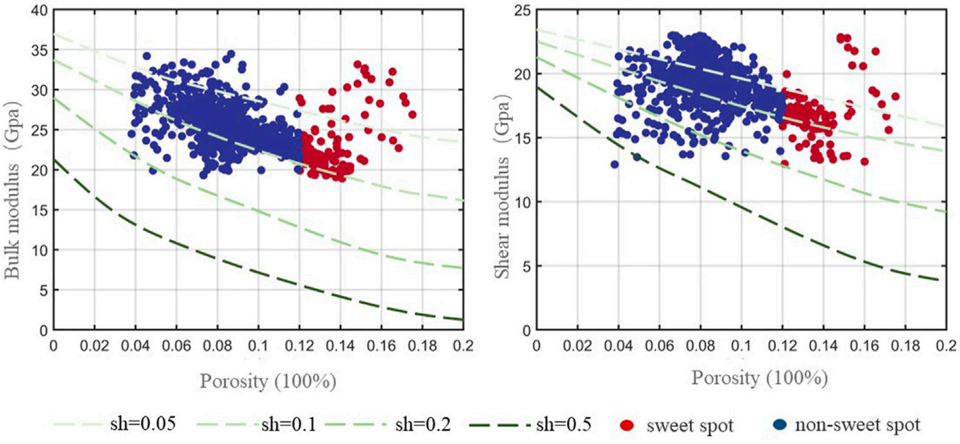

FIGURE 7 | Influence of reservoir porosity of "sweet spot" in the H3 section of the X-2 well on the volume and shear modulus.

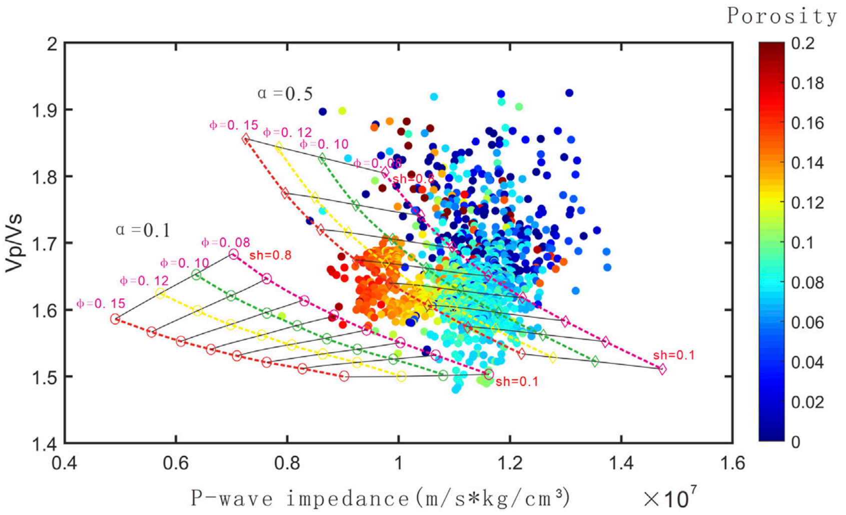

FIGURE 8 | Rock physics quantification of section H3 in Donghai X gas field.

velocity reconstruction results (blue) of the X-2 well based on the rock physical model and the actual rock physics experimental measurement data, and the relative error between the rock physics measurement results and the estimation results. It can be seen that the error between the rock physics model prediction value and the experimental measurement value is less than 3%, which indicates that the model prediction result can reflect the actual value with high accuracy, and the rock physics modeling result is more reliable.

5.2 Rock Physical Model Analysis

The effect of porosity is studied based on the constructed rock physical model of thick and low-permeability reservoirs. **Figure 7** shows the effect of the reservoir porosity on the volume and shear modulus of the "sweet spot" in the H3 section of well X-2. The curves with different colors indicate that the shale content increases gradually from top to bottom, and the blue points represent the data of the actual logging curve of the corresponding non-sweet spot reservoir. The red dots represent data from the actual log of the corresponding segment of the "sweet spot" reservoir. It can be seen from the figure that with the increase in porosity, the bulk modulus and shear modulus show a decreasing trend. Compared with the "sweet spot" data of actually good data, it is found that the porosity of the "sweet spot" reservoir is larger than that of the non-sweet spot reservoir. It is consistent with the changing trend of the rock elastic modulus calculated by the model, which confirms the reliability of the rock physics model.

Using the constructed rock physical model, the quantitative interpretation version between reservoir physical parameters and elastic parameters can be established, which can be used to predict reservoir parameters. **Figure 8** shows the the rock physics version of the reservoir in the H3 section of the x gas field.

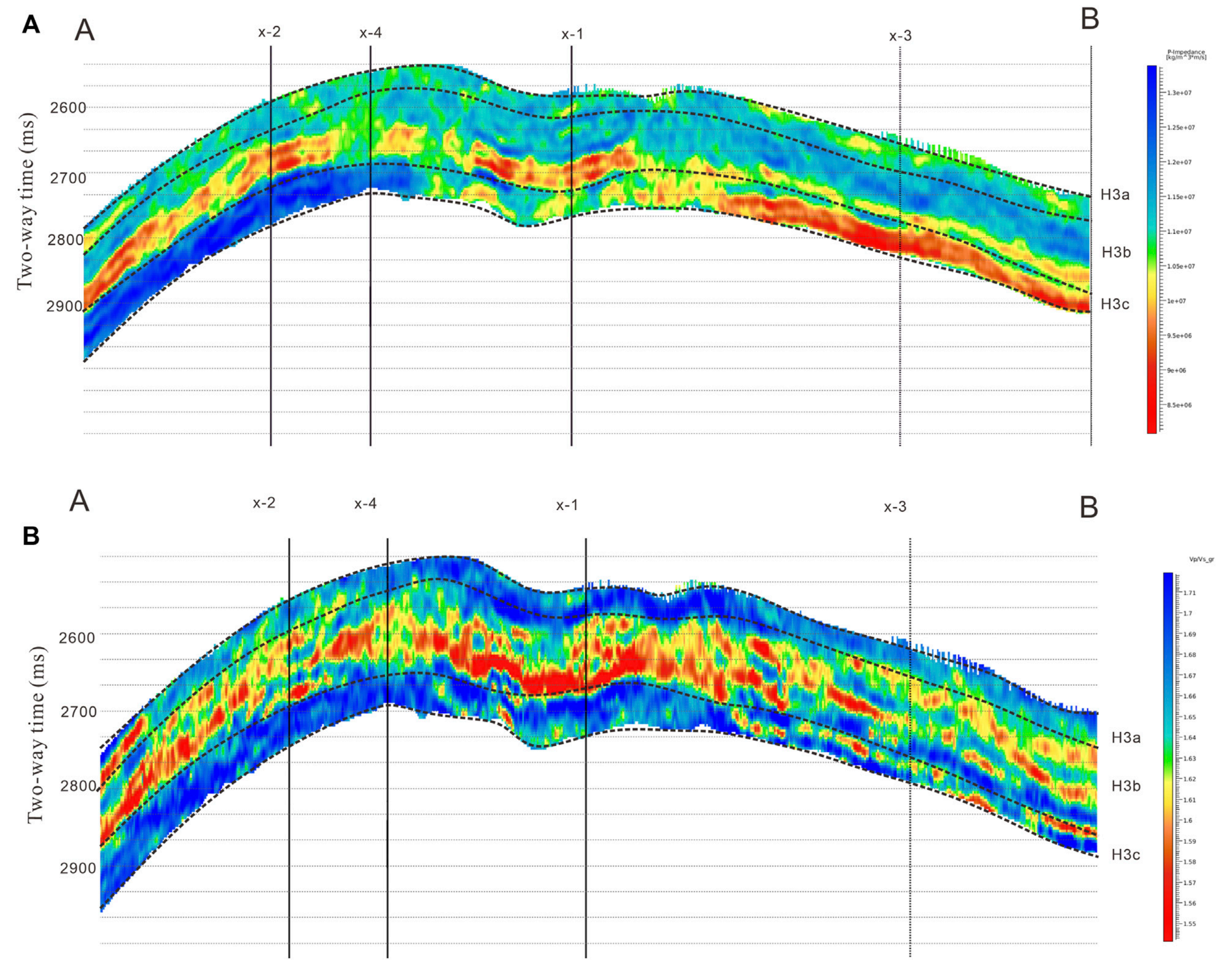

FIGURE 9 | Well-tie section for P-wave impedance and the sensitive parameter V_p/V_s in the study area. H3a, H3b and H3c represent different sub-strata of the third member of Huagang Formation.

5.3 Porosity Inversion

The physical property parameter prediction method based on linearized rock physics inversion applies to linear or slightly nonlinear rock physical models (Zhang et al., 2020b; Pan et al., 2021). For the highly nonlinear rock physical model, the empirical formula method is used to predict the porosity (Zong and Yin, 2017; Chen et al., 2017; Pan et al., 2017; Liu et al., 2022). It is to obtain a statistical empirical relationship between porosity and rock elastic parameters (such as P-wave velocity, S-wave velocity, density, and elastic impedance) by using rock physics test data and logging data and then use this statistical empirical relationship to convert the elastic parameters obtained by seismic inversion into porosity parameters.

According to the rock physics version, the fitting formula for porosity prediction is

$$\varphi = 0.183245 + 0.749747 \times Ip*10^{-8} - 0.113664 \times V_p\big/V_s. \quad (12)$$

In the formula, φ stands for porosity, Ip is the longitudinal wave impedance, and V_p/V_s is the ratio of compressional and S-wave velocities.

In this study, we used the high signal-to-noise ratio seismic data processed by a contractor. After processing, the pre-stack AVO inversion approach was implemented to estimate the elastic parameters (P-wave velocity, S-wave velocity, and density). **Figures 9A,B** show the inversion result of P-wave impedance and the estimated sensitive parameter V_p/V_s of the reservoir in the research field, respectively.

H3 has three sand bodies of H3a, H3b, and H3c (**Figure 10**), and the porosity of each sand body is predicted separately. **Figure 11** shows the well-tie profile of H3a porosity prediction, in which the top and bottom of H3a are marked with interpretation horizons. It can be seen from the figure that the porosity of the H3a reservoir is higher than that of the upper and lower mudstone formations, which is consistent

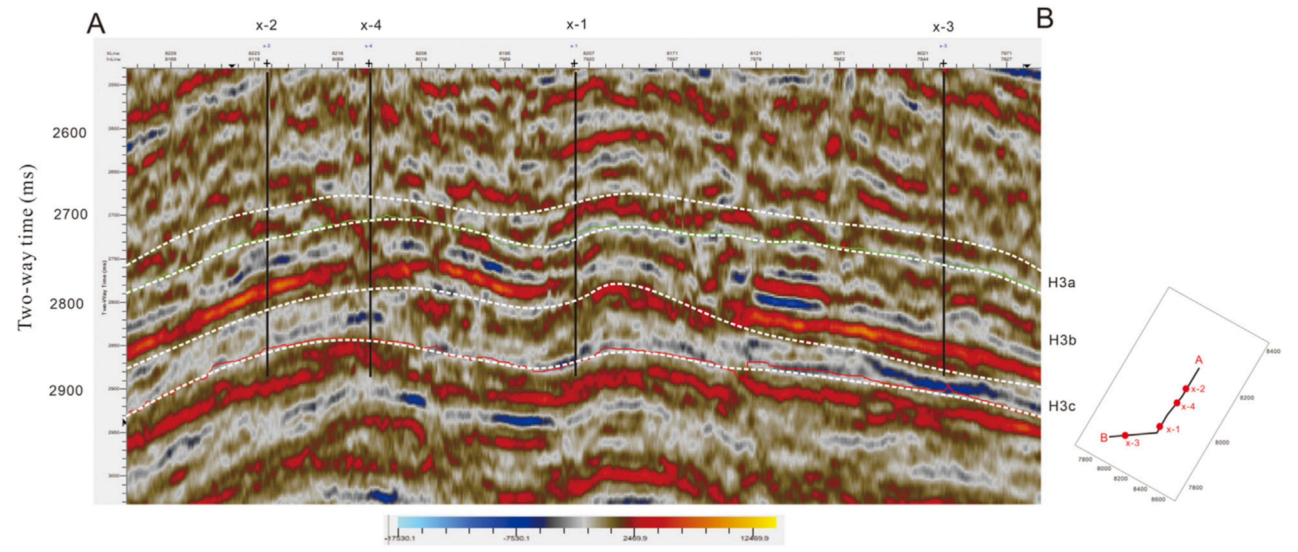

FIGURE 10 | Original seismic profile of well-tie in the study area.

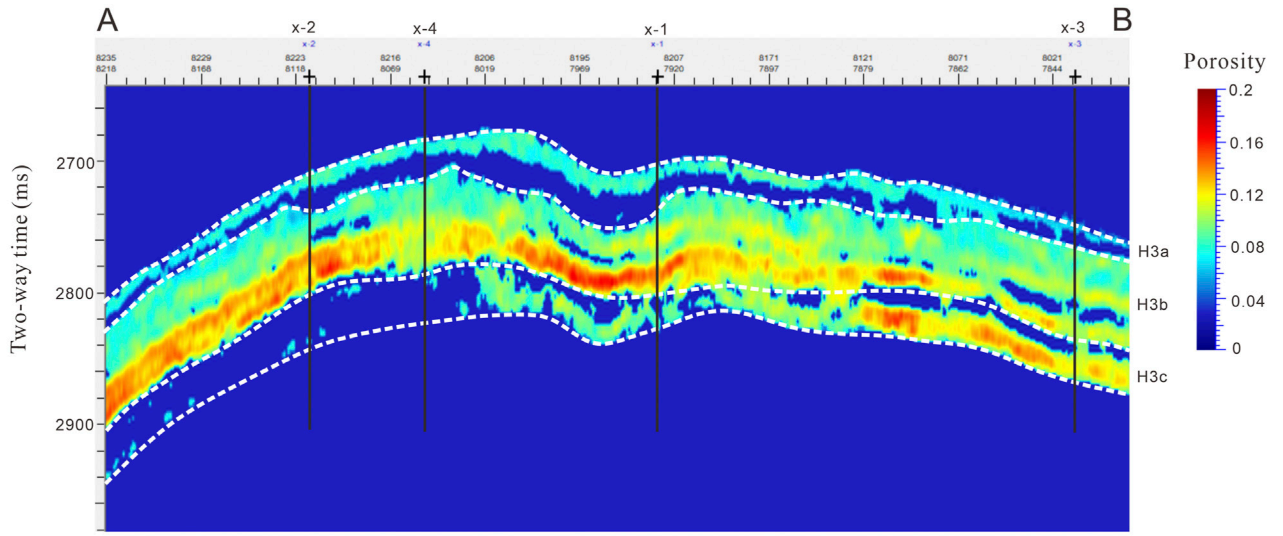

FIGURE 11 | Well-tie section for porosity prediction in the study area.

with the reservoir (lithology) prediction results. At the same time, the H3a porosity profile reflects the distribution characteristics of the H3a reservoir. That is to say, the reservoir is relatively thin, but the distribution is relatively uniform, and the reservoir is slightly thicker at well X-1. The porosity of H3b is higher than that of the upper and lower mudstone formations and the H3a reservoir, and it is a high-porosity thick reservoir, which is consistent with the prediction results of the H3b thick sand reservoir. The porosity of H3c near well X-3 and well X-1 is higher, while the porosity near well X-2 is lower, which is consistent with the prediction results of the H3c thick sand reservoir.

Figure 12 shows the attribute map of the average porosity of H3a, which is also similar to the plane distribution law of the H3a reservoir (lithology). From the attribute map, it can be seen that the porosity in the middle and northwest of the gas field is relatively high, with an average porosity of about 5%–8%, while the porosity in other areas is relatively small, with an average porosity of less than 5%. The average porosity of sandstone in the gas-bearing area changes relatively fast.

Figure 13 reveals the attribute map of the average value of H3b porosity, which is also similar to the plane distribution law of the H3b reservoir (lithology). The porosity in the northeast and middle parts of the gas field is relatively high, which can reach

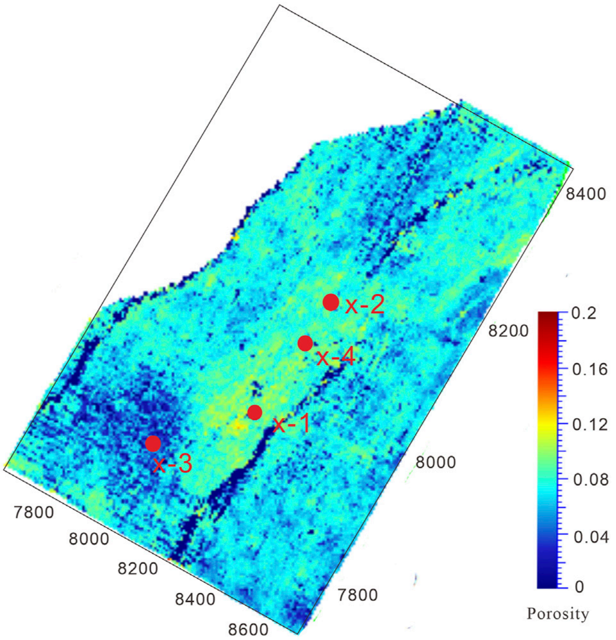

FIGURE 12 | Average attribute map of H3a porosity along with the layer.

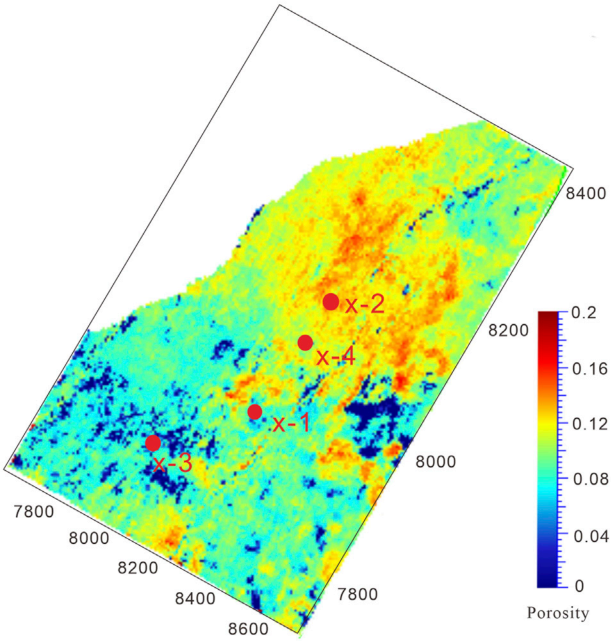

FIGURE 13 | Average attribute map of H3b porosity along with the layer.

18%–20%, while the porosity in the southwest part is relatively low, with an average porosity of 8%–12%. The average porosity of the sandstone in the gas-bearing area does not change much.

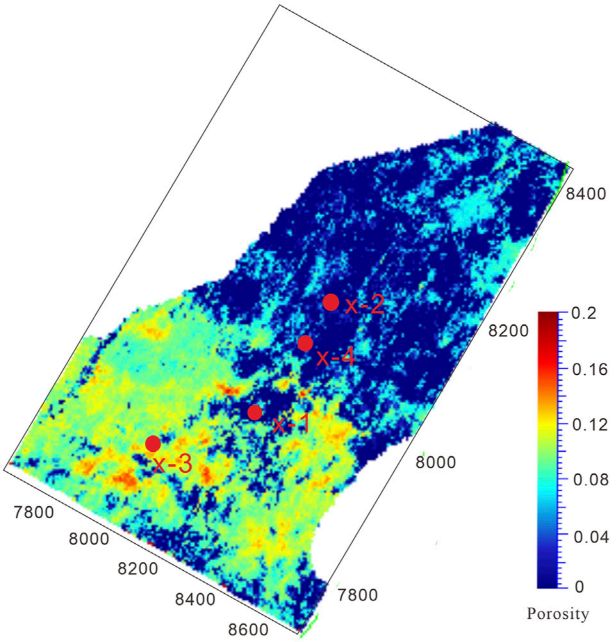

FIGURE 14 | H3c porosity average value attribute map of porosity along with the layer.

Figure 14 displays the attribute map of the average value of H3c porosity, which is also similar to the plane distribution law of the H3c reservoir (lithology). The porosity of the gas field shows a trend of high in the south and low in the north. The average porosity in the south of the gas field is around 7.5%–12%, while the average porosity in the north is less than 3%. The average porosity of sandstone in the gas-bearing area changes relatively fast and decreases gradually from south to north.

The results of the porosity prediction are very consistent with the sedimentary background of the study area. In the H3a period, the hydrodynamic is weak, the mudstone is developed in the study area, and the overall porosity is low. During the H3b period, the high-energy braided channel was mainly developed in the northeast region of the study area, with abundant and coarse-grained sediments. Influenced by the resistance of lake water, the southern waterway of the study area cannot be cut down, the grain size of sediments becomes smaller, and the thickness of sandstone becomes thinner. The low-energy braided channel is developed, which is consistent with the prediction results of porosity in the study area. During the H3c period, there was a provenance in the east of the study area. Affected by the water system from the southeast, the low-energy braided channel is mainly developed in the study area, and the sediments are mainly fine sandstones and become thinner and pinched out northward.

6 CONCLUSION

The results of the digital rock constructed using CT show that the rigid grain quartz accounts for about 70% by volume, the feldspar occupies about 25% by volume, and the clay minerals account for about 5%, which can be used as input data for rock physical modeling to establish the rock physical model of heterogeneous tight sandstone.

Tight sandstone rock physical modeling is mainly composed of a boundary average model, inclusion model, and fluid replacement model. The boundary average model is used to calculate the equivalent elastic modulus of the rock mineral matrix, the inclusion model is used to calculate the dry rock matrix modulus, and the fluid replacement model is used to fill the fluid in the pores and calculate the equivalent elastic modulus of the saturated rock. In this way, the equivalent modulus of saturated rock in a tight sandstone medium can be estimated. The error between the rock physical model prediction and the experimental measurement is less than 3%, which reveals that the model prediction results can reflect the actual value with high accuracy, and the rock physical modeling results are more reliable.

The porosity of the whole reservoir is predicted based on seismic data through rock physical modeling. The average porosity of the H3a reservoir is about 5%–8%, the reservoir is thin and evenly distributed, and the porosity in the middle and northwest regions of the gas field is relatively high. The reservoir of well X-1 is slightly thicker. The porosity of the H3b reservoir is higher than that of the upper and lower mudstone formations and H3a reservoir, with a maximum of 18%–20% and an average porosity of 8%–12%. It is a thick reservoir with high porosity, relatively high porosity in the northeast and middle regions of the gas field, and relatively low porosity in the southwest. On the whole, the porosity of H3c is higher in the south and lower regions in the north. The porosity is higher near well X-3 and well X-1, and lower near well X-2. The average porosity in the south of the gas field is between 7.5% and 12%, and the average porosity in the north is less than 3%.

DATA AVAILABILITY STATEMENT

The datasets presented in this study can be found in online repositories. The names of the repository/repositories and accession number(s) can be found in the article/Supplementary Material.

AUTHOR CONTRIBUTIONS

WG: investigation, methodology, writing—original draft, and data analysis. CL: supervision and writing—review and editing. CD: supervision and writing—review and editing. YW: writing—original draft, and processing the data. XZ: methodology. JL: writing—review and editing.

FUNDING

This study was funded by the Joint Fund Projects (NO.U19B2006), the Natural Science Foundation of China (U19B200129), the Support Program of China Postdoctoral Innovative Talents (Grant No. BX2021373), and Fundamental Research Funds for the Central Universities (Grant Nos. 22CX06006A and 19CX02001A).

ACKNOWLEDGMENTS

Special thanks go to Shikai Jian, You Zhou, Rui Yang, and Yage Wang of China University of Petroleum (East China) for their constructive suggestions and for revising the manuscript. The discussion with them has played a positive role in this research and article writing.

REFERENCES

Andrä, H., Combaret, N., Dvorkin, J., Glatt, E., Han, J., Kabel, M., et al. (2013). Digital Rock Physics Benchmarks-Part I: Imaging and Segmentation. *Comput. Geosciences* 50, 25–32. doi:10.1016/j.cageo.2012.09.005

Anselmetti, F. S., Luthi, S., and Eberli, G. P. (1998). Quantitative Characterization of Carbonate Pore Systems by Digital Image Analysis[J]. *AAPG Bull.* 82 (10), 1815–1836.

Antariksa, G., Muammar, R., and Lee, J. (2022). Performance Evaluation of Machine Learning-Based Classification with Rock-Physics Analysis of Geological Lithofacies in Tarakan Basin, Indonesia. *J. Petroleum Sci. Eng.* 208, 109250. doi:10.1016/j.petrol.2021.109250

Avseth, P., Johansen, T. A., Bakhorji, A., and Mustafa, H. M. (2014). Rock-physics Modeling Guided by Depositional and Burial History in Low-To-Intermediate-Porosity Sandstones. *Geophysics* 79 (2), D115–D121. doi:10.1190/GEO2013-0226.1

Ba, J., Xu, W., Fu, L.-Y., Carcione, J. M., and Zhang, L. (2017). Rock Anelasticity Due to Patchy Saturation and Fabric Heterogeneity: A Double Double-Porosity Model of Wave Propagation. *J. Geophys. Res. Solid Earth* 122 (3), 1949–1976. doi:10.1002/2016JB013882

Bandyopadhyay, K. (2009). *Seismic Anisotropy: Geological Causes and its Implications to Reservoir Geophysics [D]*. Stanford University.

Bloch, S., Lander, R. H., and Bonnell, L. (2002). Anomalously High Porosity and Permeability in Deeply Buried Sandstone Reservoirs: Origin and Predictability [J]. *AAPG Bull.* 86 (2), 301–328. doi:10.1306/61EEDABC-173E-11D7-8645000102C1865D

Bordignon, F., de Figueiredo, L. P., Exterkoetter, R., Barbosa Rodrigues, B., and Duarte, M. (2019). Deep Learning for Grain Size and Porosity Distributions Estimation on Micro-CT Images. Proceedings of the 16th International Congress of the Brazilian Geophysical Society and Expogef. doi:10.22564/16cisbgf2019.209

Cai, J., Perfect, E., Cheng, C. L., and Hu, X. Y. (2014). Generalized Modeling of Spontaneous Imbibition Based on Hagen-Poiseuille Flow in Tortuous Capillaries with Variably Shaped Apertures[J]. *Langmuir* 30 (18), 5142–5151. doi:10.1021/la5007204

Chen, H., Zhang, G., Chen, T., and Yin, X. (2017). Joint PP- and PSV-Wave Amplitudes versus Offset and Azimuth Inversion for Fracture Compliances in Horizontal Transversely Isotropic Media[J]. *Geophys. Prospect.* 66, 561–578. doi:10.1111/1364-2478.12567

Das, P. K., Mandal, N., and Arya, A. (2017). Effects of Cation Ordering on the Elastic and Electronic Properties of Mg-Fe Silicate Phases at High Pressures[J]. *J. Appl. Phys.* 122 (22), 225107. doi:10.1063/1.500188410.1111/1365-2478.12567

de Figueiredo, L. P., Bordignon, F., Exterkoetter, R., Barbosa Rodrigues, B., and Duarte, M. (2019). Deep 3D Convolutional Neural Network Applied to CT Segmented Image for Rock Properties Prediction[J]. *Seg. Tech. Program Expand. Abstr. 2019.* doi:10.1190/segam2019-3216835.1

Deng, J. (2009). Effect of Cement on Seismic Elastic Properties of Reservoir Sandstone [J]. *J. Petroleum Nat. Gas* 31 (4), 238–242. doi:10.1007/978-1-4020-2402-3_50

Dutta, R., and Mandal, N. (2012). Effects of Pressure on the Elasticity and Stability of Zircon (ZrSiO4): First-Principle Investigations. *Comput. Mater. Sci.* 54, 157–164. doi:10.1016/j.commatsci.2011.09.035

Fawad, M., and Mondol, N. H. (2022). Monitoring Geological Storage of CO2 Using a New Rock Physics Model[J]. *Sci. Rep.* 12 (1), 1–11. doi:10.1038/s41598-021-04400-7

Golparvar, A., Zhou, Y., Wu, K., Ma, J., and Yu, Z. (2018). A Comprehensive Review of Pore Scale Modeling Methodologies for Multiphase Flow in Porous Media. *Adv. Geo-Energy Res.* 2 (4), 418–440. doi:10.26804/ager.2018.04.07

Guo, J., and Han, X. (2016). Rock Physics Modelling of Acoustic Velocities for Heavy Oil Sand. *J. Petroleum Sci. Eng.* 145, 436–443. doi:10.1016/j.petrol.2016.05.028

He, F. (2017). *Study on Rock Physical Model of Tight Sand Considering the Effect of Pore Fluid [D]*. Qingdao: China University of Petroleum.

Hilpert, M., and Miller, C. T. (2001). Pore-morphology Based Simulation of Drainage in Totally Wetting Porous Media[J]. *Adv. Water Resour.* 24 (3-4), 243–255. doi:10.1016/s0309-1708(00)00056-7

Hossain, M. M., Arns, J. Y., and Liang, Z. (2019). Humidity Effects on Effective Elastic Properties of Rock: An Integrated Experimental and Numerical Study. *Journal of Geophysical Research: Solid Earth* 124 (8), 7771–7791. doi:10.1029/2019JB017672

Hu, Z., Li, Y., Huang, S., Lv, J., and Zhu, B. (2012). Research Progress on Destruction and Preservation Mechanism of Primary Pores in Sandstone Reservoirs [J]. *Prog. Earth Sci.* 27 (01), 14–25. doi:10.1007/s13202-020-01042-9

Jadoon, Q. K., Roberts, E., Blenkinsop, T., Wust, R. A. J., and Shah, S. A. (2016). Petrophysical Evaluation and Uncertainty Analysis of Roseneath and Murteree Shales Reservoirs in Cooper Basin, Australia (A Case Study). *J. Petroleum Sci. Eng.* 147, 330–345. doi:10.1016/j.petrol.2016.06.010

Jian, S., Fu, L., Wang, Z., Han, T. C., and Li, J. I. (2020). Elastic Equivalent Numerical Modeling Based on the Dynamic Method of Longmaxi Formation Shale Digital Rock[J]. *Chin. J. Geophys.* 63 (7), 2786–2799. doi:10.6038/cjg2020N0312

Kuster, G. T., and Toksöz, M. N. (1974). Velocity and Attenuation of Seismic Waves in Two-phase Media: Part I. Theoretical Formulations. *Geophysics* 39 (5), 587–606. doi:10.1190/1.1440450

Laird, A. D. K., and Putnam, J. A. (1951). Fluid Saturation in Porous Media by X-Ray Technique. *Pet. Trans. AIME* 3, 275–284. doi:10.2118/951275-g

Lin, C., Wu, Y., and Ren, L. (2018). Review of Digital Rock Modeling Methods[J]. *Prog. Geophys.* 33 (2), 0679–0689. doi:10.6038/pg2018BB0335

Liu, M., Grana, D., and de Figueiredo, L. P. (2022). Uncertainty Quantification in Stochastic Inversion with Dimensionality Reduction Using Variational autoencoderUncertainty Quantification in Stochastic Inversion with Dimensionality Reduction Using Variational Autoencoder[J]. *Geophysics* 87 (2), M43–M58. doi:10.1190/geo2021-0138.1

Liu, M., and Grana, D. (2018). Stochastic Nonlinear Inversion of Seismic Data for the Estimation of Poroelastic Properties Using the Ensemble Smoother and Data Reparameterization[J]. *Geophysics* 83 (3), M25–M39. doi:10.1190/geo2017-0713.1

Liu, M., and Mukerji, T. (2022). Multiscale Fusion of Digital Rock Images Based on Deep Generative Adversarial Networks. *Geophys. Res. Lett.* 49, e2022GL098342. doi:10.1029/2022GL098342

Ma, Z., Zuo, Y., Lu, C., and Miao, X. (2019). Application of Computed Tomography (CT) in the Observation of Meso-Structure of Minerals and Rocks [J]. *Miner. Metall. Process.* 48 (3), 4–8. doi:10.1016/j.jngse.2020.103591

Mao, W., Lv, Q., Peng, Y. U., and Liu, J. (2022). Analysis of Mineral Composition and Meso-Structure of Granite Using CT Images[J]. *J. Eng. Geol.* 30 (1), 216–222. doi:10.13544/j.cnki.jeg.2020-121

Markus, H., and Cass, T. M. (2001). Pore-Morphology-Based Simulation of Drainage in Totally Wetting Porous Media. *Advances in Water Resources* 24, 243–255. doi:10.1016/S0309-1708(00)00056-7

Mavko, G., Mukerji, J., and Dvorkin, J. (2009). *The Rock Physics Handbook*. Second Edition. Cambridge: Tools for Seismic Analysis of Porous MediaCambridge University Press.

Miao, T., Yu, B., Duan, Y., and Fang, Q. (2015). A Fractal Analysis of Permeability for Fractured Rocks. *Int. J. Heat Mass Transf.* 81, 75–80. doi:10.1016/j.ijheatmasstransfer.2014.10.010

Nie, X. (2014). *Research on Digital Rock Modeling and Conductivity Numerical Simulation of Shale Gas Reservoir Rock[D]*. Beijing: China University of Geosciences.

Nie, X., Zou, C., Li, Z., Meng, X., and Qi, X. (2016). Numerical Simulation of the Electrical Properties of Shale Gas Reservoir Rock Based on Digital Core[J]. *J. Geophys. Eng.* 13 (4), 481–490. doi:10.1088/1742-2132/13/4/481

Pan, G., Liang, L., and Habashy, T. M. (2019). A Numerical Study of 3D Frequency-Domain Elastic Full-Waveform Inversion. *Geophysics* 84, R99–R108. doi:10.1190/geo2017-0727.1

Pan, X., Zhang, G., and Yin, X. (2017). Azimuthally Anisotropic Elastic Impedance Inversion for Fluid Indicator Driven by Rock Physics. *Geophysics* 82, C211–C227. doi:10.1190/geo2017-0191.1

Pan, X., Zhang, P., Zhang, G., Guo, Z., and Liu, J. (2021). Seismic Characterization of Fractured Reservoirs with Elastic Impedance Difference versus Angle and Azimuth: A Low-Frequency Poroelasticity Perspective. *Geophysics* 86, M123–M139. doi:10.1190/geo2020-0492.1

Radlinski, A. P., Ioannidis, M. A., Hinde, A. L., Hainbuchner, M., Baron, M., Rauch, H., et al. (2004). Angstrom-to-millimeter Characterization of Sedimentary Rock Microstructure. *J. Colloid Interface Sci.* 274 (2), 607–612. doi:10.1016/j.jcis.2004.02.035

Reuss, A. (1929). Berechnung der Fließgrenze von Mischkristallen auf Grund der Plastizitätsbedingung für Einkristalle. *Z. angew. Math. Mech.* 9, 49–58. doi:10.1002/zamm.19290090104

Saenger, E. H., and Bohlen, T. (2004). Finite-difference Modeling of Viscoelastic and Anisotropic Wave Propagation Using the Rotated Staggered Grid. *Geophysics* 69 (2), 583–591. doi:10.1190/1.1707078

Shao, C. (2009). Inversion of S-Wave Velocity Based on Rock Physics and Multi-Mineral Analysis Using Conventional Logging Data [J]. *J. China Univ. Geosci.* 34 (4), 699–707.

Shi, Y. (2009). *Fluid Substitution Based on Gassmann Equation [D]*. Chengdu: Chengdu University of Technology.

Tang, X. (2011). Unified Theory of Elastic Wave Propagation in Porous and Fractured Media — Extension of Biot's Theory [J]. *Sci. China Earth Sci.* 41 (6), 784–795. doi:10.1007/s11430-011-4245-7

Voigt, W. (1907). Bestimmung der Elastizitätskonstanten von Eisenglanz. *Ann. Phys.* 327, 129–140. doi:10.1002/andp.19063270108

Wang, Y. (2006). Reservoir Identification Method Based on Rock Physical Simulation of Logging Data [J]. *Geophys. Prospect.* 41 (6), 644–650.

Wang, Y., Shabaninejad, M., and Armstrong, P. (2021). Deep Neural Networks for Improving Physical Accuracy of 2D and 3D Multi-Mineral Segmentation of Rock Micro-CT Images[J]. *Appl. Soft Comput.* 104, 107185. doi:10.1016/j.asoc.2021.107185

Wei, Y., Nie, X., Jin, L., Zhang, C., Xhang, C., and Zhang, Z. (2018). Investigation of Sensitivity of Shale Elastic Properties to Rock Components Based on a Digital Core Technology and Finite Element Method[J]. *Arab. J. Geosci.* 11, 1–14. doi:10.1007/s12517-018-3576-5

Wildenschild, D., and Sheppard, A. P. (2013). X-ray Imaging and Analysis Techniques for Quantifying Pore-Scale Structure and Processes in Subsurface Porous Medium Systems. *Adv. Water Resour.* 51, 217–246. doi:10.1016/j.advwatres.2012.07.018

Wu, Y., Lin, C., Ren, L., Yan, W., An, S., Chen, B., et al. (2018). Reconstruction of 3D Porous Media Using Multiple-point Statistics Based on a 3D Training Image. *J. Nat. Gas Sci. Eng.* 51, 129–140. doi:10.1016/j.jngse.2017.12.032

Wu, Y., Tahmasebi, P., Lin, C., and Dong, C. (2019c). Process-based and Dynamic 2D Modeling of Shale Samples: Considering the Geology and Pore-System Evolution[J]. *Int. J. Coal Geol.* 218, 103368. doi:10.1016/j.coal.2019.103368

Wu, Y., Tahmasebi, P., Lin, C., and Dong, C. (2020a). A Comprehensive Investigation of the Effects of Organic-Matter Pores on Shale Properties: A Multicomponent and Multiscale Modeling. *J. Nat. Gas Sci. Eng.* 81, 103425. doi:10.1016/j.jngse.2020.103425

Wu, Y., Tahmasebi, P., Lin, C., Munawar, M. J., and Cnudde, V. (2019a). Effects of Micropores on Geometric, Topological and Transport Properties of Pore Systems for Low-Permeability Porous Media. *J. Hydrol.* 575, 327–342. doi:10.1016/j.jhydrol.2019.05.014

Wu, Y., Tahmasebi, P., Lin, C., Zahid, M. A., Dong, C., Golab, A. N., et al. (2019b). A Comprehensive Study on Geometric, Topological and Fractal Characterizations of Pore Systems in Low-Permeability Reservoirs Based on SEM, MICP, NMR, and X-Ray CT Experiments. *Mar. Pet. Geol.* 103, 12–28. doi:10.1016/j.marpetgeo.2019.02.003

Wu, Y., Tahmasebi, P., Yu, H., Lin, C., Wu, H., and Dong, C. (2020b). Pore-Scale 3D Dynamic Modeling and Characterization of Shale Samples: Considering the Effects of Thermal Maturation. *J. Geophys. Res. Solid Earth* 125 (1), e2019JB018309. doi:10.1029/2019JB018309

Yang, Y., Zhou, Y., Blunt, M. J., Yao, J., and Cai, J. (2021). Advances in Multiscale Numerical and Experimental Approaches for Multiphysics Problems in Porous Media. *Adv. Geo-Energy Res.* 5 (3), 233–238. doi:10.46690/ager.2021.03.01

Yin, X., Zheng, Y., and Zong, Z. (2017). Research on the Equivalence between Digital Core and Rock Physics Models. *J. Geophys. Eng.* 14 (3), 666–674. doi:10.1088/1742-2140/aa6650

Yin, X., Zong, Z., and Wu, G. (2015). Research on Seismic Fluid Identification Driven by Rock Physics. *Sci. China Earth Sci.* 58 (2), 159–171. doi:10.1007/s11430-01404992-3

Zhang, J.-J., Zhang, G.-Z., and Huang, L.-H. (2019). Crack Fluid Identification of Shale Reservoir Based on Stress-dependent Anisotropy. *Appl. Geophys.* 16 (2), 209–217. doi:10.1007/s11770-019-0754-5

Zhang, J., Yin, X., Zhang, G., Gu, Y., and Fan, X. (2020b). Prediction Method of Physical Parameters Based on Linearized Rock Physics Inversion. *Pet. Explor. Dev.* 47 (1), 59–67. doi:10.1016/s1876-3804(20)60005-2

Zhang, J., Yin, Y., and Zhang, G. (2020a). Rock Physics Modelling of Porous Rocks with Multiple Pore Types: a Multiple-porosity Variable Critical Porosity Model. *Geophys. Prospect.* 68, 955–967. doi:10.1111/1365-2478.12898

Zhao, L., Qin, X., Han, D.-H., Geng, J., Yang, Z., and Cao, H. (2016). Rock-physics Modeling for the Elastic Properties of Organic Shale at Different Maturity Stages. *Geophysics* 81 (5), D527–D541. doi:10.1190/geo2015-0713.1

Zhou, Z. (2010). Study on the Calculation Method of S-Wave Velocity Constrained by Logging Based on Rock Physics Model [J]. *J. Geochem. Explor.* 32 (5), 536–541.

Zhu, L., Zhang, C., Zhang, C., Zhou, X., Zhang, Z., Nie, N., et al. (2019). Challenges and Prospects of Digital Core-Reconstruction Research[J]. *Geofluids* 2019, 7814180. doi:10.1155/2019/7814180

Zhu, W., Zhao, L., and Shan, R. (2017). Modeling Effective Elastic Properties of Digital Rocks Using a New Dynamic Stress-Strain Simulation Method. *Geophysics* 82 (6), MR163–MR174. doi:10.1190/geo2016-0556.1

Zong, Z., and Yin, X. (2017). Model Parameterization and P-Wave AVA Direct Inversion for Young's Impedance. *Pure Appl. Geophys.* 174 (5), 1965–1981. doi:10.1007/s00024-017-1529-7

Zong, Z., Yin, X., and Wu, G. (2015). Geofluid Discrimination Incorporating Poroelasticity and Seismic Reflection Inversion. *Surv Geophys.* 36 (5), 659–681. doi:10.1007/s10712-015-9330-6

Conflict of Interest: The authors declare that the research was conducted in the absence of any commercial or financial relationships that could be construed as a potential conflict of interest.

frontiers | Frontiers in Earth Science

REVIEW
published: 12 July 2022
doi: 10.3389/feart.2022.930474

Microstructure Characterization Techniques for Shale Reservoirs: A Review

Yujing Qian[1,2], *Ping Gao*[1,2]*, *Xianglong Fang*[1,2], *Fengrui Sun*[1,2], *Yidong Cai*[1,2] and *Yingfang Zhou*[3]

[1]School of Energy Resources, China University of Geosciences, Beijing, China, [2]Coal Reservoir Laboratory of National Engineering Research Center of CBM Development & Utilization, China University of Geosciences, Beijing, China, [3]School of Engineering, King's College, University of Aberdeen, Aberdeen, United Kingdom

The microstructure of shale reservoirs refers to the distribution of mineral–organic matter, pore–fracture features, diagenetic processes, and their interrelations. The comprehensive and accurate analysis of the shale microstructure plays a critical role in formulating a reasonable development plan and optimizing measures to enhance oil or gas recovery. To explore the microstructure characterization, the mineral and organic matter compositions as well as the pore types and distributions of organic-rich shale reservoirs were investigated using a series of advanced techniques, including focused ion beam–scanning electron microscopy and atomic force microscopy. This review establishes a model of pore distribution of the layered structure of shale reservoirs based on ideal shale laminae model. Among them, quartz and carbonate laminae can be classified as grain laminae clay minerals and organic matter and pyrite can be combined into organic matter aggregate due to the symbiotic relationship between pyrite, organic matter and clay minerals. Microcracks of diverse diagenetic origins can be classified together. This review also systematically summarizes the microcharacterization techniques and different characteristics of organic-rich shale reservoirs, thereby paving the way for the establishment of shale cross-scale characterization techniques.

Keywords: shale, microcharacterization, pore type, technology application, mineral

Edited by:
Yuqi Wu,
China University of Petroleum, China

Reviewed by:
Peng Cheng,
Guangzhou Institute of Geochemistry (CAS), China
Qin Zhou,
Guangzhou Institute of Geochemistry (CAS), China

***Correspondence:**
Ping Gao
gaoping1212@cugb.edu.cn

Specialty section:
This article was submitted to Solid Earth Geophysics, a section of the journal Frontiers in Earth Science

Received: *28 April 2022*
Accepted: *31 May 2022*
Published: *12 July 2022*

Citation:
Qian Y, Gao P, Fang X, Sun F, Cai Y and Zhou Y (2022) Microstructure Characterization Techniques for Shale Reservoirs: A Review. Front. Earth Sci. 10:930474. doi: 10.3389/feart.2022.930474

1 INTRODUCTION

In the past two decades, the increasing demand for energy and the accompanying energy has forced people to pay more attention to other energy sources that can replace conventional oil and gas. The exploration, production, and development of unconventional oil and gas resources, e.g., shale gas, have greatly solved the problem of human energy demand. Shale gas is natural gas stored in shale, which is traditionally considered to be the seal rock (Zou et al., 2015). With the characteristics of efficient development and environmental protection, shale gas has become an important strategic energy source for many countries around the world. The large-scale exploitation of shale gas helps alleviate the pressure of the energy supply. In order to reduce the dependence on foreign oil, China has experienced rapid development of shale gas reserves and development technology. By 2020, the annual output of shale gas was 200×10^8 m^3 in shallowly buried depths (<3,500 m), and major breakthroughs have also been made in the deep shale (burial depth of 3,500–4,000 m (Zou et al., 2021). The reservoir microstructure of organic-rich shale, which is composed of diagenetic minerals, organic matter, and pore

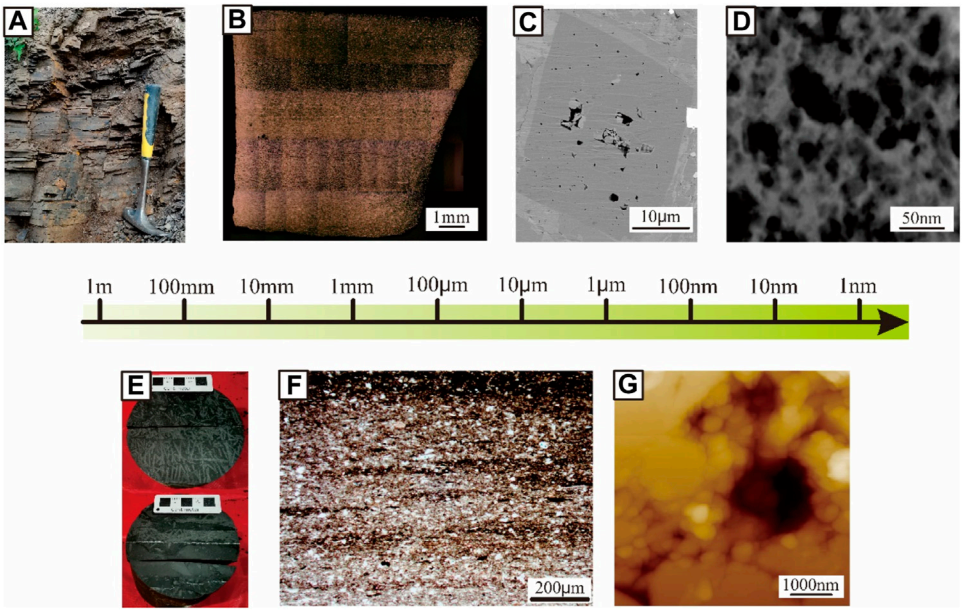

FIGURE 1 | Microscopic characteristics of shale at various scales. **(A)** XHY-1 shale outcrop of the Xiamaling Formation in the Zhangjiakou section; **(B)** Reflected light image of argon ion polished shale (PS1-2, Wufeng Formation, 5964.5 m); **(C)** FESEM image of argon ion polished shale (N228-14, Longmaxi Formation, 3,377.9 m); **(D)** Scanning transmission electron microscopy image of kerogen from the Barnett shale sample (Curtis et al., 2011); **(E)** Photos of shale cores of Longmaxi Formation in the Sichuan Basin (DY5-49, 3,811.5 m); **(F)** Single polarized light image of Longmaxi Formation shale in Yanjin (N228-1, 3,365.1 m); and **(G)** Atomic force microscopy images of micropores in polished shale (JY4-05, Wufeng Formation, 2,591.7 m).

network, is a key factor affecting the shale gas storage and seepage, thereby influencing shale gas enrichment and its yields.

With the increase in shale gas exploration, it has been found that there are great differences in the diagenetic minerals, organic matter, and pore network structure of different shales (Peltonen et al., 2009; Ross and Bustin, 2009; Xiao et al., 2015). The research methods mainly include scanning electron microscopy (SEM), mercury intrusion, and liquid nitrogen adsorption. However, the distribution of pores in shale reservoirs remains unclear, and a unified technical system and standard for the full-scale pore characterization are also lacking. Therefore, the purpose of this article is to 1) summarize the distribution of minerals, organic matter, and pore network structure; 2) conduct a comparative study on the evaluation methods of microscopic pore–fracture network structure of shale reservoirs; and 3) sort out the principles, scales, and characteristics of various testing methods. In addition, this review will provide a basis for the evaluation of shale reservoirs and the prediction of "sweet-spots," thereby providing a scientific support for shale gas exploration.

2 MICROSCOPIC CHARACTERISTICS OF SHALE RESERVOIRS

The practice of shale gas exploration shows that the gas production from shale with laminar structures is significantly different from that of conventional sandstone reservoir. From the field outcrop of the Xiamaling Formation, the shale generally exhibits gray bedding, and the thickness of a single layer is 0.5–10 cm. Fossils, mineral particles, and bedding in shale can be observed at a scale of 100 mm–100 μm. Pores in shale minerals and organic matter can be observed at the micro-nano scale, thereby showing the internal morphology of various pores (**Figure 1**). Numerous previous works have proved that the shale reservoirs display strong heterogeneity because of their bedding, and differences are found in mineral composition, organic matter distribution, and pore structure in laminated shale (Qiu and Zou, 2020; Sang et al., 2022).

As the most characteristic sedimentary feature in shale, laminar structure is an indispensable content in the basic research and exploration of unconventional oil sedimentology. In the study of laminae of marine shale and continental shale, researchers found that silty laminae demonstrate an important influence on the pore structure (Ross and Bustin, 2009; Lei et al., 2015). Many researchers have divided the Chang seven shales into bright and dark layers, and they pointed out that the contents of plagioclase and illite were the main difference between the bright and dark layers (Liu et al., 2016a; Liu et al., 2016b; Liu G. et al., 2021). Some authors have compared and evaluated the mineral compositions of argillaceous laminae and silty laminae in the Longmaxi Formation shale, and they pointed out that the contents of quartz and carbonate displayed the obvious differences (Shi et al., 2018; Liu et al., 2019a). For the pore structure of shale, researchers proposed that the development of laminae controls the size and pore-size distribution of inorganic macropores, which affects the pore structure and fracture formation of shale, and it is conducive to improving

TABLE 1 | The type of shale pores (Loucks et al., 2012).

Pore types of shale	
Interparticle pores	Pores between grains Pores between crystals Pores between clay platelets Pores at the edge of rigid grains
Intraparticle pores	Intercrystalline pores within pyrite framboids Pores within peloids or pellets Pores within fossil bodies Intraplatelet pores within clay platelets Moldic pores Dissolution-rim pores
Organic Matter pores	
Fracture pores	

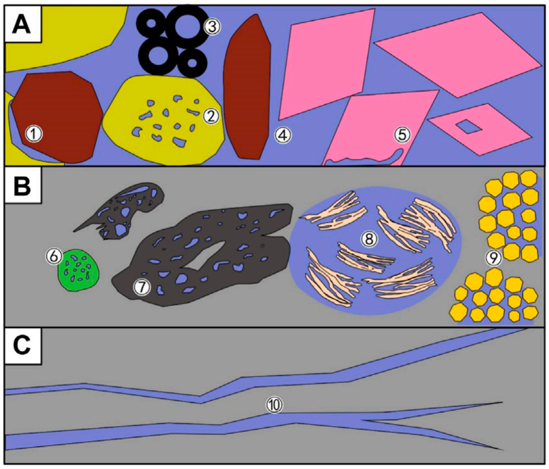

FIGURE 2 | Key components of shale microstructure and their relationships with pores. **(A)** Grain laminae: (1) pores at the edge of rigid grains, (2) moldic pores, (3) pores within fossil bodies, (4) pores between grains and crystals, and (5) dissolution-rim pores; **(B)** Organic-matter aggregates: (6) pores within peloids or pellets, (7) organic-matter pores, (8) pores between or within clay platelets, and (9) intercrystalline pores within pyrite framboids; and **(C)** (10) fracture.

the physical properties of the reservoir, especially the horizontal permeability (Li J. et al., 2015; Lai et al., 2018; Wu et al., 2019b; Wu et al., 2020a).

According to different sedimentary environments, shale can be divided into marine shale, transitional shale, and continental shale, all of which are ideal gas producing formations (Zou et al., 2017). These shales display different compositions of minerals and organic matter, and a series of measurement methods, such as X-ray diffraction, organic kerogen extraction, etc., could help us form a clear understanding of the components of shales. Generally speaking, laminae is a common feature indicating the sedimentary environment, which is also a constituent unit of minerals and organic matter. With the change in the sedimentary environment, the laminae usually contain different components, such as clay minerals, clastic minerals, such as quartz and feldspar, carbonate minerals, and organic matter (Ingram, 1954).

According to **Table 1**, pores in shale can be divided into interparticle pores, intraparticle pores, organic matter pores, and fracture according to different carriers (Loucks et al., 2012). Inspired by the laminar structure of shale (Ingram, 1954; Campbell, 1967; Lazar et al., 2015; Qiu and Zou, 2020; Yang et al., 2020), the shale can be simplified into a superimposed model of grain laminae, organic matter aggregate, and fracture (**Figure 2**). Grain laminae include carbonate and quartz-feldspar lamina, which are composed of quartz, feldspar, calcite, dolomite, etc. It can be found to be granular or crystalline under the microscope (**Figure 4**). Next, these laminae determine the brittleness of the shale and provide some stiffness to the overall structure of the rock. Organic matter aggregate is shale's important carrier of pore space. Organic matter, clay minerals, and pyrite are closely associated. Organic matter consists of kerogen and asphalt, which can be thermally cracked to be gas at the same time, thereby forming a large number of micro/nanoscaled pores. Organic matter is the parent material of hydrocarbon generation in shales and yields the important nanoscale reservoir spaces with increasing maturity. Clay minerals consist of kaolinite, chlorite, illite, and montmorillonite, which exhibit high plasticity, and under the condition of high maturity, will develop larger specific surface area of clay mineral contents of pore (Li C. et al., 2019) and store a certain amount of adsorbed gas and free gas. Next, the presence of pyrite indicates a reducing environment and often coexists with organic matter and clay. Due to its strong rigidity, intercrystalline pores may be found within pyrite framboids. Microfractures include bedding fractures, tectonic stress fractures, dissolution fractures, and contraction fractures of diagenetic dehydration/recrystallization, which are good hydrocarbon migration channels and an important part of the pore network.

Due to the existence of large number of micro-nano scale pores and fractures in shale, shale can become a natural gas reservoir; this has been proved by the practice of exploration and development at home and abroad. For shale gas reservoirs, micro/nanopores network can provide a storage space for free and adsorbed gases. On the other hand, the presence of numerous pores increases the specific surface area of the shale reservoir, thereby increasing the potential content of shale gas in the adsorbed state (Curtis, 2002). In addition, the existence of connected pores and fractures increases the seepage capacity of the reservoir to a certain extent, thereby facilitating the effective exploitation of shale gas. Therefore, the difficulty of microstructure research is the study of the spatial configuration of minerals, organic matter, and pores. The existing technology or system is only partially mature, and the splicing of scales and cross-scale research still need to be systematically improved and studied. The following is a brief introduction of several microstructural research methods focusing on pore space and mineral–organic matter associations.

3 TECHNIQUES FOR SHALE MICROSTRUCTURE CHARACTERIZATION

For the characterization of microscopic minerals, organic matter, and the pore–fracture network structure in shale reservoirs, the

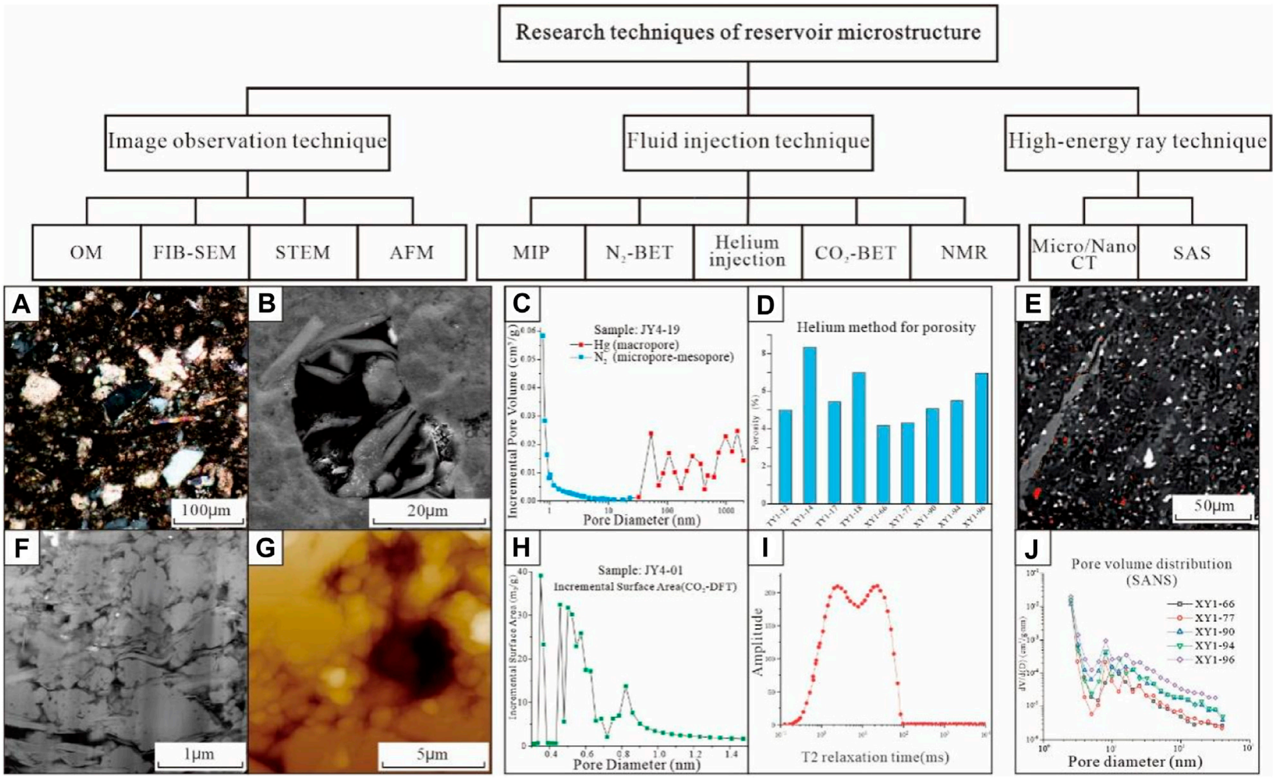

FIGURE 3 | Research method of reservoir microstructure. **(A)** Distribution of components in N228 shale under orthogonal polarization; **(B)** Focused ion beam–scanning electron microscopy images of pore fractures and minerals in XHY-1; **(C)** Characterization of shale pore distribution by mercury injection and nitrogen adsorption; **(D)** Porosity measured by helium injection; **(E)** Two-dimensional distribution of shale minerals and fractures under micro CT (Gou et al., 2019); **(F)** Shale dark field scanning transmission electron microscopy image (Peng et al., 2014); **(G)** JY4-05 (Wufeng Formation, 2591.7 m) shale surface topography under atomic force microscopy; **(H)** The surface area distribution of carbon dioxide adsorption; **(I)** Nuclear magnetic resonance of water-saturated shale (Sun et al., 2012); and **(J)** Shale pore volume distribution under small angle neutron scattering (Sun M. et al., 2017)).

techniques can be classified into three categories (**Figure 3**): image observation method, fluid injection method, and high-energy ray method. These methods for characterizing reservoir parameters exhibit certain differences. Image observation method focuses on direct observation, and resolution is the key. It is mainly used to study the size, morphology, and distribution of minerals, organic matter, and pores qualitatively. Next, the fluid injection method is an indirect measurement method, and the research scale is the key technology. It is mainly used to quantitatively analyze the size and distribution of the reservoir space. The high-energy ray method is also an indirect analysis method, and its repeatability is the key technology. Its advantage is that it can quantitatively analyze the shape, size, and distribution characteristics of closed pores and joints (**Table 2**).

3.1 Imaging Techniques and Microstructure Morphology

3.1.1 Advantage and Limitations

The image observation method mainly uses a microscope (optical microscopy, focused ion beam–SEM (FIB-SEM), atomic force microscopy (AFM), and scanning transmission electron microscopy (STEM)) to observe directly, and it carries out the statistical analysis of reservoir minerals, organic matter, and pores and fissures.

Optical microscopy is a direct observation of the thin reservoir pore structure, but the resolution is low: approximately 0.01 mm. It is mainly suitable for qualitative research on larger pores but cannot meet the needs of the observation of micro-nanopores in unconventional reservoirs. Although optical microscopy can exhibit a relatively comprehensive control of the sample, it can see the type and shape of inclusions in the thin section and then determine the gas generation stage of the target shale; at the same time, it can observe the mineral arrangement and morphological characteristics in the thin section to understand the diagenesis process. By observing the proportion and types of minerals in the reflected light mode (**Figure 4**), the source and genesis can be analyzed, but optical microscopy also exhibits the disadvantage of difficulty with quantitatively characterizing the size and connectivity of the reservoir space; thus, it needs to be used in combination with other methods.

The principle of FIB-SEM is to continuously cut the sample with a gallium ion beam and image it under the electron beam at the same time. Three-dimensional structural characteristics of shale nanopores are truly restored, and the analysis results of the three-dimensional spatial composition, pore-size distribution,

TABLE 2 | Techniques for shale microstructure characterization.

		Advantages	Disadvantages	Applicability	Limitation
Image observation technique	Optical microscope	A direct observation of the thin reservoir pore structure	The resolution is low: approximately 0.01 mm	It is mainly suitable for qualitative research on larger pores (> 0.01 mm)	It is difficult to quantitatively characterize the connectivity of the reservoir space
	FIB-SEM	Three-dimensional structural characteristics of shale are truly restored	Pores with diameters less than resolution or cutting spacing are not counted	It is suitable for studying the three-dimensional structure of nanoscale pores (>1 nm) in shales	The test does not count pores smaller than 10 nm in diameter, thereby making the experimental results smaller than the actual value
	STEM	It can characterize the three-dimensional nano structure of shale	The two-dimensional image contains both surface and interior information, which reduces the ability to characterize the pore structure of the shale surface	Suitable for the study of organic matter and mineral crystal structure (0.1 nm)	Very high requirements for sample preparation
	AFM	It can obtain the morphological features of the sample surface	Small imaging range and slow speed	It can be used to observe pore distribution (> 0.1 nm)	Very high requirements on the surface roughness of the sample
Fluid injection technique	MIP	High consistency between experimental results and physical property test results	It will destroy the sample and create artificial cracks	Describe reservoir pore-throat characteristics and seepage capacity	Experimental error exists in the measurement of pore throats with pore diameter less than 50 nm
	N2-BET	It can accurately characterize the pore volume and specific surface area of mesopores	The measurement error of rock samples with small contrast surface area is large	The test object is mesopore. Not suitable for measurement under high-temperature and high-pressure conditions	There is an error in measuring shales with a smaller specific surface area. It is not accurate enough to measure pores with pore sizes beyond 100 nm
	Helium injection	It can get the porosity parameter of connected pores	Only connected pores can be studied	It applies to the determination of porosity	It is difficult to reflect the pore-throat distribution
	CO_2-BET	The CO_2 can enter the pores with diameter of approximately 0.35 nm, which help calculate the micropore distribution in the sample	The particle size and water content of the sample affects the accuracy of the results	Mainly measures connected micropores with a pore size of 0.35–1.5 nm	May not harmonize sample handling standards and key experimental parameters
	NMR	Able to conduct research on pore distribution, oil–water distribution, and rock internal structure. The experiment process is fast, nondestructive, and intuitive	The experimental results are affected by many factors, such as the environment, instrument parameters, micropores of the sample, and fluid types	It can reflect the size, distribution, connectivity, and fluid occurrence characteristics of shale pores	The accuracy of the results is subject to the influence of test environment, fluid properties, and other factors
High-energy ray technique	Micro/ Nano-CT	It can characterize the three-dimensional structure of pores, which can be used to evaluate the connectivity of pores		It can present the three-dimensional spatial structure of pores and evaluate the connectivity of pores	The reliability of the reconstructed model needs to be verified after imaging
	SAS	1. The experimental results have high accuracy and repeatability 2. Will not destroy the sample 3. It can be combined with fluid injection method to obtain the structural characteristics of closed pores of shales	1.Expensive 2.The detection range is concentrated in the range of micropores and mesopores	It is suitable for closed pore research of shale	1. It is difficult to acquire synchrotron radiation machine 2. The pore structure interpretation model (SAS) of shale is not yet mature, which cannot explain the experimental results; 3. The particle size of shale is between 30 nm and 60 μm, and the density is more than 2 g/cm^3, which is beyond the most effective research range of SAS

and connectivity of pores are more accurate (**Figure 5**). Therefore, FIB-SEM is currently the main technical means for studying the three-dimensional structure of shale nanoscale pores (Chalmers et al., 2012; Loucks et al., 2012). Previous authors (Loucks and Reed, 2014; Cheng et al., 2018) analyzed the source of organic pores by the ion polishing–SEM method, and based on this analysis, they further proposed an evolution model of organic pores. The study of organic pores is carried out, the morphology and porosity of different types of organic pores are described in detail, and the geological factors affecting their development are

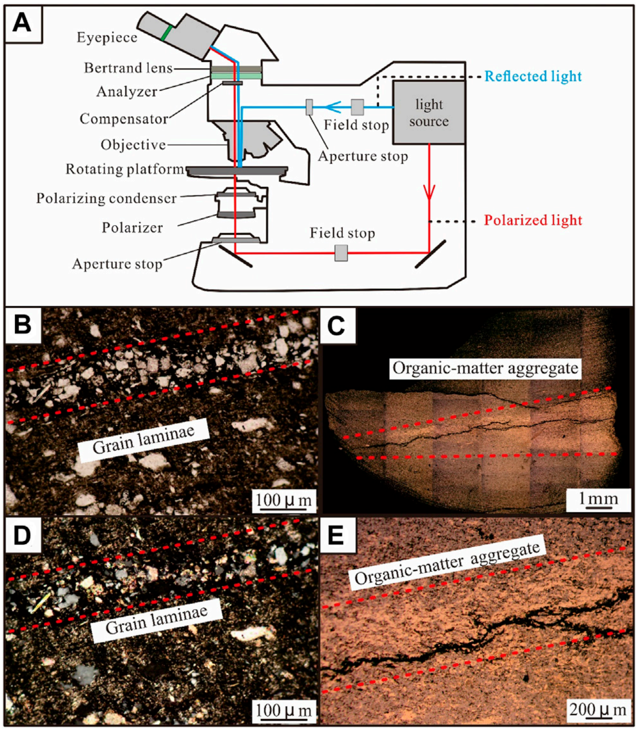

FIGURE 4 | Principle of optical microscope. **(A)** Structure of polarized and reflected light microscopes; **(B)** Grain and crystal lamina in N228-57 (Longmaxi Formation, 3,420.96) at single polarization; **(C)** Stitching picture of reflected light of shale (PS1-06) polished by argon ion; **(D)** Grain laminae in N228-57 at orthogonal polarization; and **(E)** Organic matter aggregate under a reflected light microscope (PS1-06, Longmaxi Formation, 5,957.2 m).

discussed. Using FIB-SEM technology, high-resolution SEM images can be obtained to quantitatively characterize the three-dimensional pore structure of shale at nanoscale. However, due to the limitations of experimental equipment parameters, FIB-SEM demonstrates certain limitations in studying shale porosity and connectivity. Specifically, considering the stability of the ion beam, pores with diameters less than resolution or cutting spacing were not counted, while pores with diameters less than 10 nm were developed in a large number in shale, thereby resulting in porosity results less than the actual value and affecting the calculation and judgment of connectivity (Wang et al., 2018b).

The emergence of AFM technology further improved the resolution to 0.1 nm on the basis of scanning electron microscopy technology. AFM is a scanning probe technology, which, in the early days, was mostly used in biological research. To obtain the topographical structure characteristics of the sample surface, AFM can detect the interaction between samples by measuring the force-sensitive element (**Figure 6**). In this technology, one end of the cantilever arm, which is very sensitive to weak force, is fixed, the colloidal probe at the other end is used to approach the sample to interact, and the repulsive force causes the cantilever arm to be slightly deformed. The small displacement of the cantilever arm is converted into the probe displacement with the help of the principle of optical leverage to obtain the information on the surface topography and roughness of the sample. At present, AFM is widely used in the characterization of shale pores (Cai, 2015), mainly for the observation of pores with a pore diameter of 2–50 nm in shale reservoirs and the study of shale gas storage capacity. Generally speaking, shale samples with lower surface roughness demonstrate smaller specific surface area and poor gas adsorption capacity; shale samples with higher surface roughness demonstrate larger specific surface area and can provide more gas adsorption space (Bai et al., 2016). In addition, AFM is also used to study the wettability of reservoirs. AFM probes can be directly used to measure the thickness of the oil–water film on the surface of the reservoir rock and the force between the material and the liquid film. The degree of characterization can be used to study changes in the wettability of solid surfaces (Wang et al., 2018a).

To form the image, STEM, with a resolution of 0.1–0.2 nm, uses a solid angle scattering generated by the collision of an accelerated concentrated electron beam with a very thin sample. STEM is usually applied to study the crystal structure defects of minerals (Zhang et al., 2012). Previous authors (Bernard et al., 2011; Anderson, 2014) made an attempt to study the nanoscale pore-throat structure of mud shale with different maturity using STEM. They found that organic matter displayed uniform morphological characteristics under SEM, while it showed the different properties under STEM, such as gray scale gradient and energy spectrum characteristics, thus suggesting that multiple types of organic matter exist with different lattice structures in shale, thereby enhancing the understanding of organic matter types and pore evolution of shales. In addition, STEM's penetration imaging features allow three-dimensional micro-nano structures of reservoirs to be characterized (Zhu R. et al., 2016).

Artificial cracks are distinguished in different ways under different equipment. Under an optical microscope, artificial cracks can be distinguished under orthogonal polarized light because they are completely extinct and their height is lower than other minerals. No filler is found in the artificial crack under FIB-SEM, the crack surface is not straight, and no friction mark and fixed direction exist. When scanning the topography under AFM, the crack can be directly observed. It can be judged as artificial cracks according to the fracture, no filling inside, and irregular fracture direction.

3.1.2 Pore, Mineral, and Organic Matter Morphology of Shale Reservoirs

The study of complex pore structures is the key to understanding the mechanism of shale gas accumulation. The pore structure of shale demonstrates a certain particularity due to sedimentation, diagenesis, and geological tectonic transformation (Evdokimov et al., 2006; Bustin et al., 2008). The pore–fracture system in shale includes pores and microfractures, whose pores mainly include organic pores, intragranular pores, and intergranular pores (Loucks et al., 2012; Zhou et al., 2016). Shale is mainly composed of quartz, feldspar, calcite, dolomite, clay minerals, pyrite, and other minerals. Based on the image observation, these

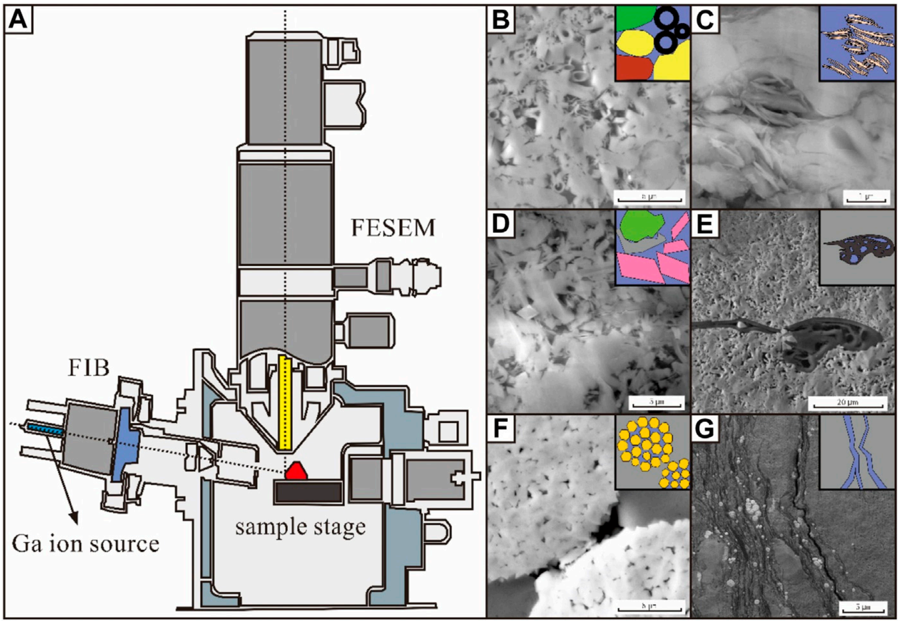

FIGURE 5 | Focused ion beam–scanning electron microscopy (FIB-SEM) structure and the image of shale pore structure: **(A)** Structure of FIB-SEM; **(B)** Intergranular pores and fossil pores; **(C)** Pores between clay platelets; **(D)** Pores between crystals and pores at the edge of rigid grains; **(E)** Organic matter pores; **(F)** Intercrystalline pores within pyrite framboids; and **(G)** Fracture pores (Anderson, 2014).

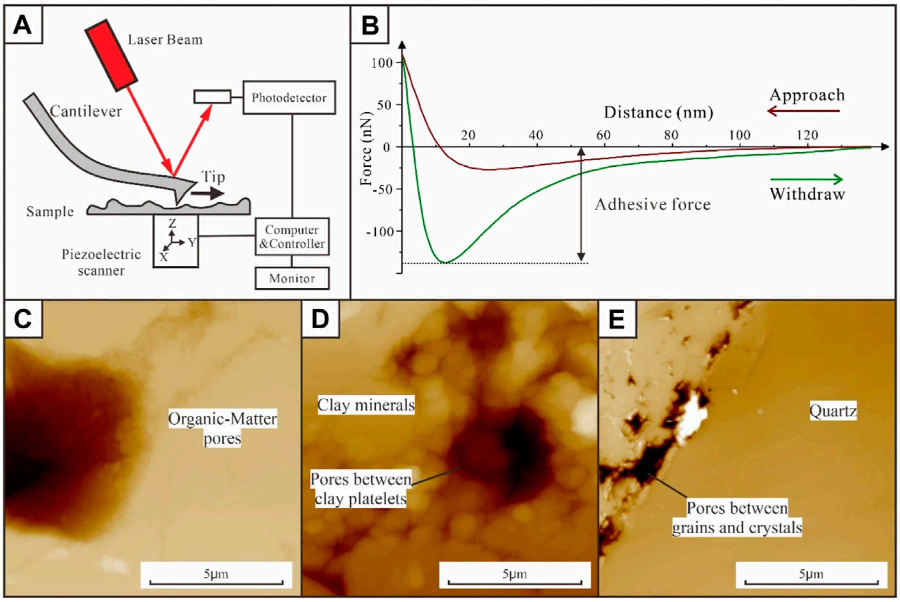

FIGURE 6 | Working principle of atomic force microscopy. **(A)** Experimental principle; **(B)** Schematic curve of force versus distance under the PeakForce QNM mode; **(C)** Organic matter pore morphology of JY4-05 (Wufeng Formation, 2,591.7 m); **(D)** Pore morphology of clay minerals; and **(E)** Intergranular pore morphology.

pores are commonly found in grain laminae and organic matter aggregate (**Table 3**). Next, organic pores are generally round, oval, and irregular in shape, and they are distributed within large continuous organic matter or bitumen filling in the intragranular pores of pyrite framboids. The space of the honeycombed pores extends widely, thereby forming more complex structures and improving pore connectivity. It has been widely accepted that organic pores demonstrate a high degree of development and good connectivity. Mineral pores are relatively few, which are mainly distributed between quartz, feldspar, calcite, and other

TABLE 3 | The type of shale pores and their genetic description.

	Shale pore type	Genetic description
Grain laminae	①Pores at the edge of rigid grains ②Moldic pores ③Pores within fossil bodies ④Pores between grains and crystals ⑤Dissolution-rim pores	Boundary pores formed by the compression of rigid grains Pores in shale formed by the dissolution of crystals or fossils A cavity inside a fossil Unfilled pores between crystals and grains during recrystallization or deposition Secondary pores formed by unstable mineral dissolution
Organic matter aggregate	⑥Pores within peloids or pellets ⑦Organic Matter pores ⑧Pores between or within clay platelets ⑨Intercrystalline pores within pyrite framboids	Micropores in biological remains or products related to biological activity Space generated by the shedding of small hydrocarbon molecules in organic matter Interlayer pores formed by the transformation of clay minerals during thermal evolution The unfilled pores left between grains when pyrite accumulates
Fracture	⑩Fracture pores	Pores formed by the dissolution of a soluble mineral by the action of water or gas over a long period

particles or in clay mineral aggregates (Wu et al., 2020b, c; Wu et al., 2019a; Wu et al., 2019c). Microfractures are relatively developed, which are mainly distributed in the boundary between organic matter and minerals, inside brittle minerals, or between clay mineral particles. However, most of them cannot be distinguished as primary fractures formed by the tectonic process or artificial fractures formed during the experimental processes. Organic pores display the characteristics of heterogeneous development due to different types, maturity, and abundance of organic matter, which are manifested as a high degree of development of pores in some places, almost no development of pores in some places, or lower than the instrument resolution (Liu et al., 2019b; Liu et al., 2019c).

3.2 Fluid Injection Techniques and Pore Connectivity in Shale Reservoir

3.2.1 Advantages and Limitations of Fluid Injection Techniques

Fluid injection methods include mercury injection, cryogenic liquid nitrogen adsorption, helium injection, carbon dioxide adsorption, and nuclear magnetic resonance. The mercury injection method can be divided into the conventional (high pressure) mercury injection method and constant-speed mercury injection method, which is mainly used to characterize reservoir pore-throat characteristics and seepage capacity. The conventional mercury injection is to record the amount of injected mercury under a certain pressure to determine the pore structure of rock (**Figure 7**). It demonstrates the characteristics of a wide range of pore sizes, reservoir space (5–995 μm in diameter), and high consistency with the test results of physical properties. However, some errors are found in the measurement of pore throats with a radius less than 50 nm and secondary pore structures with strong diagenesis. Constant-rate mercury injection technology has been widely applied in unconventional reservoir characterization. Pore and throat can be distinguished due to the changing of mercury injection pressure; thus, the size, number, and configuration relationship of pore throat and other reservoir structural characteristics can be quantitatively reflected (Song et al., 2017). However, the pore throat with diameter less than 0.12 μm cannot be generally measured (Zhao et al., 2015). The accuracy of mercury injection in the characterization of pore structure is related to shale physical properties, and it is mostly applicable to shale reservoirs with porosity greater than 5%. A high content of clay minerals and fine pore throat can easily lead to artificial cracks during the analysis, thereby reducing the accuracy (Zhu R. et al., 2016). Therefore, the combination of mercury injection and gas adsorption methods has been widely used to characterize shale reservoir microstructures (Hou et al., 2020).

Low-temperature liquid nitrogen adsorption method is suitable for the characterization of pore volume and specific surface area of micro- and mesopores, which can analyze the structural characteristics of nanopores in shale reservoirs using the adsorption effect of the pore surface on gas and capillary condensation principle, and explore its adsorption capacity and shale gas accumulation power (Gao et al., 2017). Liquid nitrogen condenses and adsorbs on the pore surface, and the thickness of the adsorbed layer thickens with the increase in relative pressure. Next, when the capillary condensation occurs, the adsorption–desorption isotherms of liquid nitrogen on shale can be yielded, thereby obtaining pore-size distribution, volume, and specific surface area (Cao et al., 2015) (**Figure 7**). The disadvantages of low-temperature liquid nitrogen adsorption method include the large measurement error of shale with a small contrast surface area and incomplete pore characterization for a pore size > 100 nm.

Helium injection method uses the characteristics of helium inert gas to calculate the effective pore volume and particle volume of the measured shale according to Boyle's law and obtain shale porosity parameters (**Figure 3D**), which reflect the size of the overall reservoir space of shale, but it is difficult to reflect the distribution of pore throat (Han et al., 2021). Low-pressure CO_2 adsorption technology is often used to analyze pore structure characteristics of < 2 nm, which demonstrates the advantages of short time and fast equilibrium (**Figure 8**). In recent years, numerous authors (Tian et al., 2012; Li T. et al., 2015; Zhu Y. et al., 2016) used low-temperature CO_2 adsorption to study the pore structure characteristics of marine, transitional, and continental shales with different maturities. Researchers

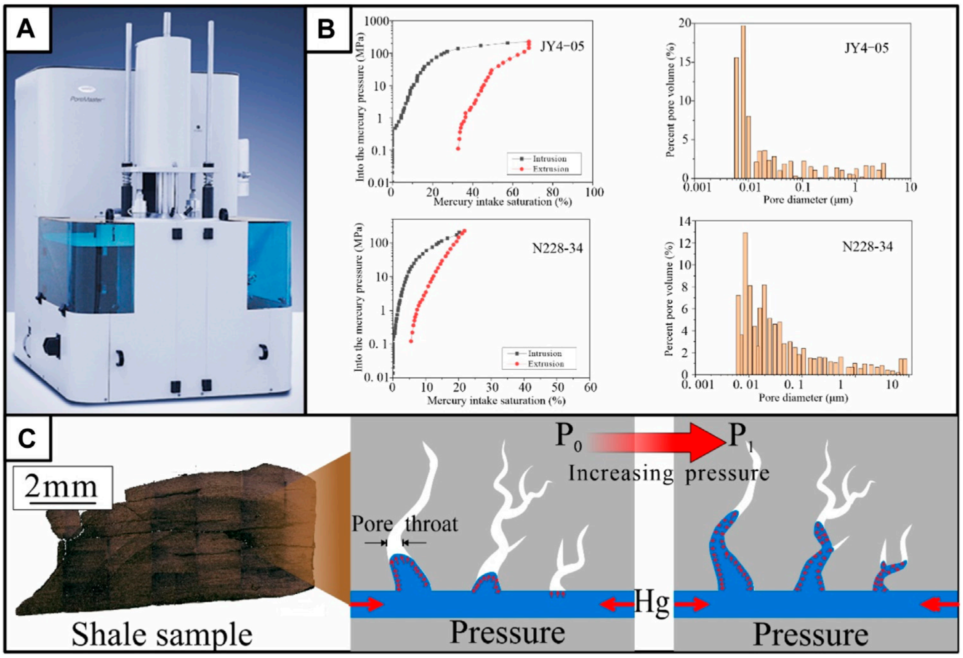

FIGURE 7 | Basic working principle of mercury intrusion porosimetry (MIP). **(A)** Experimental apparatus; **(B)** MIP data curves of different shale samples and its pore distribution characteristics (JY4-05 and N228-34 (Longmaxi Formation, 3,397.87 m)); and **(C)** Schematic diagram of mercury injecting pore throat in massive shale (JY4-09, Longmaxi Formation, 2585.7 m).

found that the low-temperature CO_2 adsorption technology cannot unify the sample processing standard, particle size, pressure boost rate, and other key experimental parameters in the early stage (Tian et al., 2012), and many theoretical models exist for explaining the micropore distribution, but the analysis results differ greatly. The limitations and validity of the total pore space characterization of shale still remain. In addition, three-dimensional characterization methods, like FIB-SEM and Nano-CT, confirmed that the pores less than 2 nm in shale reservoir account for a very small proportion of the reservoir space, and the contribution of these pores to the flow of natural gas and the migration of oil may be very small. Especially, the accuracy of CO_2 adsorption results is usually doubted for the pore structure characterization of shale within the oil window.

Nuclear magnetic resonance (NMR) technology mainly measures the relaxation characteristics of hydrogen-containing fluids in pores using magnetic spectrum and slice imaging (Liu D. et al., 2021), and it obtains the T2 map of relaxation time to characterize the pore size, distribution, connectivity, and fluid occurrence state of shale reservoirs (Ge et al., 2014). NMR images can intuitively obtain information, such as pore and fluid distribution and fracture orientation (Zhou et al., 2012; Huang et al., 2015), but the accuracy of the results is subject to the influence of test environment, fluid properties, and other factors.

According to the experimental principles of various testing methods, the pore sections corresponding to the optimal results are analyzed and superimposed. The pore volume and specific surface area of shale macropores (> 50 nm) are measured using high-pressure mercury intrusion, mesopores (2–50 nm) characterized using low-temperature liquid nitrogen adsorption method, and micropores (< 2 nm) determined by low pressure CO_2 adsorption.

3.2.2 Scaled-Span Pores and the Connectivity in a Shale Reservoir

Shale demonstrates ultra-low porosity and connectivity. The pore-size range is multiscale, thereby accounting for most of the pore volume at the nanoscale. Nanopores in organic matter account for most of the pore volume, which makes shale gas reservoirs demonstrate great methane storage capacity. Slit holes in kerogen were also observed. The spatial distribution of minerals and organic matter is uniform, and most of the pores and throats are isolated with low continuity (Heller and Zoback, 2014).

A large number of previous studies show that abundant microscale and nanoscale pores are found in shales and the pores are mainly ink-bottle organic pores and slits mineral matrix pores. The pore structures of the samples with different total organic content, organic matter type, and mineral compositions showed obvious differences. Organic matter and clay minerals mainly affect the mesopore structure. With the increase in the content of clay minerals and organic matter, the plasticity increases, the ability of shale to resist compaction weakens, and the connectivity of pores worsens (Gao et al., 2017). Next, rigid minerals, such as quartz and carbonate,

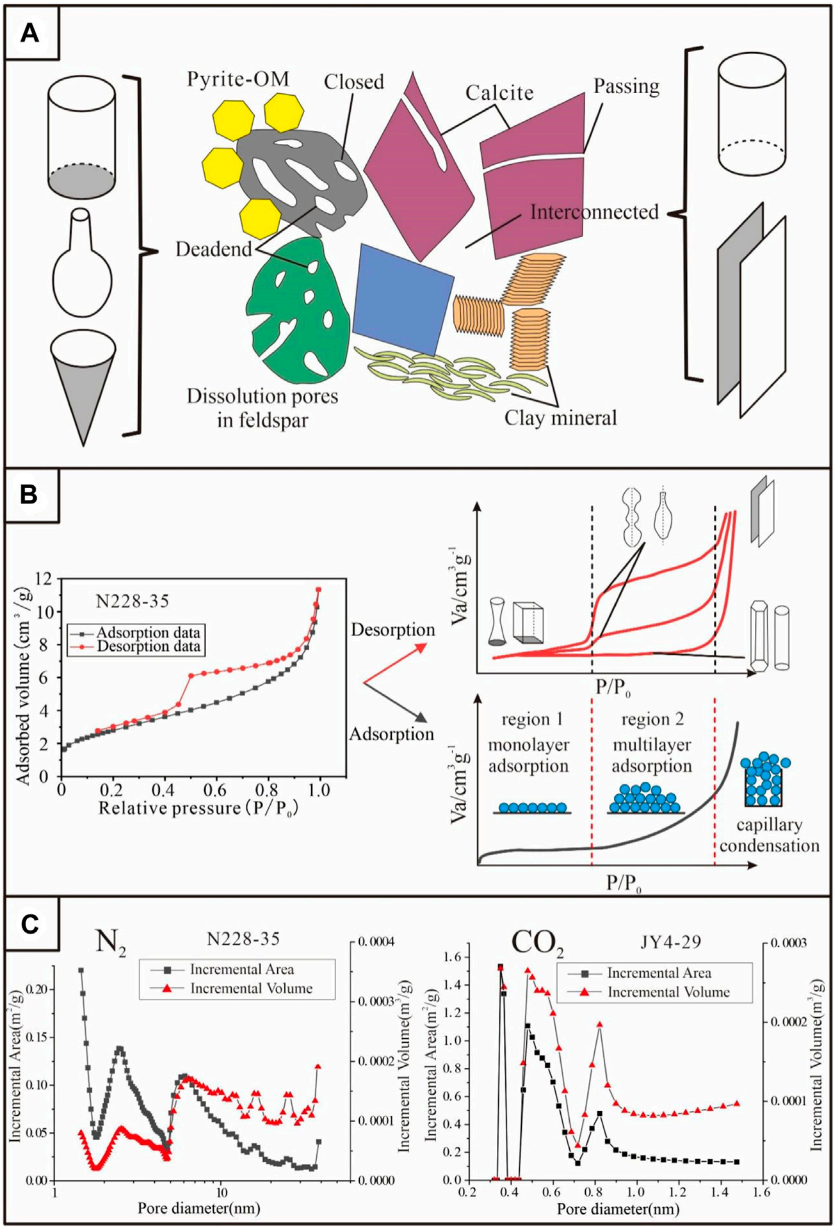

FIGURE 8 | (A) Pore morphology of the organic matter and different minerals in shales (modified from (Nie et al., 2015)); **(B)** Schematic illustration of gas molecules in the whole adsorption process and formation of gas–liquid boundary for different shapes of pores (modified from (Tang et al., 2016; Yin et al., 2019; Ni et al., 2020)); and **(C)** Pore-size distribution curves from N_2 adsorption (N228-35, Longmaxi Formation, 3,398.71 m) and CO_2 adsorption (JY4-29, Longmaxi Formation, 2,548.2 m).

mainly affect the macropore structure, and the retention of intergranular pores can increase the connectivity of pore network.

3.3 High-Energy Ray Techniques and Three-Dimensional Pore Structure

3.3.1 Advantages and Limitations of High-Energy Ray Techniques

High-energy ray method mainly includes small angle scattering and nano/micron CT. A small angle scattering (SAS) can be divided into small angle X-ray scattering (SAXS) and small angle neutron scattering (SANS) according to the source. SAXS originated from the continuous scattering of various submicroscopic particles, such as toner near the incident beam, and its principle is to study the scattering phenomenon of a focused X-ray near the sample. After irradiating it at a very small incident angle, the scattering angle 2θ is smaller than 5° (**Figure 9**). Next, SANS works in a manner similar to SAXS, but it is more sensitive to light elements and demonstrates the identification of isotopes. SAXS/SANS can study the microscopic pore structure and morphological characteristics of shale.

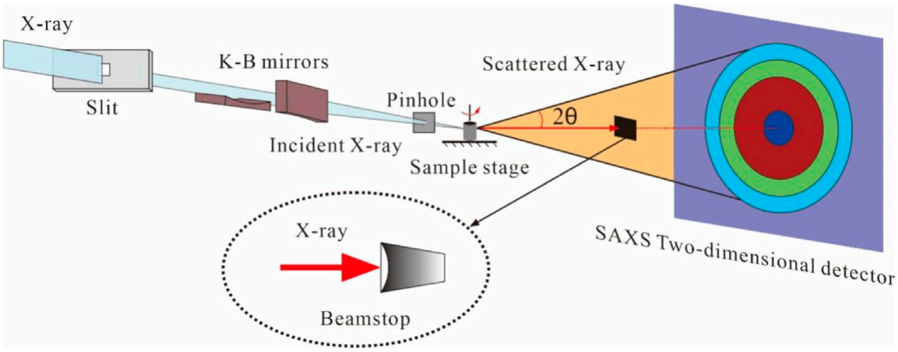

FIGURE 9 | Experimental principle of small angle X-ray scattering.

In shale samples with a relatively simple pore structure and homogeneous composition, the experimental results demonstrate high accuracy and repeatability. In specific reservoir pore characterization, the advantage of SAS is that it can be combined with the fluid injection method to obtain the structural characteristics of closed pores of shales (Zhang et al., 2021). A study on shales of the Longmaxi and Niutitang Formations (Sun et al., 2016; Sun M. et al., 2017) showed that the closed pores were mainly composed of 5–50 nm mesopores, which were related to the pore development within organic matter. Previous studies applied SAS to characterize shale obturator pores (Sun et al., 2016; Sun M. et al., 2017; Sun et al., 2018; Sun et al., 2020). It is believed that high burial depth/maturity reduces the pore connectivity of the shale and increases the content of closed pores. The continuously increasing burial depth compresses the space between mesopores and macropores (Blach et al., 2021), thereby preserving the law of micropore volume. This also means that SAS can effectively characterize the evolution of shale closed pores. On the other hand, in the study of reservoir pore structures, the SAS is still in the initial stage. The main reasons are as follows (Clarkson et al., 2012): 1) the SAS technology is based on a synchrotron radiation platform, and acquiring a synchrotron radiation machine is difficult; 2) a pore structure interpretation model of tight reservoirs, such as shale and tight sandstone, has not yet been formed, which cannot explain the experimental results; and 3) compared with the SAS, the particle diameter of shale reservoir is larger, the particle size is between 30 nm and 60 μm, and the density is more than 2 g/cm^3, which is beyond the most effective research range of SAS.

In a vacuum environment, the X conical wiring harness from the X-ray source on one side of the micro/nano-CT is transmitted to the sample rotating on the sample table and is then received and mapped by the image intensifier on the opposite side (**Figure 10**). The micro/nano-CT technology can characterize the three-dimensional spatial structure of pores, which can be used to evaluate the connectivity of pores. It is mainly based on the density difference, and the gray difference is often used to distinguish different components. For shales, the intensity range can be assigned by interactive threshold processing to characterize pores, organic matter, matrix minerals, and high-density minerals in turn. The connectivity of the pore–fracture network in shales can be simulated using the ball-and-stick model of imaging. Previous works (Guo et al., 2016; He et al., 2016) showed that pyrite in shales, such as the Longmaxi Formation, is randomly distributed on the basis of nano-CT scanning and three-dimensional reconstruction technology, and it is mainly displays elliptic and berry spherical shapes, with particle sizes ranging from several hundred nanometers to dozens of microns. Other mineral components rarely display obvious granularity, which are formed by mutual compaction and mixing. Most of the organic matter was irregularly connected, and the total volume was approximately 5%. The pores and fractures are mostly distributed in organic matter and between different minerals, and most of them are ellipsoid, with strong heterogeneity of pore volume and a significant difference in pore connectivity.

3.3.2 Three-Dimensional Pore Structure and its Impact on Gas Occurrence in Shale Reservoir

The effect of shale pore structure on gas adsorption and seepage is to establish gas flow models based on an FIB-SEM image, nano-CT image, or micron CT image. Gas flow models in shale mainly include the continuum model, discrete fracture network model, and mixed model. The continuous media model gradually developed into the dual media model, triple media model, quadruple media model, etc. Its advantage is that different seepage media have been considered separately, which can better reflect the actual situation. With the increasing complexity of the model, however, the difficulty of solving the model increases sharply. The discrete fracture model is more consistent with the flow law of the actual fluid in the reservoir, but it is difficult to divide the grid and obtain the parameters. The hybrid model fully combines the advantages of a continuum model and discrete fracture model, but it still demonstrates some problems, such as complex modeling, low computational efficiency, and inadequate applicability to faults and complex boundaries when describing seepage channels at different scales (Ozkan et al., 2010; Freeman et al., 2011; Sun H. et al., 2017; Li Z. et al., 2019).

Previous studies have shown that adsorbed gas was mainly stored in pore spaces of less than 10 nm, and free gas mainly existed in pores of more than 50 nm (Ambrose et al., 2010). The

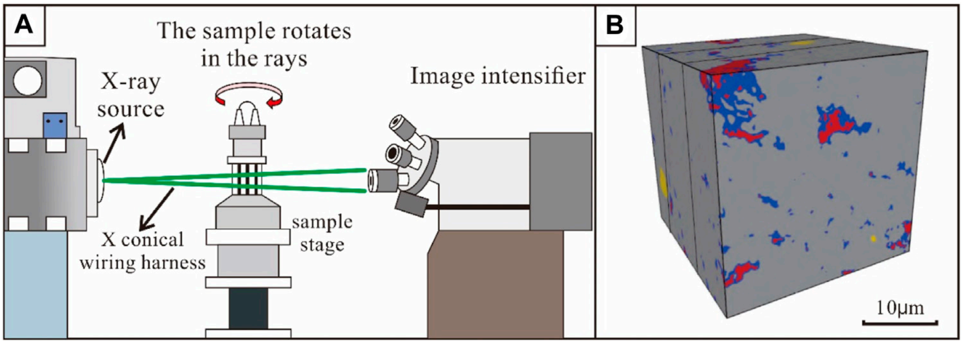

FIGURE 10 | Basic work principle of micro-computed tomography (CT). **(A)** Experimental principle; **(B)** 3D reconstruction of shale cores under CT (Gou et al., 2019).

law of gas migration in large pores is described by the Stokes equation, while the law of gas migration in micropores is described by the Darcy equation. The methane gas in macropores is desorbed faster, which accelerates the movement of methane gas in the whole system. Continuous growth of micropores can significantly enhance the overall connectivity of porous media and contribute significantly to the shale gas flow process (Huang and Zhao, 2017; Li Z. et al., 2019).

When the pore pressure is low, the ratio of the apparent permeability to the Darcy permeability is high, and the influence of temperature and gas molar mass is reduced. Knudsen diffusion is an important gas migration process in the shale system. The diffusion contribution is greater in smaller pores, lower pressures and temperatures, and at higher molar mass gases (Javadpour, 2009; Freeman et al., 2011; Sun H. et al., 2017).

Using the three-dimensional structure established by FIB-SEM or CT, pore volume, pore surface area, porosity, and connectivity can be calculated. Studies displayed that the pore surface area and pore volume were highly correlated with the gas content (Cai et al., 2013; Cai et al., 2018; Liu D. et al., 2021; Liu Z. et al., 2021). Researchers observed that microporosity can make the surface of the pore space rougher and increase the connectivity of the pore space (Li J. et al., 2015; Wu et al., 2019a; Wu et al., 2019b), which causes an increase in permeability as the absolute permeability of the pore space increases. The pore network analysis of predecessors revealed that micropores demonstrate a significant impact on pore and throat distributions, especially the throat, since most micropores act primarily as throats (Wu et al., 2019a).

4 CONCLUSION

Research on shale gas reservoirs has made continuous progress, but many challenges remain. To improve the effectiveness of marine, marine-continental transitional, and continental shale gas exploration and development, it is necessary to sort out and summarize the composition and spatial configuration of shale gas reservoirs and establish simplified models and evaluation standards based on the analysis system. In this article, the microscopic characteristics of shale reservoirs and the differences, advantages, and disadvantages of research techniques are systematically sorted out, and some ideas for the characterization of cross-scale pore networks are sorted out. The main conclusions are as follows:

1) A simplified model of the microstructure of shale can be established based on the laminae structure. Shale consists of grain laminae, organic matter aggregate, and fracture. Grain laminae is mainly composed of inorganic pores, which provide less specific surface area and contribute a certain rigidity to the whole rock. Organic matter aggregate is composed of organic matter, clay minerals, and pyrite symbiosis, which is a relatively plastic layer and a well-porous layer of shale. The fracture enhances the internal seepage capacity of the reservoir.
2) The microstructure analysis techniques of shale reservoirs can be classified into three categories: image observation method, fluid injection method, and high-energy ray method. The image observation method mainly studies the pore type, size, and distribution by means of direct observation. The fluid injection method uses indirect testing as a means to quantitatively analyze the size of the reservoir space. The high-energy ray method is an indirect analysis method, and the key technology is repeatability. It can mainly quantitatively analyze the shape, size, and distribution characteristics of the closed storage space.
3) For generally homogeneous material, the single structure and composition indicate that the local microscopic phenomenon is representative of the whole. Shale is a heterogeneous rock material, and the representation of microscopic phenomena to the whole sample becomes poor with the decreasing observation scales. Therefore, when we use the existing technology to study the microstructure of shales, it is necessary to connect with the paleosedimentary environment and use the macroscopic constraints on the research methods of microscopic features without exaggerating the role of microscopic features.

AUTHOR CONTRIBUTIONS

YQ and PG designed research; YQ and YC performed research; YQ, FS, and XF draw the pictures; and YQ and YZ wrote the article.

FUNDING

This work was funded by the National Natural Science Foundation of China (Grant nos. U19B6003-03-01 and 42030804).

REFERENCES

Ambrose, R. J., Hartman, R. C., Diaz-Campos, M., Akkutlu, I. Y., and Sondergeld, C. H. (2010). "New Pore-Scale Considerations for Shale Gas in Place Calculations," in SPE unconventional gas conference (Pittsburgh, PA: OnePetro).

Anderson, T. (2014). *Key Parameters for Liquid-Rich Unconventional Plays: Case Studies from North America. AAPG Search Discov*. Canada, 33. Article 80354.

Bai, Y., Liu, M., Yang, C., and Jiang, Z. (2016). AFM Based Pore Characterization of Shales and its Relation to the. *Anal. Gas J. Jilin Univ. (Earth Sci. Ed.* 46, 1332–1341.

Bernard, S., Horsfield, B., Schulz, H.-M., Schreiber, A., and Wirth, R. (2011). *Gas Generation Reactions in Highly Mature Gas Shales*. Houston, TX: Search and Discovery, 80162.

Blach, T., Radlinski, A. P., Vu, P., Ji, Y., de Campo, L., Gilbert, E. P., et al. (2021). Accessibility of Pores to Methane in New Albany Shale Samples of Varying Maturity Determined Using SANS and USANS. *Energies* 14, 8438. doi:10.3390/en14248438

Bustin, R. M., Bustin, A. M., Cui, A., Ross, D., and Pathi, V. M. (2008). "Impact of Shale Properties on Pore Structure and Storage Characteristics," in SPE shale gas production conference (Fort Worth, TX: OnePetro).

Cai, X. (2015). Application of Atomic Force Microscopy in the Study of Microscopic Pore Structure of Shale. *J. Chin. Electron Microsc. Soc.* 34, 326–331.

Cai, Y., Li, Q., Liu, D., Zhou, Y., and Lv, D. (2018). Insights into Matrix Compressibility of Coals by Mercury Intrusion Porosimetry and N2 Adsorption. *Int. J. Coal Geol.* 200, 199–212. doi:10.1016/j.coal.2018.11.007

Cai, Y., Liu, D., Pan, Z., Yao, Y., Li, J., and Qiu, Y. (2013). Pore Structure and its Impact on CH4 Adsorption Capacity and Flow Capability of Bituminous and Subbituminous Coals from Northeast China. *Fuel* 103, 258–268. doi:10.1016/j.fuel.2012.06.055

Campbell, C. V. (1967). Lamina, Laminaset, Bed and Bedset. *Sedimentology* 8, 7–26. doi:10.1111/j.1365-3091.1967.tb01301.x

Cao, G., Wang, L., Zhang, Y., and Yang, Z. (2015). Research on Nitrogen Physical Adsorption Method and Mercury Intrusion Method Used for Characterization of FCC Catalyst Pore Size. *distribution Refin. Chem. Industry* 26, 9–12.

Chalmers, G. R., Bustin, R. M., and Power, I. M. (2012). Characterization of Gas Shale Pore Systems by Porosimetry, Pycnometry, Surface Area, and Field Emission Scanning Electron Microscopy/transmission Electron Microscopy Image Analyses: Examples from the Barnett, Woodford, Haynesville, Marcellus, and Doig Units. *Bulletin* 96, 1099–1119. doi:10.1306/10171111052

Cheng, Z., Xue, H., Li, W., Lu, S., and Zhou, N. (2018). Quantitative Characterization of Reservoir Space of Tight Sandstones Based on a Large-View FE-SEM Splicing Technology: a Case Study on the Hetaoyuan Formation in Biyang Sag. *China Pet. Explor.* 23, 79–87.

Clarkson, C. R., Freeman, M., He, L., Agamalian, M., Melnichenko, Y. B., Mastalerz, M., et al. (2012). Characterization of Tight Gas Reservoir Pore Structure Using USANS/SANS and Gas Adsorption Analysis. *Fuel* 95, 371–385. doi:10.1016/j.fuel.2011.12.010

Curtis, J. B. (2002). Fractured Shale-Gas Systems. *AAPG Bull.* 86, 1921–1938. doi:10.1306/61eeddbe-173e-11d7-8645000102c1865d

Curtis, M. E., Ambrose, R. J., Sondergeld, C. H., and Rai, C. S. (2011). "Transmission and Scanning Electron Microscopy Investigation of Pore Connectivity of Gas Shales on the Nanoscale," in North American unconventional gas conference and exhibition (The Woodlands, TX: OnePetro).

Evdokimov, I. N., Eliseev, N. Y., Losev, A. P., and Novikov, M. A. (2006). "Emerging Petroleum-Oriented Nanotechnologies for Reservoir Engineering," in SPE Russian oil and gas technical conference and exhibition (Moscow, Russia: OnePetro). doi:10.2118/102060-RU

Freeman, C. M., Moridis, G. J., and Blasingame, T. A. (2011). A Numerical Study of Microscale Flow Behavior in Tight Gas and Shale Gas Reservoir Systems. *Transp. Porous Med.* 90, 253–268. doi:10.1007/s11242-011-9761-6

Gao, F., Song, Y., Jiang, Z., Zhang, X., and Chen, L. (2017). Influence of Clay Minerals on Shale Storage Space and Adsorptive Capacity Special Oil and Gas Reservoirs. *ACS Omega* 24, 1–8.

Ge, X., Fan, Y., Zhu, X., Chen, Y., and Li, R. (2014). Determination of Nuclear Magnetic Resonance T2 Cutoff Value Based on Multifractal Theory — an Application in Sandstone with Complex Pore Structure. *Geophysics* 80, D11–D21.

Gou, Q., Xu, S., Hao, F., Yang, F., Wang, Y., Lu, Y., et al. (2019). Study on Characterization of Micro-fracture of Shale Based on Micro-CT. *Acta Geol. Sin.* 93, 2372–2382. doi:10.1111/1755-6724.14154

Guo, X., He, S., Chen, S., Chen, X., Wang, S., and Qin, L. (2016). Research on Microstructure of Shale Pores and Distribution Features Based on. *Nano-CT Scanning Digital Core Analysis Coal Geol. China* 28, 28–34.

Han, X., Zhang, H., Mao, X., and Xu, D. (2021). A Method of Gas Porosity Measurement for Tight Reservoirs Based on Mechanical Analysis of Core Chamer Chinese. *J. Geophys.* 64, 287–297.

He, Z., Nie, H., and Zhang, Y. (2016). The Main Factors of Shale Gas Enrichment of Ordovician Wufeng Formation-Silurian Longmaxi Formation in the Sichuan Basin and its Adjacent Areas Earth. *Sci. Front.* 23, 8–17.

Heller, R., and Zoback, M. (2014). Adsorption of Methane and Carbon Dioxide on Gas Shale and Pure Mineral Samples. *J. Unconv. oil gas Resour.* 8, 14–24. doi:10.1016/j.juogr.2014.06.001

Hou, H., Shao, L., Tang, Y., Zhao, S., Yuan, Y., Li, Y., et al. (2020). Quantitative Characterization of Low-Rank Coal Reservoirs in the Southern Junggar Basin, NW China: Implications for Pore Structure Evolution Around the First Coalification Jump. *Mar. Petroleum Geol.* 113, 104165. doi:10.1016/j.marpetgeo.2019.104165

Huang, J., Xu, K., Guo, S., and Guo, H. (2015). Comprehensive Study on Pore Structures of Shale Reservoirs Based on SEM, NMR and X-CT. *Geoscience* 29, 198–205.

Huang, X., and Zhao, Y.-P. (2017). Characterization of Pore Structure, Gas Adsorption, and Spontaneous Imbibition in Shale Gas Reservoirs. *J. Petroleum Sci. Eng.* 159, 197–204. doi:10.1016/j.petrol.2017.09.010

Ingram, R. L. (1954). Terminology for the Thickness of Stratification and Parting Units in Sedimentary Rocks. *Geol. Soc. Am. Bull.* 65, 937–938. doi:10.1130/0016-7606(1954)65[937:tfttos]2.0.co;2

Javadpour, F. (2009). Nanopores and Apparent Permeability of Gas Flow in Mudrocks (Shales and Siltstone). *J. Can. Petroleum Technol.* 48, 16–21. doi:10.2118/09-08-16-da

Lai, J., Wang, G., Wang, Z., Chen, J., Pang, X., Wang, S., et al. (2018). A Review on Pore Structure Characterization in Tight Sandstones. *Earth-Science Rev.* 177, 436–457. doi:10.1016/j.earscirev.2017.12.003

Lazar, O. R., Bohacs, K. M., Macquaker, J. H. S., Schieber, J., and Demko, T. M. (2015). Capturing Key Attributes of Fine-Grained Sedimentary Rocks in Outcrops, Cores, and Thin Sections: Nomenclature and Description Guidelines. *J. Sediment. Res.* 85, 230–246. doi:10.2110/jsr.2015.11

Lei, Y., Luo, X., Wang, X., Zhang, L., Jiang, C., Yang, W., et al. (2015). Characteristics of Silty Laminae in Zhangjiatan Shale of Southeastern Ordos Basin, China: Implications for Shale Gas Formation. *Bulletin* 99, 661–687. doi:10.1306/09301414059

Li, C., Xiao, Q., Chen, Q., and Jiang, X. (2019a). Evolution Characteristics and Controls of Shale Nanopores during Thermal Maturation of Organic Matter. *Pet. Geol. & Exp.* 41, 901–909.

Li, J., Yin, J., Zhang, Y., Lu, S., Wang, W., Li, J., et al. (2015a). A Comparison of Experimental Methods for Describing Shale Pore Features - A Case Study in the Bohai Bay Basin of Eastern China. *Int. J. Coal Geol.* 152, 39–49. doi:10.1016/j.coal.2015.10.009

Li, T., Tian, H., Chen, J., and Cheng, L. (2015b). The Application of Low Pressure Gas Adsorption to the Characterization of Pore Size Distribution for Shales: An Example from Southeastern Chongqing Area. *Nat. Gas. Geosci.* 26, 1719–1728.

Li, Z., Yan, W., Qi, Z., Dong, D., Huang, X., and Yu, R. (2019b). Production Performance Model Based on Quadruple-Porosity Medium in Shale Gas Reservoirs Considering Multi-Transport Mechanisms. *Energy Sources, Part A Recovery, Util. Environ. Eff.*, 1–19. doi:10.1080/15567036.2019.1662520

Liu, D., Zou, Z., Cai, Y., Qiu, Y., Zhou, Y., and He, S. (2021a). An Updated Study on CH4 Isothermal Adsorption and Isosteric Adsorption Heat Behaviors of Variable Rank Coals. *J. Nat. Gas Sci. Eng.* 89, 103899. doi:10.1016/j.jngse.2021.103899

Liu, G., Huang, Z., Chen, F., Jiang, Z., Gao, X., Li, T., et al. (2016a). Reservoir Characterization of Chang 7 Member Shale: A Case Study of Lacustrine Shale in the Yanchang Formation, Ordos Basin, China. *J. Nat. Gas Sci. Eng.* 34, 458–471. doi:10.1016/j.jngse.2016.06.071

Liu, G., Huang, Z., Jiang, Z., Chen, J., Chen, F., and Xing, J. (2016b). Gas Adsorption Capacity Calculation Limitation Due to Methane Adsorption in Low Thermal Maturity Shale: A Case Study from the Yanchang Formation, Ordos Basin. *J. Nat. Gas Sci. Eng.* 30, 106–118. doi:10.1016/j.jngse.2016.01.026

Liu, G., Zhai, G., Huang, Z., Zou, C., Xia, X., Shi, D., et al. (2019a). The Effect of Tuffaceous Material on Characteristics of Different Lithofacies: A Case Study on Lucaogou Formation Fine-Grained Sedimentary Rocks in Santanghu Basin. *J. Petroleum Sci. Eng.* 179, 355–377. doi:10.1016/j.petrol.2019.04.072

Liu, G., Zhai, G., Yang, R., He, T., and Wei, B. (2021b). Quartz Crystallinity Index: New Quantitative Evidence for Biogenic Silica of the Late Ordovician to Early Silurian Organic-Rich Shale in the Sichuan Basin and Adjacent Areas, China. *Sci. China Earth Sci.* 64, 773–787. doi:10.1007/s11430-020-9718-2

Liu, G., Zhai, G., Zou, C., Cheng, L., Guo, X., Xia, X., et al. (2019b). A Comparative Discussion of the Evidence for Biogenic Silica in Wufeng-Longmaxi Siliceous Shale Reservoir in the Sichuan Basin, China. *Mar. Petroleum Geol.* 109, 70–87. doi:10.1016/j.marpetgeo.2019.06.016

Liu, G., Zhai, G., Zou, C., Huang, Z., Liu, B., Guo, X., et al. (2019c). Amorphous Silica and its Effects on Shale Reservoir: A Case Study about Yanchang Formation Lacustrine Shale, Ordos Basin. *Energy Sources, Part A Recovery, Util. Environ. Eff.* 41, 975–989. doi:10.1080/15567036.2018.1522395

Liu, Z., Liu, D., Cai, Y., and Qiu, Y. (2021c). Permeability, Mineral and Pore Characteristics of Coals Response to Acid Treatment by NMR and QEMSCAN: Insights into Acid Sensitivity Mechanism. *J. Petroleum Sci. Eng.* 198, 108205. doi:10.1016/j.petrol.2020.108205

Loucks, R. G., Reed, R. M., Ruppel, S. C., and Hammes, U. (2012). Spectrum of Pore Types and Networks in Mudrocks and a Descriptive Classification for Matrix-Related Mudrock Pores. *Bulletin* 96, 1071–1098. doi:10.1306/08171111061

Loucks, R. G., and Reed, R. M. (2014). Scanning-electron-microscope Petrographic Evidence for Distinguishing Organic-Matter Pores Associated with Depositional Organic Matter versus Migrated Organic Matter in Mudrock. *Gulf Coast Assoc. Geol. Soc. J.* 3, 51–60.

Ni, G., Li, S., Rahman, S., Xun, M., Wang, H., Xu, Y., et al. (2020). Effect of Nitric Acid on the Pore Structure and Fractal Characteristics of Coal Based on the Low-Temperature Nitrogen Adsorption Method. *Powder Technol.* 367, 506–516. doi:10.1016/j.powtec.2020.04.011

Nie, B., Liu, X., Yang, L., Meng, J., and Li, X. (2015). Pore Structure Characterization of Different Rank Coals Using Gas Adsorption and Scanning Electron Microscopy. *Fuel* 158, 908–917. doi:10.1016/j.fuel.2015.06.050

Ozkan, E., Raghavan, R., and Apaydin, O. G. (2010). "Modeling of Fluid Transfer from Shale Matrix to Fracture Network," in SPE Annual Technical Conference and Exhibition (Florence, Italy: OnePetro).

Peltonen, C., Marcussen, Ø., Bjørlykke, K., and Jahren, J. (2009). Clay Mineral Diagenesis and Quartz Cementation in Mudstones: The Effects of Smectite to Illite Reaction on Rock Properties. *Mar. Petroleum Geol.* 26, 887–898. doi:10.1016/j.marpetgeo.2008.01.021

Peng, Li., Ting, D., and Nicholas, B. H. (2014). *Microstructural Characterization of Gas Shales by Electron Microscopy*. Calgary, AB: AAPG Search Discov. Article 90224.

Qiu, Z., and Zou, C. (2020). Controlling Factors on the Formation and Distribution of "Sweet-Spot Areas" of Marine Gas Shales in South China and a Preliminary Discussion on Unconventional Petroleum Sedimentology. *J. Asian Earth Sci.* 194, 103989. doi:10.1016/j.jseaes.2019.103989

Ross, D. J. K., and Marc Bustin, R. (2009). The Importance of Shale Composition and Pore Structure upon Gas Storage Potential of Shale Gas Reservoirs. *Mar. petroleum Geol.* 26, 916–927. doi:10.1016/j.marpetgeo.2008.06.004

Sang, Q., Zhao, X., Liu, Y., Li, Z., and Dong, M. (2022). Effects of the Laminated-Structure and Mixed Wettability on the Oil/water Relative Permeabilities and Oil Productions in Shale Oil Formations. *J. Petroleum Sci. Eng.* 208, 109457. doi:10.1016/j.petrol.2021.109457

Shi, C., Cao, J., Tan, X., Luo, B., Zeng, W., Hong, H., et al. (2018). Hydrocarbon Generation Capability of Sinian-Lower Cambrian Shale, Mudstone, and Carbonate Rocks in the Sichuan Basin, Southwestern China: Implications for Contributions to the Giant Sinian Dengying Natural Gas Accumulation. *Bulletin* 102, 817–853. doi:10.1306/0711171417417019

Song, L., Ning, Z., Sun, Y., Ding, G., and Du, H. (2017). Pore Structure Characterization of Tight Oil Reservoirs by a Combined Mercury Method Petroleum Geology. *Experiment* 39, 700–705.

Sun, H., Yao, J., Cao, Y.-c., Fan, D.-y., and Zhang, L. (2017a). Characterization of Gas Transport Behaviors in Shale Gas and Tight Gas Reservoirs by Digital Rock Analysis. *Int. J. Heat Mass Transf.* 104, 227–239. doi:10.1016/j.ijheatmasstransfer.2016.07.083

Sun, J., Yang, Z., Liu, X., and Xiong, S. (2012). Reservoir Wettability Evaluation Using Nuclear Magnetic Resonance Technology. *Sci. Technol. Rev.* 30, 65–71.

Sun, M., Yu, B., Hu, Q., Chen, S., Xia, W., and Ye, R. (2016). Nanoscale Pore Characteristics of the Lower Cambrian Niutitang Formation Shale: A Case Study from Well Yuke #1 in the Southeast of Chongqing, China. *Int. J. Coal Geol.* 154-155, 16–29. doi:10.1016/j.coal.2015.11.015

Sun, M., Yu, B., Hu, Q., Yang, R., Zhang, Y., Li, B., et al. (2018). Pore Structure Characterization of Organic-Rich Niutitang Shale from China: Small Angle Neutron Scattering (SANS) Study. *Int. J. Coal Geol.* 186, 115–125. doi:10.1016/j.coal.2017.12.006

Sun, M., Yu, B., Hu, Q., Zhang, Y., Li, B., Yang, R., et al. (2017b). Pore Characteristics of Longmaxi Shale Gas Reservoir in the Northwest of Guizhou, China: Investigations Using Small-Angle Neutron Scattering (SANS), Helium Pycnometry, and Gas Sorption Isotherm. *Int. J. Coal Geol.* 171, 61–68. doi:10.1016/j.coal.2016.12.004

Sun, M., Zhang, L., Hu, Q., Pan, Z., Yu, B., Sun, L., et al. (2020). Multiscale Connectivity Characterization of Marine Shales in Southern China by Fluid Intrusion, Small-Angle Neutron Scattering (SANS), and FIB-SEM. *Mar. Petroleum Geol.* 112, 104101. doi:10.1016/j.marpetgeo.2019.104101

Tang, X., Ripepi, N., Stadie, N. P., Yu, L., and Hall, M. R. (2016). A Dual-Site Langmuir Equation for Accurate Estimation of High Pressure Deep Shale Gas Resources. *Fuel* 185, 10–17. doi:10.1016/j.fuel.2016.07.088

Tian, H., Zhang, S., Liu, S., and Zhang, H. (2012). Determination of Organic-Rich Shale Pore Features by Mercury Injection and Gas Adsorption Methods. *Acta Pet. Sin.* 33, 419–427.

Wang, Y., Bai, Y., Hou, B., Wang, R., Bai, Q., and Zhang, X. (2018a). Mechanistic Study on Wettability Alteration of Oil-Wet Sandstone Surface Using Mixed Cationic-Nonionic Surfactants. *J. China Univ. Petroleum* 42, 165–171.

Wang, Y., Wang, L., Wang, J., and Jiang, Z. (2018b). Three-dimension Characterization of Organic Matter Pore Structures of Shale Using Focused Ion Beam-Scanning Electron Microscope. *Rock Mineral Analysis* 37, 235–243.

Wu, Y., Lin, C., Yan, W., Liu, Q., Zhao, P., and Ren, L. (2020a). Pore-scale Simulations of Electrical and Elastic Properties of Shale Samples Based on Multicomponent and Multiscale Digital Rocks. *Mar. Petroleum Geol.* 117, 104369. doi:10.1016/j.marpetgeo.2020.104369

Wu, Y., Tahmasebi, P., Lin, C., and Dong, C. (2020b). A Comprehensive Investigation of the Effects of Organic-Matter Pores on Shale Properties: A Multicomponent and Multiscale Modeling. *J. Nat. Gas Sci. Eng.* 81, 103425. doi:10.1016/j.jngse.2020.103425

Wu, Y., Tahmasebi, P., Lin, C., and Dong, C. (2020c). Process-based and Dynamic 2D Modeling of Shale Samples: Considering the Geology and Pore-System Evolution. *Int. J. Coal Geol.* 218, 103368. doi:10.1016/j.coal.2019.103368

Wu, Y., Tahmasebi, P., Lin, C., Munawar, M. J., and Cnudde, V. (2019a). Effects of Micropores on Geometric, Topological and Transport Properties of Pore Systems for Low-Permeability Porous Media. *J. Hydrology* 575, 327–342. doi:10.1016/j.jhydrol.2019.05.014

Wu, Y., Tahmasebi, P., Lin, C., Ren, L., and Dong, C. (2019b). Multiscale Modeling of Shale Samples Based on Low- and High-Resolution Images. *Mar. Petroleum Geol.* 109, 9–21. doi:10.1016/j.marpetgeo.2019.06.006

Wu, Y., Tahmasebi, P., Lin, C., Zahid, M. A., Dong, C., Golab, A. N., et al. (2019c). A Comprehensive Study on Geometric, Topological and Fractal Characterizations of Pore Systems in Low-Permeability Reservoirs Based on SEM, MICP, NMR, and X-Ray CT Experiments. *Mar. Petroleum Geol.* 103, 12–28. doi:10.1016/j.marpetgeo.2019.02.003

Xiao, X.-M., Wei, Q., Gai, H.-F., Li, T.-F., Wang, M.-L., Pan, L., et al. (2015). Main Controlling Factors and Enrichment Area Evaluation of Shale Gas of the Lower Paleozoic Marine Strata in South China. *Pet. Sci.* 12, 573–586. doi:10.1007/s12182-015-0057-2

Yang, B., Xiong, M., Chen, L., and Huang, D. (2020). Laminae Growth Characteristic within the Lower Silurian Longmaxi Marine Shale in the Southeast Sichuan Basin. *Adv. Geosciences* 10, 555–562.

Yin, T., Liu, D., Cai, Y., and Zhou, Y. (2019). Methane Adsorption Constrained by Pore Structure in High-Rank Coals Using FESEM, CO2 Adsorption, and NMRC Techniques. *Energy Sci. Eng.* 7, 255–271. doi:10.1002/ese3.275

Zhang, J., Hu, C., Yao, C., and Fang, W. (2012). Determination of Microstructure and Defect Structure in Pyrophyllite by High- Resolution Transmission Electron Microscopy. *Acta Mineral. Sin.* 32, 65–73.

Zhang, L., Xu, Y., Sun, M., and Jiang, S. (2021). The Structure and Evolution of Closed Pores in Shale Determined by Small Angle Neutron Scattering. *Acta Sedimentol. Sin.* 39, 310–323.

Zhao, H., Ning, Z., Wang, Q., Zhang, R., Zhao, T., Niu, T., et al. (2015). Petrophysical Characterization of Tight Oil Reservoirs Using Pressure-Controlled Porosimetry Combined with Rate-Controlled Porosimetry. *Fuel* 154, 233–242. doi:10.1016/j.fuel.2015.03.085

Zhou, K., Li, J., Xu, Y., and Zhang, Y. (2012). Measurement of Rock Pore Structure Based on NMR Technology. *J. Central South Univ. Sci. Technol.* 43, 4796–4800.

Zhou, S., Yan, G., Xue, H., Guo, W., and Li, X. (2016). 2D and 3D Nanopore Characterization of Gas Shale in Longmaxi Formation Based on FIB-SEM. *Mar. Petroleum Geol.* 73, 174–180. doi:10.1016/j.marpetgeo.2016.02.033

Zhu, R., Wu, S., Su, L., and Cui, J. (2016a). Problems and Future Works of Porous Texture Characterization of Tight Reservoirs in China. *Acta Pet. Sin.* 37, 1323–1336.

Zhu, Y., Wang, Y., Chen, S., and Zhang, H. (2016b). Qualitative-quantitative Multiscale Characterization of Pore Structures in Shale Reservoirs: A Case Study of Longmaxi Formation in the Upper Yangtze Area. *Earth Sci. Front.* 23, 154–163.

Zou, C., Dong, D., Wang, Y., Li, X., and Huang, J. (2015). Shale Gas in China: Characteristics, Challenges and Prospects (Ⅰ). *Petroleum Explor. Dev.* 42, 689–701. doi:10.1016/s1876-3804(15)30072-0

Zou, C., Zhao, Q., Cong, L., Wang, H., Shi, Z., Wu, J., et al. (2021). Development Progress, Potential and Prospect of Shale Gas in China. *Nat. Gas. Ind.* 41, 1–14.

Zou, C., Zhao, Q., Dong, D., Yang, Z., Qiu, Z., and Liang, F. (2017). Geological Characteristics,main Challenges and Future Prospect of Shale Gas. *Nat. Gas. Geosci.* 28, 1781–1796. doi:10.1016/j.jnggs.2017.11.002

Conflict of Interest: The authors declare that the research was conducted in the absence of any commercial or financial relationships that could be construed as a potential conflict of interest.

frontiers | Frontiers in Earth Science

ORIGINAL RESEARCH
published: 18 July 2022
doi: 10.3389/feart.2022.943935

Characterization and Control of Pore Structural Heterogeneity for Low-Thermal-Maturity Shale: A Case Study of the Shanxi Formation in the Northeast Zhoukou Depression, Southern North China Basin

Enran Liu[1,2,3], Chenglin Liu[1,2], Dishi Shi[3], Disi Zhu[3], Qiuchen Xu[3] and Yanhong Wang[3]*

[1]State Key Laboratory of Petroleum Resources and Prospecting, China University of Petroleum, Beijing, China, [2]College of Geosciences, China University of Petroleum, Beijing, China, [3]Oil and Gas Survey, China Geological Survey, Beijing, China

The Shanxi Formation layers in the northeast of the Zhoukou Depression, Southern North China Basin, mainly consist of dark mudstone interbed with tight stone and widely developed coal seam, which is a promising target for unconventional oil and gas exploration. A series of geochemical and geological methods were used to analyze the characterization and controls of the pores structural heterogeneity in low-thermal-maturity shale. These methods include the Rock-Eval analysis, total organic carbon (TOC) analysis, scanning electron microscope observation with an energy-dispersive spectrometer (SEM-EDS), X-ray diffraction, and low-pressure N_2 adsorption. Based on these measurements, the pore diameter, specific surface area (SSA), and fractal dimension (D) were calculated, and then, the pore structure heterogeneity was analyzed. The result shows the pores of Shanxi Formation shale are mainly interparticle pores with low porosity and low permeability, and the pore structure is highly complex. The average fractal dimension of the micropore and the macropore are both 2.77, but that of the mesopore is 2.65, indicating a less-complex mesopore structure than the micropore and macropore. The S_2, S_1, and TOC exhibit no clear correlation with SSA and fractal dimension of pores, which proved the little impact of organic matter on the heterogeneity of pore structure in the low-maturity shale of the research area. The illite has a strong effect on the pore structural heterogeneity of Shanxi Formation shale. The samples with high content of illite show higher SSA, better physical properties, and low fractal dimension, reflecting low pore structural heterogeneity. However, the quartz and clay minerals show a slight correlation with SSA and no obvious relationship with the fractal dimension, indicating a little effect of them on the pore structure heterogeneity. The pore structural heterogeneity decreases along with the increase in porosity, while the permeability influenced by a variety of reasons under the compaction shows a poor relationship with SSA and fractal dimension. On the whole, the pore structural heterogeneity decreases for low-thermal-maturity shale with high content of illite and high porosity, which should be considered to be the better unconventional oil and gas reservoir in the research area.

Keywords: Zhoukou Depression, Shanxi Formation, pore structural heterogeneity, fractal dimension, specific surface area

Edited by:
Yuqi Wu,
China University of Petroleum (East China), China

Reviewed by:
Guo Xiaobo,
Xi'an Shiyou University, China
Guoheng Liu,
China University of Petroleum East China, China
Pengfei Wang,
China Geological Survey, China

****Correspondence:***
Chenglin Liu
liucl@cup.edu.cn

Specialty section:
This article was submitted to Solid Earth Geophysics, a section of the journal Frontiers in Earth Science

Received: *14 May 2022*
Accepted: *06 June 2022*
Published: *18 July 2022*

Citation:
Liu E, Liu C, Shi D, Zhu D, Xu Q and Wang Y (2022) Characterization and Control of Pore Structural Heterogeneity for Low-Thermal-Maturity Shale: A Case Study of the Shanxi Formation in the Northeast Zhoukou Depression, Southern North China Basin.
Front. Earth Sci. 10:943935.
doi: 10.3389/feart.2022.943935

1 INTRODUCTION

The usage of new technologies, including horizontal hydraulic fracturing, micro-seismic monitoring, and multi-well industrial exploitation, caused a shale gas revolution all over the world (Jarvie et al., 2007; He et al., 2018; Liu et al., 2019a; Liu et al., 2019b). Shale is a kind of fine-grained sedimentary rock composed of debris particles with diameters smaller than 0.0625 mm. In recent years, shale gas has drawn significant attention and has been proved to be stored in three different states in the geological environment: free gas in pores and natural fractures, adsorbed gas in organic matter and clay minerals, and dissolved gas in residual oil and water (Zhang et al., 2012; Tian et al., 2016; Zhou et al., 2019; Liu et al., 2021). Adsorption is one of the important mechanisms for shale gas occurrence, and the adsorption capacity of shale was used to accurately evaluate the adsorbed gas content in shale reservoirs (Rani et al., 2015; Zhou et al., 2018; Li et al., 2019).

Compared with the conventional reservoirs, the shale and tight sandstone have developed a micro-nano pore throat system, which shows large pore size span, low porosity and permeability, and strong heterogeneity in pore structure (Curtis, 2002; Zhang et al., 2012; Tan et al., 2014; Chen et al., 2019a; Chen et al., 2019b). The research on pore structure of shale reservoir has developed from qualitative description to quantitative characterization. The pore model, as an important aspect of unconventional reservoir pore structure characterization, has developed from no mineral attribute to mineral attribute, and improving the accuracy of reservoir characterization (Kennedy et al., 2002; Ji et al., 2016; Jiang et al., 2016; Gao et al., 2018; Wu et al., 2020a; Chen et al., 2021). In recent years, a series of technologies, including high-pressure mercury injection, low-temperature nitrogen and carbon dioxide adsorption, field emission scanning electron microscope, atomic force microscope, nuclear magnetic resonance, small-angle neutron scattering, and high-resolution CT scanning, improved the measurement accuracy of pore size from micron to nanoscale. Moreover, the comprehensive use of various methods increases the characterization accuracy of unconventional reservoirs (Wu et al., 2019a; Wu et al., 2019b; Wu et al., 2019c; Wu et al., 2020b; Wu et al., 2020c; Wu et al., 2020d; Zeng et al., 2022). At the same time, considering the high complexity of shale and tight sandstone samples, Euclidean geometry cannot give accurate description and characterization. Fractal dimension (D), as an important parameter used to analyze complex rock pore networks, was used to represent the pore structural heterogeneity in detail and quantificationally express the degree of complexity of the pore system (Zeng et al., 2021; Zhang et al., 2021). The fractal dimension is frequently calculated from nitrogen adsorption data according to the fractal Frenkel–Halsey–Hill (FHH) method (Yao et al., 2012).

Previous researchers mainly focused on the tectonic evolution characteristics, sedimentary facies and depositional model, reservoir and hydrocarbon of the whole sediment unit in the Zhoukou Depression from the Carboniferous to Permian or upper Palaeozoic periods (Quan et al., 2002; Sun et al., 2004; Zhai et al., 2005; Hu et al., 2006; Liu et al., 2008a; Liu et al., 2008b; Kuang et al., 2009; Li and Yao, 2011; Cao et al., 2013; Li and Ma, 2013; Zhao et al., 2017; Zhao et al., 2019; Li et al., 2020). The formation sequence of the research area has not yet been identified and classified in detail, and the microcosmic study in the reservoir needs to be quantified further. Moreover, the pore structure complexity needs more detailed characterization to meet the demand of exploration. The main purpose of this research is to investigate the pore structural heterogeneity of low-thermal-maturity shale reservoirs from the viewpoint of fractal characteristics. The relationships between organic matter, mineral content, pore structure parameters, and fractal dimension were then characterized to find out the controls on the pore structural heterogeneity.

2 REGIONAL GEOLOGICAL CHARACTERISTICS

The Southern North China Basin is located in the southeast of the North China Plate (platform) and consists of six second-order tectonic units, namely, the Kaifeng Depression, Taikang Uplift, Huaibei Uplift, Zhoukou Depression, Changshan Uplift, and Xinyang-Hefei Depression from, north to south (**Figure 1**). This basin is formed by multiple superimpositions of basin prototypes on the nearly EW-trending basement structure as many Mesozoic-Cenozoic depressions have developed. It extends in nearly EW direction and parallel to the Qinling-Dabie Orogenic Belt (Li et al., 1996).

The Zhoukou Depression, an area of about 32,600 km^2, is located in the central part of the Southern North China Basin (Li et al., 1996). Administratively, the study area is located in the northwestern part of Anhui Province and under the jurisdiction of Fuyang City, Anhui Province. Tectonically, it lies in the northeastern part of the Zhoukou Depression and is surrounded by the Taikang Uplift in the north, the Huaibei Uplift (located in the west of the Tanlu fault zone) in the east, and faces the Qinling-Dabie orogenic belt in the south. It is a Mesozoic-Cenozoic fault basin formed on a stable platform in North China, and can be divided into the northern zone and the southern zone by the Gucheng Fault. The northern zone can be then divided into Yanji sag and Wanglou uplift by a nearly NE-SW-trending reverse fault, and the southern zone can be divided into Niqiuji sag and Gucheng lower uplift by a nearly NE-SW-trending normal fault (Luoji fault) (**Figure 1**) (Liu et al., 2020).

In the research area, a total of 21 Wells were drilled, of which 5 wells showed a complete Upper Paleozoic strata, and 12 wells got oil and gas showings in the Cenozoic, Mesozoic and Paleozoic strata, revealing great oil and gas exploration potential. On the basis of analyzing the drilling, logging, and seismic data, it is concluded that the Shanxi Formation in the research area is a promising target exploration strata for unconventional oil and gas in Southern North China Basin. The Shanxi Formation was deposited in the early Permian, and is divided into 3 third-order sequences (SQs_1, SQs_2, and SQs_3) from bottom to top according to sedimentary cycles caused by sea-level eustacy. The Shanxi Formation mainly consists of dark mudstone interbed with tight sandstone, and widely developed

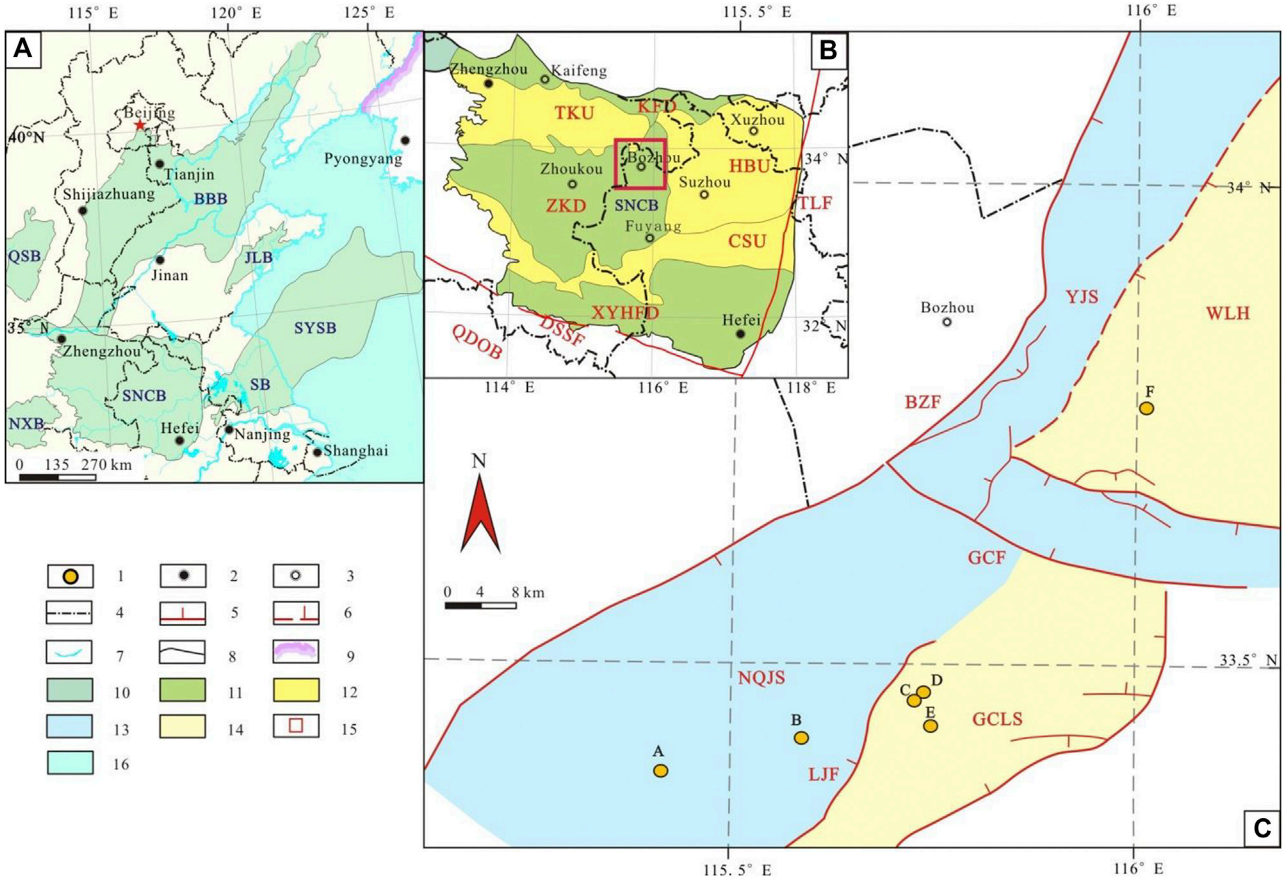

FIGURE 1 | Geological structure outline map of the northeastern part of the Zhoukou Depression. BBB, Bohai Bay Basin; BZF, Bozhou Fault; CSU, Changshan Uplift; DSSF, Danfeng-Shangnan-Shangcheng Fault; GCF, Gucheng Fault; GCLS, Gucheng lower high; HBU, Huaibei Uplift; JLB, Jiaolai Basin; KFD, Kaifeng Depression; LJF, Luoji Fault; NQJS, Niqiuji Sag; NXB, Nanxiang Basin; QDOB, Qinling-Dabie Orogenic Belt; QSB, Qinshui Basin; SB, Subei Basin; SNCB, South North China Basin; SYSB, South Yellow Sea Basin; TLF, Tan-Lu Fault; WLH, Wanglou High; XYHFD, Xinyang-Hefei Depression; YJS, Yanji Sag; ZKD, Zhoukou Depression. 1. Well location; 2. Provincial city; 3. Prefecture-level city; 4. Provincial boundary; 5. Normal fault; 6. Reverse fault; 7. Coastline, river, or lake; 8. Basin boundary; 9. National boundary; 10. Basin; 11. Depression; 12. Uplift; 13. Sag; 14. High; 15. The study area; 16. Sea. **(A)** Geological structure outline map of Southern North China Basin (SNCB); **(B)** Geological structure outline map of Zhoukou Depression (ZKD); **(C)** Geological structure outline map of research filed.

coal seam (up to 0–15 m). Shale and tight sandstone layers in the Shanxi Formation, representing the major source rock and reservoir in this research filed, are mainly developed in the SQs_2 and SQs_3 third-order sequences (**Figure 2**) (Liu et al., 2020).

The Shanxi Formation is the carbonate-clastic tidal flat sedimentary system, which can be characterized by mudstone interbedded with tight sandstone, and further divided into five microfacies namely sand flat, mixed flat, mud flat, limemud flat, and peat flat. Sand flat developed below the average low-water line, mixed flat between the average high water line and average low-water line, and mud flat above the average high water line (**Figure 2**) (Cattaneo and Steel, 2003; Cummings et al., 2006a; Cummings et al., 2006b; Su et al., 2020; Ward et al., 2020). Meanwhile, the limemud flat mainly consists of carbonate sediments in a clear-water environment, and the peat flat is characterized by the development of coal seams (Zhu, 2009; Longhitano et al., 2012; Song et al., 2018; Wang, 2018). The sediments in the sand flat mainly include fine and medium sandstone (Espitalié et al., 1977), and those in the mixed flat mostly the interbedding of thin laminated fine sandstone and mudstone, or the mixture of sandstone and silty mudstone. The sediments in the mud flat mainly include mudstone, silty mudstone, and carbonaceous mudstone (**Figure 3**). The Shanxi Formation is approximately 262.4 ft (approximately 80 m) thick on average, and the maximum thickness is 328 ft (approximately 100 m). It is buried at 4,018–8,724.8 ft (1,225–2,660 m) depths, averaging 5,105.9 ft (approximately 1,556.7 m), and thin coal seams are widely developed (**Figure 3**).

3 SAMPLING AND EXPERIMENTAL METHODS

3.1 Geochemical Characteristic Analysis

3.1.1 Vitrinite Reflectance Analyses

A total of 23 samples from the Shanxi Formation were used in vitrinite reflectance analyses. Vitrinite reflectance analyses were

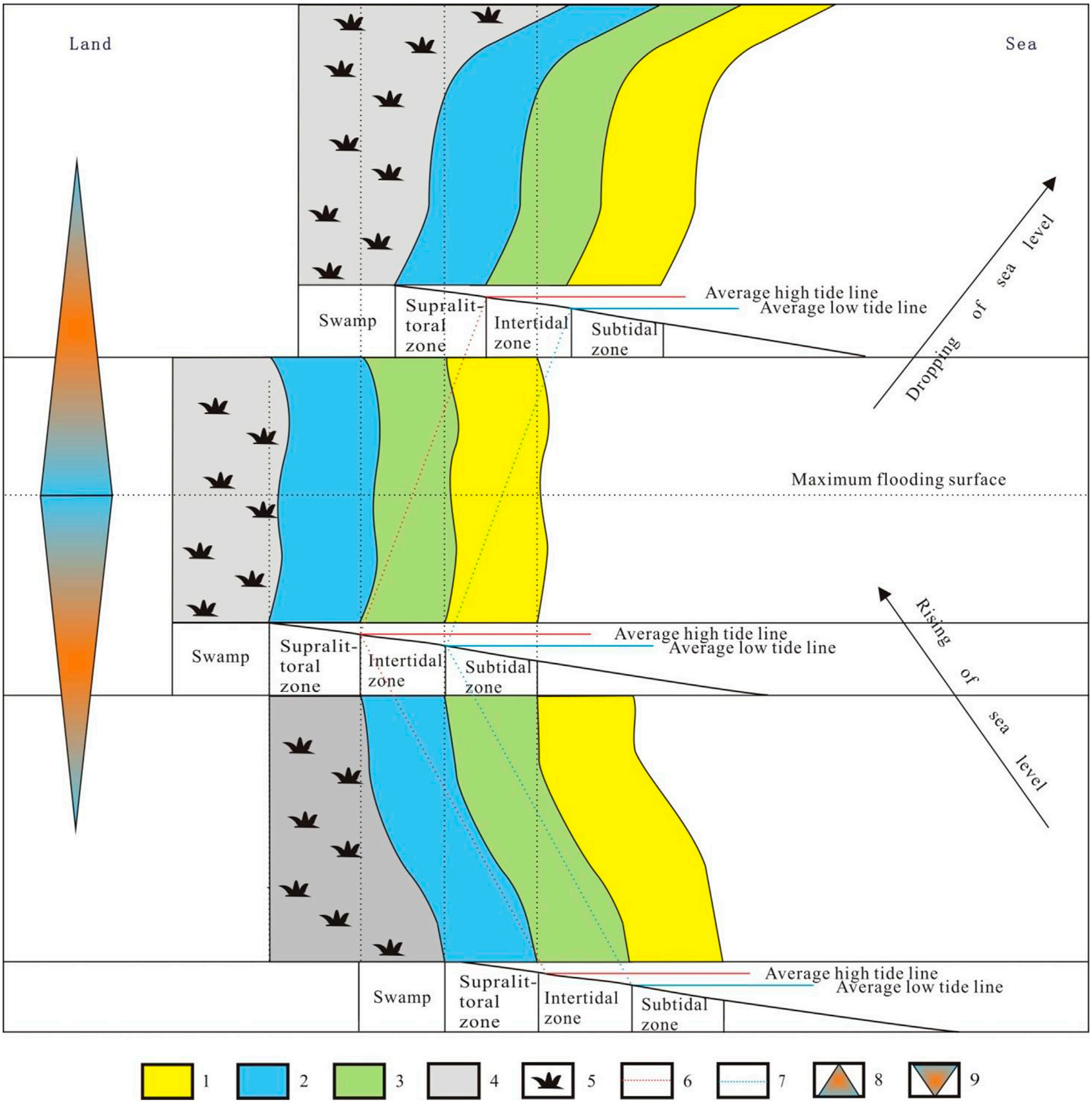

FIGURE 2 | Trends of tidal flats and lithology varying with sea level. 1. Sand flat; 2. Mud flat; 3. Mixed flat; 4. Swamp; 5. Vegetation; 6. Curve of change in average high tide line; 7. Curve of change in average low tide line; 8. Fining-upwards sequence; 9. Coarsening-upwards sequence.

conducted at the State Key Laboratory of Petroleum Resources and Prospecting of the China University of Petroleum (Beijing), using a Leica 4500P+CRAIC Spectrophotometer apparatus according to the testing standard of SY/T5124-2012, under the 23°C and 48% relative humidity testing environment.

3.1.2 Rock-Eval Analyses

A total of 84 samples from the Shanxi Formation were used in Rock-Eval analyses (**Figure 4**). This experiment is an established method for representing the type of organic matter in sedimentary rocks as well as their petroleum generation potential (Espitalié et al., 1977). The samples were subjected to programmed heating in an inert atmosphere to determine the amount of volatile gas and residual bitumen (S_1 peak) and the amounts of nonvolatile hydrocarbons and oxygen-containing organic compounds released during thermal cracking of the remaining organic matter in the rock (recorded in as S_2). In other words, S_1 presents residual bitumen in the Shanxi Formation shale samples, whereas S_2 presents hydrocarbons

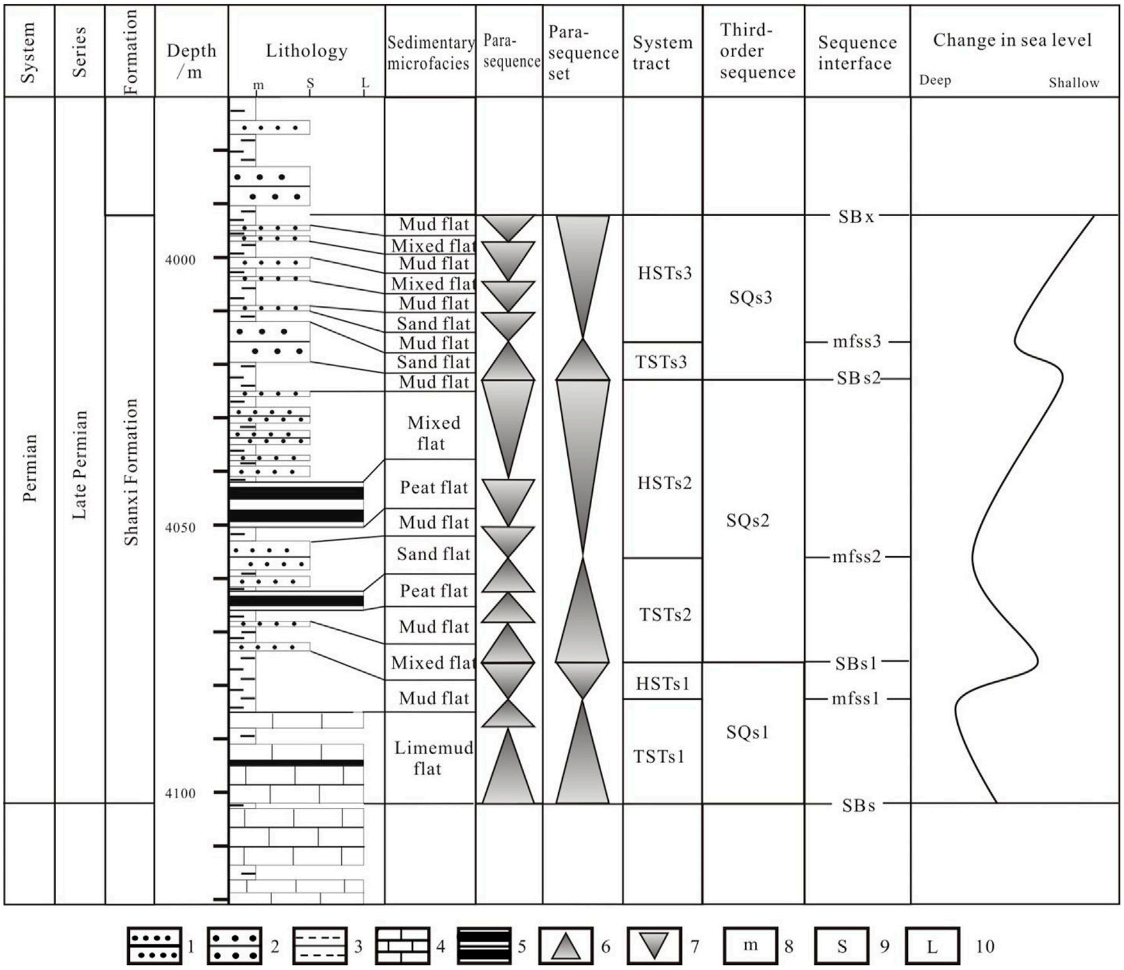

FIGURE 3 | Division of sequence stratigraphic framework of Shanxi Formation (well A) 1. Fine sandstone; 2. Medium sandstone; 3. Mudstone; 4. Limestone; 5. Coal seam; 6. Rising of sea level; 7. Dropping of sea level; 8. Width of mudstone; 9. Width of sandstone; 10. Width of limestone.

generated during the Rock-Eval process. Hence, S_2 can present the content of kerogen to some extent.

3.1.3 Mineral Composition Analysis

A total of 10 samples from the Shanxi Formation were used in mineral composition analysis. X-ray diffraction is a widely used and statistically valid method to identify minerals and clay minerals composition in shale reservoirs. The mineral composition was measured by a Bruker D8 ADVANCE X-ray poly-crystalline diffractometer.

3.1.4 Pore Image Analysis

SEM observation is a commonly method used to provide visualization of the pores. In this research, pores image analysis is supported by a scanning electron microscope (SEM) equipped with an energy-dispersive spectrometer (EDS) and electron backscatter diffraction (EBSD) (Huang et al., 2017).

3.1.5 Porosity and Permeability Analysis

A total of 10 samples from the Shanxi Formation were used in porosity and permeability analysis. The samples were evaluated by Coretest AP608 overburden pore porosity and permeability experiments, and measured by helium as a carrier gas.

3.2 Low-Pressure N_2 Adsorption Analysis

Adsorption is the accumulation of molecules on the surfaces of a material (adsorbent). This process creates a layer of adsorbate on the adsorbent's surface and is a consequence of surface energy (Gregg and Sing, 1982). Low-pressure (77K) N_2 adsorption analysis is widely used to characterize the specific surface area (SSA), especially for the mesopore (pore diameter ranges from 2 to 50 nm) (Rouquerol et al., 1994). The N_2 adsorption is measured at low pressure (<0.127 MPa) and temperature (−196°C), and the equivalent surface areas are calculated according to the Brunauer–Emmett–Teller (BET) method (Brunauer et al., 1938):

$$r_K = (-2 \times \gamma \times V_m)/(R \times T \times \mathrm{In}(P/P_0)), \tag{1}$$

$$d = 2 \times r_K, \tag{2}$$

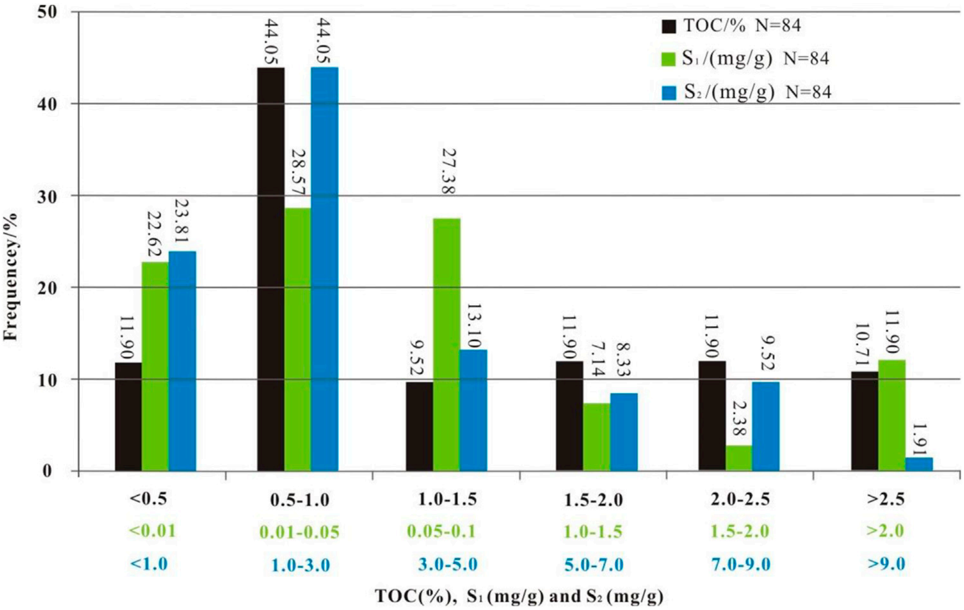

FIGURE 4 | TOC, S_1 (mg/g) and S_2 (mg/g) histogram. There are three groups of data scopes, color-coded: black, ranges of TOC data; green, ranges of S_1 data; blue, ranges of S_2 data.

where γ is the surface tension of liquid nitrogen at boiling point (8.59) (Wang et al., 2000; Qi et al., 2002a; Groen et al., 2003), V_m is the molar volume of liquid nitrogen in cm^3/mol, R is the gas constant in mol*K, T is the boiling point of nitrogen (77K), P is the gas vapor pressure in MPa, P_0 is the saturation pressure of adsorbent in MPa, d is the diameter of the pore in nanometers (nm), and r_K is the Kelvin radius of the pore in nanometers (nm).

A total of 20 samples from the Shanxi Formation shale were used in low-pressure N_2 adsorption analysis through a Micromeritics ASAP 2020 instrument, which is based on the manometric method. In the beginning, the void volume of the sample cell (SC) containing the adsorbent, is determined by helium expansion. Subsequently, specific amounts of the nitrogen gas are transferred into the sample cell and record the adsorption equilibrium pressure. The equilibrium pressure and the void volume data can be used to calculate the residual gas volume.

The quantity of adsorbed gas is then calculated as the difference between the quantity of gas transferred into the SC and the quantity of gas that could be accommodated in the void volume of the SC if no adsorption occurred (non-adsorption case). The gas dosing and equilibration steps are repeated until the N_2 pressure (P) and the saturation pressure (P_0) are equal. The SC is then gradually evacuated stepwise and the pressure is measured to calculate the amount of adsorbed gas. Hysteresis occurs due to desorption and adsorption differences (Huang et al., 2017).

3.3 Pore Structure and Fractal Dimension Analysis

Fractal dimension (D) is an important parameter used to analyze complex rock pore networks. It can represent the pore structural heterogeneity in detail and point out the degree of complexity of the pore system. The fractal dimension of the pores structure was computed in this work using the Frenkel–Halsey–Hill (FHH) (Yao et al., 2012) model:

$$\mathrm{Ln}(V/V_0) = \mathrm{constant} + (D-3)\times \mathrm{Ln}[\mathrm{Ln}(P/P_0)], \qquad (3)$$

where V is the volume of adsorbed gas molecules at equilibrium pressure in m^3/t, V_0 is the volume of monolayer coverage in m^3/t, D is the fractal dimension of the pore structure, P is the equilibrium pressure of the gas in MPa, and P_0 is the gas saturation pressure in MPa (Huang et al., 2017).

A larger fractal dimension means a coarser and more complex pore surface area. According to the measured nitrogen adsorption isotherm, the data of P/P_0 was selected and plotted in Ln [Ln (P/P_0)] with Ln (V/V_0), and then the fractal dimension was calculated according to the slope of the fitting trend line.

4 RESULTS

4.1 Organic Matter Characteristics

The total organic carbon (TOC) content of the Shanxi Formation shale ranges from 0.25% (minimum) to 3.00% (maximum) and mainly varies from 0.5% to 1.0% (**Figure 4**). The vitrinite reflectance (R_O) of shale varies from 0.85% (minimum) to 1.24% (maximum), with an average of 1.1%, whereas the R_O of shale mainly ranges from 1.0% to 1.2% (**Figure 5**).

The S_1 ranges from 0.001 mg/g (minimum) to 0.36 mg/g (maximum), with an average of 0.07 mg/g, and mainly varies from 0.01 mg/g to 0.1 mg/g (**Figure 4**). The S_2 ranges from 0.1 mg/g (minimum) to 9.30 mg/g (maximum), with an average of 2.83 mg/g, and most samples show an S_2 range of 1.0–5.0 mg/g

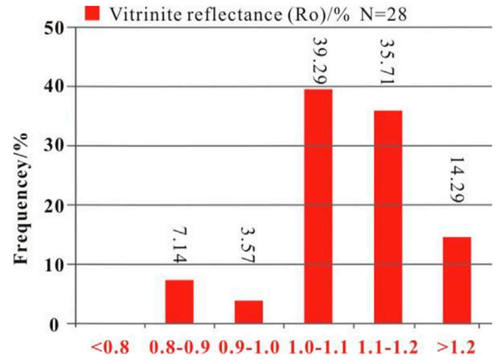

FIGURE 5 | Vitrinite reflectance (R_O) histogram.

(**Figure 4**). The T_{max} varies from 432°C to 455°C, with an average of 444°C (**Figure 5**). The organic matter in Shanxi Formation shale varies form Type II_1 to Type III, mainly Type II_2 followed by Type III. The Type II_1 organic matter is limited (**Figure 6**).

4.2 Mineral Composition Characteristics

The minerals of the Shanxi Formation shale mainly consist of clay minerals (minimum 47.5%, maximum 70.0%, and 61.0% on average) and quartz (minimum 26.0%, maximum 41.7%, and 33.7% on average). In addition, a small amount of plagioclase and siderite are also developed (average: 1.9% and 6.4%, respectively), and the K-feldspar and rutile minerals are hardly exist (**Table 1**). The samples from well E mainly consist of clay minerals (minimum 47.5%, maximum 51.1%, and average 49.3%) and quartz (minimum 36.9%, maximum 41.7%, and average 38.7%). Besides, a small amount of plagioclase and siderite is also developed (average: 2.2% and 8.5%, respectively), and the K-feldspar (the value is 0.9%) and rutile minerals are hardly exist (the average value is 0.9%) (**Table 1**). The samples in well F mainly consist of clay minerals (minimum: 61.9%, maximum: 70.0%, and average: 66.0%), and followed by quartz (minimum 26.0%, maximum 38.1%, and average 38.6%). However, K-feldspar, plagioclase, siderite, and rutile minerals are hardly exist (**Table 1**).

The clay minerals of Shanxi Formation shale consist of mixed-layer illite-smectite, illite, chlorite, kaolinite, and pyrophyllite. The mixed-layer illite-smectite accounts for the majority of clay minerals (minimum 10.0%, maximum 64.0%, and average 42.1%), which is followed by chlorite and illite (average: 17.2% and 15.6%, respectively). Besides, some of the samples developed kaolinite and pyrophyllite (the average values are 21.9% and 24.5% respectively), and the smectite-illite ratio is 17.5% (**Table 1**). The samples in well E mainly consists of kaolinite (minimum 45.0%, maximum 49.0%, and average 47.0%), and the mixed-layer illite-smectite, illite, chlorite followed by kaolinite (average: 14.7%, 22.0%, and 16.3%, respectively). The samples in well F mainly consist of mixed-layer illite-smectite (minimum 36.0%, maximum 64.0%, and average 56.9%), and chlorite, illite followed (average: 17.6% and 12.9%, respectively). Besides some of the samples developed pyrophyllite and kaolinite (average: 24.5% and 3.0%, respectively).

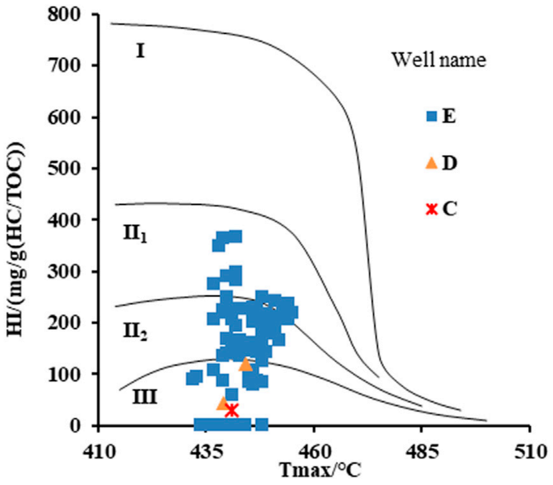

FIGURE 6 | Plot of the hydrogen index (HI) versus Tmax.

4.3 Characterization of Pores

The organic matter could be readily identified by SEM. The black points are organic matter (**Figures 7A,C**), which can be identified under high magnification (**Figure 7B**). Few pores can be observed in organic matter (**Figures 7B,C**), and only a few cracks can be observed. It is hard to ascertain that these cracks in organic matter are related to thermal evolution considering the sample processing procedure before microscopic analysis. The relatively low thermal maturity, which is reflected by the relatively low vitrinite reflectance values (R_O: 0.8–1.2%), impedes the formation of pores in organic matter of the Shanxi Formation shale.

Although the pores of organic matter are not well developed, interparticle pores occur among clay minerals (**Figures 8A,C**). The clay minerals lost their crystalline morphology and character during sedimentation, compaction, and consolidation that develop during diagenesis (Huang et al., 2017). Some clay minerals exhibit sheet-like shapes because of compaction (**Figures 8B,D**).

The porosity and permeability experimental results of Shanxi Formation shale are presented in **Figure 9**. The porosity of Shanxi Formation shale ranges from 0.8% (minimum) to 3.78% (maximum), with an average of 1.74%, and the permeability ranges from 0.0032 mD (minimum) to 0.0189 mD (maximum), with an average of 0.001 mD. This result shows the Shanxi Formation shale has low porosity and permeability (**Figure 9**). The well E is located in the south of the study area, and the Shanxi Formation shale is buried under 1400 m. The well F is located in the south part, and the Shanxi Formation shale is buried under 2600 m. From the porosity and permeability value, the porosity of well E with shallow depth is higher than well F, and the permeability distribution of well E is more compact than well F. The porosity of Shanxi Formation shale decreased as the depth increases. However, the permeability changes are irregular, which may be influenced by the geometry shape, grain size, and arrangement direction of the pores.

The porosity of Shanxi Formation shale samples of well E and well F shows a poor correlation with its permeability (**Figure 9A**). The correlation for shale samples from well F is the worst (**Figure 9B**).

TABLE 1 | Mineral composition of Shanxi Formation shale samples.

Well	Deep/ (m)	Mineral composition (%)							Clay mineral composition (%)					
		Quartz	K-feldspar	Plagioclase	Calcite	Siderite	Rutile	Clay minerals	I/S	Illite	Kaolinite	Chlorite	Pyrophyllite	I/S (S%)
E	1413.3	36.9	0.0	3.7	0.0	9.4	0.6	49.4	10.0	23.0	47.0	20.0	0.0	10.0
E	1415	37.6	0.0	2.2	0.0	11.7	1.0	47.5	19.0	17.0	49.0	15.0	0.0	15.0
E	1416	41.7	0.9	0.7	0.0	4.5	1.1	51.1	15.0	26.0	45.0	14.0	0.0	10.0
F	2695	29.8	0.0	1.2	0.0	0.0	0.0	69.0	58.0	11.0	0.0	31.0	0.0	15.0
F	2696.3	28.4	0.0	0.0	0.0	5.7	0.0	65.9	60.0	3.0	0.0	21.0	16.0	25.0
F	2699.4	30.0	0.0	0.0	0.0	0.0	0.0	70.0	36.0	4.0	2.0	11.0	47.0	30.0
F	2702.8	26.0	0.0	1.4	5.4	0.5	0.7	66.0	64.0	13.0	3.0	20.0	0.0	20.0
F	2703.9	33.1	0.0	2.1	0.0	0.0	0.0	64.8	54.0	16.0	0.0	13.0	17.0	25.0
F	2704.7	35.9	0.0	0.0	0.0	0.0	0.0	64.1	50.0	18.0	3.0	11.0	18.0	10.0
F	2706.4	38.1	0.0	0.0	0.0	0.0	0.0	61.9	55.0	25.0	4.0	16.0	0.0	15.0

"I/S," mixed-layer illite-smectite; "I/S (S%)," illite-smectite mixed-layer ratio.

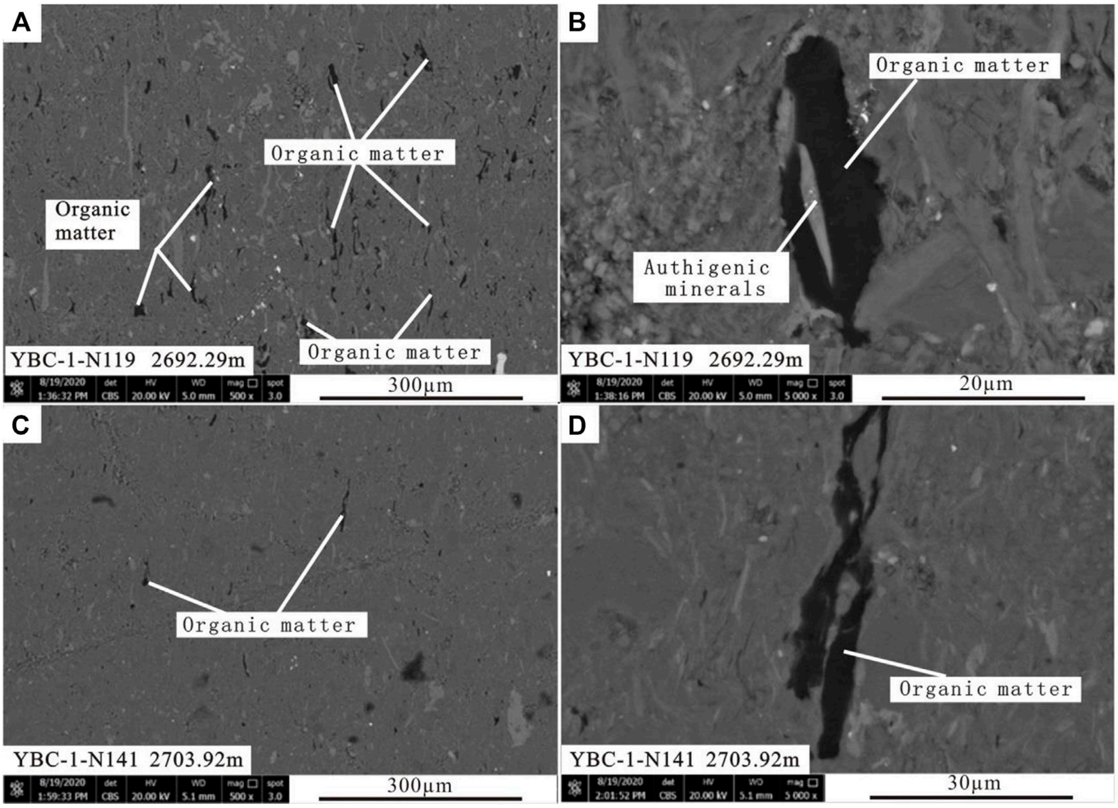

FIGURE 7 | SEM images of organic matter in Shanxi Formation shale. **(A)** organic matter pores; **(B)** organic matter pores with authigenic minerals fill in; **(C,D)** organic matter pores.

However, the correlation for shale samples from well E is better, although there are only three data points (**Figure 9C**).

Intergranular pores are well developed and pores are mainly filled with organic matter and minerals. Since upper paleozoic developed coal strata in the study area, the environment of the sedimentary is acidic-weak to acidic. The dissolution began when the mudstone was not consolidated into rock, and was associated with pressure dissolution. In this period, the early clay matrix was formed, resulting in a large number of fillings in the primary pores. After that, organic matter matured as the Shanxi Formation shale buried depth increased, and the rock is under the diagenetic stage. The filling of clay minerals and authigenic minerals in the pores, reduced the space of pores developed in the later stage. Hence, the Shanxi Formation shale in the study area shows poor physical properties of low porosity and low permeability.

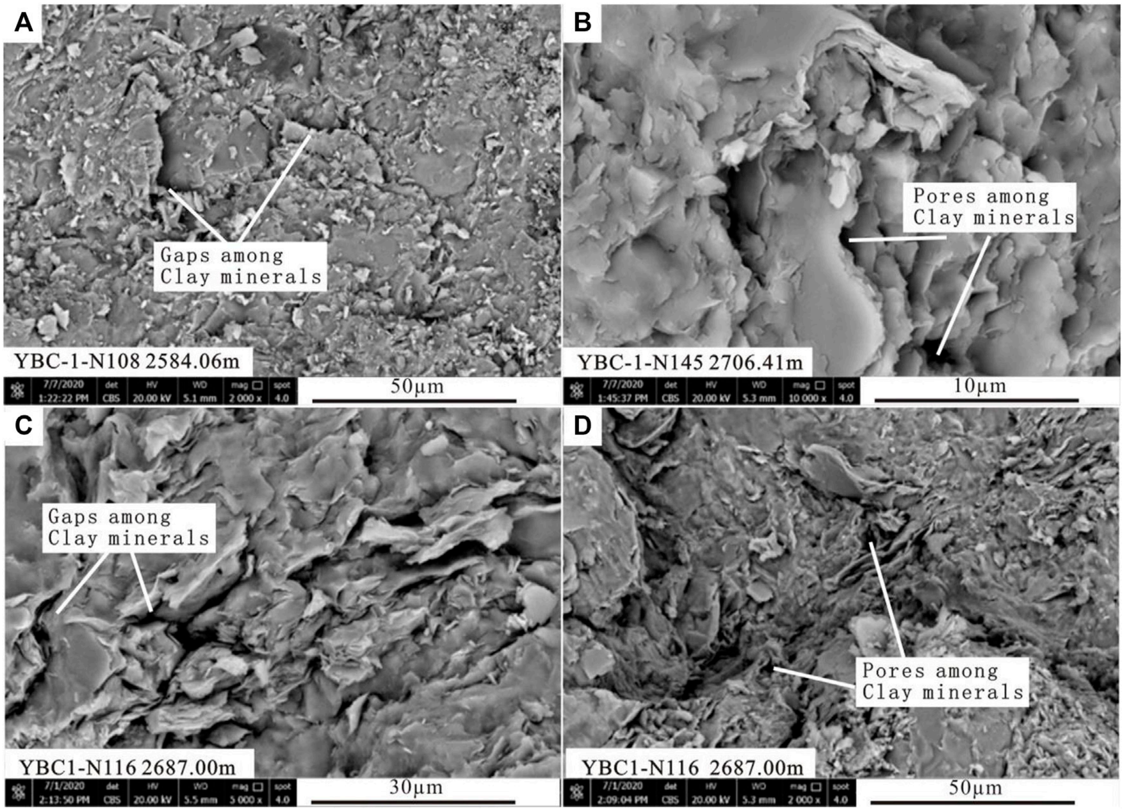

FIGURE 8 | SEM images of interparticle pores related to clay minerals in Shanxi Formation shale. **(A,C)** gaps among clay minerals; **(B,D)** pores among clay minerals.

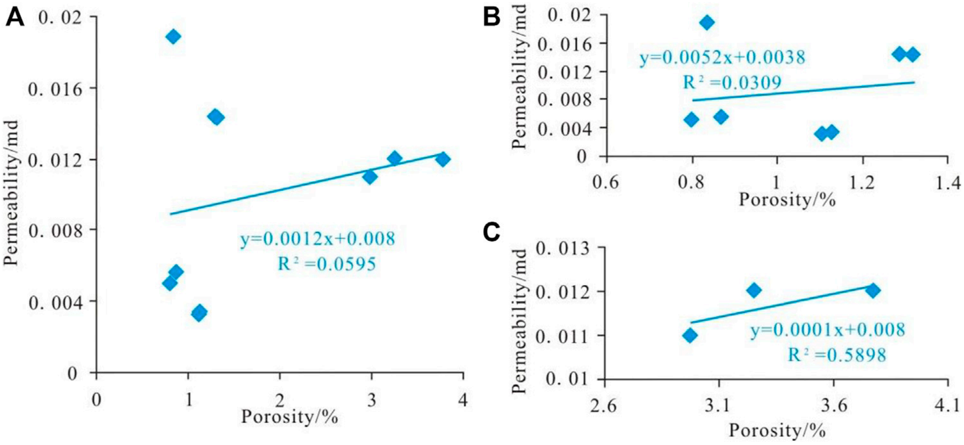

FIGURE 9 | The relationship between permeability and porosity. The relationship between permeability and porosity of **(A)** well E and well F, **(B)** well F and **(C)** well E

4.4 Low-Pressure N_2 Adsorption Analysis

4.4.1 Specific Surface Area and Pore Size Distribution

For the 20 samples of Shanxi Formation shale, the SSAs ranged from 1.67 m^2/g to 10.57 m^2/g, with an average of 3.7 m^2/g (**Figure 10**). The SSAs of well E ranged from 6.19 m^2/g to 10.57 m^2/g, with an average of 8.05 m^2/g, and those of well F ranged from 1.67 m^2/g to 7.94 m^2/g, with an average of 3.72 m^2/g. Samples from Well E exhibit much higher SSAs than well F.

The Shanxi Formation shale reservoir nitrogen adsorption and desorption curve (**Figure 11**) shows an inverse “S” shape for each

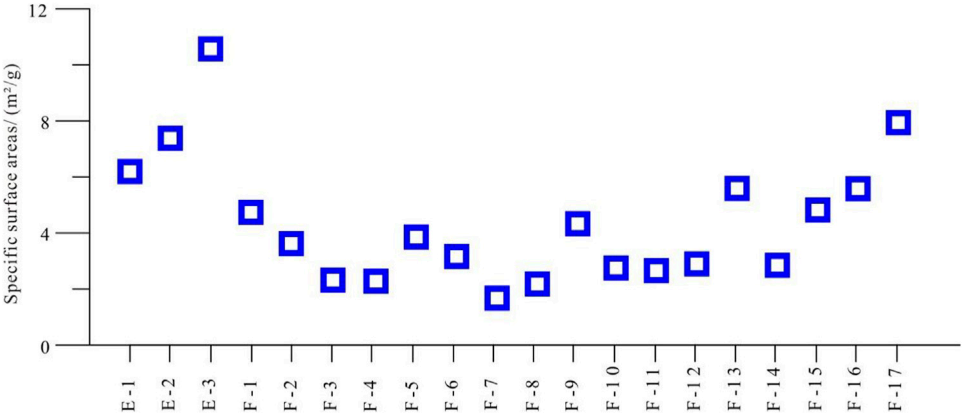

FIGURE 10 | Specific surface area of 20 samples.

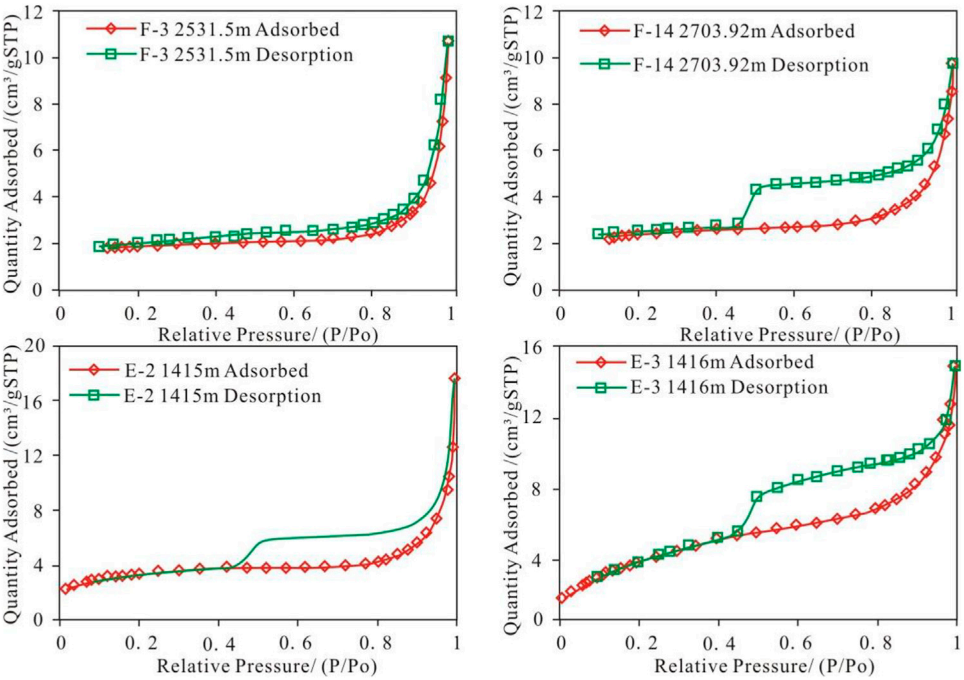

FIGURE 11 | Comparison of the isotherms and hysteresis of Shanxi Formation.

sample. The adsorption and desorption curve has little difference between each sample. In the low-pressure section ($P/P_0<0.2$), the adsorption curve slowly rises, and the curve is gentle and slightly convex, showing a monolayer of nitrogen adsorbed on the surface of reservoir pore throats. In the middle-pressure section ($0.2<P/P_0<0.8$), the adsorption capacity increased slowly as the relative pressure increased, and the adsorption curve is approximately linear, indicating the multi-molecular layer nitrogen adsorption. In the high-pressure section ($0.8<P/P_0<1.0$), the adsorption curve increased rapidly and showed a concave shape. When the equilibrium pressure is close to the saturated vapor pressure, the slope of the adsorption curve of most samples is still increasing. However, the sample did not show adsorption saturation. This shows that a small number of pore throats with pores diameter larger than 50 nm are developed in the samples. When $P/P_0>0.45$, the desorption curve is above the adsorption curve.

The nitrogen adsorption isotherms of Shanxi Formation shale show obvious hysteresis loops (**Figure 11**). The International Union of Pure and Applied Chemistry (IUPAC) classified the adsorption isotherms into six types, from Type I to Type VI. The IUPAC also classified the hysteresis patterns into four types, Type

H_1 to Type H_4. The shale samples isotherms are closely similar to Type III isotherm shape (**Figure 11**). The hysteresis is the same as Types H_3 and H_4. The Type H_3 loop is related to plate-like particles giving rise to slit-shaped pores. Similarly, the Type H_4 loop is usually associated with narrow slit-like pores (Sing, 1985; Rouquerol et al., 1994; Rouquerol et al., 1999; Jiang et al., 2010; Kuila et al., 2012). With the increase of relative pressure, the adsorption curve and desorption curve rise fast. When the relative pressure is close to 1, the curve is almost perpendicular to the P/P_0 axis and does not reach the adsorption saturation, indicating the occurrence of condensation in the pores during nitrogen adsorption. After that, the relative pressure decreased and the desorption amount decreased rapidly. There is no obvious inflection point between the adsorption curve and desorption curve. This adsorption characteristic often occurs in wedge-shaped holes with openings at both ends or in the formation of non-rigid aggregates composed of flake-like particles (Sing, 1985; Rouquerol et al., 1999; Jiang et al., 2010; Kuila et al., 2012). According to the isotherms and hysteresis description, the pores morphology of Shanxi Formation is type B (Mohammad et al., 2013; Xu et al., 2019), and means dominance of slit-plate-like pores, which is open and has good connectivity. The adsorption and desorption isotherms converge at a relative pressure (P/P_0) of 0.45–0.5, equivalent pore diameter of 2.3–2.7 nm according to the BET calculation based on the relationship between relative pressure (P/P_0) and diameter. Therefore, it is considered that the hysteresis loop and the "forced closure" of shale pores shown by nitrogen adsorption isotherm of Shanxi Formation occur in the range of pore diameter between 2.3 and 2.7 nm.

4.4.2 The Fractal Dimension

Due to the analytical temperature of the nitrogen, adsorption analyses are too low (–196°C) for nitrogen molecules to get access to the micropore. The nitrogen adsorption analyses are usually used to demonstrate the mesopore size (2–50 nm) distribution (Unsworth et al., 1989; Rouquerol et al., 1994). Moreover, the "forced closure" emerges corresponding to diameter 2.3–2.7 nm, and the area of the incremental pores fluctuates rapidly from 2–3 nm of pore diameter (**Figure 12**); hence, we divided the size of the pores in this research into three ranges with diameters <2 nm (micropore), 2–50 nm (mesopore), and >50 nm (macropore).

A scatter diagram of Ln [Ln (P_0/P)] versus Ln (V/V_0) for the shale samples data using the original low-temperature nitrogen adsorption isotherm data is represented in **Figure 13**. Most of the correlation coefficients of the linear fitting curves were larger than 0.96 for all the three ranges, and only a few of the correlation coefficients of the linear fitting curves were larger than 0.84 for all the three ranges.

Calculation results are based on the Frenkel-Halsey-Hill (FHH) model by the low-pressure N_2 adsorption data of the 20 samples. The results show only two data points of the pore size d>50 nm. It indicates that the Shanxi Formation shale has few macropores but mainly developed micropores and mesopores. The low porosity and permeability also indicate a low pore diameter for the Shanxi Formation shale.

As evident from **Table 2** and **Figure 14**, the micropore has a relatively high fractal dimension with an average of 2.77, the mesopore shows a low fractal dimension with an average of 2.65, while the macropore has a high fractal dimension with an average of 2.77. The fractal dimension reflects the structure of pores. Micropore and macropore represent the largest fractal dimensions, meaning the strongest pore structure complexity. However, the mesopore represents the lowest fractal dimensions, meaning less pore structure complexity and better pore connectivity compared with the micropore and the macropore. The fractal dimension of pores in the Shanxi Formation shows that the shale has a coarser pore surface, a lower pore connectivity, and stronger heterogeneity of the reservoir. Compared with the Yanchang Formation shale (lower-maturity shale) (Wang, 2018) in the Ordos basin of the North China Plate, the shale of Shanxi Formation shows relatively higher fractal dimensions on average but a narrow range of fractal dimensions, proving stronger pore structure complexity but lower pore structure diversity in the lower-maturity shale. Compared with highly mature marine shales, the Shanxi Formation shale in the research area represents relatively equal fractal dimensions, indicating high pore structure complexity but lower pore structure diversity in the lower-maturity shale (Yang et al., 2014; Tang et al., 2015).

5 DISCUSSION

5.1 Influence of Rock Framework Particles on Specific Surface Area

The heterogeneity of pore structure is essentially affected by the rock framework particles, which mainly include kerogen and minerals components. To analyze the influence of rock framework particles on the pore structural heterogeneity, the correlations of specific surface area and fractal dimension with S_1, S_2, TOC and quartz, clay minerals, and other types of clay minerals were established.

5.1.1 Effect of Organic Matter on Specific Surface Area

For the 20 samples, both were used in low-pressure N_2 adsorption and Rock-Eval analysis. The S_1 and TOC present no clear correlation with the SSA. The S_2 exhibits a slight positive correlation with the SSA, but with a rather low correlation coefficient (R^2 = 0.4939) (**Figure 15**). This proved that the residual bitumen of low thermal-maturity shale has no obvious effect on SSA and the kerogen slight effect on it.

5.1.2 Effect of Minerals on Specific Surface Area

For the 10 samples used both in low-pressure N_2 adsorption analysis and X-ray diffraction analysis, quartz has a positive effect on the SSA, while clay minerals show a negative correlation with the SSA (**Figure 16A**). For different types of clay minerals, the illite has a positive correlation with the SSA, while mixed-layer illite-smectite has a negative correlation with the SSA (**Figure 16**). Chlorite also has a negative correlation with the SSA, but with a rather low correlation coefficient R^2 (**Figure 16B**). Samples with higher content of quartz exhibit higher SSA, while samples with higher content of clay minerals show lower SSA. For different types of clay minerals, samples with high content of illite exhibit higher SSA, whereas samples with high content of mixed layers of illite-smectite and chlorite show lower SSA.

Quartz can keep crystal form under the compaction, high content quartz means high SSA of quartz. The content of illite

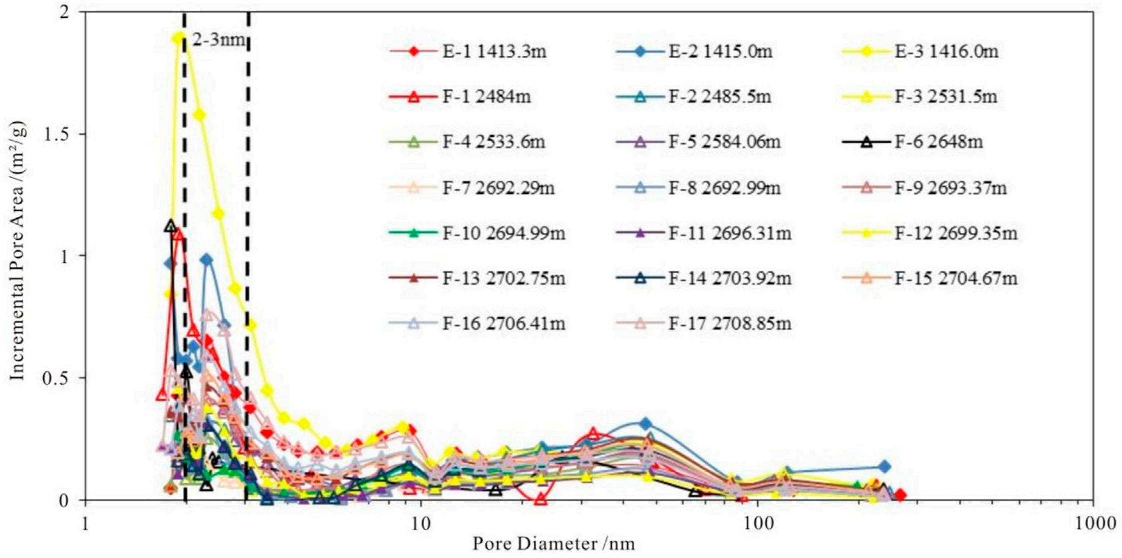

FIGURE 12 | Comparison of the pore diameter and incremental pore are of Shanxi Formation shale samples.

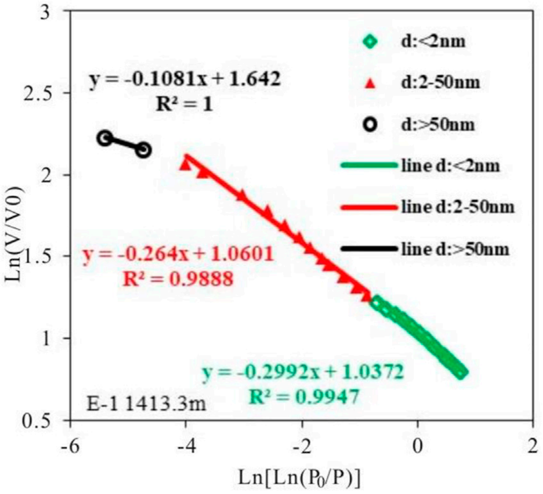

FIGURE 13 | Fractal dimensions of the pores in Shanxi Formation shale samples.

TABLE 2 | Tables of fractal dimension of Shanxi Formation shale samples.

Sample	Depth (m)	Fractal dimension					
		<2 nm		2–50 nm		>50 nm	
		D	R^2	*D*	R^2	*D*	R^2
E-1	1413.3	2.7008	0.9947	2.736	0.9888	2.8919	1
E-2	1415	2.6532	0.86	2.6494	0.9908	2.7161	1
E-3	1416	2.7948	0.8789	2.7823	0.9979	2.6895	1
F-2	2485.4	2.7948	0.9129	2.5376	0.9922	2.7971	1
F-3	2531.5	2.8811	0.9643	2.5848	0.9869	2.7087	1
F-5	2584.06	2.7255	0.984	2.636	0.9959	2.6188	1
F-7	2692.29	2.8963	0.8427	2.5979	0.9938	2.7877	1
F-8	2692.99	2.8213	0.9312	2.6215	0.9922	2.7786	1
F-9	2693.37	2.7761	0.9745	2.6793	0.9951	2.7906	1
F-10	2694.99	2.7613	0.9705	2.5025	0.9977	2.7014	1
F-11	2696.31	2.8074	0.9415	2.673	0.992	2.7457	1
F-12	2699.35	2.7649	0.9602	2.6932	0.9961	2.8692	1
F-13	2702.75	2.7696	0.9844	2.6662	0.9959	2.8333	1
F-14	2703.92	2.8158	0.9641	2.6604	0.9929	2.7163	1
F-15	2704.67	2.7621	0.9874	2.6725	0.9963	2.775	1
F-16	2706.41	2.7231	0.9867	2.7065	0.9979	2.8832	1
F-17	2708.85	2.7015	0.9893	2.7279	0.9979	2.8517	1

increased as the depth of shale increased. Clay minerals and mixed-layer illite-smectite are hard to keep crystal form under the compaction, and filled with authigenic minerals in the pores, decreased the SSA of Shanxi Formation shale. All in all, quartz and illite increase the SSA, whereas clay minerals and mixed-layer illite-smectite decrease the SSA.

5.1.3 Effect of Porosity and Permeability on Specific Surface Area

For the 10 samples that used in porosity and permeability, X-ray diffraction, and low-pressure N_2 adsorption analysis, porosity has a positive effect on the SSA (**Figure 17A**), while permeability shows no clear correlation with the SSA (**Figure 17B**). The larger the SSA is, the higher porosity of the reservoir is. High porosity means more pores or large pores developed in the reservoir. As the number of pores increased, the SSA of pores increased too. However, the result between permeability and SSA presents a poor correlation coefficient R^2. Permeability may be influenced by the geometry shape, grain size, and arrangement direction of the pores. In **Figure 16**, quartz also has a positive effect on the SSA. In fact, quartz, as rock skeleton grains, plays an important role in resistance to the compaction, and then the pores were kept. Hence, high content quartz means large porosity, and then

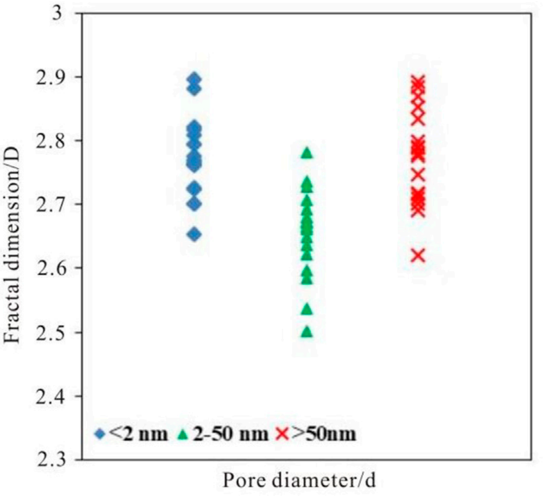

FIGURE 14 | Comparison of different pore diameter fractal dimensions of Shanxi Formation.

high SSA. Hence, the permeability affects by many influences, so the relationship with SSA is poor.

All in all, the porosity of Shanxi Formation shale increased as the SSA increasing, but the relationship between permeability and SSA is hard to be identified.

5.2 Influence of Rock Framework Particles on Fractal Dimension

5.2.1 Effect of Organic Matter on Fractal Dimension

The fractal dimension of the micropore, mesopore and macropore of the Shanxi Formation shale, each has a different correlation with the S_1 and S_2 (**Figure 18**). For the micropore, it presents a positive correlation with the S_1 and a negative correlation with the S_2. However, the correlation coefficient of the micropore is low, which shows the irrelevance of organic matter with the micropore structure heterogeneity. The fractal dimension of the mesopore presents a negative correlation with the S_1 and a positive correlation with the S_2. However, the correlation coefficient of the mesopore is low for the S_1 and S_2. This indicates that mesopore structure heterogeneity also has a low correlation with organic matter. The fractal dimension of the macropore presents a negative correlation with the S_1 and S_2, and the correlation coefficient of the macropore is the lowest, which means the macropore structure heterogeneity has no obvious relationship with organic matter, either (**Figure 18**).

All in all, for Shanxi Formation shale the fractal dimension of the micropore, mesopore, and macropore present no obvious relationship with the S_1 and S_2. It is proved that the content of organic matter does not affect the pore structure heterogeneity of Shanxi Formation shale in the research area.

5.2.2 Effect of Minerals on Fractal Dimension

The mesopore, micropore, and macropore present great differences in the correlation between fractal dimension and quartz and clay minerals. The fractal dimension of the micropore and macropore presents a negative correlation with quartz, but a positive correlation with clay minerals. On the contrary, the fractal dimension of the mesopore presents a positive correlation with quartz, but a negative correlation with clay minerals. None of the micropore, mesopore, and macropore presented a strong correlation coefficient between the fractal dimension with quartz and clay minerals (**Figure 19**).

The illite and the mixed-layer illite-smectite exhibit different correlation with the fractal dimension. The fractal dimension of micropore presented a positive correlation with the mixed-layer illite-smectite, whereas the mesopore and macropore presented a negative correlation with the mixed-layer illite-smectite. The relationship between fractal dimension and the illite of micropore presented a negative correlation with a strong correlation coefficient. However, the relationship between fractal dimension and the illite of mesopore and macropore presented a negative correlation with a poor correlation coefficient.

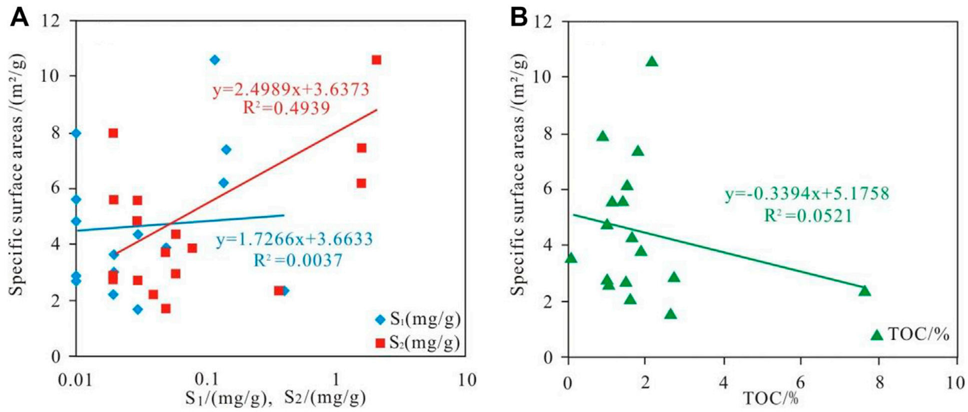

FIGURE 15 | Correlation of the average fractal dimensions with S_1, S_2, and TOC of Shanxi Formation. Average fractal dimensions with **(A)** S_1 and S_2, **(B)** TOC.

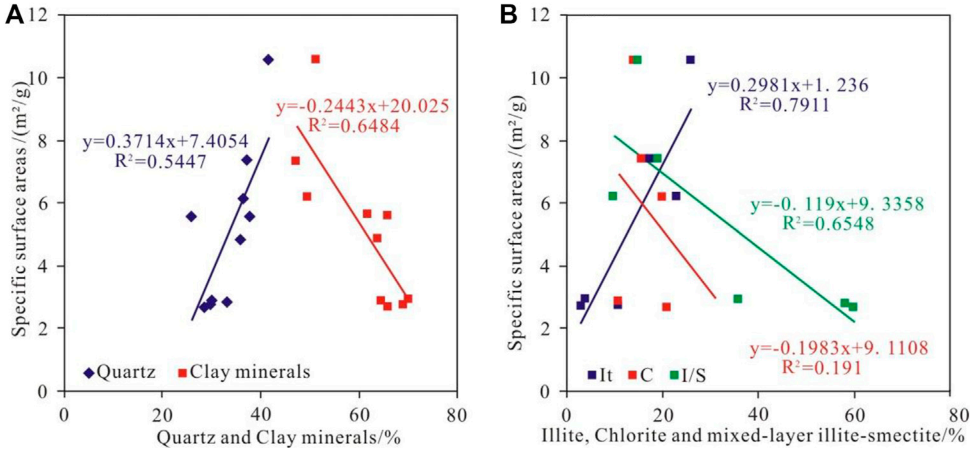

FIGURE 16 | Correlation of SSA with quartz, clay minerals and other types of clay minerals. Correlation of SSA with **(A)** quartz and clay minerals, **(B)** Illite, chlorite, mixed-layer illite-smectite (I/S). Illite (It); Chlorite **(C)**; Mixed-layer illite-smectite (I/S).

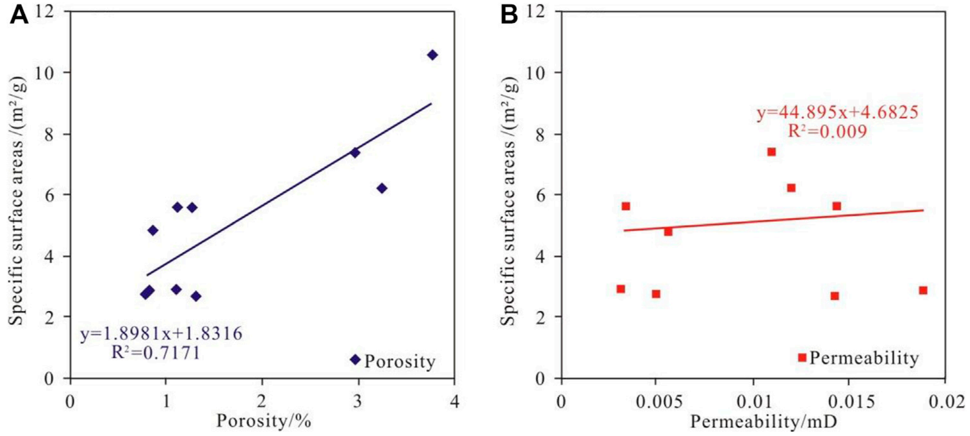

FIGURE 17 | Correlation of SSA with porosity and permeability of Shanxi Formation shale. Correlation of SSA with **(A)** porosity, **(B)** permeability.

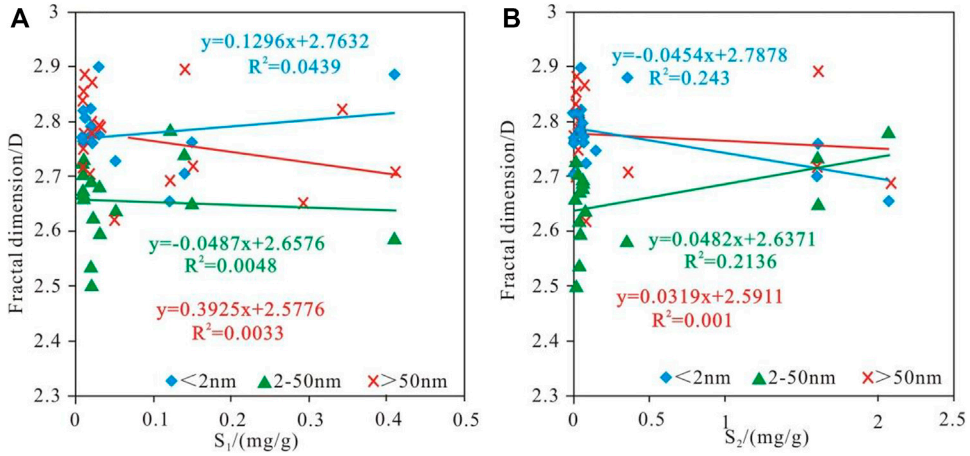

FIGURE 18 | Pore size distributions and relationship between fractal dimension and kerogen. Relationship between fractal dimension and **(A)** S_1, **(B)** S_2.

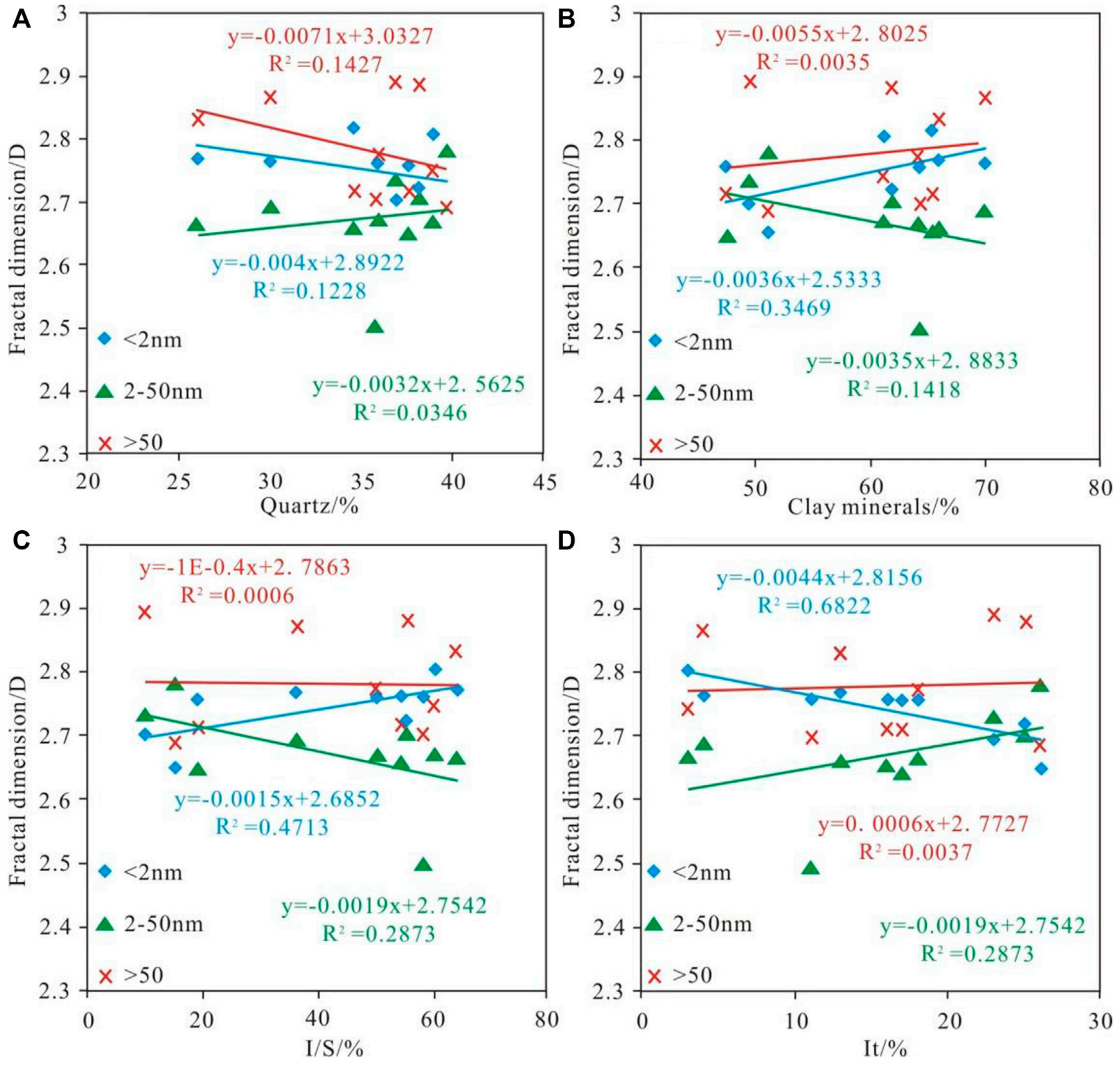

FIGURE 19 | The relationship of fractal dimension with detrital minerals and clay minerals. relationship between fractal dimension and **(A)** quartz, **(B)** clay minerals, **(C)** I/S and **(D)** It.

For all three types of pores, quartz has an inconspicuous correlation with the fractal dimension, and the correlation coefficient R^2 values are low (**Figure 19A**). This indicated that quartz does not affect the fractal dimension of the Shanxi Formation shale. For the micropores, clay minerals and the mixed-layer illite-smectite present a slightly positive correlation with fractal dimension (**Figures 19B,C**). However, the illite shows obviously negative correlation with a high correlation coefficient R^2 (**Figure 19D**). For the mesopores, the mixed-layer illite-smectite and illite also present slightly but opposite correlation with fractal dimension (**Figures 19C,D**). The former is negative and the latter is positive. For the macropores, any type of mineral shows no impact on the fractal dimension. The illite shows a hair-like or acicular form and shows a more confirmative effect of the illite minerals on structural heterogeneity for micropore (**Figure 19D**). The absolute value of the slope of correlation lines with fractal dimension for micropore is larger than mesopore and macropore (**Figure 19**). It can be concluded that the mixed-layer illite-smectite and illite affect the fractal dimension of Shanxi Formation shale. This also indicates a stronger impact of the clay minerals on structural heterogeneity for micropore.

Quartz can keep crystal form under the compaction and has a smooth surface of the mineral. The mixed-layer illite-smectite is easy to lose crystal form during the compaction. This indicates the two types of minerals mentioned above are not the main influencing factors of pore heterogeneity. As the burial depth of illite increased, the content of illite increased too. Illite has a high correlation with the fractal dimension of micropore, which improves to be the main influencing factor of pore heterogeneity. All in all, quartz, clay minerals, and mixed-layer illite-smectite present no obvious contribution to pore structural heterogeneity. However, illite decrease pore structural heterogeneity of micropore. Compaction is the main

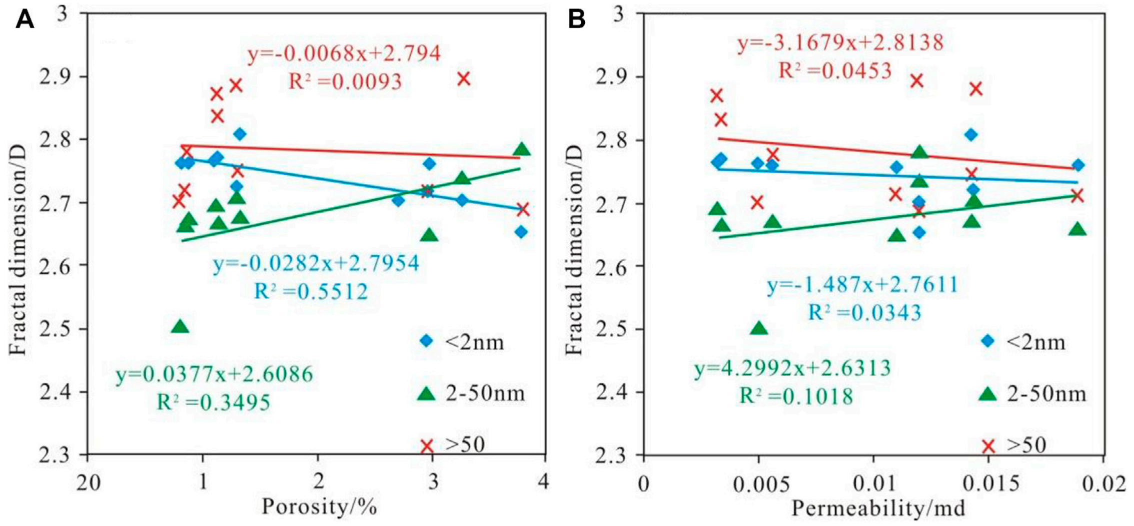

FIGURE 20 | Relationship of fractal dimension with porosity and permeability. Fractal dimension with **(A)** porosity, **(B)** permeability.

factor affecting the pores of Shanxi Formation shale in the study area.

5.2.3 Effect of Porosity and Permeability on Fractal Dimension

The fractal dimension of the micropore, mesopore and macropore of the Shanxi Formation shale, represent a similar correlation with porosity and permeability (**Figure 20**). The fractal dimension of the micropore and macropore both presented a negative correlation with porosity and permeability, while the mesopore presented a positive correlation with porosity and permeability (**Figures 20A,B**). The results only show a good negative correlation between porosity and the fractal dimension of the micropore (R^2 = 0.5512). Other pores have a poor correlation coefficient R^2 between porosity and permeability and the fractal dimension. The larger the micropore fractal dimension, the poor the porosity of the Shanxi Formation shale reservoir, and the more complex the micropore (**Figure 20A**).

All in all, for Shanxi Formation shale, the fractal dimension of the micropore presents good negative relationship with porosity. It is proved that the Shanxi Formation shale with higher porosity presents lower micropore structure heterogeneity in the research area.

6 CONCLUSION

1) The Shanxi Formation shale in the study area shows low porosity and permeability, and the pore structure is complexed. Micropore and macropore have a relatively high fractal dimension with an average of 2.77. Mesopore has a low fractal dimension with an average of 2.65. The fractal dimension average of different pores of Shanxi Formation shale is all larger than 2.5, which means all the structures of pores are complex. However, the structure of pores of the micropore and macropore is more complex than the mesopore.
2) Organic matter displays a low impact on the pore structure heterogeneity for Shanxi Formation shale in the research area. S_2, $S_{1,}$ and TOC exhibit no clear correlation with SSA, which means the organic matter has little effect on SSA. For Shanxi Formation shale the fractal dimension of micropore, mesopore and macropore present no obvious relationship with organic matter. This proved that organic matter is not the main factor affecting the heterogeneity of pore structure of Shanxi Formation shale in the research area. The low maturity is the reason for the non-influence of organic matter.
3) Illite has a strong effect on the pore structural heterogeneity of Shanxi Formation shale. It is the main factor of the pore structural heterogeneity. As the content of illite increased, the SSA increased, whereas the fractal dimension decreased. This indicates pores with high content of illite have high SSA and low fractal dimension, reflecting low pore structural heterogeneity. Although the correlation coefficients R^2 of quartz and clay minerals with SSA are more than 0.5, quartz and clay minerals have no obvious relationship with the fractal dimension. Hence, quartz and clay minerals have little impact on the pore structure heterogeneity. All in all, samples with high content of the illite present low pore structural heterogeneity. Quartz and clay minerals have little impact on the pore structure heterogeneity.
4) The Shanxi Formation shale with higher porosity presents lower micropore structure heterogeneity in the research area. However, the permeability has no correlation with pore structure heterogeneity. As the porosity increased, the SSA increased, while the fractal dimension decreased. This indicates pores with high porosity have high SSA and low fractal dimension, reflecting low pore structural heterogeneity. However, the relationship between permeability and SSA, and the relationship between permeability and fractal dimension

are poor. These may be influenced by the geometry shape, grain size, and arrangement direction of the pores in the research area, which control by compaction. Hence, the relationship between permeability and pore structural heterogeneity is not clear.

DATA AVAILABILITY STATEMENT

The original contributions presented in the study are included in the article/Supplementary Material; further inquiries can be directed to the first author.

AUTHOR CONTRIBUTIONS

Conceptualization: DZ and YW; methodology: CL and EL; formal analysis: EL, CL, and DS; investigation: EL; resources: DZ and QX; data curation: QX; writing—original draft preparation: EL; writing—review and editing: EL, CL, and DS; visualization: EL; supervision: CL and DS; project administration: CL and DS; and funding acquisition: DS. All authors have read and agreed to the published version of the manuscript.

FUNDING

This research was funded by the China Geological Survey Project, grant number "DD20210435."

ACKNOWLEDGMENTS

The authors would like to express their sincere gratitude to Pengju Yang, Jianwei Zang, and Chuanfang Jiang from SINOPEC Jiangsu Oilfield Branch Company, Yangzhou, Jiangsu, China. They appreciate the valuable comments from the editors and reviewers.

REFERENCES

Brunauer, S., Emmett, P. H., and Teller, E. (1938). Adsorption of Gases in Multimolecular Layers. *J. Am. Chem. Soc.* 60 (2), 309–319. doi:10.1021/ja01269a023

Cao, G. S., Xu, G. M., Lin, Y. X., and Yang, Q. H. (2013). Geometry Characteristics of Pre-mesozoic Basin of Eastern Part of North China. *J. Henan Polytech. Univ. (Narural Sci.* 32 (1), 46–51. (in Chinese with English abstract).

Cattaneo, A., and Steel, R. J. (2003). Transgressive Deposits: a Review of Their Variability. *Earth-Science Rev.* 62 (3-4), 187–228. doi:10.1016/s0012-8252(02)00134-4

Chen, L., Jiang, Z., Liu, Q., Jiang, S., Liu, K., Tan, J., et al. (2019a). Mechanism of Shale Gas Occurrence: Insights from Comparative Study on Pore Structures of Marine and Lacustrine Shales. *Mar. Petroleum Geol.* 104, 200–216. doi:10.1016/j.marpetgeo.2019.03.027

Chen, L., Liu, K. Y., Jiang, S., Huang, H., and Zuo, L. (2021). Effect of Adsorbed Phase Density on the Correction of Methane Excess Adsorption to Absolute Adsorption in Shale. *Chem. Eng. J.* 420, 127–678. doi:10.1016/j.cej.2020.127678

Chen, L., Zuo, L., Jiang, Z., Jiang, S., Liu, K., Tan, J., et al. (2019b). Mechanisms of Shale Gas Adsorption: Evidence from Thermodynamics and Kinetics Study of Methane Adsorption on Shale. *Chem. Eng. J.* 361, 559–570. doi:10.1016/j.cej.2018.11.185

Cummings, D. I., Arnott, R. W. C., and Hart, B. S. (2006b). Tidal Signatures in a Shelf-Margin Delta. *Geol* 34, 249–252. doi:10.1130/g22078.1

Cummings, D. I., Hart, B. S., and Arnott, R. W. C. (2006a). Sedimentology and Stratigraphy of a Thick, Areally Extensive Fluvial-Marine Transition, Missisauga Formation, Offshore Nova Scotia, and its Correlation with Shelf Margin and Slope Strata. *Bull. Can. Petroleum Geol.* 54 (2), 152–174. doi:10.2113/gscpgbull.54.2.152

Curtis, J. B. (2002). Fractured Shale-Gas Systems. *AAPG Bull.* 86 (11), 1921–1938. doi:10.1306/61eeddbe-173e-11d7-8645000102c1865d

Espitalié, J., LaPorte, J. L., Madec, M., Marquis, F., LePlat, P., Paulet, J., et al. (1977). Méthode rapide de caractérisation des roches mètres, de leur potentiel pétrolier et de leur degré d'évolution. *Rev. Inst. Fr. Pét.* 32, 23–42. doi:10.2516/ogst:1977002

Gao, F., Song, Y., Li, Z., Xiong, F., Chen, L., Zhang, Y., et al. (2018). Lithofacies and Reservoir Characteristics of the Lower Cretaceous Continental Shahezi Shale in the Changling Fault Depression of Songliao Basin, NE China. *Mar. Petroleum Geol.* 98, 401–421. doi:10.1016/j.marpetgeo.2018.08.035

Gregg, S. J., and Sing, K. S. W. (1982). *Adsorption, Surface Area, and Porosity*, 2. New York: Academic Press, 312.

Groen, J. C., Peffer, L. A. A., and Pérez-Ramıirez, J. (2003). Pore Size Determination in Modified Micro- and Mesoporous Materials. Pitfalls and Limitations in Gas Adsorption Data Analysis. *Microporous Mesoporous Mater.* 60, 1–17. doi:10.1016/s1387-1811(03)00339-1

He, J., Wang, J., Yu, Q., Liu, W., Ge, X., Yang, P., et al. (2018). Pore Structure of Shale and its Effects on Gas Storage and Transmission Capacity in Well HD-1 Eastern Sichuan Basin, China. *Fuel* 226, 709–720. doi:10.1016/j.fuel.2018.04.072

Hu, Z. Q., Zhou, X. K., and Zhu, J. H. (2006). Hydrocarbon Generation Potential of Upper Paleozoic in Eastern Part of North China. *Petroleum Explor. Dev.* 35 (6), 697–701. (in Chinese with English abstract).

Huang, Z., Liu, G., Li, T., Li, Y., Yin, Y., and Wang, L. (2017). Characterization and Control of Mesopore Structural Heterogeneity for Low Thermal Maturity Shale: A Case Study of Yanchang Formation Shale, Ordos Basin. *Energy fuels.* 31, 11569–11586. doi:10.1021/acs.energyfuels.7b01414

Jarvie, D. M., Hill, R. J., Ruble, T. E., and Pollastro, R. M. (2007). Unconventional Shale-Gas Systems: the Mississippian Barnett Shale of North-Central Texas as One Model for Thermogenic Shale-Gas Assessment. *Bulletin* 91, 475–499. doi:10.1306/12190606068

Ji, W., Song, Y., Jiang, Z., Meng, M., Liu, Q., Chen, L., et al. (2016). Fractal Characteristics of Nano-Pores in the Lower Silurian Longmaxi Shales from the Upper Yangtze Platform, South China. *Mar. Petroleum Geol.* 78, 88–98. doi:10.1016/j.marpetgeo.2016.08.023

Jiang, F., Chen, D., Wang, Z., Xu, Z., Chen, J., Liu, L., et al. (2016). Pore Characteristic Analysis of a Lacustrine Shale: a Case Study in the Ordos Basin, NW China. *Mar. Petroleum Geol.* 73, 554–571. doi:10.1016/j.marpetgeo.2016.03.026

Jiang, Y. Q., Dong, D. Z., Qi, L., Shen, Y. F., Jiang, C., and He, F. W. (2010). The Basic Characteristic and Evaluation of Shale Reservoir. *Nat. Gas. Ind.* 30 (10), 7–12.

Kennedy, M. J., Pevear, D. R., and Hill, R. J. (2002). Mineral Surface Control of Organic Carbon in Black Shale. *Science* 295 (5555), 657–660. doi:10.1126/science.1066611

Kuang, H. W., Liu, Y. Q., Peng, X. B., Yang, F., Chen, M. P., Cen, C., et al. (2009). Sedimentary and Tectonic Features and Proto-Basin of Early Cretaceous Tanzhuang - Shenqiu Sag, Zhoukou Depression, in Southern Area of North China Craton. *Geol. Rev.* 55 (6), 801–813. (in Chinese with English abstract).

Kuila, U., Prasad, M., Derkowski, A., and McCarty, D. K. (2012). "Compositional Controls on Mudrock Pore-Size Distribution: An Example from Niobrara Formation," in SPE Annual Technical Conference and Exhibition, San Antonio, Texas, USA, October 8–10, 2012, 160141.

Li, J., Wu, K., Chen, Z., Wang, W., Yang, B., Wang, K., et al. (2019). Effects of Energetic Heterogeneity on Gas Adsorption and Gas Storage in Geologic Shale Systems. *Appl. Energy* 251, 113368. doi:10.1016/j.apenergy.2019.113368

Li, P., Zhang, J. C., Tang, X., Huo, Z. P., Li, Z., Luo, K. Y., et al. (2020). Assessment of Shale Gas Potential of the Lower Permian Transitional Shanxi-Taiyuan Shales in the Southern North China Basin. *Aust. J. Earth Sci.* 68 (2), 262–284. doi:10.1080/08120099.2020.1762737

Li, S., and Yao, X. (2011). Discussion on Tectonic Evolution and Hydrocarbon Accumulation Upper Palaeozoic Formation in Northern Zhoukou Depression Belt. *Fault block Oil &Gas Field* 18 (5), 564–567. (in Chinese with English abstract).

Li, W. H., Chen, J. W., and Shao, J. (1996). Sedimentary Facies and Framework of the Lower Cretaceous Strata in the Zhoukou Depression. *Sediment. facies Paleogeogr.* 16 (1), 43–50. (in Chinese with English abstract).

Li, Y., and Ma, M. Y. (2013). Petrography and Diagenesis of Permian Sandstone Reservoirs in Zhoukou DepressionSouthern North China Basin. *Petroleum Geol. Exp.* 32 (4), 640–645. (in Chinese with English abstract).

Liu, E.-r., Shi, D. S., Shi, D.-s., Wang, Y.-h., Xu, Q.-c., Wang, B.-q., et al. (2020). Sequence Stratigraphic Framework and Sedimentary Model of Shanxi Formation in Northeast Zhoukou Depression of the North China Plate. *China Geol.* 3, 575–590. doi:10.31035/cg2020067

Liu, G., Zhai, G., Huang, Z., Zou, C., Xia, X., Shi, D., et al. (2019a). The Effect of Tuffaceous Material on Characteristics of Different Lithofacies: A Case Study on Lucaogou Formation Fine-Grained Sedimentary Rocks in Santanghu Basin. *J. Petroleum Sci. Eng.* 179, 355–377. doi:10.1016/j.petrol.2019.04.072

Liu, G., Zhai, G., Yang, R., He, T., and Wei, B. (2021). Quartz Crystallinity Index: New Quantitative Evidence for Biogenic Silica of the Late Ordovician to Early Silurian Organic-Rich Shale in the Sichuan Basin and Adjacent Areas, China. *Sci. China Earth Sci.* 64 (5), 773–787. doi:10.1007/s11430-020-9718-2

Liu, G., Zhai, G., Zou, C., Cheng, L., Guo, X., Xia, X., et al. (2019b). A Comparative Discussion of the Evidence for Biogenic Silica in Wufeng-Longmaxi Siliceous Shale Reservoir in the Sichuan Basin, China. *Mar. Petroleum Geol.* 109, 70–87. doi:10.1016/j.marpetgeo.2019.06.016

Liu, Z. W., Zhou, L. F., He, M. X., and Han, D. C. (2008b). Hydrocarbon Accumulation Conditions and Enrichment Controlling Factors of Premo-Carboniferous System in Zhoukou Depression. *Petrolume Geol. Recovery Effic.* 15 (5), 13–16. (in Chinese with English abstract).

Liu, Z. W., Zhou, L. F., and He, M. X. (2008a). Prospects for Coal-Formed Oil and Gas Exploration of Carboniferous-Permian Residual Basins in Zhoukou Depression. *Xinjiang Pet. Geol.* 29 (6), 699–702. doi:10.13673j.cnki.cn37-1359/te.2008.05.018 (in Chinese with English abstract).

Longhitano, S. G., Mellere, D., Steel, R. J., and Ainsworth, R. B. (2012). Tidal Depositional Systems in the Rock Record: A Review and New Insights. *Sediment. Geol.* 279, 2–22. doi:10.1016/j.sedgeo.2012.03.024

Mohammad, M. L., Reza, R., Ali, S., and Adnan, A. H. (2013). Evaluation of Pore Size Spectrum of Gas Shale Reservoirs Using Low Pressure Nitrogen Adsorption, Gas Expansion and Mercury Porosimetry: A Case Study from the Perthand Canning Basins, Western Australia. *J. Petroleum Sci. Eng.* 112 (12), 7–16. doi:10.1016/j.petrol.2013.11.022

Qi, H., Ma, J., and Wong, P. Z. (2002a). Adsorption Isotherms of Fractal Surfaces. *Colloids Surf.* 206 (1-3), 401–407. doi:10.1016/s0927-7757(02)00063-8

Quan, S. J., Rao, D., Kong, F. J., Liu, S. H., and Jiang, Y. F. (2002). Potential Analysis of the Upper Paleozoic Hydrocarbon Resources in the Zhoukou Depression. *Petroleum Geol. Exp.* 26 (6), 562–568. (in Chinese with English abstract).

Rani, S., Prusty, B. K., and Pal, S. K. (2015). Comparison of Void Volume for Volumetric Adsorption Studies on Shales from India. *J. Nat. Gas Sci. Eng.* 26, 725–729. doi:10.1016/j.jngse.2015.07.012

Rouquerol, F., Rouquerol, J., and Sing, K. (1999). *Adsorption by Powders and Porous Solid: Principles, Methodology and Application*. London: Academic Press.

Rouquerol, J., Avnir, D., Fairbridge, C. W., Everett, D. H., Haynes, J. M., Pernicone, N., et al. (1994). Recommendations for the Characterization of Porous Solids (Technical Report). *Pure Appl. Chem.* 66 (8), 1739–1758. doi:10.1351/pac199466081739

Sing, K. S. W. (1985). Reporting Physisorption Data for Gas/solid Systems with Special Reference to the Determination of Surface Area and Porosity (Recommendations 1984). *Pure Appl. Chem.* 57, 603–619. doi:10.1351/pac198557040603

Song, H. B., Li, Y. N., Yu, Z. F., Liu, S. X., Hu, B., and Li, Z. Y. (2018). Sedimentary Succession and Environment Evolution of the Taiyuan Formation in Northeastern Qinshui Basin, Shanxi Province. *J. Palaeogeogr. Chin. Ed.* 20 (4), 623–636. doi:10.7605/gdlxb.2018.04.045 (in Chinese with English abstract).

Su, J., Fan, D., Liu, J. P., and Wu, Y. (2020). Anatomy of the Transgressive Depositional System in a Sediment-Rich Tide-Dominated Estuary: The Paleo-Yangtze Estuary, China. *Mar. Petroleum Geol.* 121, 104588. doi:10.1016/j.marpetgeo.2020.104588

Sun, X. M., Zhang, M. S., Long, S. X., Hao, F. J., Liu, P. J., and Liu, C. Y. (2004). Overthrust Tectonic in Northern Qinling-Dabie Orogenic Belt and Basin-Controlling Faults in Zhoukou Depression and Hefei Basin. *Oil&Gas Geol.* 25 (2), 191–198. (in Chinese with English abstract). doi:10.11743/ogg20040213

Tan, J., Weniger, P., Krooss, B., Merkel, A., Horsfield, B., Zhang, J., et al. (2014). Shale Gas Potential of the Major Marine Shale Formations in the Upper Yangtze Platform, South China, Part II: Methane Sorption Capacity. *Fuel* 129, 204–218. doi:10.1016/j.fuel.2014.03.064

Tang, X., Jiang, Z., Li, Z., Gao, Z., Bai, Y., Zhao, S., et al. (2015). The Effect of the Variation in Material Composition on the Heterogeneous Pore Structure of High-Maturity Shale of the Silurian Longmaxi Formation in the Southeastern Sichuan Basin, China. *J. Nat. Gas Sci. Eng.* 23, 464–473. doi:10.1016/j.jngse.2015.02.031

Tian, H., Li, T., Zhang, T., and Xiao, X. (2016). Characterization of Methane Adsorption on Overmature Lower Silurian-Upper Ordovician Shales in Sichuan Basin, Southwest China: Experimental Results and Geological Implications. *Int. J. Coal Geol.* 156, 36–49. doi:10.1016/j.coal.2016.01.013

Unsworth, J. F., Fowler, C. S., and Jones, L. F. (1989). Moisture in Coal. *Fuel* 68 (1), 18–26. doi:10.1016/0016-2361(89)90005-7

Wang, J. X. (2018). Tidal Flat Sedimentary Characteristics of Silurian Gepingtage Formation in Tarim Basin. *Northwest. Geol.* 21 (02), 69–74. doi:10.19751j.cnki.61-1149/p.2018.02.010 (in Chinese with English abstract).

Wang, R., Shen, Y., Yang, C., Zhu, Z., Tan, M. L., Jiang, G., et al. (2000). The Surface Tension of Liquid Gases of Low Boiling Point. *Chin. J. Chem. Phys.* 13 (3), 380–384. doi:10.3969/j.issn.1674-0068.2000.03.023

Ward, S. L., Scourse, J. D., Yokoyama, Y., and Neill, S. P. (2020). The Challenges of Constraining Shelf Sea Tidal Models Using Seabed Sediment Grain Size as a Proxy for Tidal Currents. *Cont. Shelf Res.* 205, 104165. doi:10.1016/j.csr.2020.104165

Wu, S. T., Zhu, R. K., Cui, J. W., Mao, Z. G., Liu, K. Y., and Wang, X. Q. (2020). Ideas and Prospect of Porous Structure Characterization in Unconventional Reservoirs. *Geol. Rev.* 66 (s1), 151–154.

Wu, Y., Lin, C., Yan, W., Liu, Q., Zhao, P., and Ren, L. (2020). Pore-scale Simulations of Electrical and Elastic Properties of Shale Samples Based on Multicomponent and Multiscale Digital Rocks. *Mar. Petroleum Geol.* 117, 104369. doi:10.1016/j.marpetgeo.2020.104369

Wu, Y., Tahmasebi, P., Lin, C., and Dong, C. (2020). A Comprehensive Investigation of the Effects of Organic-Matter Pores on Shale Properties: A Multicomponent and Multiscale Modeling. *J. Nat. Gas Sci. Eng.* 81, 103425. doi:10.1016/j.jngse.2020.103425

Wu, Y., Tahmasebi, P., Lin, C., and Dong, C. (2020). Process-based and Dynamic 2D Modeling of Shale Samples: Considering the Geology and Pore-System Evolution. *Int. J. Coal Geol.* 218, 103368. doi:10.1016/J.COAL.2019.103368

Wu, Y., Tahmasebi, P., Lin, C., Munawar, M. J., and Cnudde, V. (2019). Effects of Micropores on Geometric, Topological and Transport Properties of Pore Systems for Low-Permeability Porous Media. *J. Hydrology* 575, 327–342. doi:10.1016/j.jhydrol.2019.05.014

Wu, Y., Tahmasebi, P., Lin, C., Ren, L., and Dong, C. (2019). Multiscale Modeling of Shale Samples Based on Low- and High-Resolution Images. *Mar. Petroleum Geol.* 109, 9–21. doi:10.1016/j.marpetgeo.2019.06.006

Wu, Y., Tahmasebi, P., Lin, C., Zahid, M. A., Dong, C., Golab, A. N., et al. (2019). A Comprehensive Study on Geometric, Topological and Fractal Characterizations of Pore Systems in Low-Permeability Reservoirs Based on SEM, MICP, NMR, and X-Ray CT Experiments. *Mar. Petroleum Geol.* 103, 12–28. doi:10.1016/j.marpetgeo.2019.02.003

Xu, Y. Q., He, Y. H., Chen, X. D., Wang, J. W., Yang, H. M., and Zhu, Y. S. (2019). Characteristics of Microscopic Pore Throats and Their Influence on Physical Properties of the Chang7 Tight Reservoir in the Longdong Area; Ordos Basin. *Geol. Explor.* 55 (3), 0870–0881. doi:10.12134/j.dzykt.2019.03.019

Yang, F., Ning, Z., and Liu, H. (2014). Fractal Characteristics of Shales from a Shale Gas Reservoir in the Sichuan Basin, China. *Fuel* 115, 378–384. doi:10.1016/j.fuel.2013.07.040

Yao, S. L., Qin, S. G., Wang, G. H., Li, Z. P., and Yu, L. J. (2012). "Multifractal Fractal Characteristics of the Heterogeneous Pore Distribution of Cores," in International Conference on Computer Distributed Control and Intelligent Enviromental Monitoring, Zhangjiajie, Hunan China, Mar. 5 2012 to Mar. 6 2012 (IEEE Computer Soc.), 424–427.

Zeng, F., Dong, C., Lin, C., Tian, S., Wu, Y., Lin, J., et al. (2022). Pore Structure Characteristics of Reservoirs of Xihu Sag in East China Sea Shelf Basin Based on Dual Resolution X-Ray Computed Tomography and Their Influence on Permeability. *Energy* 239, 122386. doi:10.1016/j.energy.2021.122386

Zeng, F., Dong, C., Lin, C., Wu, Y., Tian, S., Zhang, X., et al. (2021). Analyzing the Effects of Multi-Scale Pore Systems on Reservoir Properties-A Case Study on Xihu Depression, East China Sea Shelf Basin, China. *J. Petroleum Sci. Eng.* 203, 108609. doi:10.1016/j.petrol.2021.108609

Zhai, C. B., Huang, Z. G., and Lin, L. B. (2005). Structure and Petroleum Analysis of the Tanzhuang - Shenqiu Sag in the South of North China Basin. *Petroleum Geol. Exp.* 27 (4), 353–359. (in Chinese with English abstract).

Zhang, T., Ellis, G. S., Ruppel, S. C., Milliken, K., and Yang, R. (2012). Effect of Organic-Matter Type and Thermal Maturity on Methane Adsorption in Shale-Gas Systems. *Org. Geochem.* 47, 120–131. doi:10.1016/j.orggeochem.2012.03.012

Zhang, X. Y., Guo, H. K., Shen, R., Ren, H. C., and Luo, Y. C. (2021). Research Progress of Pore Structure Characterization Technology for Shale Oil and Gas Reservoirs. *Appl. Chem. Ind.* 50 (02), 444–449. doi:10.3969/j.issn.1671-3206.2021.02.037

Zhao, K. D., Fu, X. H., Zhang, M., Cheng, W. P., and Qu, L. Z. (2019). Evaluation of Organic Geochemical Characteristics and Hydrocarbon Generation Potential of Coal Measure Mud Shale. *Coal Sci. Technol.* 47 (11), 182–188. (in Chinese with English abstract).

Zhao, X. Y., Zhao, S., Ye, C., and Wang, D. L. (2017). Study on Multi-Stages Structural Styles in Eastern Zhoukou Depression. *China Energy Environ. Prot.* 39 (8), 44–49. (in Chinese with English abstract).

Zhou, S., Xue, H., Ning, Y., Guo, W., and Zhang, Q. (2018). Experimental Study of Supercritical Methane Adsorption in Longmaxi Shale: Insights into the Density of Adsorbed Methane. *Fuel* 211, 140–148. doi:10.1016/j.fuel.2017.09.065

Zhou, S., Zhang, D., Wang, H., and Li, X. (2019). A Modified BET Equation to Investigate Supercritical Methane Adsorption Mechanisms in Shale. *Mar. Petroleum Geol.* 105, 284–292. doi:10.1016/j.marpetgeo.2019.04.036

Zhu, X. M. (2009). *Sedimentary Petrology* (Beijing: Petroleum industry press), 319–326. (in Chinese).

Conflict of Interest: The authors declare that the research was conducted in the absence of any commercial or financial relationships that could be construed as a potential conflict of interest.

The reviewer PW declared a shared affiliation with the authors to the handling editor at the time of review.

frontiers | Frontiers in Earth Science

TYPE Original Research
PUBLISHED 31 August 2022
DOI 10.3389/feart.2022.974441

OPEN ACCESS

EDITED BY
Yuqi Wu,
China University of Petroleum (East China), China

REVIEWED BY
Laixing Cai,
Chengdu University of Technology, China
Shansi Tian,
Northeast Petroleum University, China
Chunqi Xue,
China University of Petroleum, Huadong, China

*CORRESPONDENCE
Z. X. Zhao,
zhaozhongxiang5@163.com

SPECIALTY SECTION
This article was submitted to Solid Earth Geophysics,
a section of the journal
Frontiers in Earth Science

RECEIVED 21 June 2022
ACCEPTED 29 July 2022
PUBLISHED 31 August 2022

CITATION
Zhao ZX, Wu SB, He MW and Fan YJ (2022), Effect of saline sedimentary environment on pore throats of shale.
Front. Earth Sci. 10:974441.
doi: 10.3389/feart.2022.974441

Effect of saline sedimentary environment on pore throats of shale

Z. X. Zhao[1]*, S. B. Wu[2], M. W. He[3] and Y. J. Fan[4]

[1]School of Geosciences, Yangtze University, Wuhan, Hubei, China, [2]Research Institute of Exploration and Development, Sinopec Shengli Oilfield Company, Dongying, Shandong, China, [3]CNOOC Research Institute Ltd., Beijing, China, [4]CNPC Xibu Drilling Engineering Company Limited, Urumchi, China

Shale pore throat is one of the key factors affecting shale oil and gas exploitation. In order to study the effect of saline on shale pore throat in the continental lacustrine basin, the paleo-salinity of the lacustrine basin was analyzed using the Couth and Sr/Ba methods, and the pore throat characteristics of shale were observed by thin section and scanning electron microscope. The saline stage is divided into five stages: freshwater (0.5‰–1‰), brackish water (1‰–5‰), brackish water (5‰–15‰), brackish water (15‰–30‰), and high saltwater (>30‰). Shale is mainly reserved in micropores (organic, intercrystalline, and intergranular pores) and microcracks (along-layer, high pressure, structural, and mineral shrinkage cracks). Paleosalinity affects the pore throat characteristics of shale by controlling the mineral composition, rock combination type, and texture. Carbonate minerals tend to dissolve and form dissolution pores, resulting in pore throat enlargement and better physical properties. When salinity is low, the content of carbonate minerals increases with the increase in salinity. However, in the case of high salinity, the content of carbonate minerals gradually decreases, but that of sulfate and gypsum increases with the increase in salinity. The texture is conducive to the development of microcracks. With the increase in salinity, the number of textures first increases and then decreases. When the content is 15 ‰–30‰, there are most abundant textures, making it most likely to form microcracks. The results of this study play an important role in promoting the study of shale in the continental lacustrine basin.

KEYWORDS

shale, saline sedimentary environment, pore throat, micropore, microcrack

1 Introduction

The microscopic pore structure characteristic of the shale matrix plays an important role in the occurrence, storage, and migration of shale gas (Wu et al., 2011; Liang et al., 2014; Wu et al., 2019). The pore structure is one of the key parameters to determine the quality of shale reservoirs and evaluate the potential of shale gas resources. The pore volume and connectivity have a great influence on the occurrence and migration of shale reservoirs. The distribution and structural characteristics of shale matrix pores play an important role in shale gas reservoirs (Chen et al., 2017; Zhao et al., 2017; Li et al., 2018). Therefore, the characteristics and reservoir performance have become important indicators for the exploration and development of shale reservoirs (Zhou and Kang., 2016; Chen et al., 2018; Gu et al., 2018; Zeng et al., 2019).

The formation and development of shale reservoir pores are not only controlled and affected by a single element, but also influenced by the combination of rock structure, sedimentary structure, matrix structure, total organic carbon, organic matter type, basin hydrothermal upwelling, thermal evolution degree, tectonic thermal events, sedimentary environment and rate, tectonic plate evolution, and fluid and hydrological conditions (Cao et al., 2018; Cavelan et al., 2019; Zhang et al., 2019; Pan et al., 2020).

Compared to conventional reservoirs, shale reservoirs are rich in organic matter, and their abundance, type, and maturity restrict the storage space of shale by controlling the development of organic pores (Clarkson et al., 2012; Curtis et al., 2012; Mastalerz et al., 2012). The mineral composition also has an important influence on the pore structure of shale. The influence of quartz, feldspar, carbonate, and other clay minerals on the pore structure has been greatly studied before (Liu and peng, 2017; Wei et al., 2018; Wei et al., 2019). The influence factors of pore structure in shale reservoirs are not single, and the shale experiences different sedimentary environments and structural backgrounds in different regions, leading the study of the influence factors of pore structure to be more complicated (Curtis., 2002; Jarvie et al., 2007; Chao et al., 2017; Zeng et al., 2021). The degree of salinity of inland lacustrine basin will affect the abundance, mineral composition, and diagenesis evolution of shale organic matter, so it must have an important impact on the pore structure of shale. However, scholars have not done in-depth research on this.

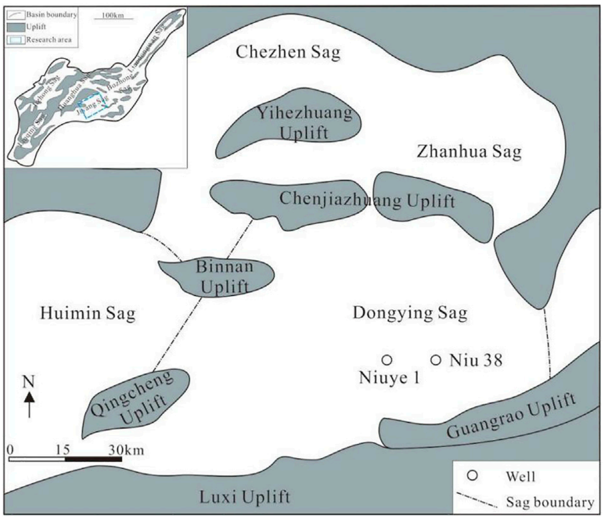

FIGURE 1
Regional geological survey of the Jiyang Depression.

Based on the influence of different salty environments on shale mineral composition, lithological combination, and grain layer, this study analyzes the influence of different salty environments on the shale pore structure and plays an important role in promoting the its influence factors.

2 Geological setting

The Jiyang Depression belongs to the secondary structural unit of the Bohai Bay Basin and is a fault depression superimposed basin formed in the period of Mesozoic and Cenozoic. The Dongying Sag is located in the south of the Jiyang Depression. The deep fault in the north contacts the Chenjiazhuang Uplift and Binxian Uplift. It extends to Southwest Shandong Uplift in the south, Qingtuozi Uplift in the East, and Linfanjia low Uplift in the west. It is a Meso-Cenozoic dustpan fault depression with a fault in the north and a super in the South (Figure 1). During the sedimentary period of the Shahejie Formation in the Paleogene, the basin entered the peak period of fault depression, and four sets of effective source rocks were developed: the upper Es_4, the lower Es_3, the central Es_3, and Es_1 (Song et al., 2004). Among them, the mud shale of the upper Es_4 deposited in salt semi-saltwater environment is mainly distributed in the Dongying and Zhanhua Sag, and Dongying Sag is the most developed. Mud shale in the lower Es_3 deposited in a brackish water environment is distributed throughout the region (Li., 2003).

3 Data and methods

3.1 Data

The data used in this research were provided by the Research Institute of Exploration and Development, Sinopec Shengli Oilfield Company, which includes core, logging, element, organic geochemistry, thin section, nuclear magnetic resonance, rock mechanical parameters.

3.2 Paleosalinity restoration method

Because shale inclusions are small and difficult to identify, and considering data factors, the Couth method and Sr/Ba ratio are used to restore paleosalinity.

Couth method: the amount of boron absorbed and fixed by clay minerals is related to the concentration of boron in solution, which is a linear function of salinity. By combining these two relations, Couth obtained a more reasonable paleosalinity

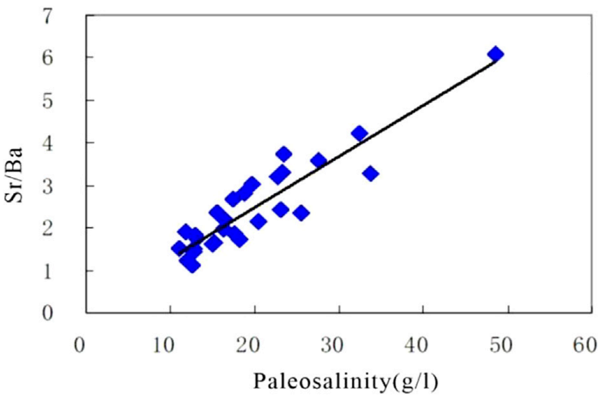

FIGURE 2
Correlation diagram between Sr/Ba values and paleosalinity in the study area.

calculation formula based on the Freundlich absorption equation and the previous research results:

$$l_gB_k = 1.28l_gS_p + 0.11 \tag{1}$$

In the previous formula, B_k is the correct boron content for kaolinite (10^{-6}) and S_P paleosalinity is used for this purpose (‰). The boron content correction in this formula is based on the ratio relationship between the total amount of sample absorbed boron and the relative content of various clay minerals, which has a wide application range of salinity (1‰–35‰).

The strontium barium method is one of the common methods to restore paleosalinity. The chemical properties of strontium and barium are similar, but they are separated in different sedimentary environments due to the differences in geochemical behavior. Therefore, the strontium and barium ratio (Sr/Ba) can be used as a marker of paleosalinity (Landergren and Carvajal., 1969). Due to the strong migration capacity of strontium, when freshwater and seawater are mixed, Ba^{2+} in freshwater and SO_4^{2-} in seawater firstly combine to form $BaSO_4$ precipitation. However, Sr^{2+} can migrate to the open sea and precipitate by biological means. Therefore, the Sr/Ba value is gradually increased as it is far away from the coast, which can qualitatively reflect the paleosalinity according to its ratio. According to the statistics of 13 seabed samples in China, generally speaking, the Sr/Ba value in freshwater sediment is less than 1, whereas the Sr/Ba value in marine sediment is greater than 1, and the Sr/Ba value of 1.0–0.6 is a brackish water environment (Zhou et al., 1984; Yan, 2013).

Studying the correlation between the Sr/Ba value and paleosalinity in the study area showed a positive correlation between the two. The study data showed that, with the increase in the Sr/Ba value, paleosalinity increased accordingly, and the correlation coefficient reached 0.84 (Figure 2).

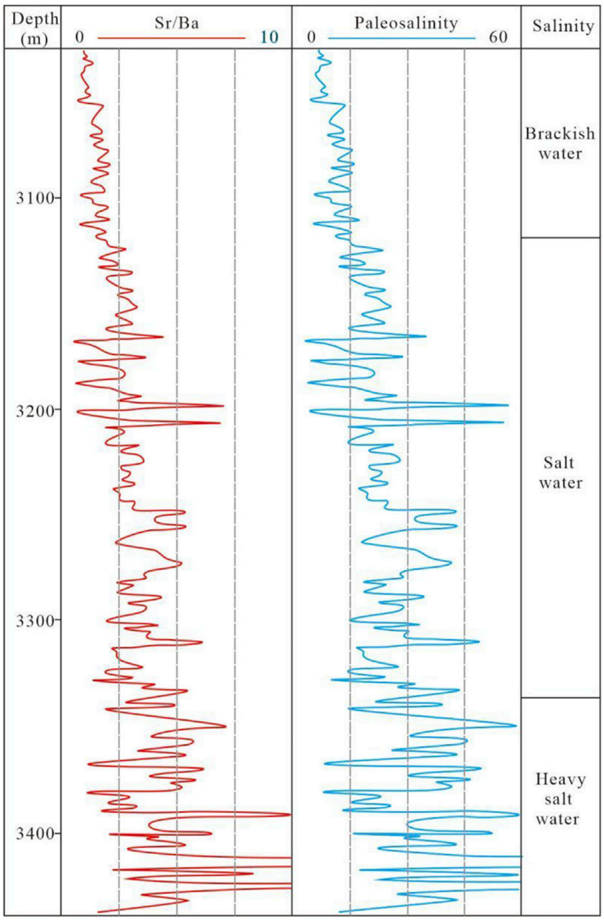

FIGURE 3
Vertical variation of paleosalinity in the Dongying Sag.

4 Results

4.1 Salinity stage division

According to the research needs, this study adopts the Huang Difan (1995) paleosalinity division scheme, dividing the salinity into five intervals: freshwater stage (0.5‰–1‰), brackish water stage (1‰–5‰), brackish water stage (5‰–15‰), mixohaline water stage (15‰–30‰), and high saline stage (>30‰).

The sedimentary period of the Shahejie Formation in Dongying Sag was generally affected by the saltwater environment. Vertically, the lower segment is mainly in the saltwater high saltwater evolution stage, and the upper segment is basically in the brackish water saltwater evolution

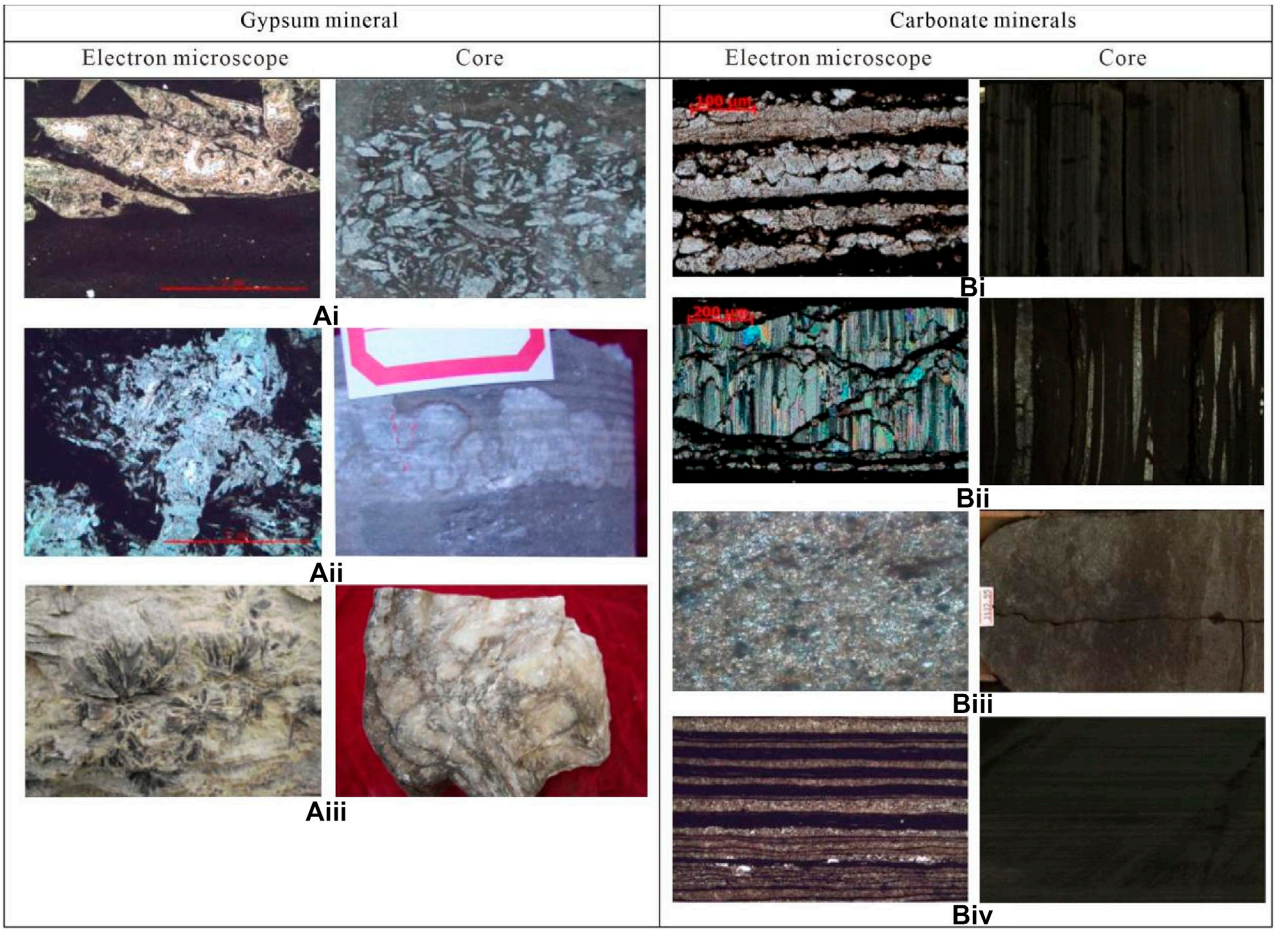

FIGURE 4
Characteristics of salt minerals in the Dongying Sag. **(Ai)**. Swallow-tailed. **(Aii)** Creep state. **(Aiii)** Branch. **(Bi)** Lamellar. **(Bii)** Lentoid. **(Biii)** Massive. **(Biv)** Dolomite.

stage (Figure 3). On the plane, most areas of the Dongying Sag are of a saline water environment. Only the edge of the sag is affected by the desalination of foreign freshwater, and the paleosalinity decreases sharply.

4.2 Shale sedimentary characteristics

4.2.1 Main salt minerals and their characteristics

There are three main types of salt minerals in the study area: carbonate, sulfate, and halides. Carbonate deposition mainly includes calcite and dolomite. Sulfate deposition mainly includes gypsum and anhydrite. Halide deposition is mainly stone salt.

The microstructure of carbonate and sulfate minerals is quite complex. The main microstructure of sulfate mainly includes swallow-tailed (Figure 4Ai), creep (Figures 4Aii), and branch (Figures 4Aiii). The microstructure of carbonate minerals mainly includes layer (Figures 4Bi), lens (Figures 4Bii), block (Figures 4Biii), and dolomite (Figures 4iv).

4.2.2 Main shale types and characteristics

From the perspective of the degree of organic matter abundance and sedimentary lithology characteristics of lithology, the research area mainly develops organic matter layer limestone, rich organic matter layer limestone, rich organic matter layer, rich organic matter, and rich organic matter grain. The various lithological microscopic characteristics are as follows:

4.2.2.1 Argillaceous limestone containing organic matter grain layer

The color is light, characterized by the horizontal distribution of light and dark layers (Figure 5A), and the light layer has low recrystallization. The light layer is calcite

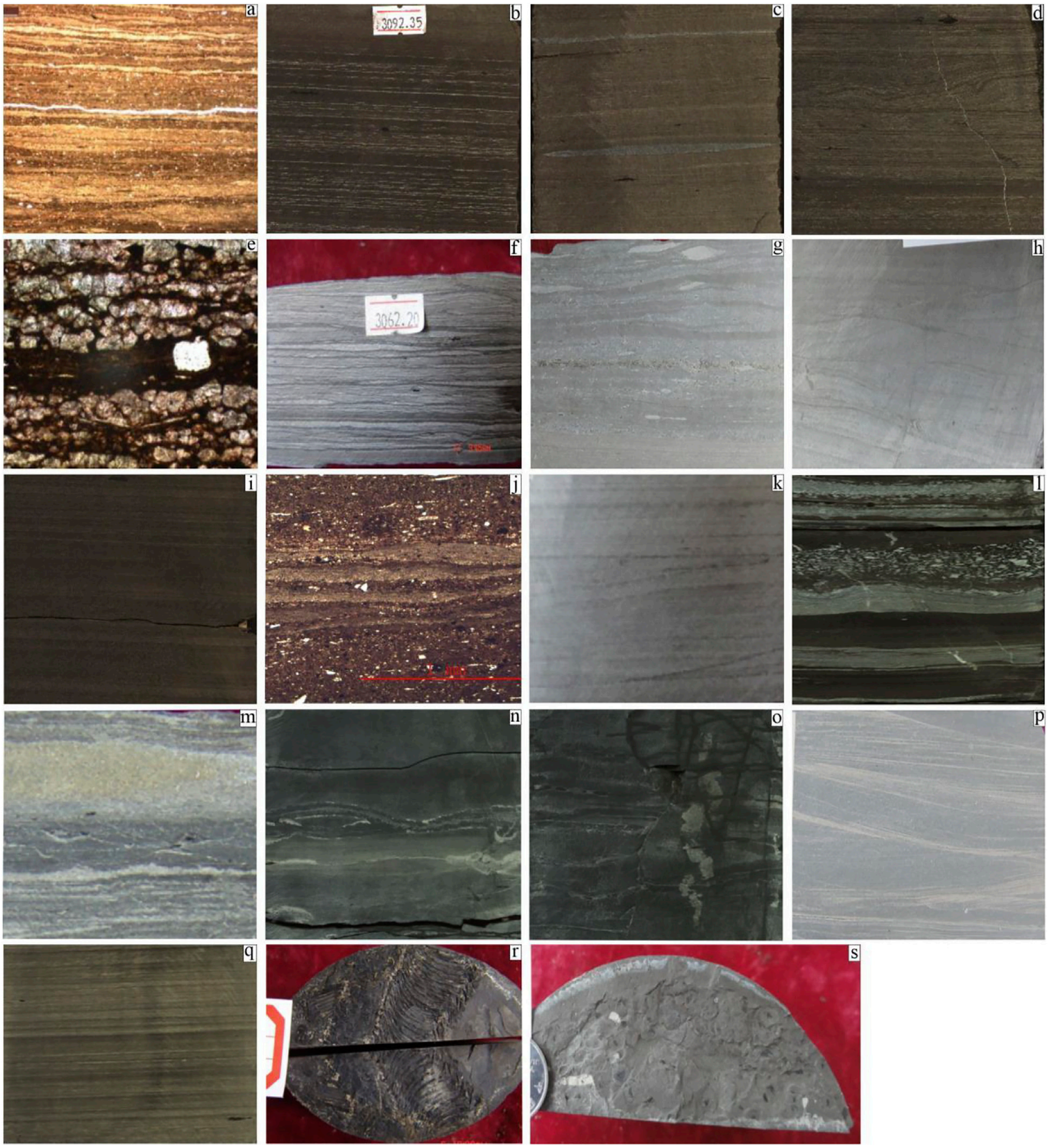

FIGURE 5
Main shale types and characteristics in the core. **(A–D)** Well Luo 69, 3,070.6–3,127.1 m, contains organic grain layered argillaceous limestone. **(E–H)** Well Luo 69, 3,040–3,070.6 m, contains organic grain layered argillaceous limestone. **(I–K)** Well Luo 69, 3,015–3,040.55 m, rich organic grain layered clay limestone. **(L,M)** Well Niuye 1, 3,490–3,500 m. **(N–P)** Well Niuye 1, 3,070–3,076.5 m, contains organic massive gray mudstone. **(Q–S)** Well Niuye 1, 3,402.7–3,452 m, rich organic grain layered gray mudstone.

(Figure 5B), and the dark layer is clay ore, occasionally silty interlayer (Figure 5C), staggered layer (Figure 5D), and rare microfossils. The main organic carbon content is mostly less than 2%. Most components are mainly carbonate rock, followed by quartz plus feldspar and clay minerals.

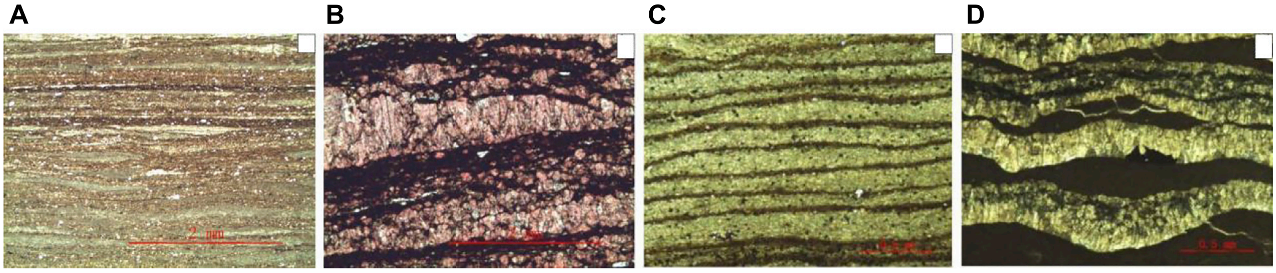

FIGURE 6
Type and characteristics of shale texture. **(A)** Sedimentary formation of grain layer. **(B)** The grain layer **(C)**, which is inherited from deposition and mainly formed by diagenesis. Granular calcite and mud layer interlayer. **(D)** Fragmented sedimentary layers are visible in the columnar calcite stripes.

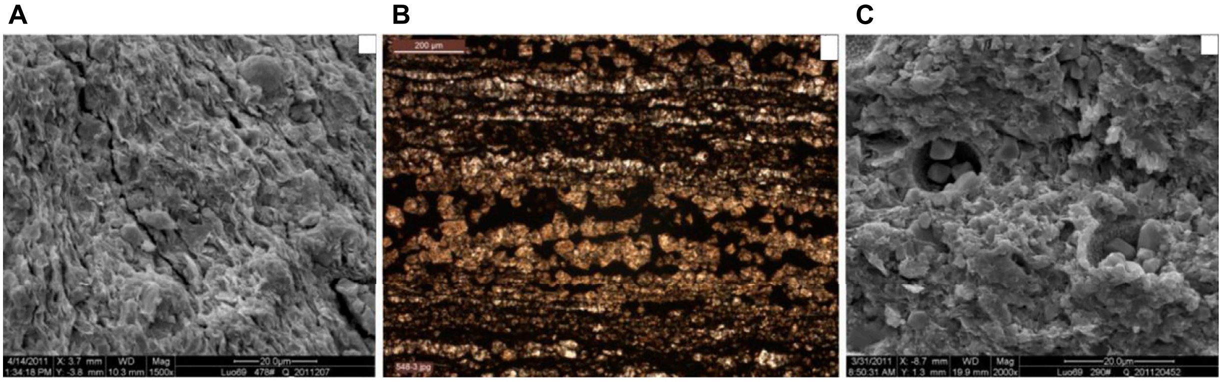

FIGURE 7
Type and characteristics of shale pore throat. **(A)** Well Luo 69, 3,039.60 m, sheet micropore development; see strawberry pyrite. **(B)** Well Luo 69, 3,055.60 m. **(C)** Well Luo 69, 2,992.60 m, Micropores were developed in calcite, clay and pyrite crystals. Asphaltene was found between calcite crystals.

4.2.2.2 Rich in organic grain layered argillaceous limestone

The color is light, characterized by a light and dark horizontal grain layer (Figure 5E), and the light color layer has a high degree of recrystallization. The light color layer is calcite, and the dark layer is clay ore (Figure 5F), with occasional lens sand strip (Figure 5G), staggered bedding, and microfossils (Figure 5H). The main organic carbon content is more than 2%. Most components are mainly carbonate rock, followed by quartz plus feldspar and clay minerals.

4.2.2.3 Organic matter-rich layered gray mudstone

The color is darker, characterized by a thin reciprocal layer distribution of the light and dark phase (Figure 5I), and the crystallization degree of the light color layer is low. The light layer is calcite, and the dark layer is clay ore (Figure 5J), occasionally lenticular sand strip, staggered layer (Figure 5K); a large number of Ostracoda fossils can be seen. The vast majority of the organic carbon content is more than 2%. The components are mainly carbonate rock, high clay mineral content, followed by quartz plus feldspar.

4.2.2.4 Compound mudstone containing organic matter layer

The color is light, characterized by a thin reciprocal layer distribution between light and dark (Figure 5L). The dark layer is gray matter mudstone, and the light color layer is plaster rock or argillaceous paste rock; a large number of pyrite can be seen (Figure 5M). The organic carbon content is very little, and the vast majority are less than 2%. On the components, there are carbonate rock, gypsum, clay minerals, and quartz plus feldspar, of which the carbonate rock content is slightly higher, followed by gypsum.

4.2.2.5 Organic matter massive gray mudstone phase

The color of this lithology is relatively light, mainly gray–blue gray. It is dominated by massive structures with visible wave

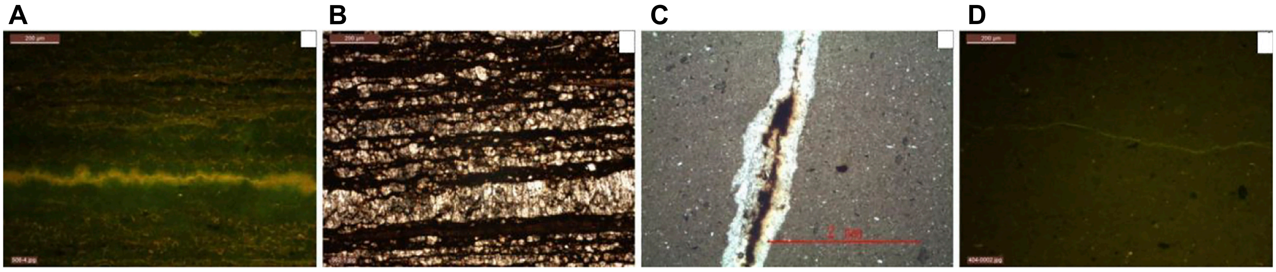

FIGURE 8
Microscopic characteristics of microcracks. **(A)** Along the layer of microcracks, bright yellow fluorescence. **(B)** Overpressure crack is filled with bright crystal calcite. **(C)** Calcite half-filling, high Angle inclined intersection joint contains oil. **(E)** Gray mudstone, unfilled with microcracks, produces green light.

bedding (Figure 5N), sandy masses (Figure 5O), and staggered bedding (Figure 5P). The organic carbon content is very little; most are less than 2%, the components with carbonate rock, clay minerals, and quartz plus feldspar, of which the content of clay minerals is slightly higher. The color mutation on the core and the organic matter content from high to low values are considered event deposition.

4.2.2.6 Rich in organic grain layered limestone mudstone

The color is darker, characterized by the horizontal distribution of the layer (Figure 5Q). The light color grain layer is calcite, recrystallization, or a mixed layer of clay minerals and cryptocrystalline calcite, and the dark color grain layer is organic matter and clay. Fossil fish species (Figure 5R) and ostracodes (Figure 5S) were visible in the core observation. Organic carbon content is very high, and most are more than 2%. There are carbonate rock, clay minerals, quartz plus feldspar, and pyrite on the components, of which the total amount of carbonate is slightly higher.

4.2.3 Type and characteristics of the shale layer

From the perspective of the causes of grain layer, the grain layers mostly formed by deposition are fine and dense and often appear as layer even, which is manifested as the combination characteristics of mud grain layer plus gray grain layer, mud grain layer plus organic grain layer, and plaster grain layer plus organic grain layer. This kind of grain layer can be understood as the seasonal pattern layer, resulting from a combination of climate, biological, and land-based material input and preservation conditions (Figure 6A).

The grain layers mainly formed by deposition and diagenesis have obvious differences. The gray matter grain layer is formed by bright crystal calcite, the thickness can reach more than 1 cm, and some cores are clearly visible. This kind of layer is a common transition state with the upper kind of layer, so it is speculated that it results from inheritance deposition and diagenetic transformation. The common bright calcite stripes arranged along the layers can be classified into two categories: granular calcite stripes and columnar calcite stripes. Granular calcite stripe is a sedimentary-diagenesis cause, mainly caused by recrystallization of sedimentary gray grain layer. In contrast, column calcite stripe is the cause of over-compression fracture filling of hydrocarbon source rock (Figure 6B).

Interbedded granulated calcite and argillaceous laminae are seasonal sedimentary laminae. The thickness of each layer is uniform and thin (generally between 0.10 and 0.30 mm). The particle size varies from fine to coarse and contains deposited impurities (the color is yellow under the monopolarizer). The residual early fine-grained structures in the laminae indicate recrystallization or multi-stage recrystallization diagenesis, which is controlled by both sedimentary and diagenetic factors (Figure 6C).

When mineralized water rich in calcium carbonate is filled in the shale, it will precipitate, crystallize, grow and fracture the shale, so fragmented sedimentary lamina can be seen in the columnar calcite streaks. The distribution of calcite laminae has poor interlaminae with mud laminae, but many parallel laminae occur, and can coexist with granular calcite laminae. The width range of calcite lamina is large, which can be less than 0.05 mm or more than 10 mm. Under the action of longitudinal tension and transverse pressure, calcite was vertically bedded into columnar growth, belonging to the single controlled diagenetic origin (Figure 6D).

4.3 Type and characteristics of shale pore throat

Fractures are a key factor in unconventional reservoir development (Zhao et al., 2021). By analyzing the characteristics of shale storage, it is believed that the shale storage space mainly has micropores (organic pores, intercrystal pores, and intergrain pores) and microcracks

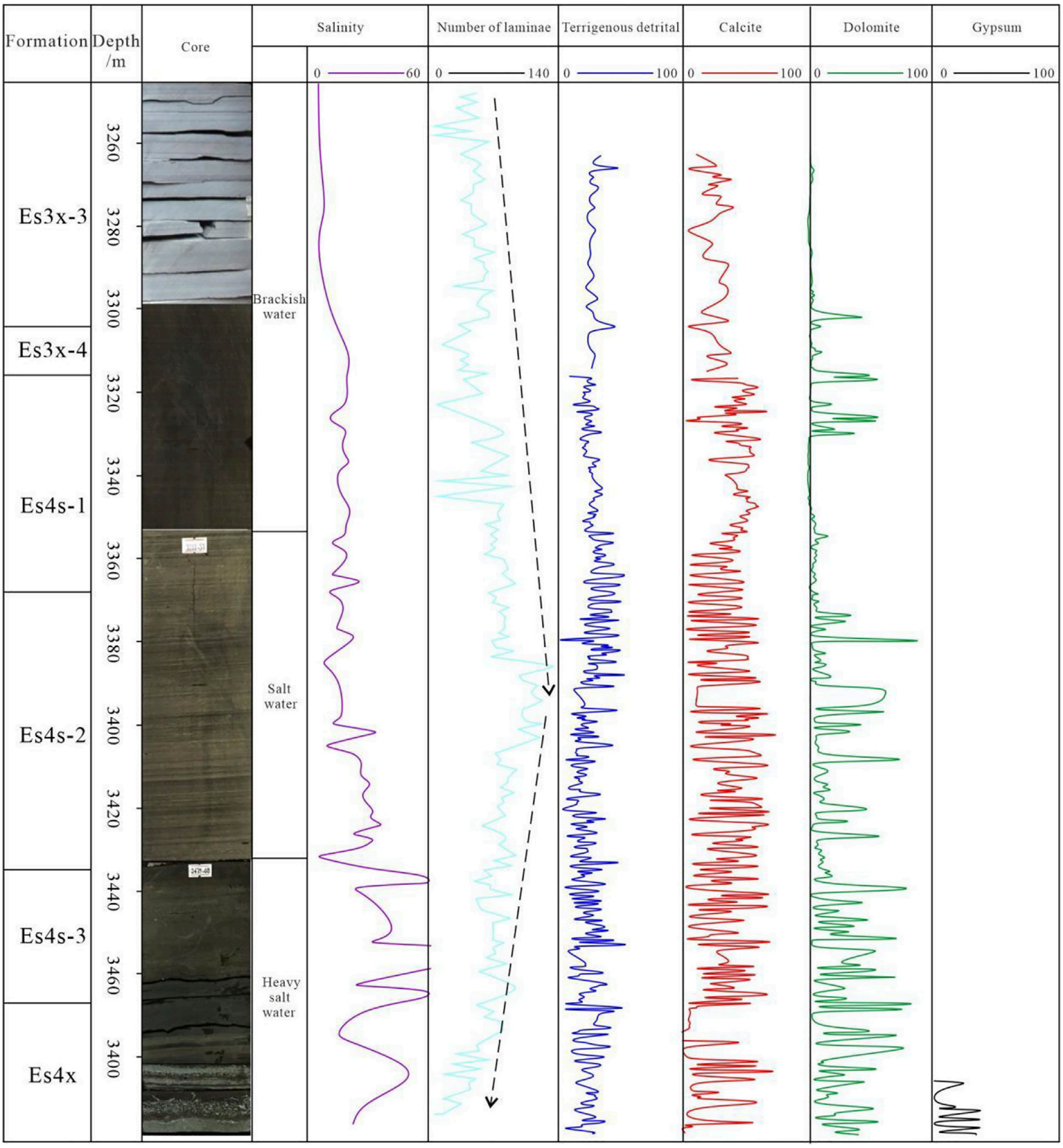

FIGURE 9
Relationship between the saline stage and lithological sedimentation and texture (Well Niu 38 and Well Niuye 1)

(along-layer cracks, high-pressure cracks, structural cracks, and mineral shrinkage joints). The type and development degree of these joints are often controlled by salinity.

4.3.1 Intercrystalline micropores of clay pore

Clay minerals are mainly illite/smectite and illite, with strong orientation, so the intercrystalline micropores are mainly sheet-shaped (Figure 7A), and the size is mostly below 5 m.

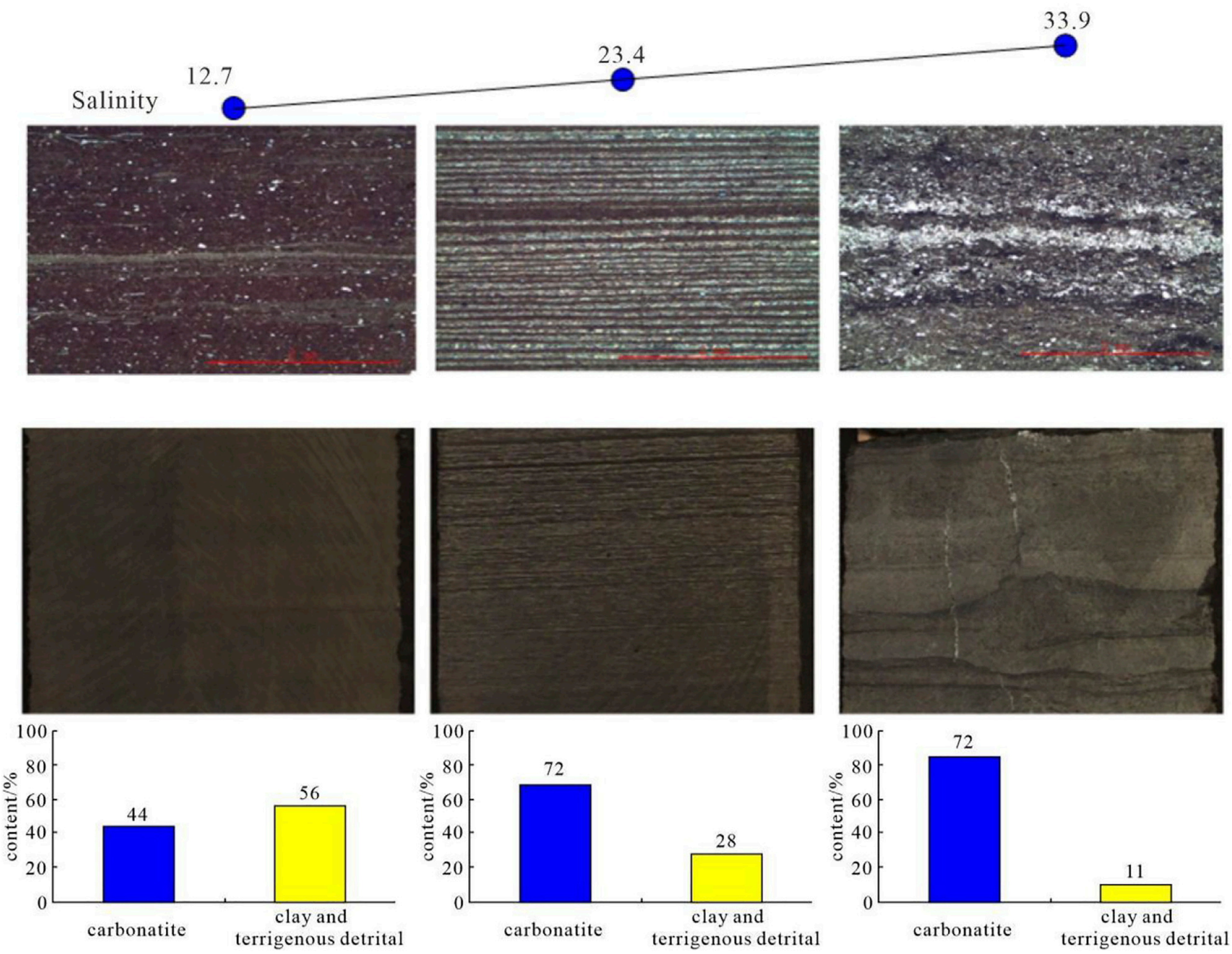

FIGURE 10
Plot of carbonate mineral structure and paleosalinity.

4.3.2 Calcite intercrystal pore

Calcite is the main mineral in this layer, the main hidden crystal structure, and part of the micro-crystal structure; it often constitutes the gray matter layer or is mixed with mud minerals output. Under the polarizing microscope, the gray crystal contains black asphaltene umen (Figure 7B), which is an important pore type, up to 50 μm; the crystal and clay ore micropores overlap (Figure 7C), so they are mostly below 5 m.

4.3.3 Pyrite intercrystalline micropores

Pyrite is a self-occurring mineral in a reducing environment. It is often dispersed as a strawberry aggregate, and its crystal shape is intact, so micropores below micrometers are often developed (Figure 7C).

4.3.4 Micropores between sand plasmids

Land-based sand is often dispersed in the mud or produced as strips. Electron microscope observation of the sand strip shows the interparticle micropores.

Pore type is closely related to rock composition, high calcite content easily forms granular intercrystalline pores, and high clay minerals mainly form sheet micropores. In addition, the pore type is also closely related to the evolution of hydrocarbon source rock. Gray matter source rock rich in organic matter easily forms overpressure cracks in the process of hydrocarbon pressurization, which is the most favorable area for forming calcite intercrystalline pores.

4.3.5 Cracks

According to the causes, it can be divided into diagenesis microcracks and structural microcracks. The former mainly

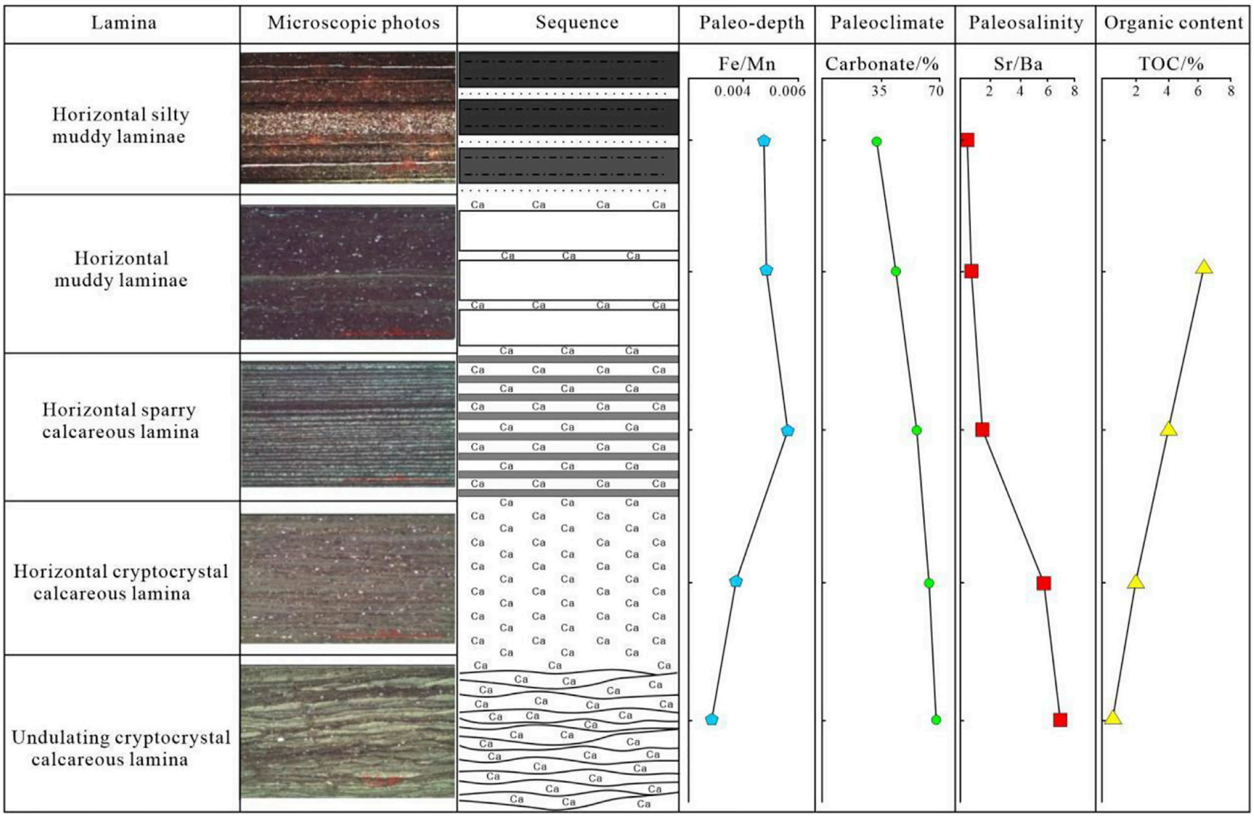

FIGURE 11
Plot of salinity and layer structure.

includes interlayer microcracks and overpressure microcracks (filled by bright crystal calcite or dolomite); the latter is mainly inclined cracks according to the production and near vertical level cracks, which can be divided into filling, semi-filling, and unfilled according to the filling degree. In general, the crack type is mainly identified by the smooth layer microcracks, followed by the structural joint.

4.3.5.1 Interlayer microcracks

It often develops between different components (Figure 8A), with a narrow width, all below 0.02 mm. However, its significance lies in the development of potential microcracks and being easy to continue along the layer.

4.3.5.2 Ultra-pressure microcracks

In the process of hydrocarbon pressurization evolution, hydrocarbon source rocks have a large number of drainage and various cations, so they often cause mineral dissolution and reprecipitation. The recrystallized calcite crystals are filled in the smooth crack produced in the pressurization process (Figure 8B), and the recrystallized crystals often develop intercrystalline pores.

4.3.5.3 Structure crack

The surface of structural fractures in the core is relatively flat, which often causes dislocation of the grain plane. These cracks are often filled with calcite, but residual pores can be seen under the mirror and filled with black bitumen umen (Figure 8C), which is evidence of oil and gas transport. In addition, irregular unfilled microcracks were found under the polarized microscope (Figure 8D).

5 Discussion

5.1 Minerals and lithological differences in different saline stages

There is a good correspondence between paleosalinity and salt minerals, which has increased significantly with the increase in paleosalinity. Before the high saline stage, carbonate minerals increased significantly with the increase in paleosalinity. However, when the paleosalinity increased to a certain extent, carbonate minerals gradually decreased, sulfate minerals and halide minerals began to

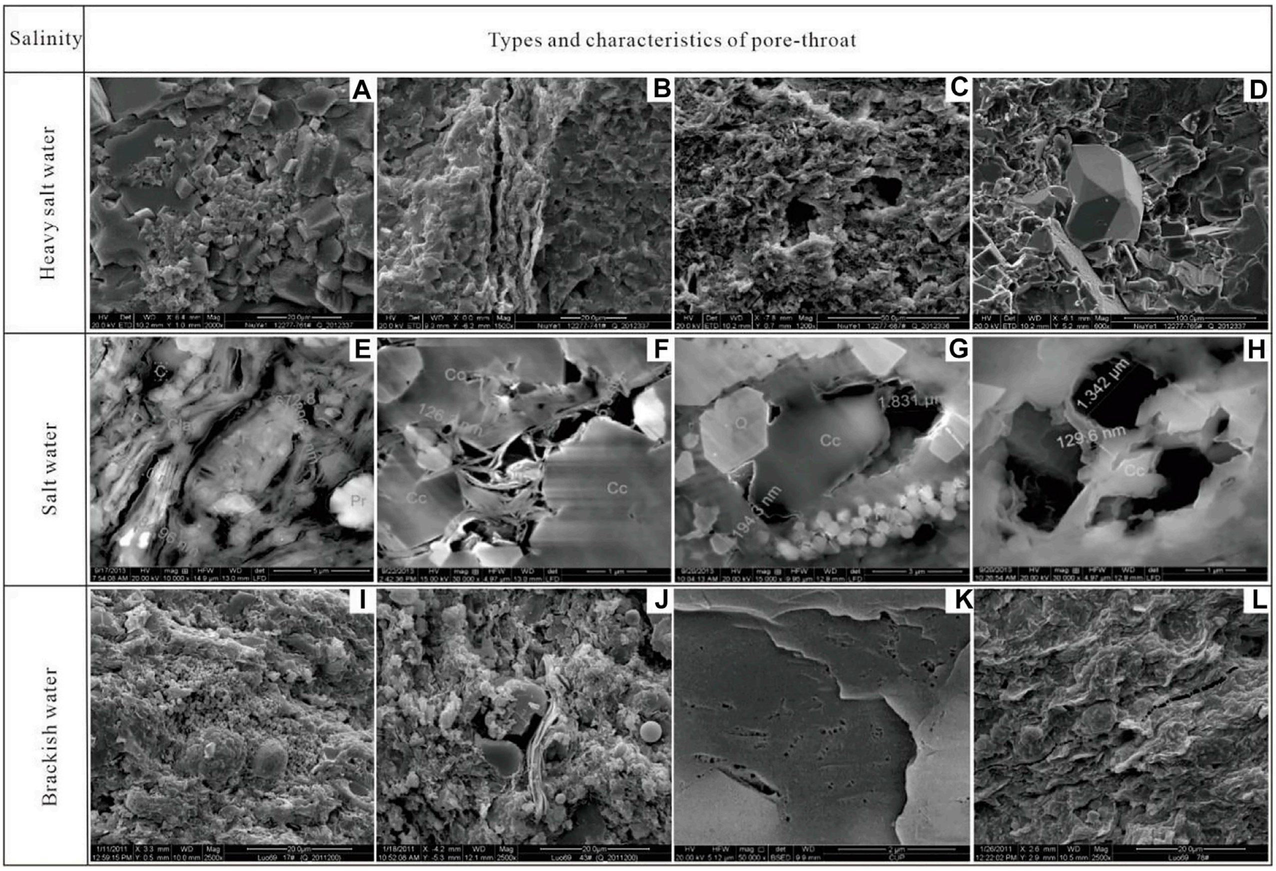

FIGURE 12
Plot of pore types in different saline stages.

TABLE 1 Statistical table of crack influencing factors.

Bedding type	Lamina		Stratiform	Bulk
	Straightness	Microwave		
Degree of microcrack development	++++	+++	++	+
Main types of microcracks	Along crack (page crack)	Along crack (page crack)	Along the crack	Astatic
Type of rock composition	Mud stone	Marlite	Grey rock, mudstone	Muddy sandstone
Degree of microcrack development	++++	++++	++	+

develop, and the content increased with the increase in salinity.

Salinity controls the evolution sequence of lithology. When the paleosalinity was in the high saline stage, the dolomite content of the three lower subsections changed a little, and the upper subsection of sand increased significantly. However, gypsum, anhydrite, rock salt, and barite only began to appear from the upper subsection of sand (pure lower subsection). The lithology in the high saline stage, brackish stage and brackish water-brackish stage is mainly composed of paste - mudstone assemblages, carbonate rocks - laminated mudstone assemblages and layered mudstone - massive mudstone assemblages, respectively. When the salinity ranges from 15‰ to 30‰, the carbonate stratum is the most developed (Figure 9).

5.2 Relationship between saline environment and shale microstructure

The degree of grain layer development is closely related to the paleosalinity. Through the statistical estimation of the pattern value in Well Luo 69 in the Bohai south area and Well Niuye 1 in the Dongying Depression and the comparative analysis of the relationship between the number of layers and the paleosalinity, it is found that, with the increase in paleosalinity and when it reaches a certain degree, the number of layers shows a trend of decreasing. When the paleosalinity is in the range of 15 ‰–30‰, the carbonate pattern layer is the most developed (Figure 9).

The microstructure of salt minerals is also closely related to their salinity. Taking the interlayer structure of carbonate minerals as an example, the study area of layered carbonate minerals appeared mostly in carbonate and mudstone (or organic matter). The results show that, with the gradual increase in paleosalinity, the content of carbonate rock increases. The carbonate content is reduced when the salinity is low. The content of clay and land-based debris is too low for developing layer deposition (Figure 10).

The internal structure of the chemical origin of stratified lithology is obviously controlled by the paleosalinity. With the evolution of paleosalinity from high to low, the microstructure of the grain layer is characterized by the change characteristics of the undulating cryptocrystal calcareous lamina, horizontal sparry calcareous lamina, horizontal muddy laminae and horizontal silty muddy laminae (Figure 11). This evolution may be related to the chemical origin of the carbonate rocks in this region.] The development of “biogenic carbonate plus mudstone/organic matter” and “muddy silt plus clay/organic matter” layer is obviously controlled by biological development and material source (Figure 12).

5.3 The relationship between saline environment and shale pore throat

The study of the relationship between salinity and lithology and storage showed that different lithological combinations developed in different salination stages, and different lithological combinations developed in different lithological combinations (Figure 12).

In the high saline stage, there are mainly paste mudstone and dolomite, corresponding to the main development of hydrgypsum intercrystalline pores (Figure 12A), dolomite intercrystalline pores (Figure 12B) and some dissolved pores (Figures 12C,D). Both gypsum and anhydrite are sulfate minerals (the gypsum chemical formula is $CaSO_4•2H_2O$, and the anhydrite chemical formula is $CaSO_4$), and Has a certain degree of plasticity. Usually, gypsum can be formed in a natural state, losing water at 80°C–90°C, converting into hydraster, and forming substable plaster at 100°C, stable plaster at 150°C, and stable plaster at 193°C. Taking Bonnan depression as an example, according to the ground temperature gradient of 3.5°C/100 m, the ground temperature can reach 123°C at 3,500 m. At this time, the gypsum has been fully transformed into anhydrite, and the ground temperature at 4,500 m is about 158°C. At this time, the gypsum has been fully transformed into anhydrite. Thus, the salt layer developed in the deep layer of Bonan depression is basically anhydrite. On the one hand, the formation of anhydrite in the Bonan depression suppresses the compaction effect, enabling the preservation of the native pores of the reservoir. On the other hand, the existence of the paste salt layer strengthens the fluid-rock action, especially the dissolution effect, making water discharged by the gypsum transformation, and dissolving organic acids, thus further dissolving rock minerals and forming secondary pore zones.

In the saltwater stage, there are mainly developed layered clay limestone/gray clay limestone and layered limestone, and corresponding to some intergranular pores (Figures 12E,F), dissolution pores(Figures 12G,H) and interlayer cracks.

The brackish water-brackish water stage mainly develops layers/massive gray mudstones/mudstones, corresponding to the main developing intergranular pores (Figures 12I,J), biological pores (Figure 12G,K) and microcracks (Figure 12I).

From the perspective of lithology, different layer types and rock compositions have a great impact on the development degree of microcracks, especially along the substrata. Statistical findings (Table 1): the smooth layer microcracks of plain layered mudstone and mudstone are the most developed, and the second is microcorrugated layered marl, layered mudstone, and limestone, and the worst is block. The contact area between straight layers is smaller than that of corrugated layers, the binding force between layers is weak, and it is relatively easy to crack into cracks under overpressure.

6 Conclusion

This study aims to clarify the effect of the continental lacustrine basin on shale pore throat. By studying the shale of the Shahejie Formation in the Jiyang Depression, China, conclusions are drawn as follows.

1. Carbonate minerals are the most abundant minerals in shale. In the case of low salinity, the content of carbonate minerals increases with the increase in salinity. In the case of high salinity, the content of carbonate minerals gradually decreases while that of sulfate and gypsum increases with the increase in salinity. The assemblage of gypsum stone-argillite, carbonate rock-laminated argillite, and laminated calcareous mudstone-massive are developed, respectively, in the high saline, saltwater, and brackish stages. The carbonate laminae are most developed when the salinity ranges from 15‰ to 30‰.
2. The texture is conducive to the development of microcracks. With the increase in salinity, the number of textures first

increases and then decreases. When the content is 15 ‰–30‰, there are most abundant textures, making it most likely to form microcracks.

3. The lithological assemblage controls the original pore throat type of shale. The carbonate minerals are prone to dissolution, which enlarges the pore throat. Microcracks are very likely to emerge on the grain layer in the later stage. The more the grain layers, the more the microcracks. Carbonate minerals and grain layers are the main factors to improve the structure of shale pores.

Data availability statement

The original contributions presented in the study are included in the article/Supplementary Material. Further inquiries can be directed to the corresponding author.

Author contributions

ZZ is responsible for writing the entire article. SW and MH are responsible for experiments and data. YF is responsible for writing ideas and revising articles.

Funding

This work was supported by Open Foundation of Top Disciplines in Yangtze University (Grant number TD2019-004) and National Natural Science Foundation of China (42002165).

Conflict of interest

Author SW was employed by Sinopec Shengli Oilfield Company. Author MH was employed by CNOOC Research Institute Ltd. Author YF was employed by CNPC Xibu Drilling Engineering Company Limited.

The remaining authors declare that the research was conducted in the absence of any commercial or financial relationships that could be construed as a potential conflict of interest.

Publisher's note

References

Cao, T., Liu, G., Cao, Q., and DengM (2018). Influence of maceral composition on organic pore development in shale: A case study of transitional longtan formation shale in eastern sichuan basin. *Oil Gas Geol.* 39 (1), 40–53. doi:10.11743/ogg20180105

Cavelan, A., Boussafir, M., Milbeau, C. L., Rozenbaum, O., and Laggoun-Defarge, F. (2019). Effect of organic matter composition on source rock porosity during confined anhydrous thermal maturation: Example of Kimmeridge-clay mudstones. *Int. J. Coal Geol.* 212, 103236. doi:10.1016/j.coal.2019.103236

Chao, P., Pan, J., and Wan, X. (2017). Effect of clay minerals of coal-bearing shale on pore structure and methane adsorption property in Yuzhou coalfield. *China coal.* 43 (06), 46–52.

Chen, K. L., Zhang, T. S., and Liang, X. (2018). Analysis of shale lithofacies and sedimentary environment on wufeng formation-lower longmaxi Formation in dianqianbei depression. *Acta Sedimentol. Sin.* 36 (04), 743–755.

Chen, L., Jiang, Z., Liu, K., Tan, J., Gao, F., and Wang, P. (2017). Pore structure characterization for organic-rich lower silurian shale in the upper Yangtze platform, south China: A possible mechanism for pore development. *J. Nat. Gas Sci. Eng.* 46, 1–15. doi:10.1016/j.jngse.2017.07.009

Clarkson, C. R., Jensen, J. L., Pedersen, P. K., and Freeman, M. (2012). Innovative methods for flow-unit and pore-structure analyses in a tight siltstone and shale gas reservoir. *Am. Assoc. Pet. Geol. Bull.* 96 (2), 355–374. doi:10.1306/05181110171

Curtis, J. B. (2002). Fractured shale-gas systems. *AAPG Bull.* 86 (11), 1921–1938.

Curtis, M. E., Cardott, B. J., Sondergeld, C. H., and Rai, C. S. (2012). Development of organic porosity in the Woodford Shale with increasing thermal maturity. *Int. J. Coal Geol.* 103, 26–31. doi:10.1016/j.coal.2012.08.004

Gu, Y., Ding, W., Yin, M., Jiao, B., Shi, S., Li, A., et al. (2018). Nanoscale pore characteristics and fractal characteristics of organic-rich shale: An example from the lower Cambrian Niutitang Formation in the Fenggang block in northern Guizhou Province, South China. *Energy Explor. Exploitation* 37 (1), 273–295. doi:10.1177/0144598718790320

Jarvie, D. M., Hill, R. J., Ruble, T. E., and Pollastro, R. M. (2007). Unconventional shale-gas systems: The Mississippian Barnett Shale of north-central Texas as one model for thermogenic shale-gas assessment. *Am. Assoc. Pet. Geol. Bull.* 91 (4), 475–499. doi:10.1306/12190606068

Landergren, S., and Carvajal, M. C. (1969). Geochemistry of boron, II. The relationship between boron concentration in marine clay sediments expressed as an adsorption isotherm. *Ark. Kem. Mineral. Geol.* 5, 13.

Li, A., Ding, W., Jiu, K., Wang, Z., Wang, R., and He, J. (2018). Investigation of the pore structures and fractal characteristics of marine shale reservoirs using nmr experiments and image analyses: A case study of the lower cambrian niutitang Formation in northern guizhou province, south China. *Mar. Pet. Geol.* 89, 530–540. doi:10.1016/j.marpetgeo.2017.10.019

Li, P. L. (2003). "Petroleum geology and exploration of continental fault basin," in *Hydrocarbon generation and resource evaluation of continental fault basin*. (Beijing: Petroleum Industry Press) Vol. 3, 4–8.

Liang, X., Zhang, T., and Yang, Y. (2014). Microscopic pore structure and its controlling factors of overmature shale in the Lower Cambrian Qiongzhusi Fm, northern Yunnan and Guizhou provinces of China. *Nat. Gas. Ind.* 34 (02), 18–26.

Liu, Y., and Peng, P. A. (2017). Research on the influences of different mineral compositions on the development of nanopores in shales. *J. CHINA COAL Soc.* 042 (003), 702–711.

Mastalerz, M., He, L., Melnichenko, Y. B., and Rupp, J. A. (2012). Porosity of coal and shale: Insights from gas adsorption and SANS/USANS techniques. *Energy fuels.* 26 (8), 5109–5120. doi:10.1021/ef300735t

Pan, B., Gong, C., Wang, X., Li, Y., and Iglauer, S. (2020). The interfacial properties of clay-coated quartz at reservoir conditions. *Fuel* 262, 116461. doi:10.1016/j.fuel.2019.116461

Song, G. Q., Wang, Y. S., Cheng, F. Q., Company, S. O., and SINOPEC (2004). Ascertaining secondary order sequence of Palaeogene in Jiyang depression and its petroleum geological significance. *Petroleum Geology and Recovery Efficiency* 21 (5), 1–7.

Wei, M., Zhang, L., Xiong, Y., and Peng, P. (2019). Main factors influencing the development of nanopores in over-mature, organic-rich shales. *Int. J. Coal Geol.* 212, 103233. doi:10.1016/j.coal.2019.103233

Wei, Z., Wang, Y., Wang, G., Sun, Z., and Xu, L. (2018). Pore characterization of organic-rich late permian da-long formation shale in the sichuan basin, southwestern China. *Fuel* 211, 507–516. doi:10.1016/j.fuel.2017.09.068

Wu, L. M., Ding, W. L., and Zhang, J. C. (2011). Fracture prediction of organic-enriched shale reservoir in lower silurian longmaxi formation of southeastern chongqing area. *J. Oil Gas Technol.* 33 (09), 43–166.

Wu, Y. Q., Tahmasebi, P., Lin, C. Y., Zahid, M. A., Dong, C., Golab, A. N., et al. (2019). A comprehensive study on geometric, topological and fractal characterizations of pore systems in low-permeability reservoirs based on SEM, MICP, NMR, and X-ray CT experiments. *Mar. Petroleum Geol.* 103, 12–28. doi:10.1016/j.marpetgeo.2019.02.003

Yan, S. C. (2013). Paleo - salinity and paleo - environmental analysis of Carboniferous in northeast Junggar basin. *Petroleum Geol. Recovery Effic.* 20 (5), 60–63.

Zeng, F., Dong, C. M., Lin, C. Y., Wu, Y. Q., Tian, S. S., Zhang, X. G., et al. (2021). Analyzing the effects of multi-scale pore systems on reservoir properties—a case study on xihu depression, East China sea shelf basin, China. *J. Petroleum Sci. Eng.* 203, 108609. doi:10.1016/j.petrol.2021.108609

Zeng, W., Ding, W., and Zhang, J. (2019). Analyses of the characteristics and main controlling factors for the micro/nanopores in Niutitang shale from China's southeastern Chongqing and northern Guizhou regions. *Earth Sci. Front.* 26 (3), 220–235.

Zhang, J., Li, X., Xiaoyan, Z., Zhao, G., Zhou, B., Li, J., et al. (2019). Characterization of the full-sized pore structure of coal-bearing shales and its effect on shale gas content. *Energy fuels.* 33 (3), 1969–1982. doi:10.1021/acs.energyfuels.8b04135

Zhao, P., Wang, Z., Sun, Z., Cai, J., and Wang, L. (2017). Investigation on the pore structure and multifractal characteristics of tight oil reservoirs using NMR measurements: Permian Lucaogou Formation in Jimusaer Sag, Junggar Basin. *Mar. Petroleum Geol.* 86, 1067–1081. doi:10.1016/j.marpetgeo.2017.07.011

Zhao, Z. X., He, Y. B., and Huang, X. (2021). China, Lithosphere, 3310886. doi:10.2113/2021/3310886Study on fracture characteristics and controlling factors of tight sandstone reservoir: A case study on the huagang Formation in the xihu depression, East China sea shelf basin, China.1

Zhou, L., and Kang, Z. (2016). Fractal characterization of pores in shales using nmr: A case study from the lower cambrian niutitang Formation in the middle Yangtze platform, southwest China. *J. Nat. Gas Sci. Eng.* 35, 860–872. doi:10.1016/j.jngse.2016.09.030

Zhou, Y. K., He, J. W., and Wang, Z. W. (1984). *Application of boron as an indicator of paleosalinity. Selected papers from conferences on Sedimentology and Organic Geochemistry*. Beijing: science press, 55–57.

frontiers | Frontiers in Earth Science

TYPE Original Research
PUBLISHED 02 September 2022
DOI 10.3389/feart.2022.994312

OPEN ACCESS

EDITED BY
Yuqi Wu,
China University of Petroleum, China

REVIEWED BY
Weichao Yan,
Ocean University of China, China
Kun Liu,
SINOPEC Petroleum Exploration and Production Research Institute, China
Huaimin Dong,
Chang'an University, China

*CORRESPONDENCE
Jianpeng Zhao,
zjpsnow@126.com

SPECIALTY SECTION
This article was submitted to Solid Earth Geophysics,
a section of the journal
Frontiers in Earth Science

RECEIVED 14 July 2022
ACCEPTED 10 August 2022
PUBLISHED 02 September 2022

CITATION
Zhao J, Chen H, Zhang J, Zhang W and Chen G (2022), Quantitative characterization of organic and inorganic pores in shale based on FIB-SEM.
Front. Earth Sci. 10:994312.
doi: 10.3389/feart.2022.994312

Quantitative characterization of organic and inorganic pores in shale based on FIB-SEM

Jianpeng Zhao[1,2]*, Hui Chen[3], Jinyan Zhang[4], Wenjiao Zhang[4] and Gang Chen[5]

[1]School of Earth Sciences and Engineering, Xi'an Shiyou University, Xi'an, China, [2]Shaanxi Key Laboratory of Petroleum Accumulation Geology, Xi'an, China, [3]Geological Research Institute, China Petroleum Logging CO., LTD., Xi'an, China, [4]Well Logging Company, Sinopec Shengli Oilfield Service Corporation, Dongying, China, [5]CCTEG XI'AN Research Institute, Xi'an, China

The pore structures of shale in the Shahejie formation of Dongying depression were quantitatively characterized by FIB-SEM three-dimensional imaging technology. FIB-SEM was used to obtain high-resolution SEM images and through image registration, geometric correction and image segmentation, the organic pores and inorganic pores in the shale were distinguished. The pore space was converted into a structured pore network model via maximal ball method. Then, the pore size distributions and volume contributions of shale organic pores and inorganic pores, and the coordination number of the total pore network model were statistically analyzed via the pore network model. The results showed that due to the low thermal maturity of organic matter in the Shahejie formation, fewer organic pores were observed in the shale samples, and the number of pores was dominated by inorganic pores. Statistical analysis of the pore network model indicated that the studied shale samples considerably included mesopore (size of 2–50 nm) which accounted for 61.1%, but their contribution to the total pore volume was small (4.2%). Macropores (>50 nm) accounted for a relatively small proportion (38.9%) in number, but they provided the main storage space (95.8%) for the shale oil and gas. The volume contribution of pores to the total pore space at a certain bin size is controlled by the combination of pore number and the pore size. The coordination numbers of the two samples were mainly 0 and 1, indicating that the pore connectivity was poor and isolated pores accounted for most part. These results are critical for further reliable petrophysical simulations based on shale digital rocks as well as for the accurate understanding of their petrophysical properties.

KEYWORDS

FIB-SEM, digital rock, shale, Shahejie formation, Dongying depression

1 Introduction

The characterization of shale pore structure has always been the core work of shale oil and gas resource evaluation, and it is also a research hotspot and frontier in the field of oil and gas geology (Tang et al., 2016; Cao et al., 2019; Ma X. et al., 2019). The classification of shale rock pore types is of great significance to the qualitative and quantitative characterization of pores in shale. There are various types of pores in shale reservoirs, which can be classified into organic pores and inorganic pores in terms of genesis (Jarvie et al., 2007; Li et al., 2014). The pore type affects the wettability of the rock. Typically, organic pores are strongly oil-wet, and inorganic pores are strongly water-wet, which in turn affects the distribution of fluid in the pore space and the electrical resistivity of the rock (Nie et al., 2016; Yan et al., 2019; Wu et al., 2020). The percolation mechanism and occurrence state of shale oil and gas in organic and inorganic pores are also different (Wu et al., 2019a). Free gas is mainly stored in inorganic pores, while adsorbed gas is mainly adsorbed on the surface of organic matter and into the organic pores (Yao et al., 2018). Considering the differences in the influence of different pore types on petrophysical properties of shale, it is of great significance to quantitatively analyze the microstructure of organic and inorganic pores respectively. The commonly used experimental methods to study pore structure include high pressure mercury injection (MICP), gas (N_2 or CO_2) adsorption, nuclear magnetic resonance (NMR), scanning electron microscope (SEM) and CT scanning method, etc. (Tian et al., 2012; Tiwari et al., 2013; Liu et al., 2015; Wu et al., 2019b; Cui et al., 2020; Li et al., 2022; Golsanami et al., 2021 and 2022). High pressure mercury injection method and gas adsorption method are indirect means to obtain pore structure and morphology information. They can determine the overall pore size distribution of the sample through experimental results and some theoretical formula, but cannot distinguish between organic and inorganic pores. Scanning electron microscope is a commonly used method to describe the pore types and pore morphology of rocks, but it only reflects the two-dimensional information of the pores and cannot reflect the distribution information of the pores in the three-dimensional space. Nuclear magnetic resonance analysis can determine the T_2 spectrum of oil-wet and water-wet pores. The pore size distribution of organic and inorganic pores can be obtained via establishing the quantitative relationship between T_2 and pore size. However, this method cannot reflect the connectivity of the pores (Li et al., 2016). Although nano-CT based on the X-ray imaging (Dong et al., 2018; Dong et al., 2019) can obtain the three-dimensional reconstruction of shale pores, it is difficult to distinguish the organic pores and inorganic pores, since the gray values of organic pores and inorganic pores in CT image are very close (Kelly et al., 2016). Different from the methods discussed above, FIB-SEM is one of the most effective means to identify and analyze the organic and inorganic pores of shale. This technology can directly characterize the pore micro structure of shale on two-dimensional and three-dimensional scales both qualitatively and quantitatively. In the already existing studies, the researchers have mainly focused on the quantitative characterization of the total pore space of shale, and did not focus on the segmentation and quantitative characterization of shale's organic pores and inorganic pores (Chalmers et al., 2012; Curtis et al., 2012; Zhou et al., 2016; Liu et al., 2017; Saif et al., 2017; Zhou et al., 2017). In this paper, two shale samples of the Shahejie formation in Dongying depression, Bohai Bay Basin were taken as an example, and FIB-SEM was used to establish three-dimensional digital rock of shale. Based on the difference in depth of field and pore distribution characteristics of organic pores and inorganic pores, the core image data was segmented twice by a double threshold method, then the fine division of organic and inorganic pores was achieved through image logic operations and algebraic operations. Finally, the maximal ball method was used to obtain the pore space topology model. The pore size distribution, volume contribution distribution of organic pores and inorganic pores and coordination number of the total pore network were respectively counted so as to quantitatively characterize the organic and inorganic pores in the studied shale samples. This method provides an effective method for quantitative characterization of shale microscopic pores which is critical for further reliable petrophysical simulations.

2 Test samples and methods

2.1 Sample characteristics

The samples used in this study were drilled from Well Fanye 1 in Dongying depression, Bohai Bay Basin. This well is a pre-prospecting well for unconventional oil and gas exploration and is the first key well deployed in Fanjia block by the Shengli oil field, which is of great significance for understanding the reservoir characterization and hydrocarbon-bearing conditions of the shale in the lower section of E*s*3, and upper section of E*s*4 in the Boxing Sag (Yan et al., 2018). The samples were from the lower section of E*s*3, which belongs to the semi-deep to deep lake depositional environment (Wu et al., 2016). The mineral composition of the shale samples in the Shahejie formation is rather complex and can be divided into clay minerals (average 24.2%), carbonate minerals (average 45.1%), quartz and feldspar (average 26.9%), and a small amount of pyrite, siderite, etc. The clay minerals are mainly illite followed by the mixed layer of illite/smectite, and a small amount of kaolinite and chlorite. The main type of kerogen belongs to I-type, and the vitrinite reflectance, Ro, is between 0.51% and 0.93%, which indicates the immature to low-mature stage (Sun, 2017). The lithology of the two samples selected for in this study is dark gray laminar lime-bearing mudstone (S1) and dark gray laminar lime-bearing mudstone (S2). The basic information is shown in Table 1.

TABLE 1 Characteristics of Shale Samples from the Lower section of Es3 in Dongying Depression, Bohai Bay Basin.

Sample ID	Depth (m)	Porosity (%)	Permeability ($10^{-3}\mu m^2$)	Density (g/cm^3)	TOC (%)
S1	3201.49	7.8	0.478	2.29	8.35
S2	3135.06	4.3	0.178	2.51	1.65

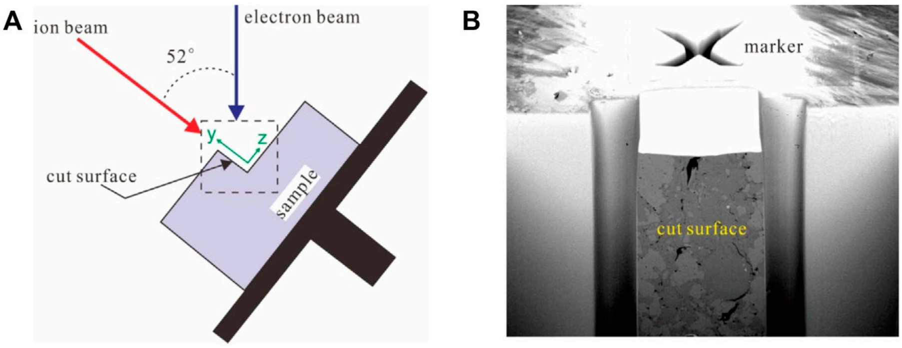

FIGURE 1
Schematic diagram of milling and imaging in the FIB-SEM system. **(A)** The characteristic of a typical FIB-SEM system. **(B)** Cross-section of a shale sample cut by an ion beam in BSE mode.

2.2 Focused ion beam-scanning electron microscope cutting and imaging

FIB-SEM is a dual beam system formed by the focused ion beam (FIB) coupled with the scanning electron microscope (SEM). The common double beam equipment is that the electron beam is installed vertically, and the ion beam is installed at a certain angle with the electron beam, as shown in Figure 1A. The point of intersection of the focal planes of the electron beam and the ion beam is usually referred to as the concentric height position. By combining the gas deposition device, nanomanipulator, various detectors, controllable sample stage, and other accessories, FIB-SEM has become an analytical instrument integrating micro area imaging, processing, analysis, and manipulation. The ion source is the key component in the dual beam system and is used to generate the ion beam. Currently, the most commonly used ion source in commercial systems is gallium (Ga). The diameter of the gallium ion beam can be controlled to the nanometer scale by adjusting the lens system and the aperture strip. The cutting function of the ion beam is realized by sputtering out the atoms on the surface of the sample through the collision between the electron beam and the surface atoms, and the interaction of the electron beam with the sample surface can generate a signal for creating a high-resolution image of the sample. The cutting and scanning of the shale sample in this experiment were done with FEI Helios 650 instrument. First, emery paper and argon ion beam are used to polish the surface of the shale sample, and the sample is fixed to the stage with conductive carbon glue. Then turn on the electron beam, use the backscatter (BSE) mode to observe the polished shale surface, select the region of interest (ROI), and plate the surface of the area with platinum to avoid the ion beam from damaging the sample surface during the cutting process. Then rotate the sample table 52° (the ion beam is perpendicular to the sample surface during the cutting process), and use the gallium ion beam to cut off the shale on both sides and in front of the sample target area, exposing a new shale section; cut a "×" mark near the ROI as an alignment reference for continuous ion beam cutting (Figure 1B). Then control the ion beam and electron beam to perform continuous cutting and imaging. Every time the ion beam cuts a 10 nm thick slice of the sample, the electron beam scans the surface of the sample and records the signal used to form a nanoscale image. A sequence of continuous high-resolution SEM images can be obtained via successive and repeated cutting and imaging and the shale microstructure information can be extended from two-dimensional to three-dimensional scale (Lemmens et al., 2011).

3 Image data processing

3.1 Image registration

In the continuous cutting and scanning process of FIB-SEM, there will inevitably be a slight offset between two adjacent images in the image sequence generated by the SEM (Curtis

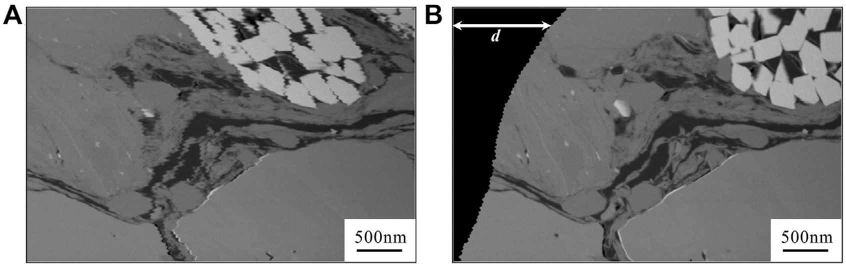

FIGURE 2
FIB-SEM image alignment (result from sample S1). **(A)** section image before alignment. **(B)** section image after alignment, where *d* is the translational distance relative to the reference image.

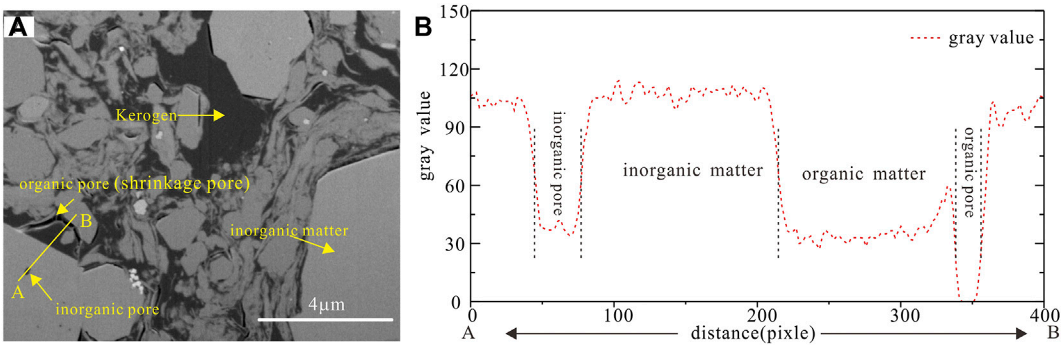

FIGURE 3
FIB-SEM image characteristics of shale samples from Shahejie formation. **(A)** section image from sample S1 produced by FIB-SEM. **(B)** the gray distribution on line AB in **(A)**.

et al., 2012), which affects the subsequent segmentation, pore structure analysis, and petrophysical numerical simulation. An image registration algorithm can be used to align the images produced by FIB-SEM. Image registration is a method of optimally mapping one or more images to a target image based on a certain evaluation criterion. In image registration, the commonly used geometric transformation models mainly include rigid body transformation, affine transformation, projective transformation, and polynomial transformation (Goshtasby, 2005). Rigid body transformation can be decomposed into translation and rotation. Its characteristic is that after the points in the image are transformed, the Euclidean distance remains unchanged, and the relationship between the two straight lines such as parallel or perpendicular remains unchanged. In two-dimensional space, the process of point (x, y) being transformed to point (x', y') through a rigid body transformation can be expressed as:

$$\begin{bmatrix} x' \\ y' \\ 1 \end{bmatrix} = \begin{bmatrix} \cos\theta & -\sin\theta & t_x \\ \sin\theta & \cos\theta & t_y \\ 0 & 0 & 1 \end{bmatrix} \begin{bmatrix} x \\ y \\ 1 \end{bmatrix} \tag{1}$$

Where θ, t_x and t_y are the rotation angle, the translational distance in x direction, the translational distance in y direction, respectively. In general, the first captured SEM image in the image sequence is used as the reference image, and all other images are aligned with it. The results before and after image alignment are shown in Figure 2. Before image registration, the boundaries of each component are uneven and jagged. After image registration, the boundaries of each component become relatively smooth. After the image is registered, the edge part that does not contain any information of the sample needs to be cut out.

3.2 Geometric correction

During the continuous cutting and scanning process, the electron beam is not perpendicular to the cross-section of the sample. For the Helios 650 FIB-SEM system, the electron beam usually has an angle of 52° with the ion beam (Figure 1A). Therefore, the actual scan size of the SEM is the projection of the

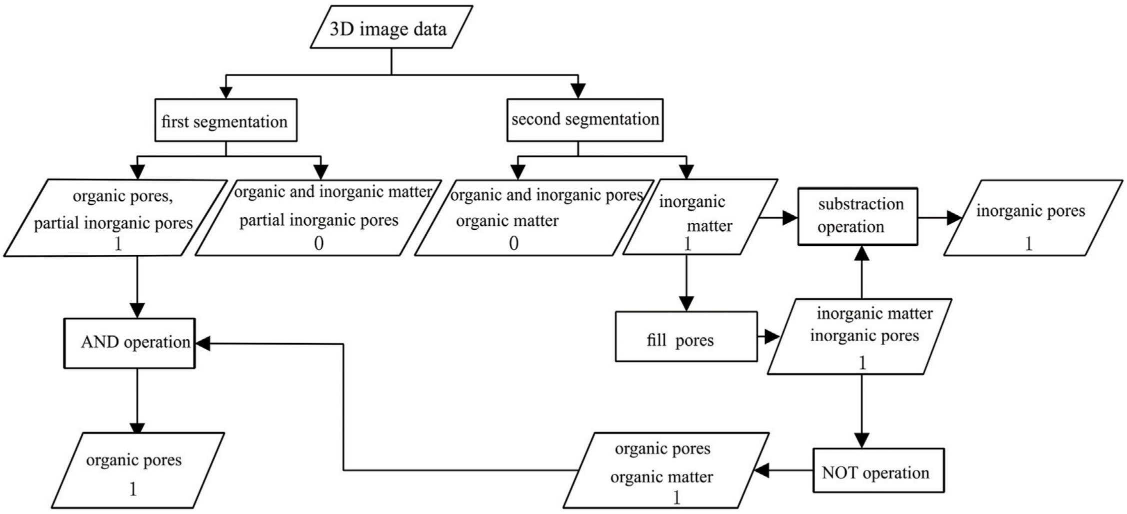

FIGURE 4
Flow chart of separation of organic pores and inorganic pores.

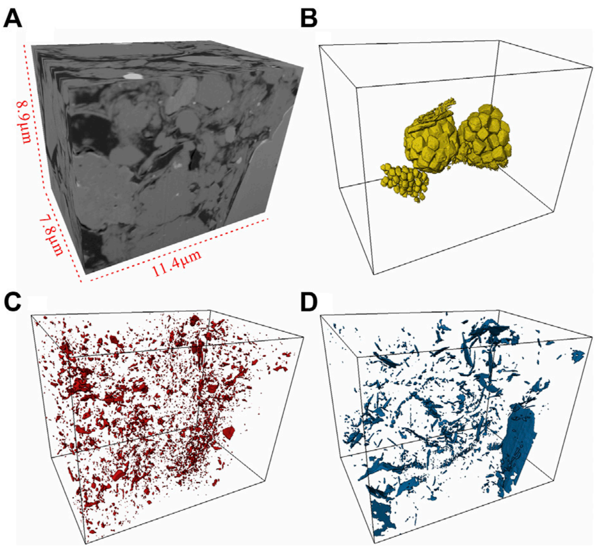

FIGURE 5
Image segmentation results of sample S1. **(A)** A digital rock reconstructed from S1. With multithreshold segmentation, pyrite **(B)**, inorganic pores **(C)**, and organic pores **(D)** were segmented out.

sample section on the horizontal plane, not the actual size of the sample section (Sun et al., 2016). The SEM image size can be converted to the actual size of the sample cross-section by multiplying a correction factor in the y direction. For an angle of 52°, the correction factor is 1/sin (52°).

3.3 Image segmentation

The accurate segmentation of the digital rock skeleton and pore space is the key problem to the quantitative characterization of the shale microstructure. Image binarization is a commonly used approach in digital rock image segmentation (Liu, 2010). This method uses a fixed threshold to separate the three-dimensional digital rock image into two parts: skeleton and pore space. However, due to the high resolution of SEM imaging, the internal details of pores will be displayed in the SEM image influenced by the depth of field (Sun et al., 2016), which leads to different grayscale distributions of organic pores and inorganic pores, that is, the pores have different gray values. The gray value of some inorganic pores is close to or even greater than the gray value of organic matter (Figure 3). Therefore, the traditional binary segmentation method cannot meet the requirements of shale digital rock image segmentation.

Based on the gray value of pores and the distribution characteristics of organic pores and inorganic pores, the image data was segmented twice with two different thresholds, and then the organic pores and inorganic pores were finely divided through image logic operations and algebraic operations. The specific image segmentation and operation process are shown in Figure 4, where “0” and “1” are the values of specific phases after image segmentation or operation. For the first binarization segmentation, using the maximum gray value of organic pores as the segmentation threshold, the image data could be divided into two parts:

- Organic pores and part of inorganic pores (denoted as 1).

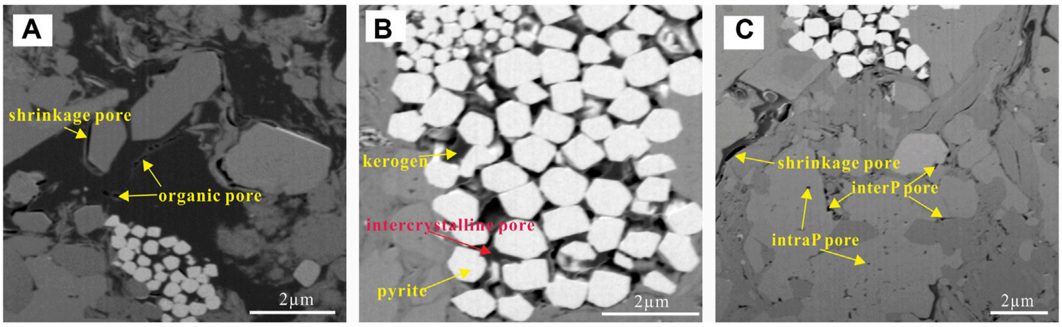

FIGURE 6
Pore types of shale samples from Shahejie formation. **(A)** a small amount of organic pores distributed in kerogen, and shrinkage pores between kerogen and inorganic minerals **(B)** Pyrite intercrystalline pore filled with kerogen containing organic pores, **(C)** InterP pores between brittle minerals and IntraP pores within quartz or feldspar particles.

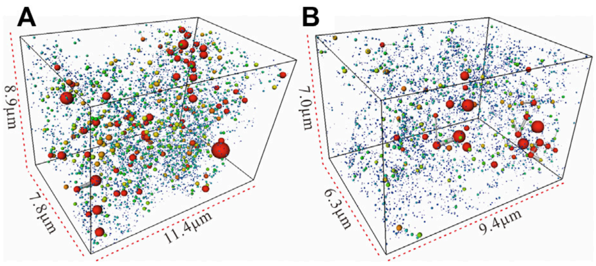

FIGURE 7
Pore network model extraction results of sample s1 **(A)** and s2 **(B)**.

- Organic matter, inorganic matter, and part of inorganic pores (denoted as 0).

For the second binarization segmentation, using the maximum gray value of inorganic pores as the segmentation threshold, the core could be divided into two parts:

- All organic pores, all organic matter and all inorganic pores (denoted as 0).
- Inorganic matter (denoted as 1).

Image segmentation result of sample S1 is shown in Figure 5, in which Figure 5A is the 3D reconstructed digital rock of sample S1. The digital rock is composed of 781 continuous SEM images, and the size is 11.4μm × 8.9μm × 7.8 μm. Using the image processing procedure described in Figure 4, different components such as pyrite, inorganic pores and organic pores were segmented out. Figures 5B–D show the renderings of the pyrite, inorganic pores, and organic pores, respectively. All the samples in Table 1 were analyzed using the same processing procedure, which laid the foundation for the subsequent quantitative characterization of inorganic and organic pores in shale.

4 Results and discussion

4.1 Pore types

Taking into account the wettability of shale pores and the differences in their impact on petrophysical properties (electrical property, percolation property), the shale pores of the Shahejie formation in the Dongying depression are classified into two categories from the perspective of genesis, organic pores, and inorganic pores. Organic pores are oil-wet and are divided into shrinkage pores and internal pores formed in the process of thermal evolution and hydrocarbon generation of organic matter, so they are important storage places for shale oil and gas. The two-dimensional SEM image showed that the organic pores in the shale samples of the study area are less developed. The organic pores in this formation are mainly composed of shrinkage pores between organic matter and inorganic minerals, and the pores within the organic matter are less (Figure 6A). The observation results are consistent with the previous research results (Ma H. et al., 2019). The degree of organic pore development is quite different from the Longmaxi Shale in China (Zhou et al., 2016; Xie et al., 2019) and the Barnett Shale in the United States (Loucks et al., 2012). This is because the degree of organic pore development is related to the thermal maturity of the organic matter in the shale (Klaver et al., 2016; Zhang et al., 2020). The thermal evolution degree of shale samples in the research area is in the stage of immaturity to low-maturity (Liu et al., 2017). Inorganic pores are relatively developed in shale samples of Shahejie Formation, including interparticle (interP) pores and intraparticle (intraP) pores. Interparticle pores reflect the contact relationship between different mineral particles, and are mainly developed between brittle minerals, such as quartz and feldspar.

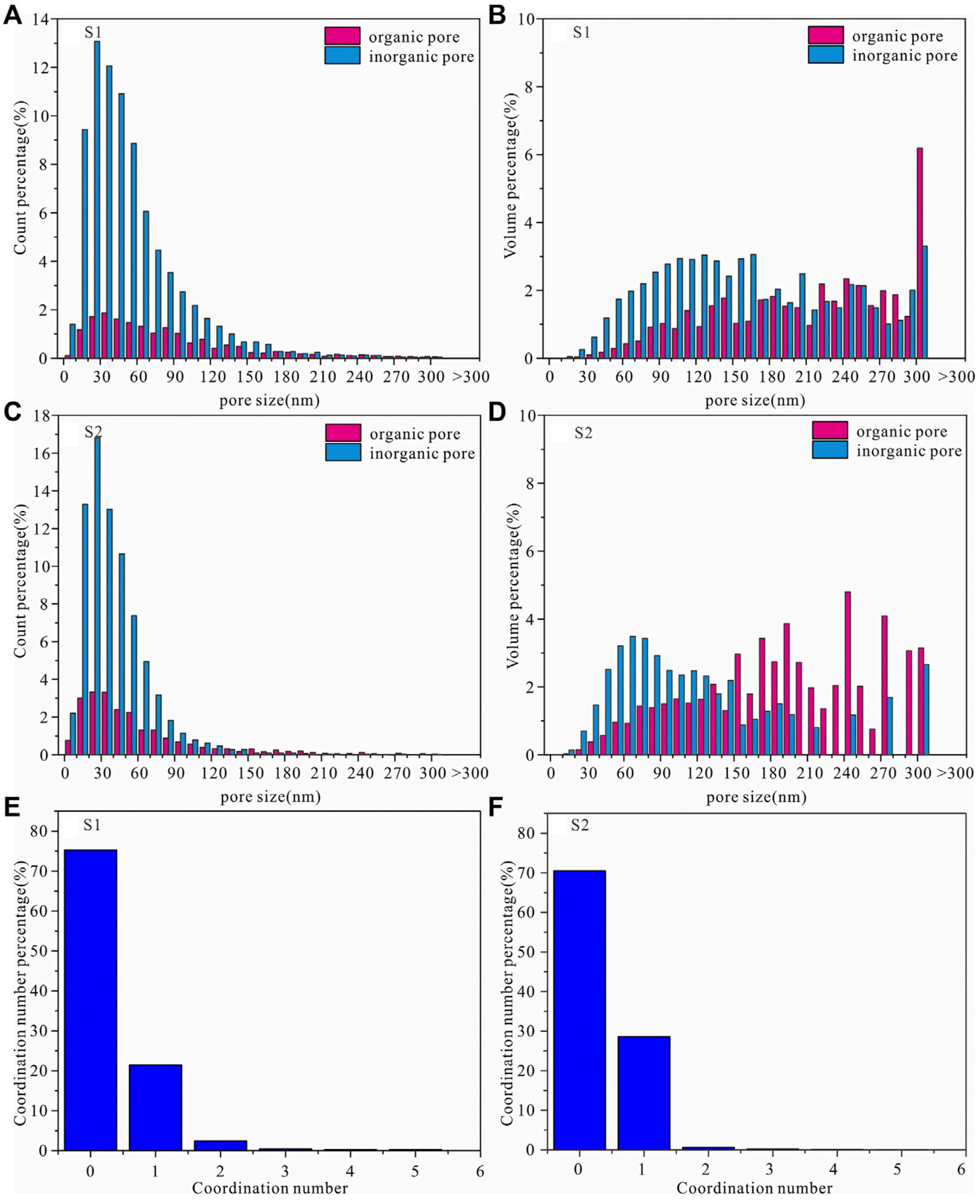

FIGURE 8
Distributions of pore size and coordination number of shale samples from Shahejie Formation in Dongying depression. **(A)** and **(B)** are pore count percentage and volume contribution to the total pore space of sample S1 at a given bin size, respectively; **(C)** and **(D)** are pore count percentage and volume contribution to the total pore space of sample S2 at a given bin size, respectively; and **(E)** and **(F)** are distributions of coordination numbers of sample S1 and S2, respectively.

Intraparticle pores reflect the pores inside mineral particles (Figures 6B,C).

4.2 Pore network model

The pore network model simplifies the complex and irregular pore space of the shale digital rock. The model not only retains the pore space distribution characteristics of the original digital rock, but also facilitates the use of mathematical statistics to quantify pore structure parameters. The commonly used maximal ball method (Dong and Blunt, 2009) was adopted to extract regularized pore structure models from the organic pores and inorganic pores which were segmented using the procedure discussed in Section 2.3. The maximal ball method is to select a point in the pore pixel and extend it around until it touches the nearest matrix pixel, and the set of all pixels in the formed area is called the maximum sphere. The largest sphere can overlap with the adjacent largest sphere whose radius is smaller than it, thus forming the multiple clusters of the largest spheres. The pore space of 3D digital rock can be represented by the largest spheres with different radius. The "pore" and "throat" in the pore network model are determined by finding the local maximum sphere and the smallest sphere between the two largest spheres in the ball string. Finally, the pore space of the 3D digital rock can be simplified into a network model with "pore" and "throat" as the basic units. Figure 7 is the extraction results of the pore network model of samples S1 and S2, where the ball represents the pore and the tube represents the throat.

Based on the pore network model of shale, the quantitative characterization of the microscopic pore structure can be established by analysis the size of organic pores and inorganic pores and the coordination number of the entire network model.

The classification of pore types in shale reservoirs plays a significant role in further analyzing the micropores in shale. Based on the pore size, scholars have proposed different pore classification schemes. Loucks et al. (2009) classified shale pores of the Mississippian Barnett shale into micro-pores (>=0.75 μm) and nano-pores (<0.75 μm). Zhang et al. (2017) divided shale pores of Paleogene Xin'gouzui Formation in the Jianghan basin into I-type micro-pores (<25 nm), II-type micro-pores (25–100 nm), mesopores (100–1000 nm) and macropores (>1000 nm). At present, the most widely used quantitative classification scheme of shale pores is proposed by "International Union of Pure and Applied Chemistry (IUPAC)". According to the pore classification scheme of the IUPAC (Rouquerol et al., 1994), shale pores can be divided into: micropores (less than 2 nm), mesopores (2–50 nm) and macropores (greater than 50 nm). Figure 8 is the pore size distribution and coordination number distribution obtained by statistical analysis of the pore network model of organic pores and inorganic pores. The size of the inorganic pores of sample S1 is mainly distributed in the range of 10–100 nm, and the peak distribution is between 20 and 30 nm. The size of the organic pores is mainly distributed in the range of 10–60 nm, and with a peak value between 20 and 30 nm (Figure 8A). Organic pores in 2–50 nm account for 12.8% of the total pores, and inorganic pores in 2–50 nm account for 55.9% of the total pores, but the corresponding pore volume contribution are 1.1%, and 4.8%, respectively. The organic pores with the largest volume contribution have a pore size distribution interval of 240–250 nm. The largest volume contribution of inorganic pore size distribution is in the range of 60–70 nm (Figure 8B). Similarly, by statistically analyzing the pore network model of the sample S2, the pore size distribution characteristics and pore volume distribution can be obtained. In sample S2, the inorganic pores are mainly distributed in the range of 10–60 nm, and the peak value is between 20 and 30 nm. The organic pores are mainly distributed in the range of 10–90 nm and the peak value is between 30 and 40 nm. The number of organic pores and inorganic pores in 2–50 nm accounted for 6.5% and 46.9%, respectively. The corresponding volume contributions to the total pore volume are 0.3%, and 2.1%, respectively. The size of the organic pores and inorganic pores with the largest volume contribution both are above 300 nm (Figures 8C,D). The distributions of pore size and volume contribution show that the mesopores in the shale samples in the study area are obviously dominant in number, but they contribute less to the total pore volume. Macropores account for a small proportion in number, but they provide the main storage space for shale oil and gas. The pore volume contribution is controlled by a combination of pore number and pore size.

Pore connectivity is of great significance to the accumulation and migration of shale oil and gas. The connectivity of the pores can be expressed by the coordination number (referring to the number of throats connected to the pores), which reflects the connectivity between the pores. The larger the coordination number, the better the pore connectivity, and the smaller the coordination number, the worse the pore connectivity. Figures 8E,F are the histograms of the coordination number distribution of rock sample S1 and S2, respectively. The coordination numbers of the two samples are mainly 0 and 1, which means that isolated pores dominate in number and the pore connectivity is poor.

5 Conclusion

In this paper, FIB-SEM and digital rock technology were used to quantitatively characterize the organic pores and inorganic pores of continental shale reservoirs in the Shahejie Formation in Dongying depression, and the following conclusions could be drawn:

(1) The shale reservoir of Shahejie Formation in Dongying depression is widely developed with nano-pores. Compared with the shale of the Longmaxi Formation, the thermal evolution degree of the shale in the study area is in the immaturity to low-maturity stage, therefore, organic pores were less developed in the shale sample, and inorganic pores dominate in the number of the Shahejie formation in the Dongying depression.

(2) The mesopores (2–50 nm) of the shale samples in the study area are obviously dominant in number, but they contribute less to the total pore volume. Macropores (>50 nm) account for a small proportion in number, but they provide the main storage space for shale oil and gas. The pore volume contribution is controlled by a combination of pore number and pore size. The pore connectivity analysis showed that isolated pores in the

shale samples in the study area are dominant in number, and the pore connectivity is poor.

(3) FIB-SEM can directly and accurately obtain the three-dimensional spatial distribution characteristics of organic pores and inorganic pores in shale rocks, which can not only obtain the distribution characteristics of organic and inorganic pores, but also the connectivity of the entire pore space. The digital rock also provides a medium for the simulation study of petrophysical properties of shale oil reservoirs.

Data availability statement

The original contributions presented in the study are included in the article/supplementary material, further inquiries can be directed to the corresponding author.

Author contributions

JpZ: investigation, methodology, writing—original draft, and data analysis. HC: supervision and writing—review and editing. JyZ: data analysis. WZ: writing—original draft, and processing the data. GC: methodology.

Funding

This work was supported in part by the National Natural Science Foundation of China (42102350), and the General fund of China Coal Science and Industry Group (2022-2-TD-MS005).

Conflict of interest

HC was employed by the China Petroleum Logging CO., LTD. JyZ and WZ were employed by the Sinopec Shengli Oilfield Service Corporation. GC was employed by the CCTEG Xi’an Research Institute.

The remaining authors declare that the research was conducted in the absence of any commercial or financial relationships that could be construed as a potential conflict of interest.

Publisher’s note

References

Cao, G., Lin, M., Ji, L., Jiang, W., and Yang, M. (2019). Characterization of pore structures and gas transport characteristics of longmaxi shale. *Fuel* 258, 116146. doi:10.1016/j.fuel.2019.116146

Chalmers, G. R., Bustin, R. M., and Power, I. M. (2012). Characterization of gas shale pore systems by porosimetry, pycnometry, surface area, and field emission scanning electron microscopy/transmission electron microscopy image analyses: Examples from the barnett, woodford, haynesville, marcellus, and doig units. *Am. Assoc. Pet. Geol. Bull.* 96, 1099–1119. doi:10.1306/10171111052

Cui, L., Sun, J., Yan, W., and Dong, H. (2020). Multi-scale and multi-component digital core construction and elastic property simulation. *Appl. Geophys.* 17, 26–36. doi:10.1007/s11770-019-0789-7

Curtis, M. E., Sondergeld, C. H., Ambrose, R. J., and Rai, C. S. (2012). Microstructural investigation of gas shales in two and three dimensions using nanometer-scale resolution imaging. *Am. Assoc. Pet. Geol. Bull.* 96, 665–677. doi:10.1306/08151110188

Dong, H., and Blunt, M. J. (2009). Pore-network extraction from micro-computerized-tomography images. *Phys. Rev. E* 80, 036307. doi:10.1103/physreve.80.036307

Dong, H., Sun, J., Cui, L., Golsanami, N., Yan, W., Huaimin, D., et al. (2019). Characteristics of the pore structure of natural gas hydrate reservoir in the qilian mountain permafrost, northwest China. *J. Appl. Geophys.* 164, 153–159. doi:10.1016/j.jappgeo.2019.03.005

Dong, H., Sun, J., Golsanami, N., Cui, L., Jiang, L., Yan, G., et al. (2018). A method to construct high-precision complex pore digital rock. *J. Geophys. Eng.* 15, 2695–2703. doi:10.1088/1742-2140/aae04e

Golsanami, N., Fernando, S. G., Jayasuriya, M. N., Yan, W., Dong, H., Cui, L., et al. (2021). Fractal properties of various clay minerals obtained from SEM images. *Geofluids* 1–18. doi:10.1155/2021/5516444

Golsanami, N., Jayasuriya, M. N., Yan, W., Fernando, S. G., Liu, X., Cui, L., et al. (2022). Characterizing clay textures and their impact on the reservoir using deep learning and lattice-Boltzmann simulation applied to SEM images. *Energy* 240, 122599. doi:10.1016/j.energy.2021.122599

Goshtasby, A. A. (2005). *2-d and 3-d image registration: For medical, remote sensing, and industrial applications*. New York: John Wiley & Sons.

Jarvie, D. M., Hill, R. J., Ruble, T. E., and Pollastro, R. M. (2007). Unconventional shale-gas systems: The mississippian barnett shale of north-central Texas as one model for thermogenic shale-gas assessment. *Am. Assoc. Pet. Geol. Bull.* 91, 475–499. doi:10.1306/12190606068

Kelly, S., El-Sobky, H., Torres-Verdin, C., and Balhoff, M. T. (2016). Assessing the utility of fib-sem images for shale digital rock physics. *Adv. Water Resour.* 95, 302–316. doi:10.1016/j.advwatres.2015.06.010

Klaver, J., Desbois, G., Littke, R., and Urai, J. L. (2016). Bib-sem pore characterization of mature and post mature posidonia shale samples from the hils area, Germany. *Int. J. Coal Geol.* 158, 78–89. doi:10.1016/j.coal.2016.03.003

Lemmens, H. J., Butcher, A. R., and Botha, P. (2011). Fib/sem and sem/edx: A new dawn for the sem in the core lab? *Petrophysics* 52, 452–456.

Li, B., Nie, X., Cai, J., Zhou, X., Wang, C., and Han, D. (2022). U-net model for multi-component digital rock modeling of shales based on ct and qemscan images. *J. Petroleum Sci. Eng.* 216, 110734. doi:10.1016/j.petrol.2022.110734

Li, J., Jin, W., Liang, W., Wu, Q., Lu, J., and Hao, S. (2016). Quantitative evaluation of organic and inorganic pore size distribution by nmr: A case from the silurian Longmaxi Formation gas shale in fuling area, sichuan basin. *Oil Gas Geol.* 37, 129–134. doi:10.11743/ogg20160118

Li, J., Lu, J., Li, Z., Wu, Q., and Nan, Z. (2014). ’four-pore’modeling and its quantitative logging description of shale gas reservoir. *Oil Gas Geol.* 35, 266–271. doi:10.11743/ogg20140214

Liu, X. (2010). *Numerical simulation of elastic and electrical properties of rock based on digital cores[D]*. China: China University of Petroleum East China.

Liu, X., Xiong, J., and Liang, L. (2015). Investigation of pore structure and fractal characteristics of organic-rich yanchang formation shale in central China by nitrogen adsorption/desorption analysis. *J. Nat. Gas Sci. Eng.* 22, 62–72. doi:10.1016/j.jngse.2014.11.020

Liu, Y., Lu, Z., Feng, M., Wang, J., Tian, T., et al. (2017). Micro-pore characteristics of shale oil reservoirs of the shahejie formation in the dongying sag, bohai bay basin. *Acta Geol. Sin.* 91, 629–644. doi:10.7623/syxb201203011

Loucks, R. G., Reed, R. M., Ruppel, S. C., and Hammes, U. (2012). Spectrum of pore types and networks in mudrocks and a descriptive classification for matrix-related mudrock pores. *Am. Assoc. Pet. Geol. Bull.* 96, 1071–1098. doi:10.1306/08171111061

Loucks, R. G., Reed, R. M., Ruppel, S. C., and Jarvie, D. M. (2009). Morphology, genesis, and distribution of nanometer-scale pores in siliceous mudstones of the mississippian barnett shale. *J. Sediment. Res.* 79, 848–861. doi:10.2110/jsr.2009.092

Ma, H., Xia, Z., Wen, Q., and Zhang, P. (2019). Micro-pore characteristics of shale in zhanhua sag, bohai bay basin. *Petroleum Geol. Exp.* 41, 149–156. doi:10.11781/sysydz201901149

Ma, X., Guo, S., Shi, D., Zhou, Z., and Liu, G. (2019). Investigation of pore structure and fractal characteristics of marine-continental transitional shales from longtan formation using micp, gas adsorption, and nmr (guizhou, China). *Mar. Petroleum Geol.* 107, 555–571. doi:10.1016/j.marpetgeo.2019.05.018

Nie, X., Zou, C. C., Meng, X. H., Jia, S., and Wan, Y. (2016). 3d digital core modeling of shale gas reservoir rocks: A case study of conductivity model. *Nat. Gas. Geosci.* 27, 706–715. doi:10.11764/j.issn.l672-1926.2016.04.0706

Rouquerol, J., Avnir, D., Fairbridge, C. W., Everett, D. H., Haynes, J. M., Pernicone, N., et al. (1994). Recommendations for the characterization of porous solids (technical report). *Pure Appl. Chem.* 66, 1739–1758. doi:10.1351/pac199466081739

Saif, T., Lin, Q., Butcher, A. R., Bijeljic, B., and Blunt, M. J. (2017). Multi-scale multi-dimensional microstructure imaging of oil shale pyrolysis using x-ray micro-tomography, automated ultra-high resolution sem, maps mineralogy and fib-sem. *Appl. Energy* 202, 628–647. doi:10.1016/j.apenergy.2017.05.039

Sun, C. (2017). *The characteristics, formation and evolution of shale oil reservoir space in Dongying Sag[D]*. China: Nanjing University.

Sun, L., Wang, X., Jin, X., Li, J., and Wu, S. (2016). *Three dimensional characterization and quantitative connectivity analysis of micro/nano pore space*. Thailand: Petroleum Exploration and Development.

Tang, X., Jiang, Z., Jiang, S., and Li, Z. (2016). Heterogeneous nanoporosity of the silurian longmaxi formation shale gas reservoir in the sichuan basin using the qemscan, fib-sem, and nano-ct methods. *Mar. Petroleum Geol.* 78, 99–109. doi:10.1016/j.marpetgeo.2016.09.010

Tian, H., Zhang, S., Liu, S., and Zhang, H. (2012). Determination of organic-rich shale pore features by mercury injection and gas adsorption methods. *Acta Pet. Sin.* 33, 419–427. doi:10.7623/syxb201203011

Tiwari, P., Deo, M., Lin, C. L., and Miller, J. (2013). Characterization of oil shale pore structure before and after pyrolysis by using x-ray micro ct. *Fuel* 107, 547–554. doi:10.1016/j.fuel.2013.01.006

Wu, J., Jiang, Z., Tong, J., Yang, L., Li, J., and Nie, H. (2016). Sedimentary environment and control factors of fine-grained sedimentary rocks in the upper fourth member of paleogene shahejie formation, dongying sag. *Acta Pet. Sin.* 37, 464–473. doi:10.7623/syxb201604005

Wu, Y., Lin, C., Yan, W., Liu, Q., Zhao, P., and Ren, L. (2020). Pore-scale simulations of electrical and elastic properties of shale samples based on multicomponent and multiscale digital rocks. *Mar. Petroleum Geol.* 117, 104369. doi:10.1016/j.marpetgeo.2020.104369

Wu, Y., Tahmasebi, P., Lin, C., Munawar, M. J., and Cnudde, V. (2019a). Effects of micropores on geometric, topological and transport properties of pore systems for low-permeability porous media. *J. Hydrology* 575, 327–342. doi:10.1016/j.jhydrol.2019.05.014

Wu, Y., Tahmasebi, P., Lin, C., Zahid, M. A., Dong, C., Golab, A. N., et al. (2019b). A comprehensive study on geometric, topological and fractal characterizations of pore systems in low-permeability reservoirs based on sem, micp, nmr, and x-ray ct experiments. *Mar. Petroleum Geol.* 103, 12–28. doi:10.1016/j.marpetgeo.2019.02.003

Xie, T., Zhang, C., Yang, Y., Xia, X., Li, Q., Wang, X., et al. (2019). Shale pore characteristics and controls in well qian xy 1, zunyi city, guizhou province. *Petroleum Geol. Exp.* 41, 68–75. doi:10.11781/sysydz201901068

Yan, J., Fan, J., Wang, M., Li, Z., Hu, Q., and Chao, J. (2018). Rock fabric and pore structure of the shahejie sandy conglomerates from the dongying depression in the bohai bay basin, east China. *Mar. Petroleum Geol.* 97, 624–638. doi:10.1016/j.marpetgeo.2018.07.009

Yan, W., Sun, J., Golsanami, N., Li, M., Cui, L., Dong, H., et al. (2019). Evaluation of wettabilities and pores in tight oil reservoirs by a new experimental design. *Fuel* 252, 272–280. doi:10.1016/j.fuel.2019.04.130

Yao, J., Sun, H., Huang, Z., Zhang, L., Zeng, Q., Sui, H., et al. (2018). Key mechanical problems in the development of shale gas reservoirs. *Sci, Sin.-Phys. Mech. Astron.* 43, 1527–1547. doi:10.1360/132013-97

Zhang, P., Lu, S., Li, J., Xue, H., Li, W., and Zhang, P. (2017). Characterization of shale pore system: A case study of paleogene xin'gouzui Formation in the Jianghan basin, China. *Mar. Petroleum Geol.* 79, 321–334. doi:10.1016/j.marpetgeo.2016.10.014

Zhang, Y., Yu, B., Pan, Z., Hou, C., Zuo, Q., and Sun, M. (2020). Effect of thermal maturity on shale pore structure: A combined study using extracted organic matter and bulk shale from sichuan basin, China. *J. Nat. Gas Sci. Eng.* 74, 103089. doi:10.1016/j.jngse.2019.103089

Zhou, S., Liu, D., Cai, Y., Yao, Y., and Li, Z. (2017). 3d characterization and quantitative evaluation of pore-fracture networks of two Chinese coals using fib-sem tomography. *Int. J. Coal Geol.* 174, 41–54. doi:10.1016/j.coal.2017.03.008

Zhou, S., Yan, G., Xue, H., Guo, W., and Li, X. (2016). 2d and 3d nanopore characterization of gas shale in longmaxi formation based on fib-sem. *Mar. Petroleum Geol.* 73, 174–180. doi:10.1016/j.marpetgeo.2016.02.033

frontiers | Frontiers in Earth Science

TYPE Original Research
PUBLISHED 20 September 2022
DOI 10.3389/feart.2022.1016122

OPEN ACCESS

EDITED BY
Yuqi Wu,
China University of Petroleum, China

REVIEWED BY
Zhipeng Huo,
Northeastern University at Qinhuangdao, China
Hongjian Zhu,
Yanshan University, China
Jianglin He,
China Geological Survey, China
Cui Mao,
Northeast Petroleum University, China

*CORRESPONDENCE
Zhe Liu,
liuzhe@gdupt.edu.cn

SPECIALTY SECTION
This article was submitted to Solid Earth Geophysics,
a section of the journal
Frontiers in Earth Science

RECEIVED 10 August 2022
ACCEPTED 07 September 2022
PUBLISHED 20 September 2022

CITATION
Li J, Fu G, Zhu D, Cao L, Li Z, Lv Y, Li W, Hu M and Liu Z (2022), Reservoir characteristics and factors influencing shahejie marl in the shulu sag, bohai bay basin, eastern China.
Front. Earth Sci. 10:1016122.
doi: 10.3389/feart.2022.1016122

Reservoir characteristics and factors influencing shahejie marl in the shulu sag, bohai bay basin, eastern China

Jiajing Li[1,2], Guang Fu[1], Douxing Zhu[3], Lanzhu Cao[4], Zhaolong Li[5], Yanfang Lv[1], Wenke Li[6], Ming Hu[2] and Zhe Liu[2]*

[1]School of Earth Sciences, Northeast Petroleum University, Daqing, Heilongjiang, China, [2]School of Petroleum Engineering, Guangdong University of Petrochemical Technology, Maoming, Guangdong, China, [3]Geological Research Center, GRI, BGP Inc., CNPC, Zhuozhou, Hebei, China, [4]PetroChina Huabei Company, Renqiu, Hebei, China, [5]No.1 Data Acquisition Branch Company, No.1 Geo-Logging Company, Daqing Drilling and Exploration Engineering Corporation, Daqing, Heilongjiang, China, [6]The Research Institute of Petroleum Exploration and Development, Beijing, China

Shahejie marl in the Shulu Sag is a crucial resource for unconventional hydrocarbon exploration in China. Although breakthroughs have been made in tight oil exploration in this area, the mechanisms underlying the formation of this marl reservoir and factors controlling its 'sweet spots' have not been thoroughly studied. To understand the pore structure characteristics and factors influencing the marl reservoir, we analyzed core samples from Wells ST1 and ST3. A series of experiments was conducted on the samples, such as X-ray diffraction, focused ion beam scanning electron microscopy, micro-CT, and total organic carbon test. Additionally, the physical properties of different marl rock fabrics were studied with auxiliary tests, such as mercury intrusion capillary pressure analyses, nuclear magnetic resonance, porosity and permeability tests, and thin-section observation. The results revealed that the marl reservoir is characterized by low porosity (1.61%) and low permeability (2.56mD). The porosity and permeability (1.61% and 3.26mD) of laminated marl were better than those (0.92% and 1.68mD) of massive marl. Clay minerals and quartz content in laminated (11.8 and 8.2%) was less than in massive marl (16.2 and 13.3%). The marl pores include intercrystalline pores, dissolution pores, and microfractures. Additionally, the laminated marl pores were primarily distributed along the dark lamina, with good connectivity. A few isolated and uniform holes were observed in the massive marl. Influenced by rock fabric and mineral composition, layered fractures were mainly developed in the laminated marl, while structural fractures were the main type of microfractures in the massive marl. The primary sedimentary mechanism was the main geological action underlying the differences in marl rock fabric; this mechanism affects the physical properties of the marl reservoir, which are key factors to be considered when searching for the marl reservoir 'sweet spots'. Particular attention should be paid to these factors during tight oil exploration and development in similar sedimentary basins.

KEYWORDS

marl, tight reservoir, pore structure, reservoir characteristics, tight oil, shulu sag

Introduction

Tight oil, an important unconventional hydrocarbon energy resource, has attracted considerable attention from major oil companies worldwide (Jia et al., 2012a; Jia et al., 2012b; Zou et al., 2012). Since the discovery of tight hydrocarbon energy in Bakken, Eagle Beach, and other areas in the USA and North America, tight oil has emerged as an important hot spot in the oil exploration industry (He et al., 2018; James et al., 1983; Jiang and Mokhtari, 2019; Lin et al., 2011; Miller et al., 2008). Tight oil reservoirs are often characterized by low porosity and ultra-low permeability, severely restricting the pace of tight oil as well as gas exploration and development (Jia et al., 2012a; Shan et al., 2017; Hou et al., 2018; Li et al., 2022). Therefore, finding a reservoir 'sweet spot' suitable for oil and gas production is quintessential.

China has made considerable progress in the exploration of tight hydrocarbon reservoirs. A set of marlstones formed by lacustrine carbonate lime-mud and terrigenous carbonate clasts are present in the Shulu Sag, Bohai Bay Basin (Qiu et al., 2010; Zhao et al., 2015; Cui et al., 2021). The marl has a high organic matter content, large thickness, and wide dispersion. This marl is the main source of hydrocarbons, even though it is the main tight hydrocarbons reservoir (Zhao et al., 2014a). The ST1 and ST3 wells drilled in the study area yielded industrial oil flow, offering good tight oil exploration prospects (Zhao et al., 2014b). With the breakthrough of hydrocarbon exploration in the Shulu Sag marl, several notable achievements have been made in studying reservoir characteristics. For instance, a multi-dimensional lithologic classification scheme for marl was established based on rock fabric and mineral composition (Cui et al., 2015). The marl can be divided into structural, interbedded, and mixed rock and is characterized by nine lithofacies (Jiang et al., 2007; Liang et al., 2007). Furthermore, with respect to its genesis, marl can be categorized as seasonal and turbidite (Kong et al., 2020, 2016). Due to technical limitations, the reservoir spaces, reservoir properties, and factors underlying the marl-based reservoir are still unclear (Han et al., 2015; Liu et al., 2020; Liu et al., 2022a); thus, the exploration of tight hydrocarbons in the Shulu Sag remains in the preliminary stage.

Reservoir research is one of the most important steps in the exploration and development of unconventional hydrocarbon resources. However, traditional experimental methods can no longer meet the needs of tight oil and gas reservoirs in terms of microscopic pore structure, physical properties, and diagenetic mineral content. Moreover, the measurement accuracy, efficiency, and visualization of measurement results can hardly meet the needs of the industry. With the rapid development of scanning electron microscopy (SEM), graphics processing technologies, and machine learning, digital rock physics has become an important and effective means to analyze of reservoir pore microstructure and predict effective physical properties of porous media in the petroleum industry (Zhao et al., 2016; Liu and Grana, 2018; Wu et al., 2018, 2019a, 2020a, 2022a; Bordignon et al., 2019; Qian et al., 2022). The marl of the Shahejie Formation is a key horizon for tight oil exploration in the Shulu Sag; however, the processes underlying the reservoir formation, microscopic pore structure, and factors controlling the reservoir 'sweet spots' have not been rigorously studied. Here, we obtained samples from wells ST1 and ST3. SEM was used to analyze the 2D pore structure of the samples, whereas the 3D pore structure was revealed by a field emission scanning electron microscope (FE-SEM) and micro-CT measurements. Concomitantly, combined with other testing methods, such as mercury intrusion capillary pressure (MICP) analyses, total organic carbon (TOC) content analyses, X-ray diffraction (XRD), porosity and permeability tests, and thin-section observations, the oil storage capacity of marl samples differentiated along the lines of rock fabric were studied, which is essential for understanding the accumulation of tight oil in the Shulu Sag.

Geological setting

The Shulu Sag is located south of the Jizhong Depression of the Bohai Bay Basin in eastern China (Figure 1A) (Zhou et al., 2020). It is a long, narrow dustpan fault depression formed in the Paleozoic crystalline basement. The Shulu Sag is bounded by the Xinhe Fault in the east, Ningjin Uplift in the west, and the Shenxian Sag in the north through Hengshui Fault, covering an area of ~ 700 km^2 (Figure 1B; Fu et al., 2019). The Shahejie and Dongying formations of the Paleogene, the Guantao and Minghuazhen formations of the Neogene, and the Quaternary strata are developed from bottom to top in this depression (Figure 1C, Figure 2).

The Ningjin Uplift west of the Shulu Sag is an important provenance area. Under the influence of the Ningjin Uplift, carbonate conglomerate and mixed marl exist mainly in the Es_3^x members (Zhang et al., 2021). The marl is mostly formed in a semi--to-deep lake environment (Han et al., 2015; Li et al., 2016; Huo et al., 2020). In recent years, significant breakthroughs have been made in tight oil exploration in the Shulu Sag. Specifically, 20 wells have been drilled, 17 of which encountered oil and gas, and five yielded industrial oil flow. Drilling revealed that the marl is mainly distributed in the gentle slope zone and trough area of the sag. Overall, the marl is a wedge-shaped sedimentary body with thickness ranging from 100 to 1,500 m, with the greatest thickness being in the center of the sag.

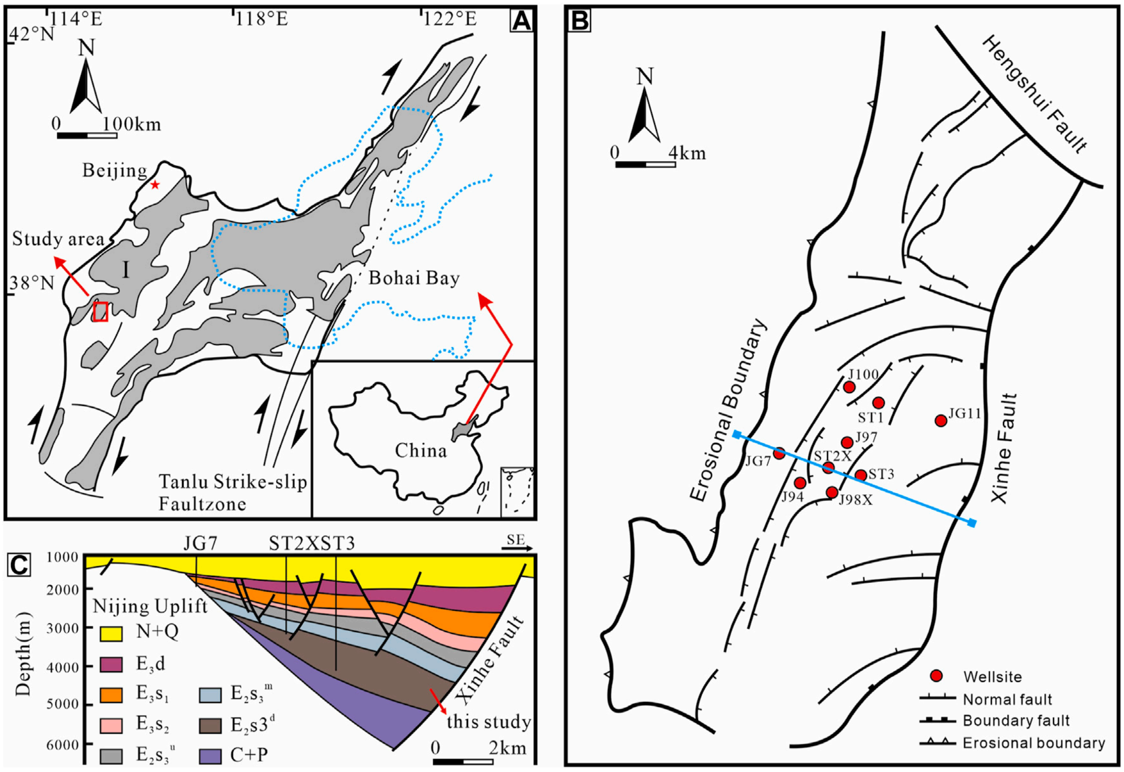

FIGURE 1
Location and structural map of the Shulu Sag: **(A)**, tectonic setting of the Shulu Sag, located in the southwestern corner of the Jizhong Depression (I); **(B)**, structural outline map of the Shulu Sag; **(C)**, transverse section across the middle segment of the Shulu Sag, the position of the section is represented as a blue line in **(B)**.

Samples and experimental methods

Sampling

More than 100 core samples were collected from wells ST1 and ST3 in the Jizhong Depression Shulu Sag (Figure 1B). All samples were chosen among the Es_3^x members. A total of 13 core samples were thoroughly studied using a variety of methodologies; specifically, these samples consisted of six and seven core samples from the laminated and massive marls, respectively. The sample information is shown in Table 1.

Experimental methods

Petrological analysis

The core samples were cut into thin pieces and examined under a polarized light microscope and a cathodoluminescence microscope, allowing the fabric of the rock to be identified.

A TTR-type XRD device was used to analyze the mineral component of core samples. Powdered samples (300 mesh size) were soaked with ethylene glycol for 8 h at 60 °C before being heated for 3 h at 550°C (Cui et al., 2021). To collect specimens, minerals were removed from the solution. Air-dried specimens were X-rayed with a diffractometer outfitted with a Cu-target Ceramic X-ray tube with emissive and receiving slits of 0.6 and 8 mm, respectively. The Rochquan+2012 program, developed by The Research Institute of Petroleum Exploration and Development (RIPED), was used to calculate the mass percentage of each mineral.

The TOC test was carried out on the samples using the LCO CS230 instrument, following the Chinese National Standard method GB/T 19145–2003 (He et al., 2018).

To identify pore types and morphologies in the samples, a Quanta 650 FE-SEM was employed. The resolution and accelerating voltage of the SEM were 1.2 nm and 30 kV (Zhang et al., 2020), respectively.

Porosity and permeability measurements

Porosity and permeability tests were outsourced at PetroChina Huabei Oilfield Company. Core plugs with a diameter of 2.5 cm and length of 5 cm were drilled from the

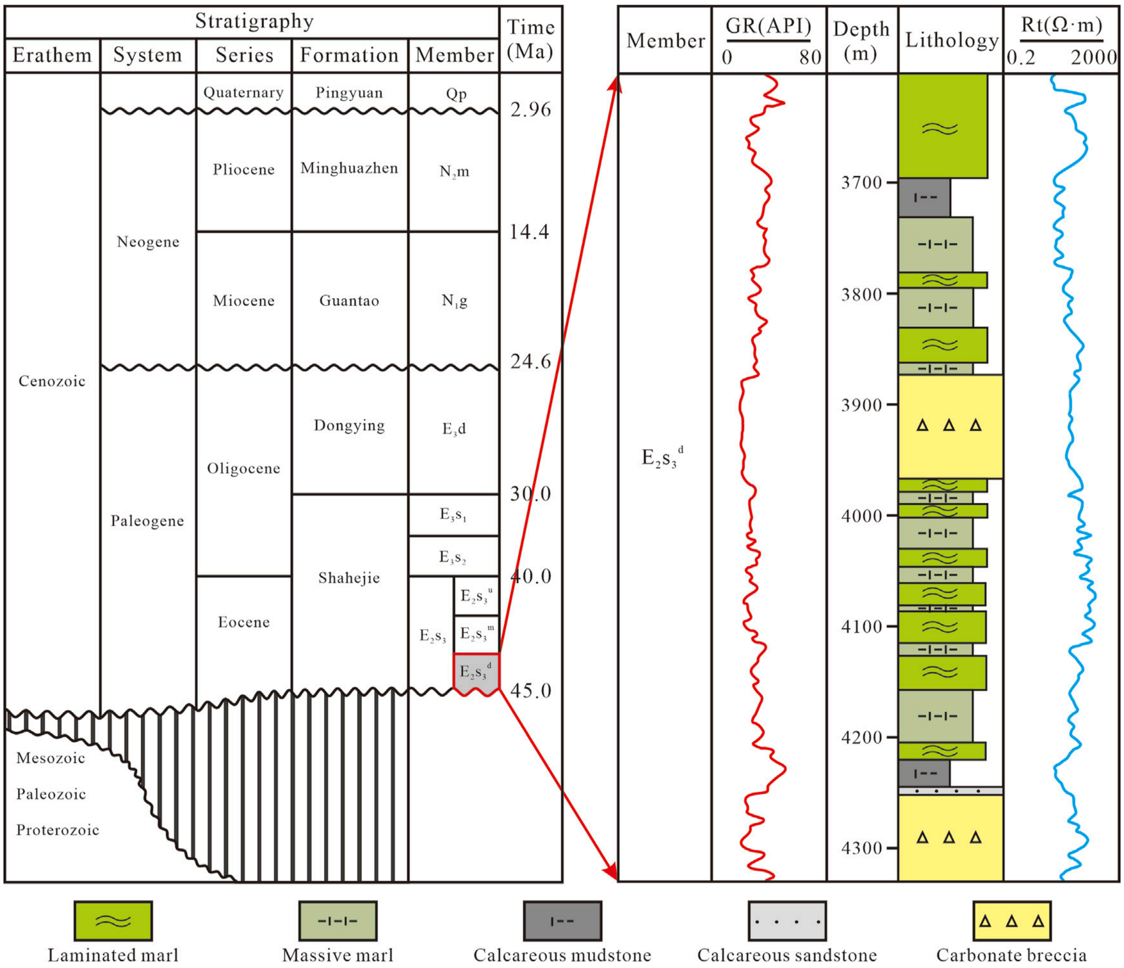

FIGURE 2
Stratigraphic systems of the Shulu Sag.

massive and laminated marl. Using Boyle's law, the porosity of core samples was measured using Ultra-pore 200A and the He permeability of core samples was measured using Ultra-perm TM200. The core plug was cleaned in benzene and alcohol for 1 month to remove residual oil, dried, and finally analyzed for petrophysical properties. The test methods were conducted per the Chinese National Standard method SY/T5336-2006 (Zhang et al., 2018).

Pore-throat structure analysis

Thirteen core plugs (25 × 25 mm) were subjected to MICP analysis with the Auto Pore IV equipment at the State Key Laboratory of China University of Petroleum (Beijing) to assess the pore architecture and pore throat distribution. A throat radius of 6 nm corresponds to a mercury intrusion pressure maximum of 200 MPa. The test premise for the experiment was SY/T5346-2005/4, and conditions were 18°C (room temperature) and 55% humidity (Zhang et al., 2020). The injection curves and other data were acquired to assess the properties of pore-throat structures.

Under 100% water saturation, the nuclear magnetic resonance (NMR) T_2 spectrum of each core sample was produced using the NUMAG's C12-010 V low-field NMR spectrometer. The three-dimensional pictures of nano- and micron-scale pores were characterized using CT scanning technology (Wu et al., 2020b, 2020c; Liu et al., 2022b; Guo et al., 2022; Liu et al., 2022), which facilitated the analysis of the marl micropores and their three-dimensional connectivity. An Ultra XRM-L200 microscope was used to perform a three-dimensional CT scan of the full-diameter core samples (XRM). The equipment included a 150 kV/15 W high-power focus X-ray tube with a maximum resolution of 1.0 µm. Cylindrical core samples were mounted vertically onto the sample holder to ensure a central field of view for the scanner. Each sample was scanned using a conical ion beam emitted from the X-ray

TABLE 1 Mineral composition, total organic carbon, and porosity of the samples from well ST1.

Sample ID	Rock type	Depth/m	Rock mineral composition (wt%)						TOC (%)	Porosity (%)
			Clay	Quartz	Calcite	Dolomite	Feldspar	Pyrite		
LM1	Laminated marl	3678.1	16.95	11.10	57.95	11.84	0.00	2.15	1.2	1.8
LM2		3789.5	9.86	5.92	70.01	12.16	1.24	0.80	1.1	0.9
LM3		3850.4	10.92	3.81	74.24	9.62	0.00	1.41	0.6	0.9
LM4		3975.3	13.99	18.82	46.32	12.59	1.23	7.05	0.2	1.1
LM5		4001.2	7.96	3.81	81.01	5.50	0.00	1.72	1.8	1.5
LM6		4048.6	7.96	8.04	66.42	16.50	0.00	1.09	1.9	1.4
LM7		4152.3	13.78	8.35	65.78	10.36	0.00	1.72	2.1	0.8
LM8		4220.5	13.04	5.92	37.86	37.02	0.00	6.17	1.5	1.1
MM1	Massive marl	3721.5	15.00	22.98	45.12	15.84	0.00	1.05	1.4	1.4
MM2		3768.3	14.81	7.18	64.81	11.21	0.00	1.99	1.5	0.7
MM3		3818.4	18.96	8.65	52.45	16.84	0.00	3.10	0.8	0.8
MM4		3875.3	34.81	13.21	37.78	8.10	2.14	3.98	1.4	0.9
MM5		3985.6	17.13	24.45	37.50	19.00	0.74	1.19	0.7	1.0
MM6		4015.7	12.88	16.82	61.24	6.98	0.95	1.14	1.2	1.7
MM7		4064.1	8.92	10.93	35.09	45.07	0.00	0.00	2.3	1.0
MM8		4089.4	5.05	9.81	34.00	49.92	0.00	1.22	2.6	1.1
MM9		4122.1	8.14	6.54	69.12	15.04	0.00	1.15	1.9	1.3
MM10		4174.6	11.81	7.16	64.98	14.06	0.00	1.99	1.4	0.6
MM11		4236.2	30.89	18.10	31.90	17.18	0.74	1.19	1.8	1.1

source. The X-ray intensity was attenuated as it passed through the sample, and these signals were recorded by the detector. Samples were rotated and scanned at different angles, yielding a 360° perspective. The NMR experiment and CT scans were conducted in RIPED.

Results

Petrographical characteristics and oil-bearing properties

In this study, the rock fabric of the marl was divided into laminated and massive marl to facilitate a structured discussion of the entire tight marl reservoir (Fu et al., 2019). The rhythmic layer consisting of alternating laminae was observed microscopically (Figure 3). The bright lamina was mainly of chemical precipitation origin, and the mineral composition mainly consisted of micritic and microcrystalline calcite and dolomite, with an orange-red cathode luminescence (Figures 3B,D,F). The dark lamina was mainly of mechanical deposition origin, and the mineral composition primarily consisted of, micritic calcite and dolomite, argillaceous, carbonate sand, quartz, organic matter, and pyrite. The cathode luminescence color was dark and scattered (Figures 3B,D,F). Laminated marl was deposited by interbedded mixing. The laminae of laminated marl were mainly in three forms: 1) Thin dark gray mudstone and light micritic limestone interbedded in unequal thickness, with parallel or non-parallel laminae boundaries (Figures 3A,B). These were formed in a still-water environment with few terrigenous materials, mainly carbonate water deposits. 2) Continental clay-bearing calcitic mudstone interbedded with micritic limestone with or without mud, and thin silt-fine sandstone interbeds that commonly occur (interbedded intercalation) with parallel lamination boundaries (Figures 3C,D). This mudstone was formed in the offshore deep-water areas or terrigenous deep-water environments with sufficient intermittent supply. 3) A grain boundary clear wavy grain layer (Figures 3E,F) formed on steep slopes, resulting in deposit layers that were not consolidated, due to slope sliding deformation dynamics. The massive marl was mainly formed through mixed structural deposition and was divided into terrigenous and endogenous components. The former component, containing argillaceous and carbonate rock of terrigenous clastic rich in organic matter (mainly consisting of calcite), was prioritized. This component also contained a bit of quartz, feldspar, and other terrigenous clastic material, occasionally interspersed with unevenly distributed granular pyrite unevenly distributed within (Figure 3G); the cathode luminescence was distorted and dark (Figure 3H). The latter component primarily contained *in situ* sedimentary micritic calcite, with only a little terrigenous carbonate arene, quartz,

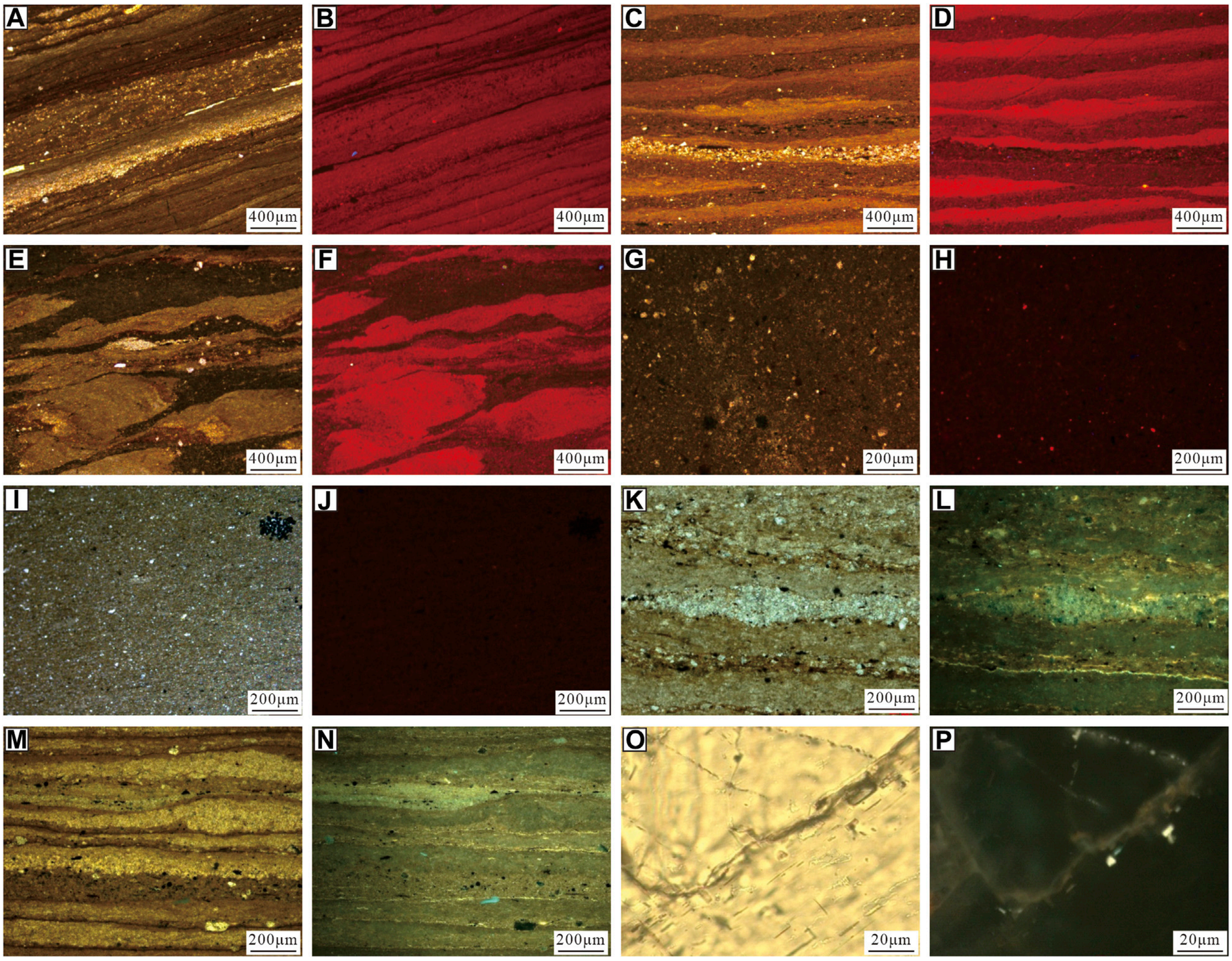

FIGURE 3
Petrographic characteristics of marl reservoir under single polarization **(A,C,E,G,I,K,M,O)**, cathode luminescence **(B,D,F,H,J)**, and fluorescence microscopy **(L,N,P)**: **(A,B)**, laminated marl with different lamina thickness, ST3, 3,664.9 m; **(C,D)**, laminated marl of equal lamina thickness, ST3, 3,681.49 m; **(E,F)**, wavy laminated marl, ST3, 3,677.61 m; **(G,H)**, terrigenous massive marl, ST3, 3,817.65 m; **(I,J)**, endogenous massive marl, ST3, 4097.06 m; **(K,L)**, laminated marl of mechanical origin, ST3, 3,978.76 m; **(M,N)**, laminated marl of chemical origin, ST3, 3,675.09 m; **(O,P)**, massive marl, ST3, 3,983.83 m.

feldspar, and clay minerals (Figure 3I); this component exhibited orange cathodoluminescence that was relatively homogenous (Figure 3J).

The thin fluorescent thin section shows that the lamina of mechanical deposition was oil-bearing in the laminated marl. Crude oil molecules were distributed along the lamina in a banded and non-uniform manner (Figure 3K, Figure 3L). The occurrence of crude oil molecules was characterized by oil in various matrix micropores, oil in lamina cracks, and adsorption of organic matter bands. The micritic limestone lamina of chemical sedimentary origin contained less oil, and crude oil molecules were evenly distributed (Figure 3M, Figure 3N). The massive marl crude oil was mainly enriched in matrix pores or structural fractures (Figure 3O, Figure 3P). In terms of oil enrichment and oil content, the oil-bearing properties of laminated marl were better than those of massive marl.

As shown in Table 1, the minerals in the marl in the Shulu Sag included calcite, dolomite, clay minerals, quartz, pyrite, and feldspar. In terms of mineral composition, laminated and massive marl mainly consisted of calcite and dolomite. The average content of calcite and dolomite in laminated marl was 62.4 and 14.4%, respectively (Figure 4A); the average content of these two minerals in massive marl was 48.5 and 19.9%, respectively (Figure 4B). The contents of clay minerals and quartz were 11.8 and 8.2%, in laminated marl and 16.2 and 13.3%, in massive marl, respectively. The average pyrite content in laminated and massive marl was 2.8 and 1.6%, respectively, while the marl of these two fabrics contained little to no feldspar.

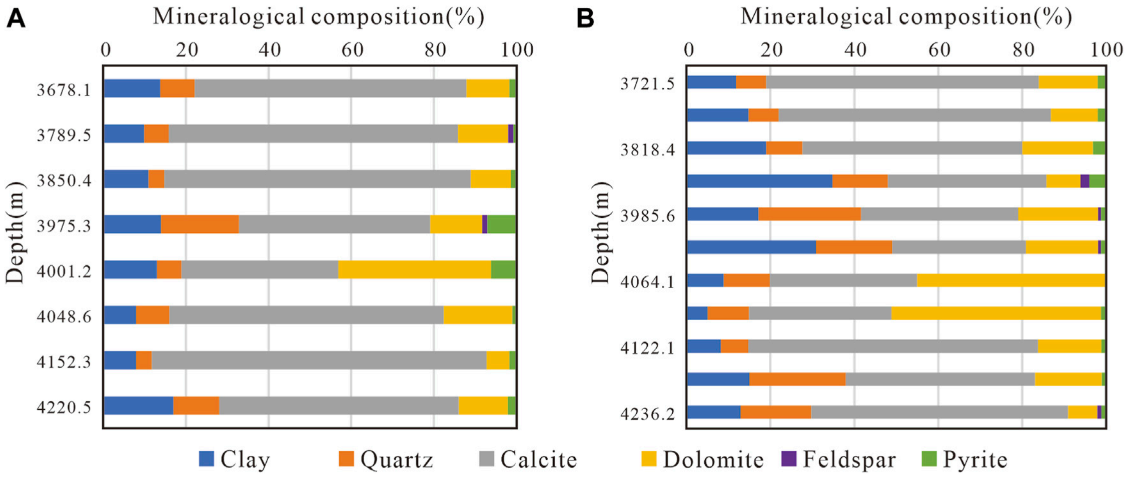

FIGURE 4
Bar chart of mineral components in marl reservoir: **(A)** mineral composition of the laminated marl reservoir; **(B)** mineral composition of the massive marl reservoir.

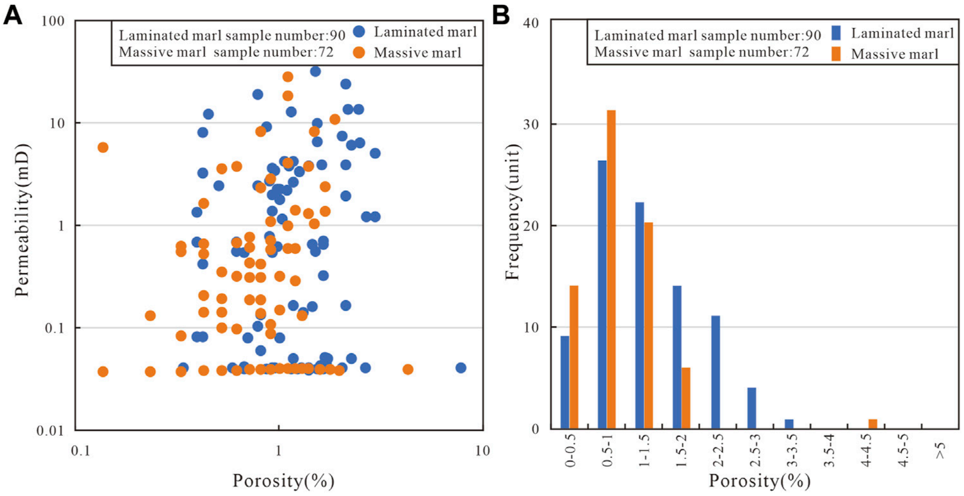

FIGURE 5
Marl reservoir porosity distribution and the porosity-permeability relationship of Shahejie Formation in the Shulu Sag: **(A)**, the relationship between porosity and permeability; **(B)**, reservoir porosity distributions showing the porosity variation mainly in the range of 0–2.5%.

Petrophysical properties

Helium porosity measured in the laboratory represents the connected porosity of rock samples. Laboratory helium porosity tests show that the porosity of laminated marl was slightly higher than that of massive marl (Figure 5A). The porosity of marl ranged from 0.34 to 13.19%, with an average of 1.61% (Figure 5A), mostly varying in the range of 0–2.5% (Figure 5B). The porosity of laminated marl ranged from 0.34 to 13.19%, with an average of 1.61%. The porosity of massive marl ranged from 0.14 to 4.31%, with an average of 0.92% (Figure 5A). Laboratory permeability tests showed that the average permeability of marl was 2.56mD, and the permeability of laminated and massive marl was relatively small. The average permeability of the former was 3.26 mD, and that of the latter was 1.68 mD. A non-functional relationship between porosity and permeability was noted (Figure 5A).

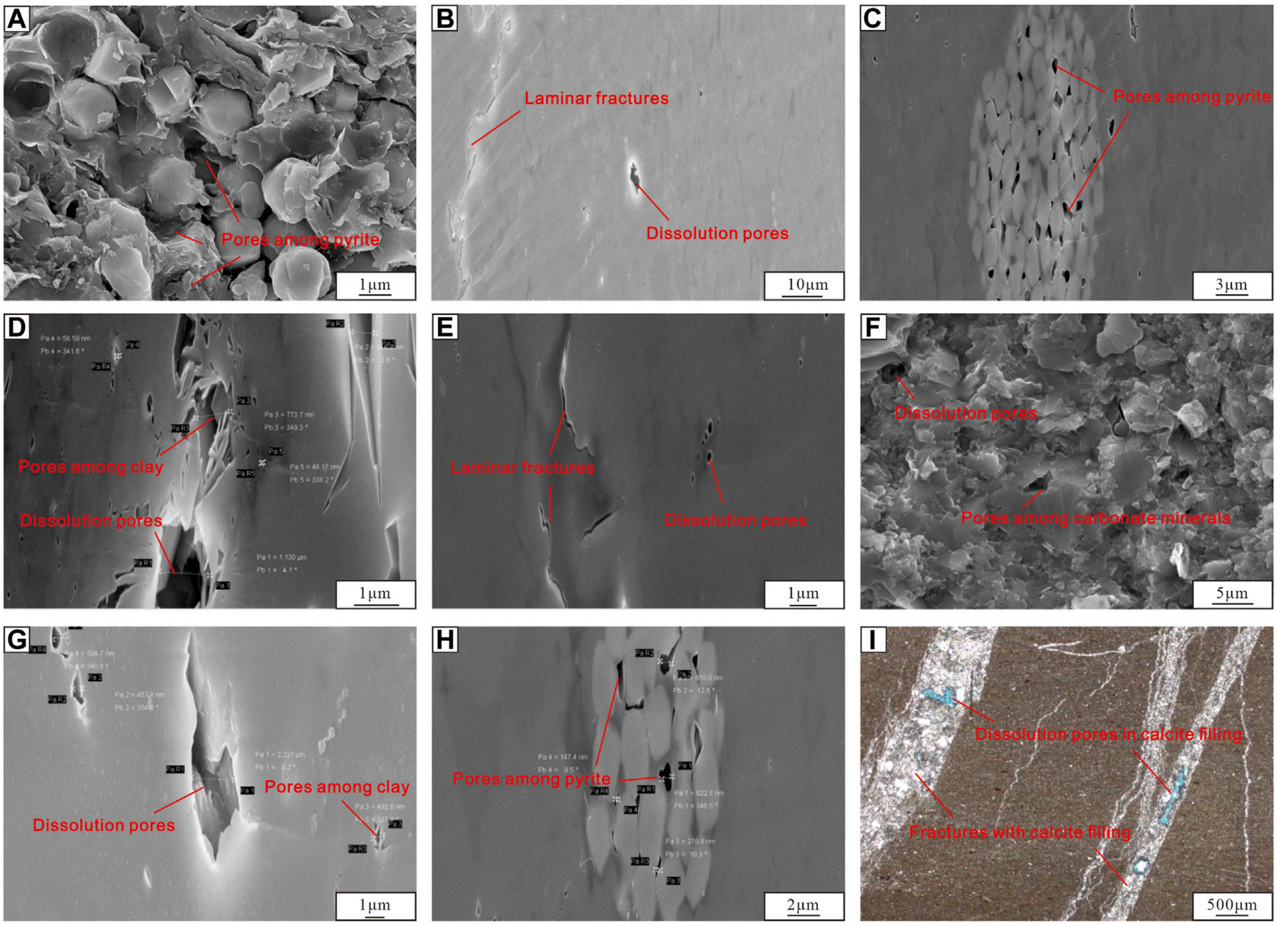

FIGURE 6
Typical pore types found in marl reservoir in the Shulu Sag: **(A)**, intercrystalline pores of pyrite in laminated marl with SEM observation, ST3, 3,670 m; **(B)**, laminar fractures and dissolution pores associated with organic bands in laminated marl, ST3, 3,670.89 m; **(C)**, intercrystalline pores of pyrite in laminated marl, ST3, 3,677.05 m; **(D)**, intercrystalline pores of clay minerals in laminated marl, ST3, 3,978.76 m; **(E)**, nanoscale bedding micro-cracks and dissolution pores in laminated marl, ST3, 3,981.93 m; **(F)**, intercrystalline pores in the massive marl, ST3, 3,999.38 m; **(G)**, dissolution pores and intercrystalline pores of clay minerals in the massive marl, ST3, 3,817.65 m; **(H)**, intercrystalline pores of pyrite in the massive marl, ST3, 3,817.65 m; **(I)**, local dissolution pores occur in calcite, filling in fractures and pore spaces, and they primarily occur concurrently with structural fractures, ST3, 3,983.83 m.

Pore type and pore structure

Based on castings of thin sections and FE-SEM, three types of pores were identified in the marl reservoir. The pores include intercrystalline pores, dissolution pores, and microfractures (Figure 6).

Intercrystalline pores mainly exist between carbonate minerals (Figure 6F), clay minerals (Figures 6D,G), and pyrite (Figures 6C,H). The intercrystalline pore diameter of clay minerals was the largest, and that of carbonate minerals was the smallest. The intercrystalline pore morphology was mainly elongated, curved, and irregular. Intercrystalline pores among pyrite are formed in strawberry pyrite aggregates deposited in a reducing environment. The intercrystalline pore diameters of pyrite in laminated marl were 45–1,185 nm, with a variation range slightly larger than that of massive marl (60–985 nm). The intercrystalline pores among clay minerals were formed during the dehydration transformation process. The intercrystalline pores in marl clay were both nanometer and micron pores. The intercrystalline pores among clay minerals in laminated marl were 90–1815 nm, slightly smaller than those in massive marl (107–2,860 nm). The intercrystalline pore diameters of carbonate minerals in laminated marl were 20–540 nm, slightly larger than those of massive marl (13–125 nm) (Figure 7).

Dissolution pores were widely present in marl reservoirs and were usually densely distributed (Figures 6B,E,G,I). The shape of the dissolution pores was mostly circular, elliptical elongated, or irregular, with the long axis laying along the bedding direction. The Es3 was an important source rock in the Shulu Sag (Huo et al., 2020); thus, the formation of dissolution pores was mainly

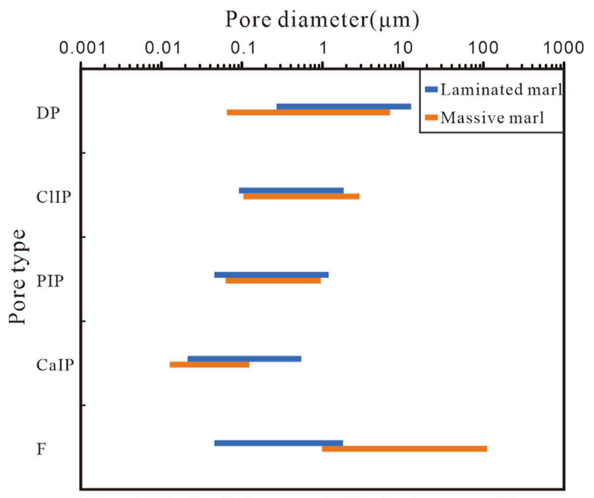

Where, DP is dissolution pore; ClIP is clay intercrystalline pores; PIP is pyrite intercrystalline pores; CaIP is carbonate intercrystalline pores; F is fractures

FIGURE 7
Pore diameters distribution range of different types of marl reservoir in the Shulu Sag.

related to organic acid dissolution in the early stage of hydrocarbon generation (Zhou et al., 2020). The dissolution pores appeared to be circular, elliptical elongated, or irregular. The long axis of the dissolution hole was parallel to the bedding direction (Figure 6B). The dissolution pores of the marl reservoir were mainly nanometer pores, with a certain amount of micron pores. The range of dissolution pores of laminated marl was 260 nm–12.2 μm, significantly larger than that of massive marl at 60 nm–7.1 μm (Figure 7).

The microfractures in the marl reservoir can be divided into laminar and structural fractures (Figures 6B,E). Laminar fractures were mainly formed in the laminar marl. Noticeably, due to the difference in mineral composition and sedimentary mode, laminar fractures were easily formed in the diagenetic process of the laminar marl. Laminar slit widths ranged from 45 to 1860 nm, mainly on the nanometer scale, with a small amount of micron-scale. Under the action of regional tectonic stress, marl with a high brittle mineral content easily produced structural fractures (Figure 6I). The filling material of the structural fractures was mainly calcite. Secondary dissolved pores were also found in calcite veins (Figure 6I). The width of structural fractures ranged from 1 to 11 μm, mainly on the micron scale (Figure 7).

Pore-throat size distribution

The MICP test results of the nine marl samples are shown in Figure 8. The mercury injection curve of laminated marl was characterized by a lower displacement pressure, higher mercury saturation, and higher mercury withdrawal rate. The capillary pressure curve showed a double-step characteristic (Figure 8A). The results show that the pore-throat structure of laminated marl was complex, and the micron and nanometer scale pores were well-developed (Figure 8B). The laminated marl was characterized by a double porosity medium of lamination fracture-pore.

Compared with the laminated marl, the mercury injection curve of the massive marl exhibited higher displacement pressure, lower mercury intake saturation, and mercury withdrawal rate for the massive marl. The ‘single step’ characteristic of the capillary pressure curve was noticeable (Figure 8C). The results revealed that the massive marl reservoir exhibited poor pore connectivity, mainly nanoscale-pores (Figure 8D), which were not conducive to fluid flow.

The marl comprehensive pore distribution can be reflected by the NMR T_2 spectrum (Wu et al., 2021; Zhao et al., 2022). The T_2 spectrum of laminated marl revealed clear bimodal characteristics (Figure 9A), and the right peak was more noticeable, indicating that laminated marl developed not only nanometer micropores but also a certain amount of micrometer macropores. The massive marl showed a single-peak T_2 spectrum (Figure 9B), with the main peak on the left, indicating that nanometer micropores dominated the massive marl, with a few micrometer pores.

In the micro-CT scanning experiment, the greater resolution allowed for a detailed understanding of the size of material components (Wu et al., 2019b, 2020d; Wu et al., 2020e; Wu et al., 2022b). The small pixels were identified as a set of large pixels. Therefore, the connected pores could be identified as macro pore aggregates. A micro-CT scan showed that the laminated marl pores were mainly distributed along the dark lamina with good connectivity (Figure 10A). The massive marl had fewer pores, which were isolated and uniform (Figure 10B).

Discussion

Influence of original sedimentary environment on reservoir quality

The physical properties of the reservoir are mainly affected by the original sedimentary and diagenetic processes (Liu et al., 2016; Zhu et al., 2017; Lu and Liu, 2021), among which, the sedimentary mechanism was the most important. Specifically, the original sedimentary environment and mechanism determine the material basis of the reservoir, while the subsequent geological processes only modify it.

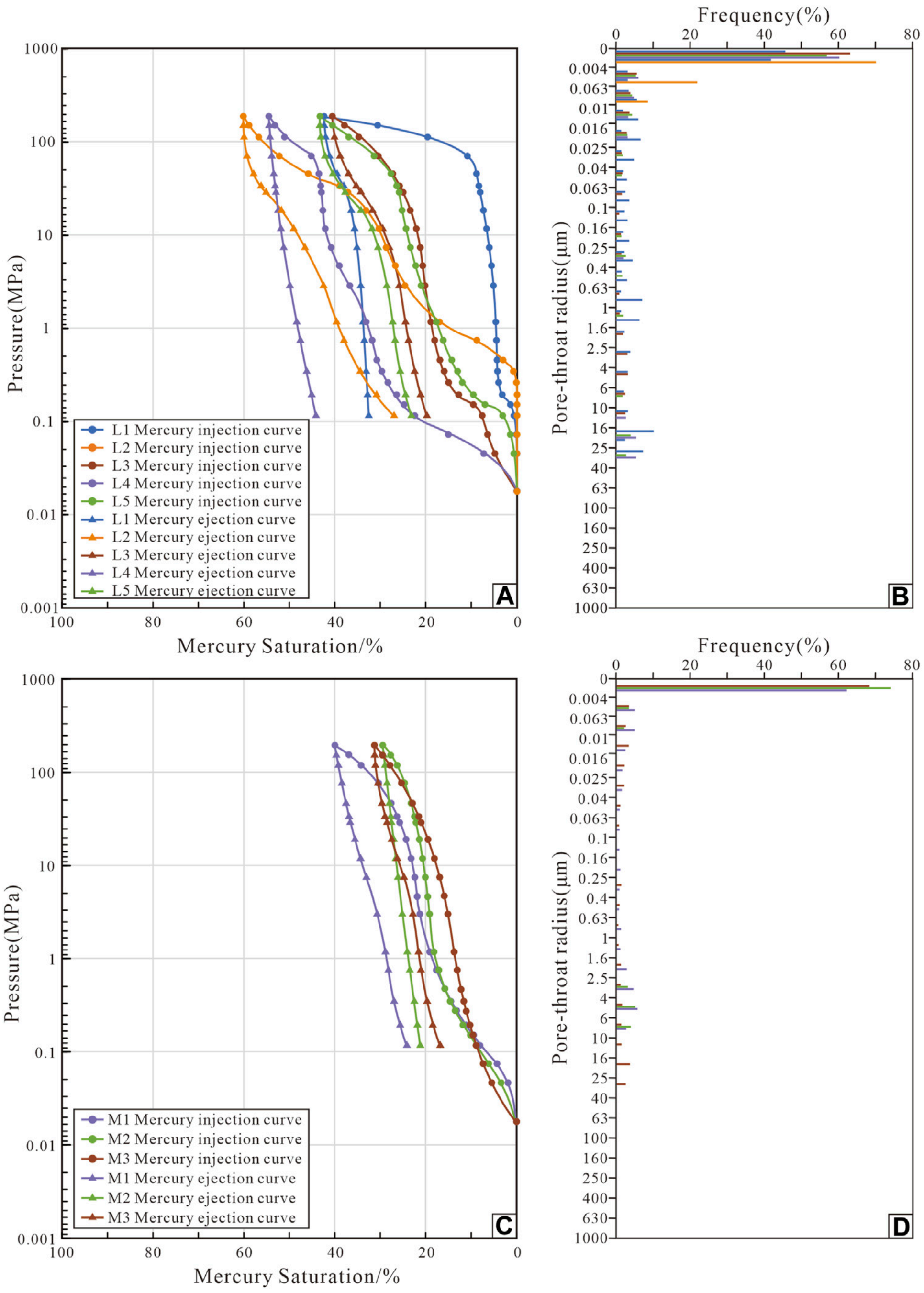

FIGURE 8
Intrusion-extrusion curves and pore size distribution by mercury intrusion capillary pressure (MICP) experiments for tight marl samples in the Shahejie Formation in the Shulu Sag: **(A,B)**, laminated marl reservoir; **(C,D)**, massive marl reservoir.

The sedimentary environment of the lower E_2s_3 strata in the Shulu Sag is characterized by shallow to deep lake subfacies. From the sag slope to the trough area, the water gradually deepened. This sedimentary environment determined the marl of the stratum under E_2s_3, characterized by abundant organic matter enrichment. Drilling confirmed that the thickness of marl in the study area exceeded 1,200 m (Zhao et al., 2014a), providing an ideal environment for the marl to function as a reservoir in the study area.

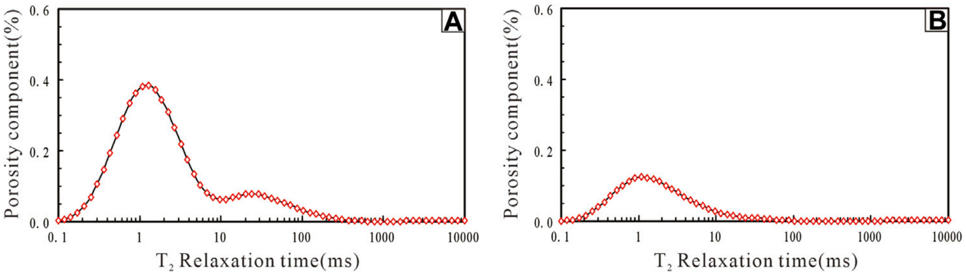

FIGURE 9
The saturated NMR T_2 spectra of marl: **(A)**, laminated marl, ST1, 4257 m; **(B)**, massive marl, ST1, 4263 m.

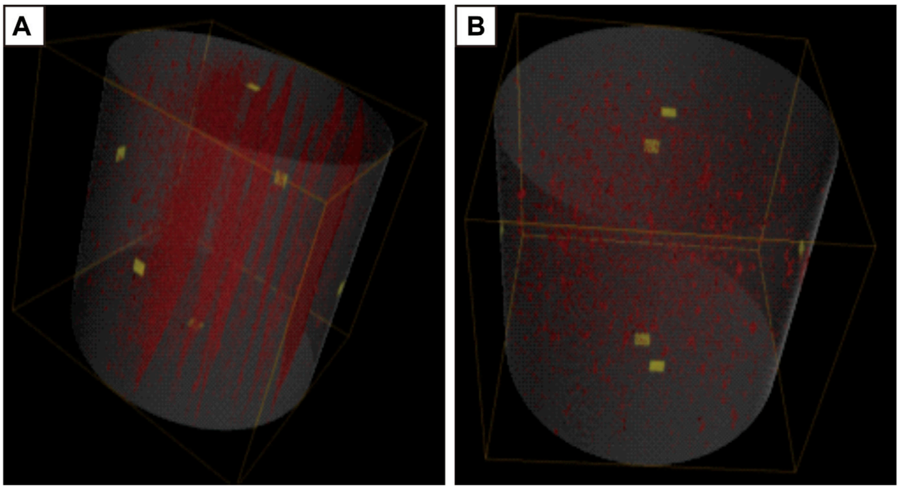

FIGURE 10
Micro-CT showing the 3D pore and connectivity in the marl reservoir: **(A)**, laminated marl, ST3, 3,670.89 m; **(B)**, massive marl, ST3, 3,817.65 m.

The laminated marl in the Shulu Sag is mainly a rhythmic lamination affected by seasonal factors (Fu et al., 2019). The seasonal rhythmic laminae have an apparent binary structure, which consists of chemically deposited carbonate minerals and clastic grains stemming from physical deposition. Laminated marl mainly occurs in shallow and semi-deep lakes near the provenance. The laminated marl had a large pore space, good horizontal connectivity, and its organic matter exhibited continuous distribution in a large area, rendering it an ideal reservoir for oil and gas enrichment (Figure 3L, Figure 3N).

During the formation of the massive marl near the provenance, terrigenous clasts were formed in the sediments. These clasts are rich in organic matter and have the potential for hydrocarbon generation. However, when the massive marl was formed away from the provenance, the carbonate rocks primarily experienced *in situ* chemical deposition.

Influence of rock composition on reservoir quality

Quartz

The presence and content of quartz minerals in marl reportedly affect the pore type and structure (Zhu et al., 2022). The cross plot of quartz content and total porosity reveals a positive correlation between quartz content and total porosity (Figure 11A). The compaction of hard quartz minerals is good for pore preservation, resulting in the development of several intercrystalline pores (Figures 6A,F) in marl reservoirs. Compared with laminated marl, the quartz content in massive marl was expectedly higher, explaining why the massive marl is more likely to produce structural fractures than laminated marl. Influenced by the sedimentary environment of the deep and semi-deep lake, the supply of terry-derived material is limited, and the quartz

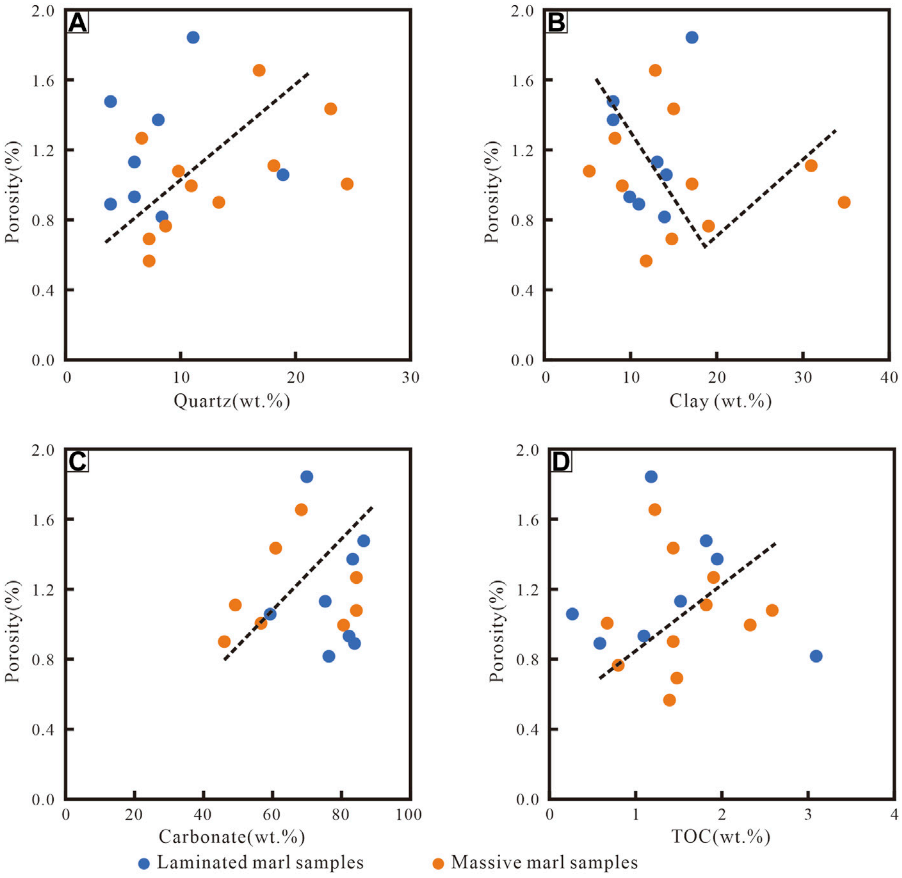

FIGURE 11
Relationships between the material composition and porosity of the marl samples from the ST1, Shulu Sag: **(A)**, relationship between quartz content and total porosity; **(B)**, relationship between clay content and total porosity; **(C)**, relationship between carbonate content and total porosity; **(D)**, relationship between TOC content and total porosity.

content in marl is relatively modest, generally ranging from 5 to 25%.

Clay

With the increase in clay mineral content, the total porosity of marl first decreased first and then increased (Figure 11B). When the content of clay minerals was low, the clay minerals were more plastic and tended to seal intercrystalline pores of carbonate minerals under compaction, resulting in the underdevelopment and poor continuity of nano-pores. Therefore, clay mineral content inversely correlated with the total porosity. As the content of clay minerals increased, they absorbed a great amount of organic matter, which was conducive to the development of dissolution pores in hydrocarbon generation and acid discharge. In addition, intercrystalline pores of clay minerals were formed in large quantities and had good connectivity. Therefore, when the clay mineral content exceeded a certain amount, it positively correlated with the total porosity. This threshold was approximately 15% in laminated marl 20% in massive marl. Nevertheless, it is essential to note that marl porosity does not increase indefinitely as the mud content continues to increase beyond this threshold due to the influence of marl rock skeleton and organic acid production.

Carbonate minerals

The marl is rich in carbonate minerals; its content generally ranges of 50–90%. Carbonate minerals are an important determinant of total porosity; and these two elements show a positive correlation in the cross plot (Figure 11C). The existence of carbonate minerals is conducive to the subsequent formation of dissolution pores (Figures 6B,E,G). In addition, the brittle carbonate minerals tended to produce fractures under the action of tectonic stress, increasing pore connectivity (Figure 6I).

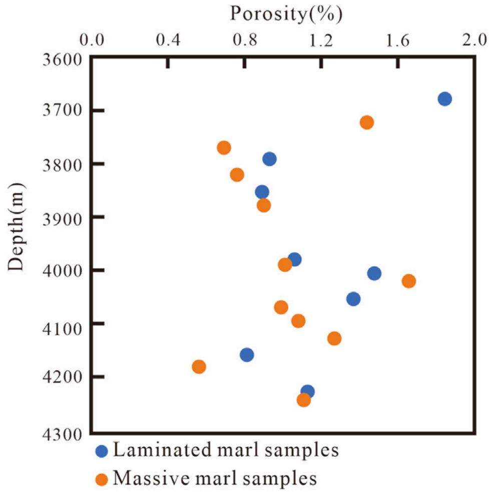

FIGURE 12
Relationship between depth and total porosity of the marl samples from the ST1, Shulu Sag.

TOC

The marl in the study area is an important source of rock that is rich in organic matter and exhibits self-generation and self-storage (Huo et al., 2020). Previous studies showed that TOC content in marl increased significantly from shallow lake subfacies to deep lake subfacies (Zhao et al., 2015). In this study, TOC content was mainly distributed in the range of 1–4%. In the process of hydrocarbon generation, the organic acids associated with marl rich in organic matter catalyze dissolution, directly leading to the formation of dissolution pores. Therefore, TOC content in marl was positively correlated with total porosity (Figure 11D).

Influence of diagenesis and tectonism on reservoir quality

Diagenesis shapes the porosity and permeability of sedimentary basins (Rahman and Worden, 2016; Wang et al., 2021; Du et al., 2022). During the diagenetic process of marl, compaction, cementation, and dissolution are the key geological processes driving the formation and development of marl reservoir space. Moreover, regional and local post-diagenetic tectonism is critical for reservoir transformation.

Compaction

Under compaction, burial depth and the porosity of the clastic reservoir are inversely correlated (Zhu et al., 2019a; Zhang et al., 2020). However, the porosity of the marl reservoir did not decrease with increasing depth (Figure 12), mainly because marl is different from a clastic rock; in the early diagenetic stage, many primary intercrystalline pores are cemented and filled, and in the subsequent deep burial stage, burial depth compaction has little influence on reservoir porosity. Simultaneously, as a large amount of organic matter in marl gradually reaches maturity, it generates hydrocarbon and organic acids. Finally, large dissolution pores are formed, translating to an increased porosity in the marl.

Dissolution

Dissolution significantly improves the quality of the marl reservoir (Yang et al., 2022). SEM revealed the widespread dissolution pores with large diameters (Figures 6B,E,G,I). Dissolution mainly occurs in the margins and interiors of calcite, dolomite, and clay minerals. Dissolution pores are generally elliptic or elongated, irregularly shaped with the long axis parallel to the bedding direction. As mentioned above, dissolution pores in laminated marl were mainly nanoscale pores with a certain amount of micron-scale pores developed along the bedding direction. In this case, the mercury injection curve showed double-step features (Figure 8A), and the T_2 spectrum revealed a double peak (Figure 9A). Dissolution pores are formed in marl under the action of acids, leading to a spatial fracture network characterized by smooth fluid flow and improved reservoir quality.

Tectonism

Marl is rich in brittle carbonate minerals. The content of brittle minerals was higher in massive marl, than in laminated marl. Marl, especially massive marl, is prone to produce structural fractures under regional tectonic stress. The diameter of structural fractures was usually 1-2 orders of magnitude larger than the pore diameter (Figure 7). Of note, the structure fracture had higher porosity than the pores (Figure 6I), significantly improving the physical properties of the marl reservoir (Kong et al., 2019). After the marl diagenesis, Shulu Sag underwent many tectonic movements, and many faults were formed (Zhao et al., 2015; Zhu et al., 2018; Zhu et al., 2019b; Zhu et al., 2020; He et al., 2022). The vicinity of these faults tended to be characterized by a concentration of stress, which was conducive to the occurrence of microfractures associated with faults, which played a key role in improving the physical features of the reservoir. The analysis of the physical properties of marl showed that the permeability of massive marl exceeded 10mD due to structural fractures. However, the permeability was mainly in the range of 0.1-1mD in the absence of structural fractures (Figure 5A). In laminated marl, most fractures were laminated fractures (Figures

3A,C,E), which can also improve the permeability of laminated marl (Figure 5A).

Conclusion

1) The mineral content of laminated and massive marl differed. The calcite content of laminated marl was higher than that of massive marl, while the content of dolomite, clay minerals, and quartz was lower in laminated marl than in massive marl. The two marl fabrics contained little or no feldspar.
2) Three types of pores were developed in the marl reservoir of Shulu Sag, namely, intercrystalline pores, dissolution pores, and microfractures. The intercrystalline and dissolution pores of laminated marl were slightly larger than those of massive marl. Lamellar fractures were formed mainly in laminated marl, whereas microfractures were primarily associated with massive marl and were prone to calcite filling.
3) Laminated marl presented better physical property than massive marl. The micron and nanometer pores of laminated marl were well-developed with lamellar fissures and pores, as well as good connectivity. However, the massive marl reservoir had poor pore connectivity and was dominated by nanoscale pores, not conducive to fluid flow. The massive marl presented a few isolated and uniform holes.
4) The physical properties of the marl reservoir in Shulu Sag were mainly driven by sedimentation and diagenesis. Seasonal factors and the relationship with the provenance location were the main drivers of physical differentiation between laminated and massive marl reservoirs. In addition, the high quartz content and TOC were conducive to the formation of 'sweet spot' reservoirs. Compaction depth was beneficial to hydrocarbon generation and the acid discharge of organic matter to improve reservoir quality. Dissolution and tectonism shaped the construction of reservoirs.

Data availability statement

The original contributions presented in the study are included in the article/Supplementary Material, further inquiries can be directed to the corresponding author.

Author contributions

JL: investigation, methodology, writing—original draft, and data analysis. GF: supervision and writing—review and editing. DZ: writing—review and editing. LC: writing—original draft and processing the data. ZlL: writing—review and editing. YL: supervision and writing—review and editing. WL: methodology—original draft. MH: methodology—review and editing. ZeL: writing—review and editing.

Funding

This work was supported by the National Natural Science Foundation of China (41602154), CNPC Innovation Foundation (2015D-5006-0103), and Projects of Talents Recruitment of GDUPT (2018rc01).

Acknowledgments

Special thanks go to Zhanwen Yu from PetroChina Huabei Company. His constructive suggestions and manuscript review positively influenced this research and article writing.

Conflict of interest

DZ was employed by the Company BGP Inc.

LC was employed by the PetroChina Huabei Company.

ZL was employed by the Data Acquisition Branch and Geo-Logging Company.

The remaining authors declare that the research was conducted in the absence of any commercial or financial relationships that could be construed as a potential conflict of interest.

The reviewer CM declared a shared affiliation with the authors GF and YL to the handling editor at the time of review.

Publisher's note

Supplementary material

The Supplementary Material for this article can be found online at: https://www.frontiersin.org/articles/10.3389/feart.2022.1016122/full#supplementary-material

References

Bordignon, F., Figueiredo, L. D., Exterkoetter, R., Rodrigues, B., and Duarte, M. (2019). "Deep learning for grain size and porosity distributions estimation on micro-CT images," in *Proceedings of the 16th international congress of the Brazilian geophysical Society&Expogef (Radiology)* (Rio de Janeiro: SBGf - Sociedade Brasileira de Geofísica). doi:10.22564/16cisbgf2019.209

Cui, J., Yuan, X., Wu, S., Zhang, R., Jin, S., and Li, Y. (2021). Rock types and reservoir characteristics of shahejie formation marl in shulu sag, jizhong depression, bohai bay basin. *J. Earth Sci.* 32 (4), 986–997. doi:10.1007/s12583-020-1092-5

Cui, Z., Guo, Y., Li, Y., Wu, J., Li, B., Li, C., et al. (2015). Calcilutite-rudstone petrological characteristics in the lower part of Member 3 of Shahejie formation, Shulu sag. *Acta Pet. Sin.* 36 (S1), 21–30. doi:10.7623/syxb2015S1003

Du, X., Tian, C., Wang, Y., Liu, Z., and Qin, G. (2022). Sedimentary and reservoir characteristics of an Oligocene-Miocene mixed siliciclastic-carbonate succession in southeast Iraq. *Mar. Pet. Geol.* 138, 105533. doi:10.1016/j.marpetgeo.2022.105533

Fu, X., Wu, J., Shou, J., Wang, X., Zhou, J., Zhang, T., et al. (2019). Tight oil reservoir characteristics of lacustrine mixed marlstone in the palaeogene Shahejie Formation of shulu sag, bohai Bay Basin. *Oil GAS J.* 40 (01), 78–91. doi:10.11743/ogg20190108

Guo, W., Dong, C., Lin, C., Wu, Y., Zhang, X., and Liu, J. (2022). Rock physical modeling of tight sandstones based on digital rocks and reservoir porosity prediction from seismic data. *Front. Earth Sci. (Lausanne).* 10, 932929. doi:10.3389/feart.2022.932929

Han, C., Tian, J., Zhao, R., Luo, D., Qu, Y., Yu, Z., et al. (2015). Reservoir space types and its Genesis in tight calcilutite-rudstone reservoir of the lower part of Member 3 of Shahejie Formation, Shulu sag. *Acta Pet. Sin.* 36 (S1), 31–39. doi:10.7623/syxb2015S1004

He, J., Wang, J., Yu, Q., Cheng, C., and Milsch, H. (2022). Stress-Dependent permeability of naturally Micro-Fractured shale. *Geosciences* 12 (4), 150. doi:10.3390/geosciences12040150

He, J., Wang, J., Yu, Q., Liu, W., Ge, X., Yang, P., et al. (2018). Pore structure of shale and its effects on gas storage and transmission capacity in well HD-1 eastern Sichuan Basin, China. *Fuel* 226, 709–720. doi:10.1016/j.fuel.2018.04.072

Hou, H., Shao, L., Li, Y., Li, Z., Zhang, W., and Wen, H. (2018). The pore structure and fractal characteristics of shales with low thermal maturity from the Yuqia Coalfield, northern Qaidam Basin, northwestern China. *Front. Earth Sci.* 12 (1), 148–159. doi:10.1007/s11707-016-0617-y

Huo, Z., Tang, X., Meng, Q., Zhang, J., Li, C., Yu, X., et al. (2020). Geochemical characteristics and hydrocarbon expulsion of lacustrine marlstones in the shulu sag, bohai bay basin, eastern China: Assessment of tight oil resources. *Nat. Resour. Res.* 29 (4), 2647–2669. doi:10.1007/s11053-019-09580-8

James, W., Schmoker, T, C., and Hester, C. (1983). Organic carbon in bakken formation, United States portion of williston basin. *Am. Assoc. Pet. Geol. Bull.* 67, 2165–2174. doi:10.1306/ad460931-16f7-11d7-8645000102c1865d

Jia, C., Zheng, M., and Zhang, Y. (2012a). Unconventional hydrocarbon reseurces in China and the prospect of exploration and development. *Petroleum Explor. Dev.* 39 (02), 129–136.

Jia, C., Zou, C., Li, J., Li, D., and Zheng, M. (2012b). Assessment criteria, main types, basic features and resource prospects of the tight oil in China. *Acta Pet. Sin.* 33 (03), 343–350.

Jiang, S., and Mokhtari, M. (2019). Characterization of marl and interbedded limestone layers in the Eagle Ford Formation, DeWitt county, Texas. *J. Pet. Sci. Eng.* 172, 502–510. doi:10.1016/j.petrol.2018.09.094

Jiang, Z., Chen, D., Qiu, L., Liang, H., and Ma, J. (2007). Source-controlled carbonates in a small eocene half-graben lake basin (shulu sag) in central hebei province, north China. *Sedimentology* 54 (2), 265–292. doi:10.1111/j.1365-3091.2006.00834.x

Kong, X., Jiang, Z., Han, C., and Zhang, R. (2020). Organic matter enrichment and hydrocarbon accumulation models of the marlstone in the shulu sag, bohai Bay Basin, northern China. *Int. J. Coal Geol.* 217, 103350. doi:10.1016/j.coal.2019.103350

Kong, X., Jiang, Z., Han, C., Zheng, L., Yang, Y., and Liu, Y. (2016). Laminations characteristics and reservoir significance of fine-grained carbonate in the lower 3rd member of Shahejie Formation of Shulu sag. *Petroleum Geol. Recovery Effic.* 23 (4), 19–26. doi:10.3969/j.issn.1009-9603.2016.04.003

Kong, X., Jiang, Z., Han, C., Zheng, L., and Zhang, J. (2019). The tight oil of lacustrine carbonate-rich rocks in the Eocene Shulu Sag: Implications for lithofacies and reservoir characteristics. *J. Pet. Sci. Eng.* 175, 547–559. doi:10.1016/j.petrol.2018.12.028

Li, J., Fu, G., and Liu, Z. (2022). Quantitative characterization of the lower limit of the physical properties of tight oil reservoirs in Nano-Material porous media. *Integr. Ferroelectr.* 227 (1), 288–303. doi:10.1080/10584587.2022.2072118

Li, Q., Jiang, Z., You, X., Zhao, X., and Zhang, R. (2016). Role of organic facies in evaluation of unconventional petroleum reservoirs: A case study of organic-matterrich marlstone reservoirs in the shulu sag. *J. Northeast Petroleum Univ.* 40 (03), 1–9. doi:10.3969/j.issn.2095-4107.2016.03.001

Liang, H., Kuang, H., Liu, J., Guo, Y., and Su, J. (2007). Discussion on origin for marls of the member 3 of Shahejie Formation of Paleogene in Shulu sag of central Hebei depression. *J. Palaeogeogr.* 02, 167–174. doi:10.3969/j.issn.1671-1505.2007.02.005

Lin, S., Zou, C., Yuan, X., and Yang, Z. (2011). Status quo of tight oil exploitation in the United States and its implication. *Lithol. Reserv.* 23 (04), 25–30. doi:10.3969/j.issn.1673-8926.2011.04.005

Liu, E., Liu, C., Shi, D., Zhu, D., Xu, Q., and Wang, Y. (2022). Characterization and control of pore structural heterogeneity for low-thermal-maturity shale: A case study of the shanxi Formation in the northeast zhoukou depression, southern north China basin. *Front. Earth Sci. (Lausanne).* 10, 943935. doi:10.3389/feart.2022.943935

Liu, M., and Grana, D. (2018). Stochastic nonlinear inversion of seismic data for the estimation of petroelastic properties using the ensemble smoother and data reparameterization. *Geophys. J. Soc. Explor. Geophys.* 83 (3), M25–M39. doi:10.1190/GEO2017-0713.1

Liu, X., Rendle-Bühring, R., Meyer, I., and Henrich, R. (2016). Holocene shelf sedimentation patterns off equatorial East Africa constrained by climatic and sea-level changes. *Sediment. Geol.* 331, 1–11. doi:10.1016/j.sedgeo.2015.10.009

Liu, Z., Li, W., Li, J., Wang, W., Fu, G., and Zhang, H. (2022a). Characteristics of tight oil reservoir based on nano-CT. *Adv. Mater. Sci. Eng.* 2022, 1–11. doi:10.1155/2022/7863047

Liu, Z., Li, W., Zhang, L., and Li, J. (2022b). Petrophysical properties of tight marl reservoir and its influence on fluid percolation capacity. *Integr. Ferroelectr.* 227 (1), 273–287. doi:10.1080/10584587.2022.2072116

Liu, Z., Yu, Z., Lv, Y., and Li, J. (2020). Characteristics and oil content of tight oil marl reservoirs in Es3L of shulu sag. *J. Guangdong Univ. Petrochem. Technol.* 30 (04), 1–4. doi:10.3969/j.issn.2095-2562.2020.04.001

Lu, Y., and Liu, K. (2021). Pore structure characterization of eocene Low-Permeability sandstones via fractal analysis and machine learning: An example from the dongying depression, bohai bay basin, China. *ACS Omega* 6 (17), 11693–11710. doi:10.1021/acsomega.1c01015

Miller, B. A., Paneitz, J. M., Mullen, M. J., Meijs, R., Tunstall, K. M., and Garcia, M. (2008). "The successful application of a compartmental completion technique used to isolate multiple Hydraulic-Fracture treatments in horizontal bakken shale wells in North Dakota," in SPE Annual Technical Conference and Exhibition, September 21–24, 2008 (Denver, Colorado, USA: Society of Petroleum Engineers), 1–11. doi:10.2118/116469-MS

Qian, Y., Gao, P., Fang, X., Sun, F., Cai, Y., and Zhou, Y. (2022). Microstructure characterization techniques for shale reservoirs: A review. *Front. Earth Sci. (Lausanne).* 10, 930474. doi:10.3389/feart.2022.930474

Qiu, L., Jiang, Z., Liang, H., Li, C., and Sun, B. (2010). Limemudstone: A kind of carbonate rock of terrigenous mechanical origin. *J. China Univ. Petroleum* 34 (06), 1–7. doi:10.3969/j.issn.1673-5005.2010.06.001

Rahman, M. J. J., and Worden, R. H. (2016). Diagenesis and its impact on the reservoir quality of miocene sandstones (surma group) from the bengal basin, Bangladesh. *Mar. Pet. Geol.* 77, 898–915. doi:10.1016/j.marpetgeo.2016.07.027

Shan, C. A., Zhang, T., Wei, Y., and Zhang, Z. (2017). Shale gas reservoir characteristics of Ordovician-Silurian formations in the central Yangtze area, China. *Front. Earth Sci.* 11 (1), 184–201. doi:10.1007/s11707-016-0565-4

Wang, D., Ning, F., Lu, J., Lu, H., Kang, D., Xie, Y., et al. (2021). Reservoir characteristics and critical influencing factors on gas hydrate accumulations in the Shenhu area, South China Sea. *Mar. Pet. Geol.* 133, 105238. doi:10.1016/j.marpetgeo.2021.105238

Wu, J., Yang, S., Gan, B., Cao, Y., Zhou, W., Kou, G., et al. (2021). Pore structure and movable fluid characteristics of typical sedimentary lithofacies in a tight conglomerate reservoir, mahu depression, northwest China. *ACS Omega* 6 (36), 23243–23261. doi:10.1021/acsomega.1c02952

Wu, Y., Lin, C., Ren, L., Yan, W., An, S., Chen, B., et al. (2018). Reconstruction of 3D porous media using multiple-point statistics based on a 3D training image. *J. Nat. Gas. Sci. Eng.* 51, 129–140. doi:10.1016/j.jngse.2017.12.032

Wu, Y., Lin, C., Yan, W., Liu, Q., Zhao, P., and Ren, L. (2020a). Pore-scale simulations of electrical and elastic properties of shale samples based on multicomponent and multiscale digital rocks. *Mar. Pet. Geol.* 117, 104369. doi:10.1016/j.marpetgeo.2020.104369

Wu, Y., Tahmasebi, P., Lin, C., and Dong, C. (2020c). A comprehensive investigation of the effects of organic-matter pores on shale properties: A multicomponent and multiscale modeling. *J. Nat. Gas. Sci. Eng.* 81, 103425. doi:10.1016/j.jngse.2020.103425

Wu, Y., Tahmasebi, P., Lin, C., and Dong, C. (2020b). Process-based and dynamic 2D modeling of shale samples: Considering the geology and pore-system evolution. *Int. J. Coal Geol.* 218, 103368. doi:10.1016/J.COAL.2019.103368

Wu, Y., Tahmasebi, P., Lin, C., and Dong, C. (2022a). Using digital rock physics to investigate the impacts of diagenesis events and pathways on rock properties. *J. Pet. Sci. Eng.* 208, 108025. doi:10.1016/j.petrol.2020.108025

Wu, Y., Tahmasebi, P., Lin, C., Ren, L., and Dong, C. (2019a). Multiscale modeling of shale samples based on low- and high-resolution images. *Mar. Pet. Geol.* 109, 9–21. doi:10.1016/j.marpetgeo.2019.06.006

Wu, Y., Tahmasebi, P., Lin, C., Ren, L., and Zhang, Y. (2020d). Quantitative characterization of non-wetting phase in water-wet porous media based on multiphase flow experiment and numerical simulation(Article). *J. Pet. Sci. Eng.* 188, 106914. doi:10.1016/j.petrol.2020.106914

Wu, Y., Tahmasebi, P., Lin, C., Zahid, M. A., Dong, C., Golab, A. N., et al. (2019b). A comprehensive study on geometric, topological and fractal characterizations of pore systems in low-permeability reservoirs based on SEM, MICP, NMR, and X-ray CT experiments. *Mar. Pet. Geol.* 103, 12–28. doi:10.1016/j.marpetgeo.2019.02.003

Wu, Y., Tahmasebi, P., Liu, K., Fagbemi, S., Lin, C., An, S., et al. (2022b). Two-phase flow in heterogeneous porous media: A multiscale digital model approach. *Int. J. Heat. Mass Transf.* 194, 123080. doi:10.1016/j.ijheatmasstransfer.2022.123080

Wu, Y., Tahmasebi, P., Yu, H., Lin, C., Wu, H., and Dong, C. (2020e). Pore-scale 3D dynamic modeling and characterization of shale samples: Considering the effects of thermal maturation. *J. Geophys. Res. Solid Earth* 125 (1), e2019J–e18309J. doi:10.1029/2019JB018309

Yang, J., Zhang, J., Ji, Y., Lv, W., Wu, H., He, Z., et al. (2022). Pore structure characteristics and controlling factors of a tight sandstone reservoir in the paleogene shahejie formation, nanpu sag, bohai bay basin, China. *ACS Omega* 7 (2), 1740–1756. doi:10.1021/acsomega.1c04573

Zhang, J., Liu, G., Torsaeter, O., Tao, S., Jiang, M., Li, G., et al. (2020). Pore-throat structure characteristics and its effect on flow behavior in Gaotaizi tight siltstone reservoir, northern Songliao Basin. *Mar. Pet. Geol.* 122, 104651. doi:10.1016/j.marpetgeo.2020.104651

Zhang, R., Chen, K., Zhu, J., Tang, X., Yu, Z., Zhang, Y., et al. (2021). Tight gas reservoir forming condition and resource potential in the lacustrine carbonate in the middle-deep layer of Shulu Sag of Jizhong Depression,Bohai Bay Basin. *Nat. Gas. Geosci.* 32 (05), 623–632. doi:10.11764/j.issn.1672-1926.2020.12.004

Zhang, S., Tang, S., Zhang, J., and Pan, Z. (2018). Pore structure characteristics of China sapropelic coal and their development influence factors. *J. Nat. Gas. Sci. Eng.* 53, 370–384. doi:10.1016/j.jngse.2018.03.022

Zhao, F., Dong, Z., Wang, C., Zhang, W., and Yu, R. (2022). Pore connectivity characteristics and controlling factors for black shales in the Wufeng-Longmaxi formation, southeastern sichuan basin, China. *Energies* 15 (8), 2909. doi:10.3390/en15082909

Zhao, L., Qin, X., Han, D., Geng, J., Yang, Z., and Cao, H. (2016). Rock-physics modeling for the elastic properties of organic shale at different maturity stages. *Geophys. J. Soc. Explor. Geophys.* 81 (5), D527–D541. doi:10.1190/GEO2015-0713.1

Zhao, X., Jiang, Z., Zhang, R., Li, H., Yang, D., Cui, Z., et al. (2015). Geological characteristics and exploration practices of special-lithology tight oilreservois in continental rift basinsi a case sludy of tight oil in Sha-hejie Formation, Shulu sag. *Acta Pet. Sin.* 36 (S1), 1–9. doi:10.7623/syxb2015S1001

Zhao, X., Li, Q., Jiang, Z., Zhang, R., and Li, H. (2014a). Organic geochemistry and reservoir characterization of the organic matter-rich calcilutite in the shulu sag, bohai Bay Basin, north China. *Mar. Pet. Geol.* 51 (2), 239–255. doi:10.1016/j.marpetgeo.2013.12.014

Zhao, X., Zhu, J., Zhang, R., Yu, Z., Wang, J., and Guo, Y. (2014b). Characteristics and exploration potential of tight calcilutite-rudstone reser-voirs in Shulu sag, Jizhong depression, North China. *Acta Pet. Sin.* 35 (04), 613–622. doi:10.7623/syxb201404001

Zhou, L., Lu, S., Wu, J., and Guo, Y. (2020). Characteristics of tight-oil reservoir and accumulation areaprediction in Lower part of the 3rd Shahejie Formation of Shulu sag. *Geol. Rev.* 66 (S1), 123–125. doi:10.16509/j.georeview.2020.s1.048

Zhu, H., Ju, Y., Huang, C., Chen, F., Chen, B., and Yu, K. (2020). Microcosmic gas adsorption mechanism on clay-organic nanocomposites in a marine shale117256. *Energy* 197, 117256. doi:10.1016/j.energy.2020.117256

Zhu, H., Ju, Y., Huang, C., Han, K., Qi, Y., Shi, M., et al. (2019a). Pore structure variations across structural deformation of silurian longmaxi shale: An example from the chuandong thrust-fold belt. *Fuel* 241, 914–932. doi:10.1016/j.fuel.2018.12.108

Zhu, H., Ju, Y., Qi, Y., Huang, C., and Zhang, L. (2018). Impact of tectonism on pore type and pore structure evolution in organic-rich shale: Implications for gas storage and migration pathways in naturally deformed rocks. *Fuel* 228, 272–289. doi:10.1016/j.fuel.2018.04.137

Zhu, H., Ju, Y., Yang, M., Huang, C., Feng, H., Qiao, P., et al. (2022). Grain-scale petrographic evidence for distinguishing detrital and authigenic quartz in shale: How much of a role do they play for reservoir property and mechanical characteristic? *Energy* 239, 122176. doi:10.1016/j.energy.2021.122176

Zhu, H., Zhang, T., Zhong, D., Li, Y., Zhang, J., and Chen, X. (2019b). Binary pore structure characteristics of tight sandstone reservoirs. *Petroleum Explor. Dev.* 46 (6), 1297–1306. doi:10.1016/S1876-3804(19)60283-1

Zhu, X., Zeng, H., Li, S., Dong, Y., Zhu, S., Zhao, D., et al. (2017). Sedimentary characteristics and seismic geomorphologic responses of a shallow-water delta in the Qingshankou Formation from the Songliao Basin, China. *Mar. Pet. Geol.* 79, 131–148. doi:10.1016/j.marpetgeo.2016.09.018

Zou, C., Zhu, R., Wu, S., Yang, Z., Tao, S., Yuan, X., et al. (2012). Types, characteristics, Genesis and prospeets of eonventional and unconventional hydrocarbon accumulations:Taking tight oil and tight gas in China as an instance. *Aeta Perolei Sin.* 33 (02), 173–187.

frontiers | Frontiers in Earth Science

TYPE Original Research
PUBLISHED 21 September 2022
DOI 10.3389/feart.2022.1016924

OPEN ACCESS

EDITED BY
Yuqi Wu,
China University of Petroleum, China

REVIEWED BY
Ziliang Liu,
Chengdu University of Technology,
China
Hu Li,
Southwest Petroleum University, China

*CORRESPONDENCE
Qin Zhang,
zhangqin@cup.edu.cn

SPECIALTY SECTION
This article was submitted to
Solid Earth Geophysics,
a section of the journal
Frontiers in Earth Science

RECEIVED 11 August 2022
ACCEPTED 08 September 2022
PUBLISHED 21 September 2022

CITATION
Zhang Q, Zhang Y-X, Wang B-H, Yin S,
Wu X-S and Yuan C-S (2022),
Comprehensive evaluation and
reservoir classification in the Quan
3 Member of the Cretaceous Quantou
Formation in the Fuxin Uplift,
Songliao Basin.
Front. Earth Sci. 10:1016924.
doi: 10.3389/feart.2022.1016924

Comprehensive evaluation and reservoir classification in the Quan 3 Member of the Cretaceous Quantou Formation in the Fuxin Uplift, Songliao Basin

Qin Zhang[1,2]*, Ya-Xiong Zhang[3], Bo-Han Wang[4], Shuai Yin[5], Xin-Song Wu[1,2] and Cheng-Shuai Yuan[6]

[1]College of Geosciences, China University of Petroleum (Beijing), Beijing, China, [2]State Key Laboratory of Petroleum Resources and Prospecting, China University of Petroleum (Beijing), Beijing, China, [3]Petroleum Exploration and Production Research Institute, SINOPEC, Beijing, China, [4]Sinopec Chongqing Fuling Shale Gas Exploration and Development Co, Ltd, Chongqing, China, [5]Xi'an Shiyou University, School of Earth Science and Engineering, Xi'an, China, [6]State Key Laboratory of Geological Processes and Mineral Resources, China University of Geosciences, Beijing, China

Continental tight oil sandstone reservoirs are developed in the Cretaceous Quentou Formation in the Songliao Basin, China. At present, there is still a lack of research on the reservoir microstructures, reservoir physical properties, and the division scheme of reservoir types in the Quan 3 Member of the Quanzhou Formation. Therefore, in this paper, taking the Quan 3 Member in the Fuxin Uplift Belt of the Songliao Basin as an example, the microscopic pore structure characteristics of tight oil sandstones have been systematically studied, and the classification standard of tight sandstones has been formulated. Furthermore, the sweet spots of the main production layers are predicted. The results show that the I sandstone group in the Quan 3 Member in the study area belongs to shallow water delta facies. Feldspar lithic fine sandstones are developed in the target layer, and calcareous sandstone is locally developed. Moreover, the mian pore types of the target layer include dissolved intergranular and intragranular pores, followed by primary intergranular pores, while micro-fractures are occasionally seen. According to the mercury intrusion test results, the pore-throat structures of the reservoir in the Quan 3 Member are divided into four types: 1) small-pore medium-throat type (point bar and delta distributary channel), 2) small-pore micro-throat type (point bar), 3) small-pore micro-throat type (natural levee), 4) micro-pore micro-throat type (river floodplain and inter-tributary bay). The lower limits of the physical properties of the effective reservoirs in the Quan 3 Member has been determined: the porosity is 10% and the permeability is 0.1 mD. Finally, combined with the study of the mercury intrusion curves, the physical properties and the sedimentary facies, the classification standard of the Quan 3 Member reservoirs was formulated. For the I sandstone group, the sweet spots of the Type I reservoirs are mainly developed in the Fuyu Oilfield in the southeast areas. The sandstones in this area suffered less compaction, and primary and secondary pores suffered from late dissolution are mainly developed.

KEYWORDS

Songliao Basin, tight oil sandstone, Quan 3 Member, reservoir classification, sweet spot prediction

Introduction

In recent years, the research focus of clastic oil and gas reservoirs has gradually developed from conventional to unconventional reservoirs such as tight reservoirs, deep reservoirs or volcanic rock reservoirs (Kassem et al., 2021; Lv and Li, 2021; Boutaleb et al., 2022; Cui and Radwan., 2022). The different scales of reservoir heterogeneity, the reasons for the formation of tight oil and gas reservoirs, the origin of various secondary pores, and the division of reservoir types have all become the focus of reservoir geology (Li et al., 2013; Haile et al., 2018; Qiao et al., 2019; Wu et al., 2019; Bello et al., 2021).

Qualitative evaluation has been unable to meet the requirements of fine evaluation of tight reservoir properties. Therefore, the quantitative evaluation of multi-parameter joint characterization has become the mainstream of fine reservoir evaluation (Enayati-Bidgoli and Saemi., 2019; Hijaz et al., 2020; Mirzaei-Paiaman and Ghanbarian., 2021). The previous usually use effective permeability, rock density, effective porosity and permeability of matrix as the core parameters for quantitative evaluation of reservoir properties (Sun et al., 2014; Mahmi et al., 2018; Wu et al., 2020a; Khan et al., 2020; Jabir et al., 2021). In recent years, some new data processing techniques, such as artificial neural network, CT scanning, etc., have also been used to evaluate the oil and gas-bearing properties of tight reservoirs (Li et al., 2005; Liu et al., 2019; Wang et al., 2020).

There are many countries with developed continental sedimentary oil fields. Therefore, oil and gas exploration of fluvial and lacustrine facies sand bodies has received great attention (Yang et al., 2013; Wang et al., 2016; Wu et al., 2020b; Wu et al., 2020c). Fluvial reservoirs are an important type of oil and gas reservoirs in China, accounting for about 38% of the total reserves. The Songliao Basin, located in northeastern China, is a sedimentary basin with the earliest oil discovery in China. At present, the sand bodies of the Quan 3 Member of the Quantou Formation in the Fuxin Uplift, Songliao Basin have complex development characteristics and a low degree of oil and gas exploration. The lack of basic research limits the efficient development of tight sandstone reservoirs in the Quan 3 Member.

On the basis of years of oil and gas exploration achievements in the Fuxin Uplift Belt, this study systematically studies the microscopic pore structure characteristics, reservoir classification standards and sweet spot prediction of the main producing layers of the Quan 3 Member. This study has important theoretical and practical significance for guiding the in-depth oil and gas exploration of the Quan 3 Member of the Fuxin Uplift Belt in the Songliao Basin.

Geological background

The Fuxin Uplift is located in the central depression in the south of the Songliao Basin in northeastern China (Figure 1A). The area covers the Xinbei, Xinmiao, Xinmin, Xinli, Mutou and Fuyu Oil Fields. The good source-reservoir-caprock combination makes the Fuxin Uplift area have the characteristics of contiguous distribution of reservoirs and good oil-bearing properties. The configuration of oil-generating sags and long-term inherited structural belts has resulted in large-scale accumulation of oil and gas in the Fuxin Uplift area.

The stratigraphic unit division of the Fuxin Uplift belt is shown in Figure 1B. Oil and gas are mainly distributed in the Cretaceous strata. The Cretaceous strata are divided into the Denglouku, Quantou, Qingshankou, Yaojia and Nenjiang Formations, from bottom to top. High-resolution sequence stratigraphy studies show that the Quan 3 Member of the Quan Formation develops a base level rising semi-cycle and a base level falling semi-cycle. Moreover, the Quan 3 Member of the Quantou Formation is divided into 6 sandstone groups, of which the main oil-bearing formation is the I sandstone group.

Methods

In this paper, core observation (35 wells), ordinary and cast thin section identification (total 120 samples), scanning electron microscope (total 10 sample), physical properties (total 885 samples), mercury intrusion testing (total 109 samples), and X-diffraction experiments (total 20 samples) from the Quan 3 Member were carried out systematically. The testing instrument for the ordinary and cast thin sections is a Nikon Eclipse LV100N POL polarizing microscope; an FEI Quanta 200F SEM was used for SEM observations; a PoroPDP-200 overburden porosity-permeability tester was used for physical property testing; an AutoPore V mercury porosimeter was used for mercury porosimetry; and a D2 Phaser diffractometer was used to perform X-ray diffraction experiments.

In this paper, the petrological characteristics, physical properties, pore types and development characteristics of the reservoirs, and the prediction of favorable reservoirs in the Quan 3 Member of the Quantou Formation were conducted systematically. The specific steps of these studies are:

1) Research on petrological characteristics of reservoirs: Through the observation of cores, identifications of ordinary and cast thin sections, X-diffraction and scanning electron microscopy experiments in the target layer, the composition and structural characteristics of the clastic

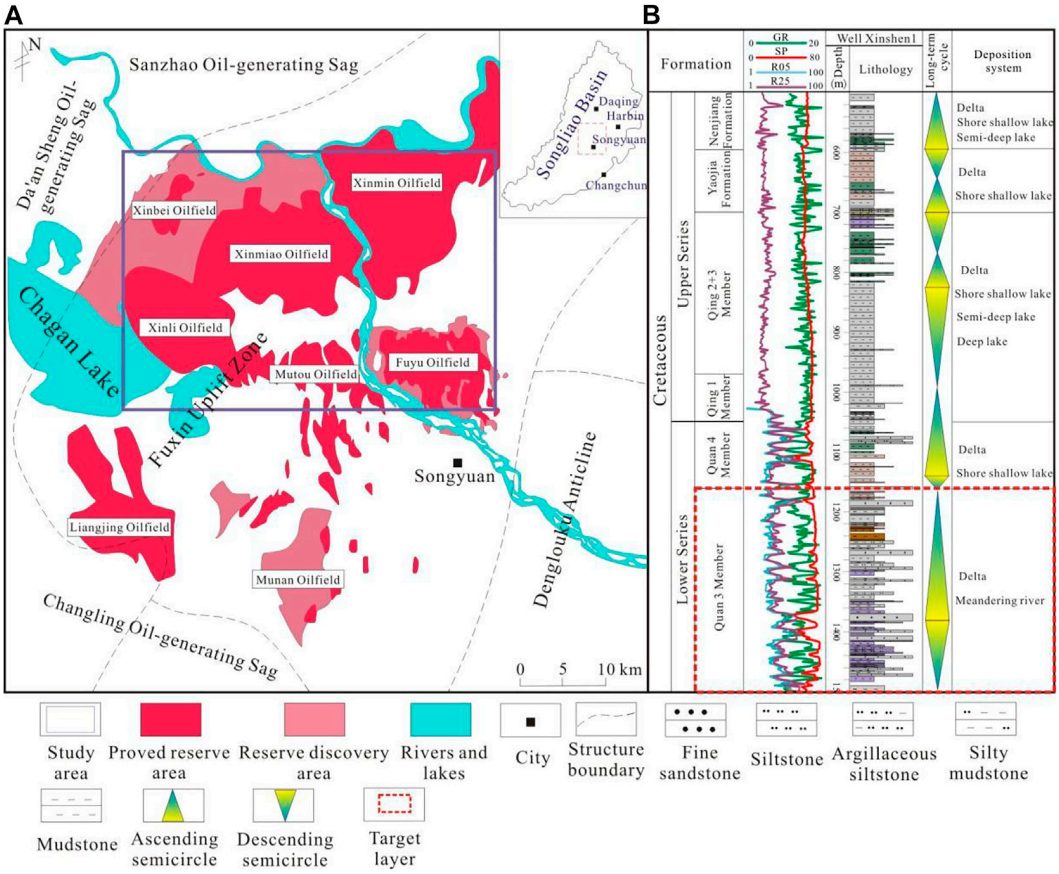

FIGURE 1
Location of the study area (Fuxin Uplift) **(A)** and the comprehensive stratigraphic histogram **(B)** of this area (From Mei et al., 2020; modified).

particles of the tight sandstones are analyzed. Furthermore, the lithology and the development characteristics of different mineral compositions of the target layer were determined.

2) Research on reservoir physical properties: Based on reservoir physical property data, pore observation results based on cast thin sections and scanning electron microscope, the porosity-permeability relationship and its relationship with oil-bearing properties were studied and the lower limits of the physical properties (porosity and permeability) were determined.
3) Pore types and their development characteristics: According to the observations of cast thin section and scanning electron microscope, and the classification of mercury intrusion curves, the microscopic reservoir characteristics of the reservoir in the Quan 3 Member of the Quantou Formation are systematically studied. The research carried out includes classification of pore types, characterization of pore structures, and classification schemes for pore-throat combinations.
4) Prediction of sweet spot reservoirs: Based on the above research, a method for classifying reservoir types is formulated, and then the distribution of high-quality reservoir sweet spots is determined.

Results

Sedimentary facies

Based on the sedimentary structures, lithofacies, and logging response characteristics of the Fuxin Uplift Belt, the Quan 3 Member of the Quantou Formation can be divided into three depositional environments, namely meandering river, shallow water delta and lake. Seven microfacies were identified in the Quan 3 Member, including river channel, point bar, lateral border of channel, floodplain lake, delta plain distributary channel, delta front sheet sand and shore-shallow lake (Figure 2, Figure 3). Reservoirs are mainly in the river channel, point bar, delta distributary channel and delta front sheet sand microfacies (Figure 2).

FIGURE 2
Core characteristics of the Quan 3 Member in the Fuxin Uplift. Notes: **(A)** Point bar, fine sandstone with wedge cross bedding, Well J+28−015.1,1272.62m; **(B)** Distributary channel, fine sandstone with argillaceous gravel, Well J+2−014, 1373.97m; **(C)** Distributary channel, silt-finesandstone with small-scale cross bedding, Well M102, 1353.95m; **(D)** Delta front underwater distributary channel, fine sandstone with convolution bedding, Well J30, 439.73m.

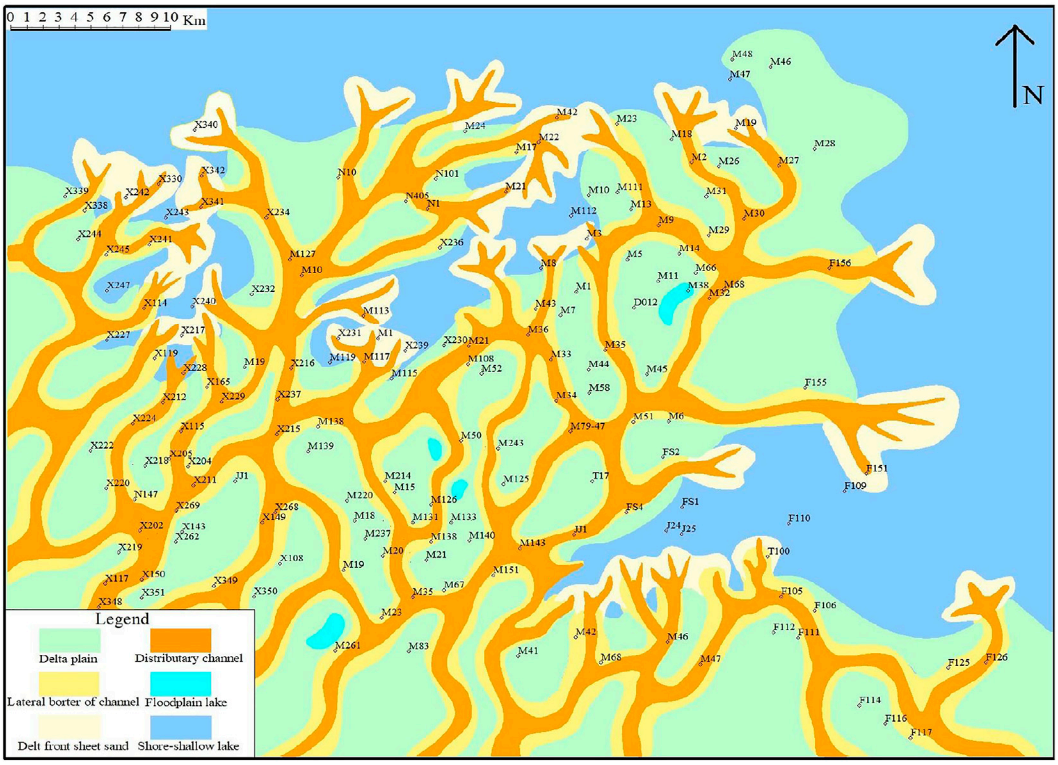

FIGURE 3
Distribution of sedimentary facies of the I sandstone group of the Quan 3 Member in the Fuxin Uplift.

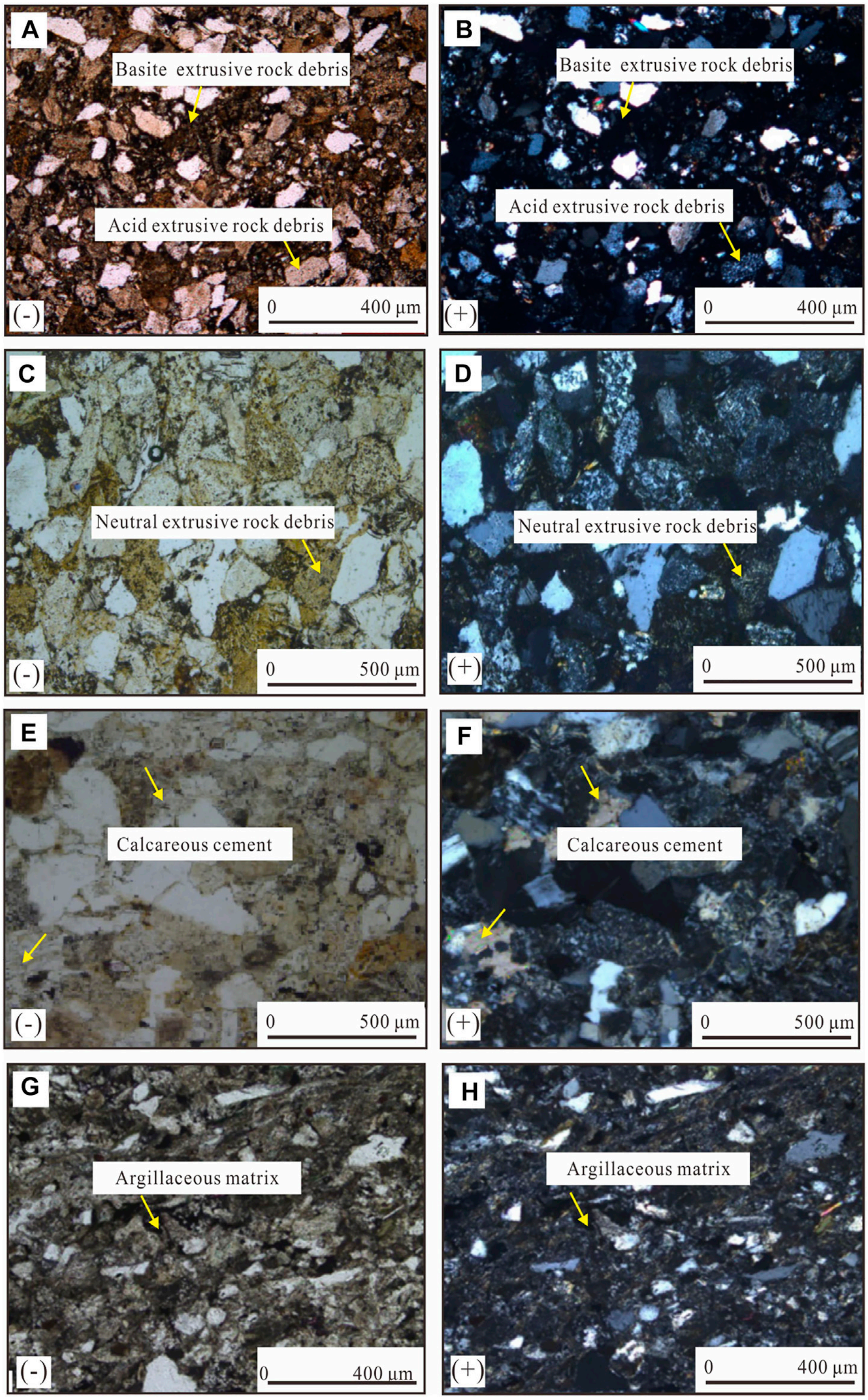

FIGURE 4
Microscopic characteristics of sandstones in Quan 3 Member in the Fuxin Uplift. Notes: **(A)** Feldspar debris sandstone, Jian 25 well, 389.32m; **(B)** Feldspar debris sandstone, Jian 25 well, 389.32m; **(C)** Feldspar debris sandstone, Jian 24 well, 504.26m; **(D)** Feldspar debris sandstone, Jian 24 well, 504.26m; **(E)** Calcareous sandstone, Ji+28−15.1 well, 1364.68m; **(F)** Calcareous sandstone, Ji+28−15.1 well, 1364.68m; **(G)** Argillaceous siltstone, Mu+126−024 well, 954.07m; **(H)** Argillaceous siltstone, Mu+126−024 well, 954.07m.

TABLE 1 Reservoir property of Quan 3 Member in different oil field in the Fuxin Uplift.

Area (oil field)	Porosity (%)	Permeability (mD)	Average porosity (%)	Average permeability (mD)	Samples /wells
Fuyu	3–34.9	0.02–3167	24.89	142.72	514/7
Xinmu	4.9–15.5	0.004–8	13.4	0.609	108/3
Xinbei	7–13	0.3 ~ 0.9	10.12	0.39	20/2
Xinli	3–21.5	0.03–21.3	10.97	1.86	180/16
Xinmiao	7.7–13.6	0.06–0.47	11	0.19	37/2
Xinmin	5.1–16.6	0.01–8.1	13.79	2.12	26/1

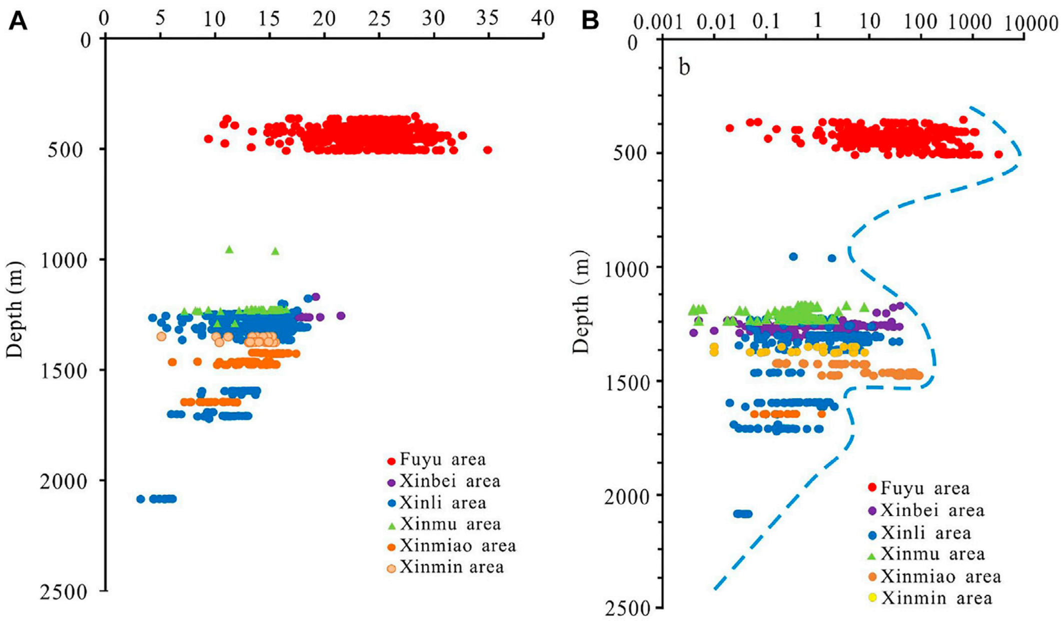

FIGURE 5
Distribution of reservoir properties of Quan 3 Members in different burial depth. Notes: **(A)** Varition of porosity with depth; **(B)** Varition of permeability with depth.

Rock types and characteristics

The evaluation and classification of reservoirs are controlled by petrological property parameters (Yang and Chen., 2001; Zhang J. Y. et al., 2014; Radwan et al., 2021; Nabawy et al., 2022). In order to better study the reservoir properties of the Quan 3 Member in the Fuxin Uplift Belt, the rock characteristics of the reservoir were first analyzed, and then the rock types, components and structural characteristics were clarified.

In this study, the petrological characteristics of the target layer in the study area were qualitatively and quantitatively analyzed using the data of ordinary thin section identifications, X-diffractions and scanning electron microscope analysis.

Under the microscope, it is found that there are differences in the lithological development characteristics of different regions and different depths, and the oil content is quite different. The feldspar lithic sandstone is mainly developed in the target layer, and the calcareous sandstone is developed in the local layers. Among them, feldspar and debris components are mostly chloritized. The debris composition is dominated by medium-acid extrusive debris (Figures 4A,B), and contains a certain amount of basic extrusive debris (Figures 4C,D). Perpendicular to the bedding direction, the particle size is relatively finer from bottom to top, but the degree of fine-graining is not large, and the average particle size of each small layer is between 0.1 and 0.15 mm. In addition, some

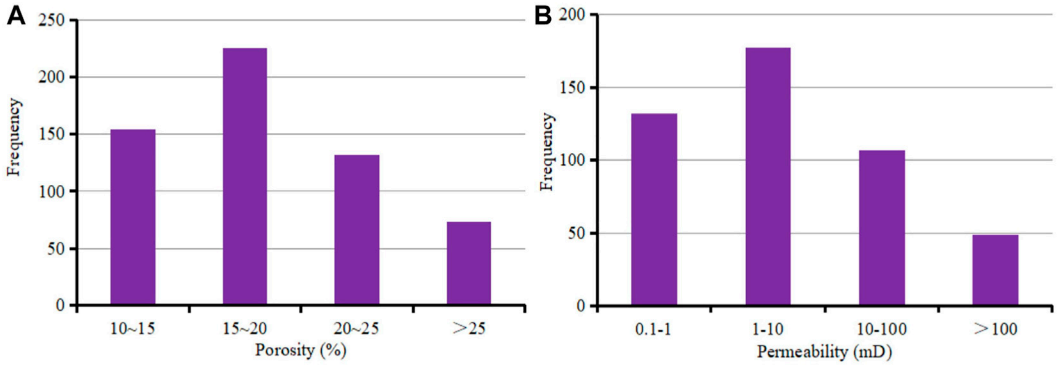

FIGURE 6
Distribution of porosity and permeability of I sandstone group in Quan 3 Member. **(A)** Porosity distribution histogram; **(B)** Permeability distribution histogram.

sandstone segments have high calcareous content (Figures 4E,F) and argillaceous matrix (Figures 4G,H).

Distribution of reservoir property

In this study, a statistical analysis was carried out on the measured physical property data (Table 1; Figure 5) of the sandstone cores of the Quan 3 Member. The results show that the porosity of the target layer is distributed between 3% and 34.9%, with an average of 14.3%. It has two peak intervals, the main peak is 10%–15%, and the secondary peak is 15%–20%. In addition, its permeability has a minimum value of 0.01 mD, a maximum value of 3167 mD, and an average of 3.84 mD. The permeability also has two peak intervals, the main peak is located at 1 mD-10 mD, and the secondary peak is located at 0.1 mD-1 mD. Obviously, the Quan 3 Member reservoir has moderately low porosity and low permeability (Figure 5).

Controlled by various factors such as deposition and diagenesis, the distribution of physical properties on the plane is non-uniform, reflecting the obvious heterogeneity of reservoir physical properties (Zhang et al., 2014b; Xiao et al., 2019; Zhang et al., 2020; Zhang et al., 2022). The reservoir porosity of the Quan 3 Member is significantly different between the eastern and western regions (Table 1; Figure 5). The sand bodies in the east are buried shallow, so the porosity is higher than that in the west. The distribution of reservoir permeability is consistent with the distribution of porosity, and the permeability in the east is higher than that in the west.

Among the three sandstone groups in the Quan 3 Member, the sandstone group I has the best physical properties (Figure 6). The main peak of porosity is between 15% and 20%, and the main peak of permeability is between 1 mD-10 mD. The areas with porosity greater than 25% and permeability greater than 100 mD in the I sandstone group are mainly concentrated in the southeastern region. However, the areas with porosity greater than 20% and permeability greater than 1 mD are concentrated in the eastern part of the I sandstone group. The southwestern part of the study area is the Xinli Structure, and the permeability and porosity are basically above 1 mD and 15%. On the whole, the physical properties of the reservoir have a distribution pattern of “better in the southeast, poor in the southwest, and moderate to poor in the north".

Classification and characteristic of pore types

The type of pores plays an important role in the accumulation of oil and gas (Wang and Yang., 2017; Santosh and Feng., 2020; Zhang et al., 2021; Su et al., 2022). The pore types of the target layer are mainly dissolved intergranular and intragranular pores, followed by primary intergranular pores, and micro-fractures are occasionally seen.

1) Secondary pores

The secondary pores developed in the target layer are mainly dissolved pores. For example, dissolved intragranular pores, dissolved intergranular pores (dissolved and expanded intergranular pores, cement dissolved pores) and mold pores.

①Intragranular dissolution pores

The most common is the dissolution of feldspar particles. Due to the cleavage of feldspar, when the acidic fluid enters, the feldspar is dissolved in a grid-like manner, and a dissolved residual edge is formed (Figures 7A,B). Neutral and basic debris in the study area contain feldspar, and the feldspar component can also be dissolved, resulting in dissolved intragranular pores in the debris (Figures 7C,D).

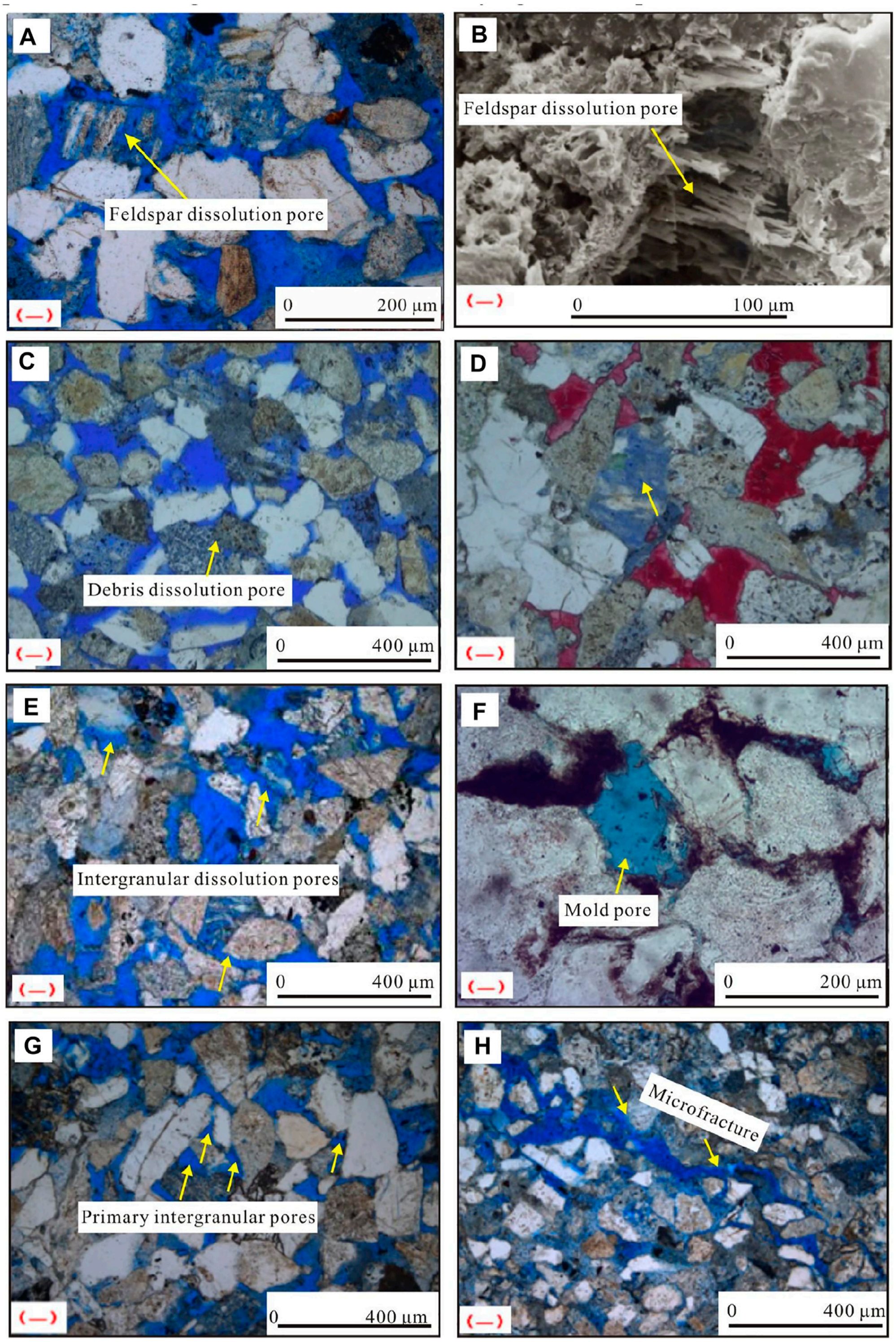

FIGURE 7
Development characteristics of pores in the sandstone of the target layer. Notes: **(A)** Feldspar dissolution pores, Jian 25 well, 460.24m; **(B)** Feldspar dissolution pore, Ji 41 well, 1369.76m; **(C)** Detritus dissolution pores, Jian 24 well,495.4m; **(D)** Debris dissolution pores, Ji+28–15.1 well, 1324.42m; **(E)** Fine feldspar debris-siltstone, well developed pores, Jian 30 well, 370.0m; **(F)** Mould pores, Ji +28–015.1 well, 1364.75m; **(G)** Primary pores, Jian 30 well, 458.1m; **(H)** Fine feldspar debris-siltstone, micro-fractures, Jian 25 well, 418.34m.

②Intergranular dissolution pores

Dissolution and enlarged intergranular pores can also be seen in the target layer (Figure 7E). The acidic fluid dissolves the unstable components around the primary pores, so that the primary pores are enlarged. The pore space around the particles is mostly irregular or harbor-shaped.

③Mold pores

For selective dissolution, the relatively soluble particles are completely dissolved, leaving a dissolved pore with the same size and shape as the dissolved particles, that is, a mold pore. The mold pores produced by the complete dissolution of feldspar particles by organic acids can be seen in the target layer (Figure 7F).

2) Primary pores

Primary pores refer to the pores formed during the deposition of rocks and preserved to the present. After they are formed, they have not suffered from major diagenesis, such as dissolution or cementation, to reform the intergranular pores, so they have the characteristics of regular shape and straight edges (Tang et al., 2009; Sun et al., 2013). The preserved primary pores are generally developed between the clast particles, and are mostly triangular, and the pore boundaries retain relatively straight boundaries. Moreover, some primary pores are developed between the clay mineral crystals, such as the intercrystalline pores of kaolinite and illite. They are distributed in irregular shapes. The content of primary pores in the target layer is low, and the connectivity between pores is poor (Figure 7G).

3) Micro-fractures

Structural fractures and pressure-solution fractures are mainly developed in the target layer (Figure 7H). Structural fractures generally pass around the grains, and the fracture surfaces are curved. The pressure-dissolution fractures are generally distributed in the same direction on the feldspar particles, showing the direction of the overlying load compressive stress.

Pore throat types and characteristics

According to the mercury intrusion test results, the pore-throat structures of the reservoir in the Quan three Member are divided into four types: 1) small-pore medium-throat type, 2) small-pore micro-throat type, 3) small-pore micro-throat type, 4) micro-pore micro-throat type.

Type I: small-pore medium-throat type. The pore throats in this type of pore-throat system are relatively large, with ϕ (porosity) between 24% and 27%, permeability between 368 and 603 mD, average pore throat radius distribution around 10 μm, displacement pressure between 0.02 MPa and 0.2 MPa, and median pressure of saturation between 0.4 MPa and 0.9 MPa. Moreover, the mercury injection curve has a certain length of gentle slope platform, and the mercury removal efficiency is between 12% and 14%, with an average of 13%. This type of reservoir has fine pore throat and good sorting, and is mainly developed in the Fuyu Oilfield. It is the best reservoir in the Quan 3 member of the Quanzhou Formation, and is generally distributed in point bars and delta distributary channels (Figure 8A).

Type II: small-pore micro-throat type. The pore throat radius in this type of pore throat system is lower than that of the Type I pore throats. Its ϕ is between 15% and 22%, with an average value of 17.3%. There is almost no near-horizontal segment in the mercury intrusion curve. The average displacement pressure is 0.2 MPa, and the average pore throat radius is between 0.1 and 1 mm. Moreover, the maximum mercury saturation is 82%–87%, with an average of 84%, and the mercury removal efficiency is 28%–50%, with an average of 37.8%. The permeability distribution range of this type of reservoir is 0.5mD-1.7mD, and the porosity is mostly less than 18%. This type of reservoir has fine pore throats, poor sorting, and small seepage space, and is generally distributed in point bar sand bodies (Figure 8B).

Type III: small-pore micro-throat type. The pores and roars in the pore-throat system of this type of reservoir are smaller than those of Type II. Its ϕ is between 14% and 18%, with an average value of 15.7%. The mercury intrusion curve is similar to Type II. The average pore radius is distributed in the range of 1–3 μm, with an average value of 2.0 μm. The displacement pressure is distributed in the range of 0.15–2.08 MPa. This type of reservoir is generally distributed in natural levee (Figure 8C).

Type IV: micro-pore micro-throat type. Its ϕ is between 11% and 14%, with an average value of 13.1%; the average pore radius is between 0.17 and 0.97 μm, with an average value of 0.64 μm. In addition, the displacement pressure is > 4 MPa. This type of reservoir is mainly developed in floodplains and inter-tributary bays (Figure 8D).

Discussion

The lower limits of physical properties

The reservoirs below 1500 m in the study area have poor physical properties and tend to be densified evidently (Figure 5). When the reservoir is tight, industrial-grade oil flow cannot be produced. Combining the observations of the core and the data of liquid production and physical properties, it can be seen that the physical property boundary between oil-free and oil-bearing in the core is between the porosity of 10% and the permeability of

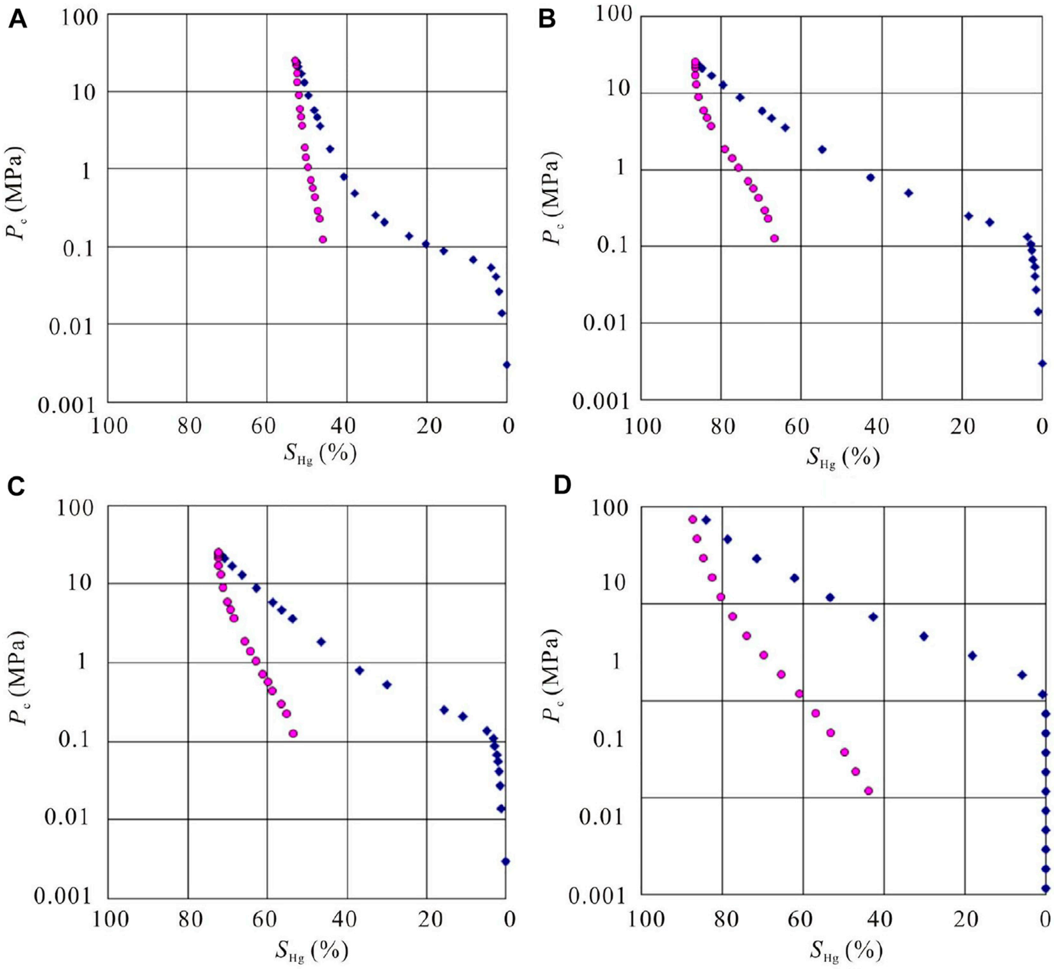

FIGURE 8
Classification results of pore throat types of tight sandstones in the Quan 3 Member. Notes: **(A)** Type I reservoir, Jian 24 well, 364.93m; **(B)** Type II reservoir, Jian 24 well, 418.55m; **(C)** Type III reservoir, Xin 269 well, 1264.45m; **(D)** Type IV reservoir, Xin 207 well, 1180.00m.

0.1 mD (Figure 9). The limit of daily liquid production less than 1t is between $\phi = 10\%$ and $K = 1$ mD (Figure 10). Therefore, the lower limits of the effective reservoir physical properties of the Quan 3 Member reservoir is: porosity of 10% and permeability of 0.1 mD.

Criteria for reservoir classification

According to the mercury intrusion curve characteristics, physical properties, pore-throat combinations, and sedimentary facies, the target layers are divided into four categories (Table 2): Medium-small pore, medium-throat, medium-high permeability reservoir (Type I); small-pore, fine-throat, low-permeability reservoir (Type II), small pore,d fine throat, extra-low permeability reservoir (Type III), and micro-pore, micro-throat, ultra-low permeability reservoir (Type IV).

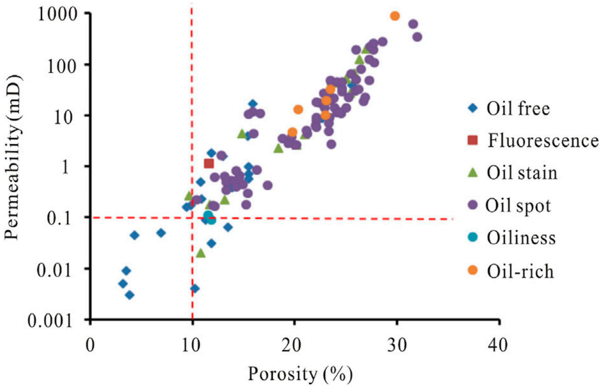

FIGURE 9
Relationship between oil content and physical properties revealed by the cores of the Quan 3 Member.

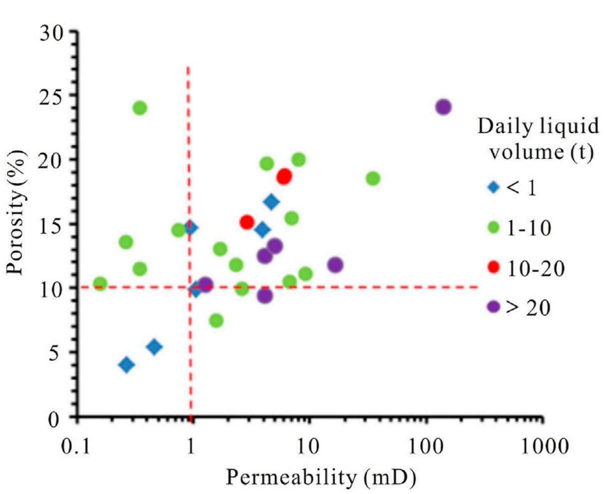

FIGURE 10
Relationship between liquid production and physical properties in the Quan 3 Member.

Type I reservoir: It is dominated by medium-small pore and medium-throat, and the permeability is between 200 mD and 900 mD, with an average value of 433 mD; ϕ (porosity) > 25%, the average value of ϕ is 26.7%, and the average pore radius is > 4.5 μm; the maximum mercury saturation is between 61% and 93%, and the displacement pressure is between 0.04 MPa and 0.1 MPa. This type of reservoir is mainly located in the Fuyu Oilfield, and it is mainly developed in (underwater) distributary channels and point bars.

Type II reservoir: It is dominated by small pores and fine throats, and the permeability is between 13 mD and 80 mD, with an average value of 52.4 mD; ϕ = 20%–25%, the average value is 22.3%; the average pore radius is between 1 and 4μm, and the average value is 2.5 μm; moreover, the displacement pressure is between 0.09 MPa and 0.15 MPa, and the average value is 0.11 MPa. This type of reservoir is mainly developed in point bar.

Type III reservoir: It is mainly composed of small pores and fine throats, and the permeability is between 1 mD and 40 mD, with an average value of 18 mD; ϕ = 15%–20%, the average value is 15.7%; the average pore radius is between 1 and 3 μm, and the average value is 2.0 μm; the displacement pressure is between 0.15 and 2.08 MPa. Reservoirs of this type are mainly located in the Xinmu and Xinmiao Oilfields, and are mainly developed in natural levees and inter-tributary bays.

Type IV reservoir: It is mainly composed of micro-pores and micro-throats, with a permeability of 0.5 mD to 5 mD and an average value of 2.12%; ϕ = 11%–14%, and its average is 13.1%; the average pore radius ranges from 0.17 to 0.97 μm, and the average value is 0.64 μm; the displacement pressure is greater than 4 MPa. Reservoirs of this type are mainly located in the Xinli Oilfield, and are mainly developed in floodplains and inter-tributary bays.

Prediction of sweet spots

In this paper, the planar distribution of different types of reservoirs in the I sandstone group of the Quan three Member is predicted according to the established reservoir classification standard. In the sandstone group I, the overall quality of the reservoir is good, the effective reservoir can reach the entire Fuxin Uplift Belt, and the sand bodies are well connected with each other.

Type I reservoir sweet spots are mainly developed in the Fuyu Oilfield in the southeast (Figure 11). The sandstones in this area suffered less compaction, and mainly developed primary pores and secondary pores formed by late dissolution.

Type II reservoirs are mainly developed in point bar bodies of the Xinmin Oilfield in the northeast (Figure 11). There are also a small number of Type II reservoirs in the point bars in the southeast of the Xinmu Oilfield, which are mainly due to shallow burial, less compaction and lower cement content. In addition, a certain amount of Type II reservoirs are developed in the northern part of the Xinli and Xinmiao Oilfields, which are mainly controlled by organic acid dissolution. The organic acid dissolution effectively improves the physical properties of the reservoir (Zhang et al., 2014c; Yin and Wu., 2020).

TABLE 2 Statistical results of physical properties of different types of reservoirs in the Quan 3 Member of the Quantou Formation in the study area.

Reservoir category	Pore throat feature	Permeability type	Sedimentary facies	Porosity (%)	Permeability (mD)	Average throat radius (μm)
Type I	Medium-small pore-medium throat	Medium-high	(Underwater) distributary channels and point bar	> 25%	>100	> 4.5
Type II	Small pore - thin throat	Low	Branch channel and point bar	20%–25%	10–100	1–4
Type III	Small pore - thin throat	Extra Low	Natural levees and interchannel branch	15%–20%	1–10	1–3
Type IV	Micropore - microthroat	Extra Low-ultra-low	Floodplain	10%–15%	0.1–1	0.2–1
Tight layer	Micropore - microthroat	Dense	Floodplain and flooding lake	< 10	< 0.1	< 0.2

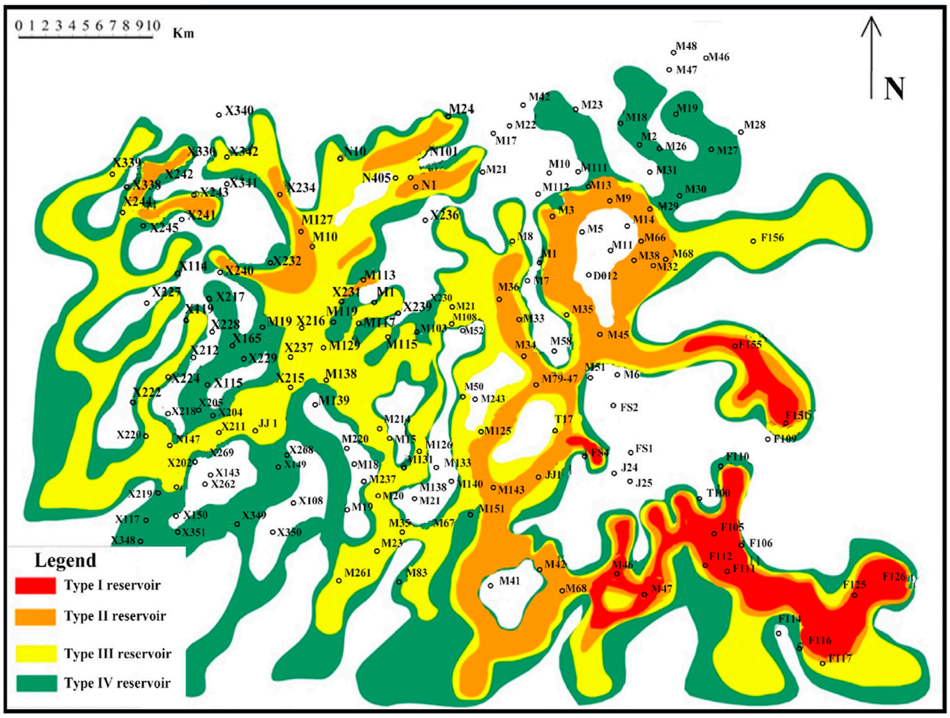

FIGURE 11
Prediction of the reservoir distribution of the I sandstone group in the Quan 3 Member of the Quantou Formation in the study area.

Type III reservoirs are mainly developed in the branch channel sand bodies of the Xinmu, Xinbei and Xinmin Oilfields in the central part (Figure 11). Due to its small particle size and lack of organic acid dissolution, its physical properties are relatively poor. A certain amount of Type III reservoirs are also developed in the west of the Xinli Oilfield, which are mainly located in the Xinli Structural Belt, and their burial depth is relatively shallow.

Type IV reservoirs are mainly developed in the point bars of the Xinli Oilfield (Figure 11). Its burial depth is relatively large, and the compaction effect is strong. The diagenetic stage is mostly in the middle diagenetic A2 stage, which has been cemented by iron calcite, and it is difficult to effectively improve its physical properties by dissolution.

Conclusion

1) In this paper, taking the Quan 3 Member in the Fuxin Uplift Belt of the Songliao Basin as an example, the microscopic pore structure characteristics of tight oil sandstones have been systematically studied, and the classification standard of tight sandstones has been formulated. Furthermore, the sweet spots of the main production layers are predicted.
2) The sedimentary facies of the Quan 3 Member in the study area are meandering river facies and shallow water delta facies. Feldspar lithic fine sandstones are developed in the target layer, and calcareous sandstone is locally developed. Moreover, the mian pore types of the target layer include dissolved intergranular and intragranular pores, followed by primary intergranular pores, and micro-fractures are occasionally seen.
3) According to the mercury intrusion test results, the pore-throat structures of the reservoir in the Quan 3 Member are divided into four types: (1) small-pore medium-throat type (point bar and delta distributary channel), (2) small-pore micro-throat type (point bar), (3) small-pore micro-throat type (natural levee), (4) micro-pore micro-throat type (river floodplain and inter-tributary bay).
4) The lower limits of the physical properties of the effective reservoirs in the Quan 3 Member has been determined: the porosity is 10% and the permeability is 0.1 mD. Finally, combined with mercury intrusion curves, physical property tests and sedimentary facies characteristics, the classification standard of the Quan 3 Member reservoirs was formulated.
5) For the I sandstone group, the sweet spots of the Type I reservoirs are mainly developed in the Fuyu Oilfield in the southeast areas. The sandstones in this area suffered less compaction, and primary and secondary pores that suffered from late dissolution are mainly developed.

Data availability statement

The original contributions presented in the study are included in the article/Supplementary Material, further inquiries can be directed to the corresponding author.

Author contributions

QZ is responsible for the idea and writing of this paper, and YZ, BW, SY, XW, and CY are responsible for the data and analysis.

Funding

This manuscript was supported by the National Natural Science Foundation of China (Grant No. 41872134 and No. 41302081) and Jilin Oilfield Branch Company Ltd., PetroChina (Grant No. HX20180033).

Conflict of interest

YZ was employed by the Petroleum Exploration and Production Research Institute, SINOPEC. BW was employed by the Sinopec Chongqing Fuling Shale Gas Exploration and Development Co., Ltd.

The remaining authors declare that the research was conducted in the absence of any commercial or financial relationships that could be construed as a potential conflict of interest.

Publisher's note

References:

Bello, A. M., Jones, S., Gluyas, J., Acikalin, S., and Cartigny, M. (2021). Role played by clay content in controlling reservoir quality of submarine fan system, Forties Sandstone member, Central Graben, North Sea. *Mar. Petroleum Geol.*, 128, 105058. doi:10.1016/j.marpetgeo.2021.105058

Boutaleb, K., Baouche, R., Sadaoui, M., and Radwan, A. E. (2022). Sedimentological, petrophysical, and geochemical controls on deep marine unconventional tight limestone and dolostone reservoir: Insights from the Cenomanian/Turonian oceanic anoxic event 2 organic-rich sediments, Southeast Constantine Basin, Algeria. *Sediment. Geol.* 429, 106072. doi:10.1016/j.sedgeo.2021.106072

Cui, X., and Radwan, A. E. (2022). Coupling relationship between current *in-situ* stress and natural fractures of continental tight sandstone oil reservoirs. *Interpretation* 10 (3), SF9–SF21. doi:10.1190/int-2021-0200.1

Enayati-Bidgoli, A., and Saemi, E. (2019). Effects of late diagenesis on primary reservoir quality of a quartz arenite unit: A case study from the lower cretaceous successions of SW Iran. *Pet. Sci.* 16 (2), 267–284. doi:10.1007/s12182-019-0306-x

Haile, B. G., Klausen, T. G., Czarniecka, U., Xi, K., Jahren, J., and Hellevang, H. (2018). How are diagenesis and reservoir quality linked to depositional facies? A deltaic succession, edgeøya, svalbard. *Mar. Petroleum Geol.* 92, 519–546. doi:10.1016/j.marpet-geo.2017.11.019

Hijaz, K. H., Adrian, S., Meor, H. A. H., and Abdullah, W. H. (2020). Digital core analysis: Characterizing reservoir quality through thin sandstone layers in heterolithic rocks, *J. Appl. Geophys.*, 182, 178–210. doi:10.1016/j.jappgeo.2020.104178

Jabir, A., Cerepi, A., Loisy, C., and Rubino, J. L. (2021). Evaluation of reservoir systems in Paleozoic sedimentary formations of Ghadames and Jefarah basins, *J. Afr. Earth Sci.*, 183, 104324–104327. doi:10.1016/j.jafrearsci.2021.104324

Kassem, A. A., Hussein, W. S., Radwan, A. E., Anani, N., Abioui, M., Jain, S., et al. (2021). Petrographic and diagenetic study of siliciclastic Jurassic sediments from the Northeastern Margin of Africa: Implication for reservoir quality. *J. Petroleum Sci. Eng.* 200, 108340. doi:10.1016/j.petrol.2020.108340

Khan, E. U., Saleem, M., Naseem, A. A., Ahmad, W., Yaseen, M., and Khan, T. U. (2020). Microfacies analysis, diagenetic overprints, geochemistry, and reservoir quality of the jurassic samanasuk. Formation at the kahi section, nizampur basin, NW himalayas, Pakistan. *Carbonates Evaporites* 35 (3), 95–96. doi:10.1007/s13146-020-00622-4

Li, F. J., Wang, D. Y., and Xu, X. H. (2005). The influential factors and charactristics of triassic yanchang formantion reservoir in longdong area, ordos basin. *Pet. Exp. Geol.* 27 (4), 355–370. doi:10.1016/j.molcatb.2005.02.001

Li, J. J., Wang, Z. Z., and Zhang, Z. H., (2013). The sedimentary facies of member-3 of Quantou Formation in Xinli oilfield, Songliao Basin. *Xinjiang Pet. Geol.*, 5(8), 534–537.

Liu, D. K., Sun, W., and Ren, D. Z., (2019). Experimental investigation of pore structure and movable fluid traits in tight sandstone, *Process. (Basel).*, Experimental investigation of pore structure and movable fluid traits in tight sandstone. Processes, 7(3), 149–156. doi:10.3390/pr7030149

Lv, T. X., and Li, Z. P. (2021). Quantitative characterization method for microscopic heterogeneity in tight sandstone. *Energy Explor. Exploitation* 13, 1076–1096. doi:10.1177/0144598721993937

Mahmi, O., Dypvik, H., and Hammer, E. (2018). Diagenetic influence on reservoir quality evolution, examples from Triassic conglomerates/arenites in the Edvard Grieg field, Norwegian North Sea. *Mar. Petroleum Geol.* 93, 247–271. doi:10.1016/j.marpetgeo.2018.03.006

Mirzaei-Paiaman, A., and Ghanbarian, B. (2021). A new methodology for grouping and averaging capillary pressure curves for reservoir models. *Energy Geosci.* 2 (1), 52–62. doi:10.1016/j.engeos.2020.09.001

Nabawy, B. S., Abudeif, A. M., Masoud, M. M., and Radwan, A. E. (2022). An integrated workflow for petrophysical characterization, microfacies analysis, and diagenetic attributes of the Lower Jurassic type section in northeastern Africa margin: Implications for subsurface gas prospection. *Mar. Petroleum Geol.* 140, 105678. doi:10.1016/j.marpetgeo.2022.105678

Qiao, J. C., Zeng, J. H., Jiang, S., Feng, S., Feng, X., Guo, Z., et al. (2019). Heterogeneity of reservoir quality and gas accumulation in tight sandstone reservoirs revealed by pore structure characterization and physical simulation, *Fuel*, 253, 1300–1316. doi:10.1016/j.fuel.2019.05.112

Radwan, A. E., Rohais, S., and Chiarella, D. (2021). Combined stratigraphic-structural play characterization in hydrocarbon exploration: A case study of middle miocene sandstones, gulf of suez basin, Egypt. *J. Asian Earth Sci.*, 218, 104686. doi:10.1016/j.jseaes.2021.104686

Santosh, M., and Feng, Z. Q. (2020). New horizons in energy geoscience. *Energy Geosci.* 1 (1–2), 1–2. doi:10.1016/j.engeos.2020.05.005

Su, Y., Zha, M., Jiang, L., Ding, X., Qu, J., Jin, J., et al. (2022). Pore structure and fluid distribution of tight sandstone by the combined use of SEM, MICP and X-ray micro-CT, *J. Petroleum Sci. Eng.*, 208, 109241–109245. doi:10.1016/j.petrol.2021.109241

Sun, Y., Chen, C., and Ma, S. Z., (2013). Hydrocarbon migration mechanism and mccumulation models of the Fuyu oil layer in southern Fuxin uplift, Songliao Basin. *Geol. Rev.*, 59 (3), 501–509. doi:10.16509/j.georeview.2013.03.006

Sun, Y., Zhang, J. Y., and Ma, S. Z., (2014). Analysis of high-resolution sequence stratigraphy of Fuyu oil layer in the southern Fuxin Uplift. *Geol. Rev.*, 3, 473–480.

Tang, Z. X., Bai, L. D., and Gui, P. (2009). Exploration practice of old oil area in Fuxin uplift, southern Songliao Basin. *Pet. Geol.* 4, 17–20. doi:10.3969/j.issn.1672-7703.2009.04.004

Wang, W. G., Lin, C. Y., Zhang, X. G., Dong, C., Ren, L., and Lin, J. (2020). Effect of burial history on diagenetic and reservoir-forming process of the Oligocene sandstone in Xihu sag, East China Sea Basin, *Mar. Petroleum Geol.*, 112, 104034–104035. doi:10.1016/j.marpetgeo.2019.104034

Wang, W., Li, R. L., and Zhao, H. W., (2016) Combined pattern of controlled depression fault and its influence on hydrocarbon accumulation in southern part of Songliao Basin Fault Group. *Unconv. oil gas*, 3(5), 14–20.

Wang, Z., and Yang, G. Q., (2017). Some research hot spots of tight oil and gas reservoir. *Chin. foreign energy*, 16(8), 37–42.

Wu, Y., Tahmasebi, P., Lin, C., Zahid, M. A., Dong, C., Golab, A. N., et al. (2019). A comprehensive study on geometric, topological and fractal characterizations of pore systems in low-permeability reservoirs based on SEM, MICP, NMR, and X-ray CT experiments. *Mar. Petroleum Geol.* 103, 12–28. doi:10.1016/j.marpetgeo.2019.02.003

Wu, Y., Tahmasebi, P., Lin, C., and Dong, C. (2020c). A comprehensive investigation of the effects of organic-matter pores on shale properties: A multicomponent and multiscale modeling. *J. Nat. Gas. Sci. Eng.* 81, 103425. doi:10.1016/j.jngse.2020.103425

Wu, Y., Tahmasebi, P., Lin, C., and Dong, C. (2020b). Process-based and dynamic 2D modeling of shale samples: Considering the geology and pore-system evolution. *Int. J. Coal Geol.* 218, 103368. doi:10.1016/J.COAL.2019.103368

Wu, Y., Tahmasebi, P., Yu, H., Lin, C., Wu, H., and Dong, C. (2020a). Pore-scale 3D dynamic modeling and characterization of shale samples: Considering the effects of thermal maturation. *J. Geophys. Res. Solid Earth* 125 (1), 1–10. doi:10.1029/2019JB018309

Xiao, Z. K., Ding, W. L., Hao, S. Y., Taleghani, A. D., Wang, X., Zhou, X., et al. (2019). Quantitative analysis of tight sandstone reservoir heterogeneity based on rescaled range analysis and empirical mode decomposition: A case study of the chang 7 reservoir in the dingbian oilfield, *J. Petroleum Sci. Eng.*, 182, 106326–106347. doi:10.1016/j.petrol.2019.106326

Yang, S. S., Zhang, J. C., and Huang, W. D., (2013). "Sweet spot" types of reservoirs and gGenesisof tights and stone gas in Kekeya area, Turpan-Hami Basin. *J. petroleum*, 34(2), 272–282.

Yang, X. P., and Chen, L. H. (2001). Study on diagenetic facies of low permeability reservoir of Yanchang Formation in Shanbei Slope. *Petroleum Explor. Dev.* 28 (4), 38–40. doi:10.3321/j.issn:1000-0747.2001.04.011

Yin, S., and Wu, Z. (2020). Geomechanical simulation of low-order fracture of tight sandstone. *Mar. Petroleum Geol.* 100, 359–369. doi:10.1016/j.marpetgeo.2020.104359

Zhang, B., Shen, B., and Zhang, J. (2020). Experimental study of edge-opened cracks propagation in rock-like materials. *J. Min. Strata Control Eng.* 2 (3), 033035. doi:10.13532/j.jmsce.cn10-1638/td.20200313.001

Zhang, J. Y., Sun, Y., and Tian, X. L., (2014a). Provenance analysis on the Fuyu reservoir in xinmiaoxi-xinbei regions of the northern Fuxin uplift, Songliao Basin. *Sci. Technol. Eng.*, 14 (26): 200 ~ 204.

Zhang, Q., Wu, X., Radwan, A., Wang, B., Wang, K., Tian, H., et al. (2022). Diagenesis of continental tight sandstone and its control on reservoir quality: A case study of the quan 3 member of the cretaceous Quantou Formation, Fuxin uplift, Songliao Basin. *Mar. Petroleum Geol.* 145, 1–10. doi:10.1016/j.marpetgeo.2022.105883

Zhang, Q., Zhu, X. M., and Mao, L. (2021). Pore evolution and Genesis of secondary pores in the paleogene dainan formation, jinhu sag, subei basin. *Earth Sci. Front.* 28 (1), 190–201. doi:10.13745/j.esf.sf.2020.5.18

Zhang, Q., Zhu, X. M., and Steel, R. J., (2014b). Variation and mechanisms of clastic reservoir quality in the paleogene shahejie formation of the dongying sag, bohai bay basin, *China. China Petroleum Science*, 11(2), 200–210. doi:10.1007/s12182-014-0333-6

Zhang, Q., Zhu, X. M., Steel, R. J., Wang, G., and Ji, H. (2014c). Fluid inclusions and their application in hydrocarbon history and Genesis. *Petroleum Sci. Technol.* 32, 2911–2920. doi:10.1080/10916466.2014.933976

frontiers | Frontiers in Earth Science

TYPE Original Research
PUBLISHED 16 January 2023
DOI 10.3389/feart.2022.931611

OPEN ACCESS

EDITED BY
Bjarne Sven Gustav Almqvist,
Uppsala University, Sweden

REVIEWED BY
Xinpeng Pan,
Central South University, China
Jing Ba,
Hohai University, China

*CORRESPONDENCE
Luanxiao Zhao,
zhaoluanxiao@tongji.edu.cn

SPECIALTY SECTION
This article was submitted
to Solid Earth Geophysics,
a section of the journal
Frontiers in Earth Science

RECEIVED 29 April 2022
ACCEPTED 27 October 2022
PUBLISHED 16 January 2023

CITATION
Ali Hussein AA, Zhao L, Chen Y and Wang J (2023), Rock physics characteristics of marine sediments in the South China sea: The link between the geological factors and elastic properties.
Front. Earth Sci. 10:931611.
doi: 10.3389/feart.2022.931611

Rock physics characteristics of marine sediments in the South China sea: The link between the geological factors and elastic properties

Abdullah Ali Ali Hussein[1], Luanxiao Zhao[1]*, Yuanyuan Chen[1] and Jiliang Wang[2]

[1]State Key Laboratory of Marine Geology, Tongji University, Shanghai, China, [2]Institute of Deep-sea Science and Engineering, Chinese Academy of Sciences, Sanya, China

Understanding the geological factors behind the physical and elastic properties of marine sediments and unconsolidated rock is essential for the interpretation of geophysical measurements, hazard assessment, and ocean engineering applications. Core and well logging data from the six drilling sites of the Ocean Drilling Program/International Ocean Discovery Program (ODP/IODP) were used to analyze the rock physical characteristics in the South China sea. The depositional environment plays a significant role in affecting the physical properties of marine sediments. The sediments deposited under shallow water conditions show a higher velocity than the basin, slope, and deeper shelf carbonate deposits. Moreover, the non-depositional hiatus along the Oligocene-Miocene boundary displays a notable control on the variation of rock physical properties. It is found that the lithofacies and physical compaction remarkably influence the elastic characteristics of P-impedance and Vp/Vs ratio. The calcareous-rich sediment and ooze have very low P-impedance and high Vp/Vs ratio, whereas the siltstone and coarse sand present high P-impedance and low Vp/Vs ratio characteristics. With the enhancement of the consolidation degree, the Vp/Vs ratio significantly decreases from 6 to less than 2, suggesting that the shear wave velocity is highly sensitive to physical compactions. The basalt at site U1431 is considerably lower in its P-wave velocity than that at the site of U1433, which is probably caused by the intense fracturing occurring at the site of U1431 associated with different tectonic environments. We establish the link between geological factors and elastic characteristics of marine sediments of SCS, laying the foundation for characterizing depositional environments, lithofacies, and compaction degrees using geophysical measurements.

KEYWORDS

South China sea, rock physics, depositional environment, elastic properties, lithofacies

Introduction

Many geological factors, including lithological variations, compaction conditions, depositional environment, mechanical, and chemical diagenesis, and tectonic activities, can exert notable influence on the elastic characteristics of marine sediments (Ymd, 1973; Hamilton, 1974, 1976, 1980; Hamilton et al., 1982; Richardson et al., 1997; Breitzke, 2000; Eberli et al., 2003; Stewart et al., 2003; Fabricius, 2007, 2014; Ba et al., 2017; Zhang et al., 2020; Zhao et al., 2020; Lyu et al., 2021; Zhang et al., 2021). As a consequence, understanding the rock physical characteristics (especially the elastic signatures) of the marine sediments and unconsolidated rocks plays a critical role in linking geology to geophysical measurements (sonic and surface seismic data). In addition, it also provides important insights into economic resource development, hazard assessment, and ocean engineering applications (Cai et al., 2015; Hughes et al., 2015; Martin et al., 2015; Hou et al., 2018; Graw et al., 2020; Gatter et al., 2021; Ayoub et al., 2022). The primary objective of this study is to systematically analyze the rock physical characteristics in the SCS and their influencing factors based on the ODP/IODPdata.

Using the IODP core and logging data, many researchers have made efforts to understand how the geological factors influence the physical properties of different rocks (e.g., velocity, density, porosity, and attenuation) (Hamilton, 1972; Van der Lingen and Packham, 1975; Nobes et al., 1991; Bassinot et al., 1993; Urmos, 1994; David et al., 1999; Kenter et al., 2002; Kim and Kim, 2005; Courville et al., 2007; Pola et al., 2012; Christeson et al., 2018; Xie et al., 2018; Lee et al., 2021). According to Nobes et al. (1991), the diagenesis, carbonate content, tectonism, lithology, and depositional hiatuses significantly affected the physical rock properties of marine sediments at leg 114 in the South Atlantic. They also point out that the carbonate content and diagenesis decrease porosity and hence increase velocity. Christeson et al. (2018) observed significant variability in velocity, density, and porosity measurements at Hole M0077A due to lithological composition, rate of deposition, shock intensity, and nature of deformation (i.e., density, connectivity, and secondary filling of fractures). Similarly, Van der Lingen and Packham (1975) use DSDP Sites 288 and 289 to evaluate the physical properties of marine sediments, and they found that the differences in physical properties (especially in the porosity) were indicative of differences in diagenesis degree. Furthermore, the results of Kenter et al. (2002) and Eberli et al. (2003) from ODP site 1003 and leg 166, respectively, indicated that porosity, especially the heterogeneous pore structure significantly affects the elastic responses of the carbonate rocks.

It is worth mentioning that the rock physical characteristics of marine sediments and unconsolidated rocks in the SCS are sparsely reported. The SCS has experienced a rapid and narrow transition from the continental breakup with basalt-type magmatism to igneous oceanic crust (Larsen et al., 2018). Based on the results of the ODP/IODP drilling in the SCS, the geological features display a radical contrast reflecting a shift of the depositional facies from terrestrial to shallow and then deep marine (Jian et al., 2019). New drilling results from IODP expeditions 349 and 367/368 represent a change in the depositional environment from the Eocene's coastal-shallow shelf to the Oligocene's outer shelf-slope settings, where the controlling factors might be the nutrient supply and water temperature (Ma et al., 2019). The unique tectonic and depositional environment of the South China Sea may significantly control the physical properties of marine sediments. Moreover, the SCS is a typical deep-water basin, exhibiting high pressure and temperature characteristics. Therefore, the rock physical characteristics in SCS might be different from that of other well-studied marginal seas (e.g., Gulf of Mexico, North Sea), hence affecting its corresponding elastic signatures (Wang et al., 2021).

Therefore, the primary contribution of this study is to systematically analyze the rock physical characteristics in the SCS based on the analysis of the ODP/IODP core and logging data at different sites (U1148, U1431, U1433, U1499, U1501, and U1505). Additionally, we explore the different influences of geological factors such as depositional environment, non-depositional hiatus, lithofacies, physical compaction, and tectonic activity on the physical properties of rocks. We compare and evaluate the rock physical characteristics of different sites in the SCS.

The paper is organized as follows: First, we briefly introduced the geological setting and IODP data of the SCS. Then, we presented a detailed analysis of geological factors' influence on the rock physical properties, especially the elastic signature of P-wave impedance and Vp/Vs ratio. Subsequently, we explored the effects of the carbonate content on the rock physics characteristics and discussed the implications for seismic stratigraphy interpretation.

Geological setting and data description

The South China Sea is considered one of the vast marginal seas in East Asia. As shown in Figure 1, the SCS's deep-sea basin can be further subdivided into three sub-basins, namely the Southwest Sub-basin (SWSB), Northwest Sub-basin (NWSB), and East Sub-basin (ESB). These sub-basins are bounded by the Zhongnan Fault (Figure 1) (Li et al., 2014). The average depth of the SCS oceanic basin is about 4700 m. It is characterized by a complex depositional system that serves as a final basin of sediment particles transported by different currents (Zhou et al., 2019).

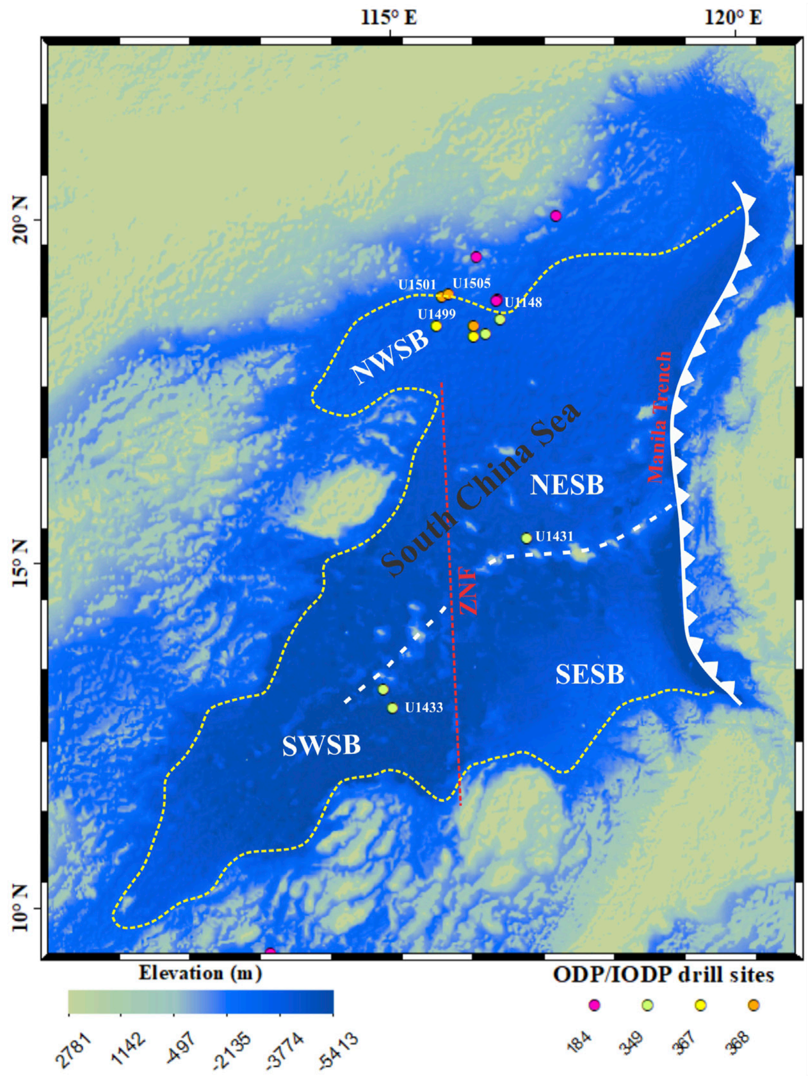

FIGURE 1
Bathymetric map of the (SCS) area. The solid yellow line indicates the ocean continent boundary whereas the red dashed line indicates the Zhongnan Fault (ZNF). The white dashed line shows the fossil-spreading ridge, while white solid line represent the subduction along the Nansha Trough and the Manila Trench. The circles indicate the location of ODP/IODP sites used in this study. SWSB is an abbreviation of the Southwest Sub-basin, NESB, Northeast Sub-basin; SESB, So utheast Sub-basin; NWSB, Northwest Sub-basin.

As displayed in Figure 2, four lithostratigraphic units (I, II, III, and IV) were identified according to the analysis of physical properties and depositional environments by the comparison among the six drilling sites (U1148, U1431, U1433, U1499, U1501, and U1505) in the study area. These units predominantly consist of different lithologies including claystone and clay with common silt, carbonate turbidites, and siliciclastic sediments with the rare existence of thin layers of volcanoclastic breccia in some areas. The early Miocene's lower unit (lithostratigraphic Unit IV) consists mainly of basaltic igneous rocks and a very small amount of clay-rich thin-bedded rocks. A brief description of the four lithostratigraphic units is given as follows:

1) Unit I of the early Miocene to Pleistocene age was deposited in the deep-water environment and dominated by nannofossil carbonate ooze with clay/claystone and negligible silt in some areas. This unit has a relatively high biogenic carbonate content.

2) Unit II includes late Eocene to late Oligocene siliciclastic deposits (Figure 2). The lower part of this unit

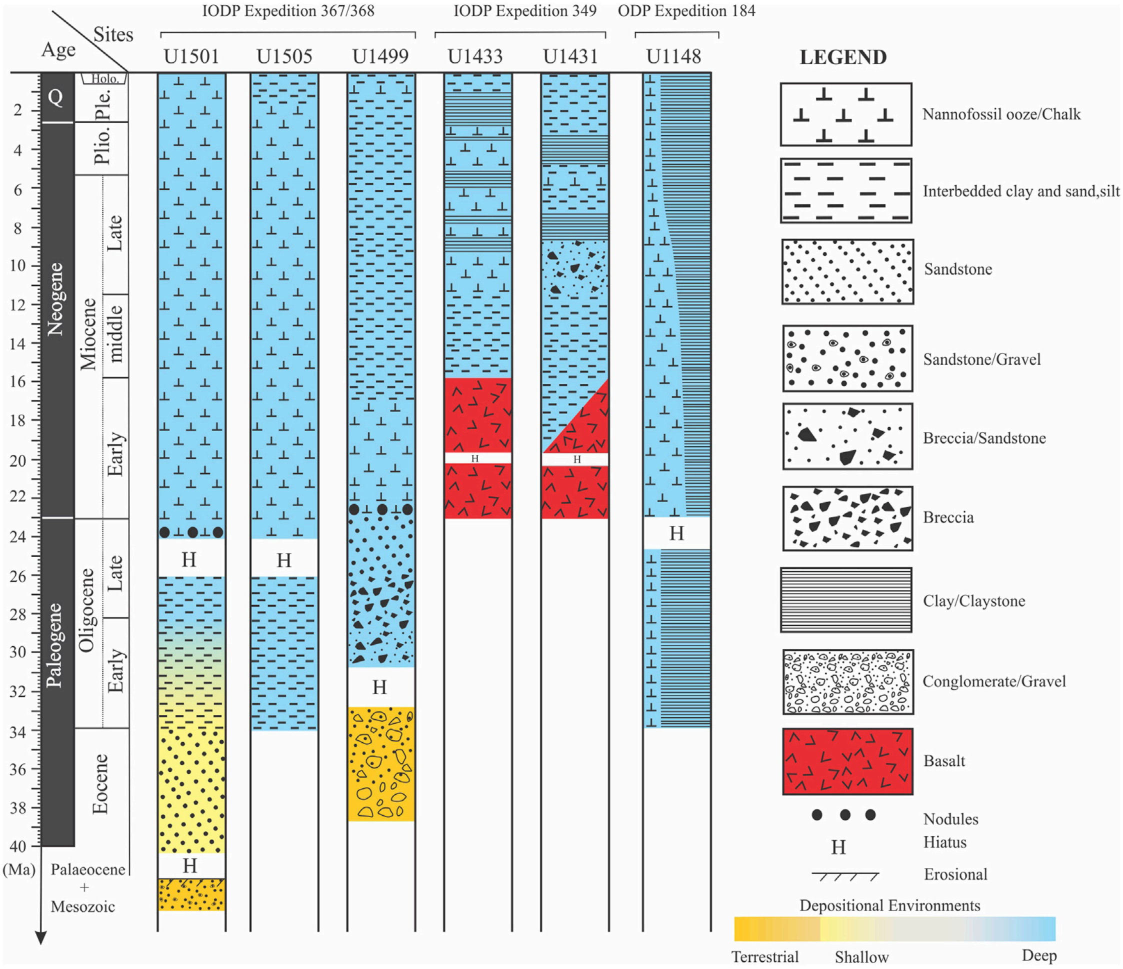

FIGURE 2
A summary of the stratigraphic columns based on deep-sea drilling results from the ODP/IODP South China Sea Sites.

encompasses intervals of coarse sand dominated by shallow water interbedded with dark grey clayey silt containing organic matter. However, the upper part generally reveals a fining upward of clastic material reflecting deep basin situations from the bottom (shallow marine) to the top (bathyal depths). Compared to Unit I, this unit consists of low carbonate content (Figures 3A,B). In contrast, Unit II of the late Miocene to early Pleistocene age at IODP Sites U1431 and U1433 is composed mainly of clay and carbonate ooze interpreted as turbidite deposition, and volcanoclastic breccia interbedded with sandstone, respectively (Li et al., 2015b) indicating high-energy environments. The distinctive layer of volcaniclastic breccia is mainly formed due to several eruptions of volcanic activities from the adjacent seamount (Yan et al., 2014), whereas the source of carbonate turbidite is likely from Dangerous Grounds or Reed Bank (Hutchison and Vijayan, 2010; Franke et al., 2011; Yao et al., 2012; Ding et al., 2013). This suggests rapid redeposition from shallower water settings to a deep-water basin by turbidity currents (Li et al., 2015b).

3) Unit III, of possibly Eocene age, mainly contains coarse sand intervals with clasts up to the size of pebbles at both IODP Sites U1501and U1499. As illustrated in Figure 3B, the sandstone differs from Unit II to Unit III in terms of its physical characteristics, color, degree of lithification, and composition of clastic components. Therefore, Unit III was considered to be established in a littoral-terrestrial environment.
4) Unit IV of the early Miocene is mainly composed of massive basalt lava flows separated by a layer of claystone up to 5 m thick, which clearly shows a variation in the physical properties of the rocks.

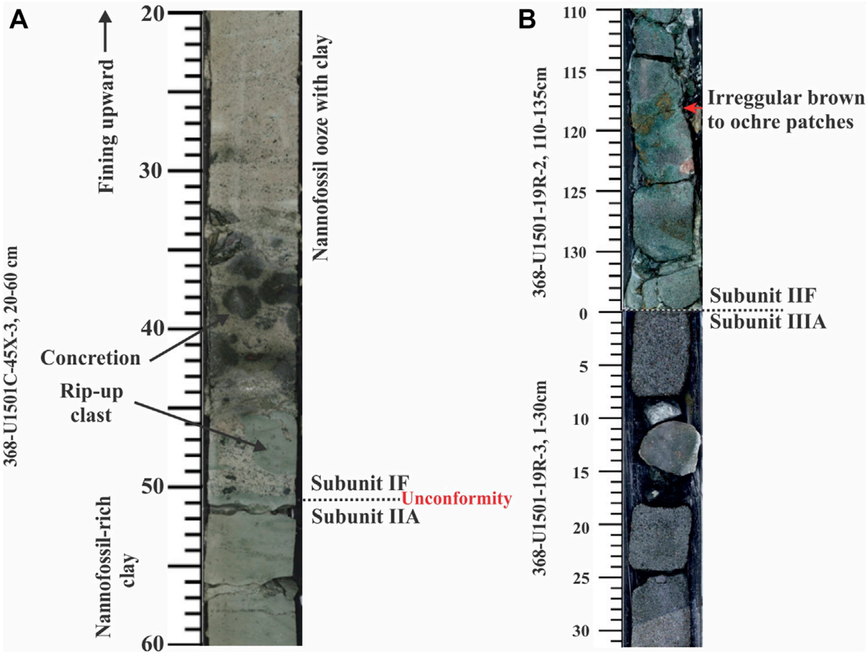

FIGURE 3
(A) Core photo showing the boundary between Units I and II (368-U1501C-45X-3, 20–60 cm) which represent unconformity. Nannofossil ooze with clay and dominates Subunit IF with centimeter-sized concretions at the lower boundary and rip-up clasts. Subunit IIA is dominated by nannofossil-rich clay; **(B)** Images of core section from IODP site U1501 showing the change of lithology from Subunit IIF to Subunit IIIA and the boundary represent non-depositional hiatus. The lower red arrow of Subunit IIF shows irregular brown to ochre and purple patches inferred to be related to diagenetic alteration (Sun et al., 2018).

The data used in this study include cores and well-logging data. Figure 1 shows the sampling locations, and the available data are listed in Table 1. Four sites (U1148, U1499, U1505, and U1501) were drilled in the continental slope and abyssal basin during ODP/IODP Expeditions 184, 367, and 368. They comprise the Cenozoic sediments overlying the basement, and two sites (U1431 and U1433) were drilled in the central basin during IODP Expedition 349 (Table 1). The depth of sites varied between 0 and 1072.15 m from the Eocene to the Pleistocene. The collected data from the expeditions were used to interpret and analyze the rock physical properties such as density, P-wave velocity, and porosity.

Rock physics characteristics and analysis of influencing factors

Influences of depositional units

Figures 4, 5 show the density, velocity, and porosity characteristics of the cored interval of ODP/IODP sites (U1148, U1431, U1433, U1501, and U1505). It is evident that the porosity tends to be inversely related to velocity, whereas density tends to be positively related to velocity.

It can be noted that the different depositional units show distinct rock physical attributes. In unit I, there is a clear increasing trend with depth in density from 1.3 to 1.9 g/cc, P-wave velocity from 1450 to 1930 m/s, and P-impedance from 2000 to 3500 m/s*g/cc. However, the porosity decreases with depth from 79% to 46% (Figures 4A–C). This is most likely due to the loss of organic matter as a result of the water shallowing. It is also associated with an abrupt increase in carbonate content (30 wt%–65 wt%), as nannofossil ooze replaces clay over this interval.

The transitions from unit I to unit II at ODP/IODP sites U1148, U1501, and U1505 show a notable reduction in bulk densities, velocities, and P-impedance as well as an obvious increase in porosities at the Miocene/Oligocene boundary (Figures 4A–C). This change in physical properties showed that the northern SCS was affected by various provenances across the Oligocene/Miocene boundary with non-depositional hiatus possibly formed. At this boundary, the hiatus may have been caused by the effect of a rising sea level, a low supply of terrigenous materials, and comparatively stronger currents in the course of the provenance change (Li et al., 2011). The carbonate-to-clay ratio alters significantly across this boundary. Moreover, more calcareous microfossils are present in Unit 1 than those in Unit II, thus indicating a progressive change of depositional

TABLE 1 Summary of rock physics data used in this study from ODP/IODP Sites in the South China sea.

Expedition	Sites	Depth (m)	Core data					Well log data			
			Porosity	Density	Velocity	Ai	CaCO3	Vp	Vs	Density	Porosity
IODP368	U1501	643.19	✓	✓	✓	✓	✓	✗	✗	✗	✗
	U1505	479.87	✓	✓	✓	✓	✓	✓	✓	✓	✗
IODP 367	U1499	1072.15	✓	✓	✓	✓	✓	✓	✓	✓	✓
IODP 349	U1433	856.69	✓	✓	✓	✓	✓	✓	✓	✓	✗
	U1431	1006.67	✓	✓	✓	✓	✓	✗	✗	✗	✗
ODP 184	1148	844.49	✓	✓	✓	✓	✓	✓	✗	✓	✓

environments from shallow water to deep (lower slope). Such a change is attributed to a reduction in carbonate content from 65% to 10%.

It is necessary to point out that unit II at IODP Site U1501, which comprises siliciclastic sediments, shows some variation in physicalcharacteristics. This is linked to the chaotic depositional environment as well, with the intervening coarse sand to the overall fining of clastic material. The lower part of Unit II between 440 and 600 m comprises coarse sand intervals indicating shallow marine depositional environments with up to pebble-sized clasts, the P-wave velocity, density, and P-impedance can be significantly high, and the porosity can be as low as 8%. It is also interesting to note that the change in depositional environment from shallow water to brackish facies between 510 and 550 m, is associated with a change of lithology from calcareous sandstones to dark grey clayey silt containing organic matter. As we can see in Figure 4B, it shows a higher P-impedance, density, and P-wave velocity than those in the other parts of unit II. The upper part of Unit II between 440 and 380 m shows the overall fining of clastic material indicating shallow water with carbonate content >10%, displaying an increasein density, P-wave velocities, and an abrupt reduction in porosity (from 60% to 35%). In contrast, the major variation in physical properties (increase in P-wave velocity, density, and a decrease in porosity) within Unit II at IODP Sites U1431 and U1433, reflects the massive carbonate and thick breccia interbedded with sandstone (Figures 5A,B), respectively. The transitions from Unit II to Unit III at IODP Sites U1499 and U1501are characterized by a sudden variation in physical properties. An increase in P-wave velocity from 1844–4500 m/s, bulk density

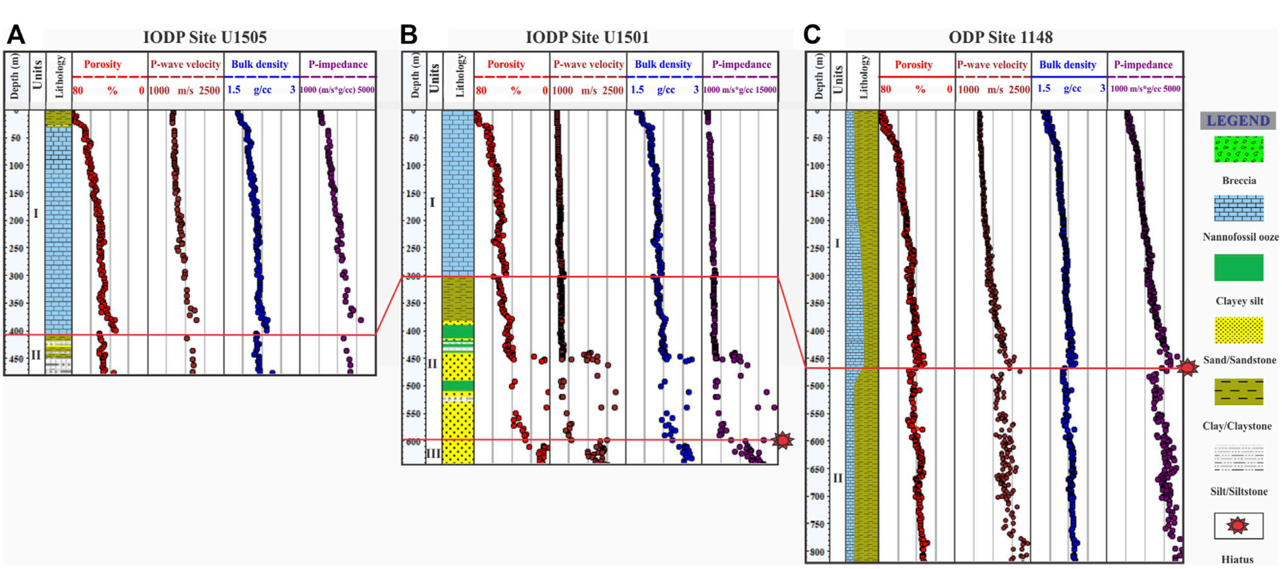

FIGURE 4
Core data results of the studied sites U1501, U1505, and U1148 and the position of non-depositional hiatus, with measurements of moisture, density (MAD), P-wave velocity (PWC), and P impedance. **(A)** Data from IODP site U1505; **(B)** Data from IODP site U1501; **(C)** Data from ODP site 1148.

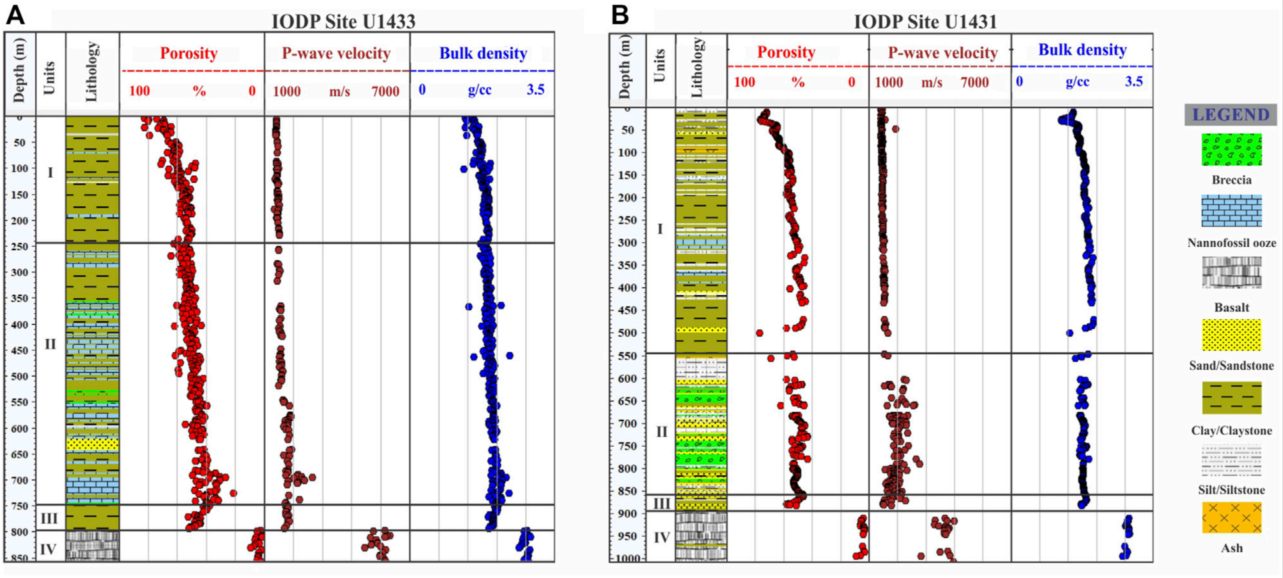

FIGURE 5
Core data results of the studied sites U1433 in the (SWSB) and U1431 in the (ESB), with measurements of moisture, density (MAD) and, P-wave velocity(PWC). **(A)** Data from IODP site U1433; **(B)** Data from IODP site U1431.

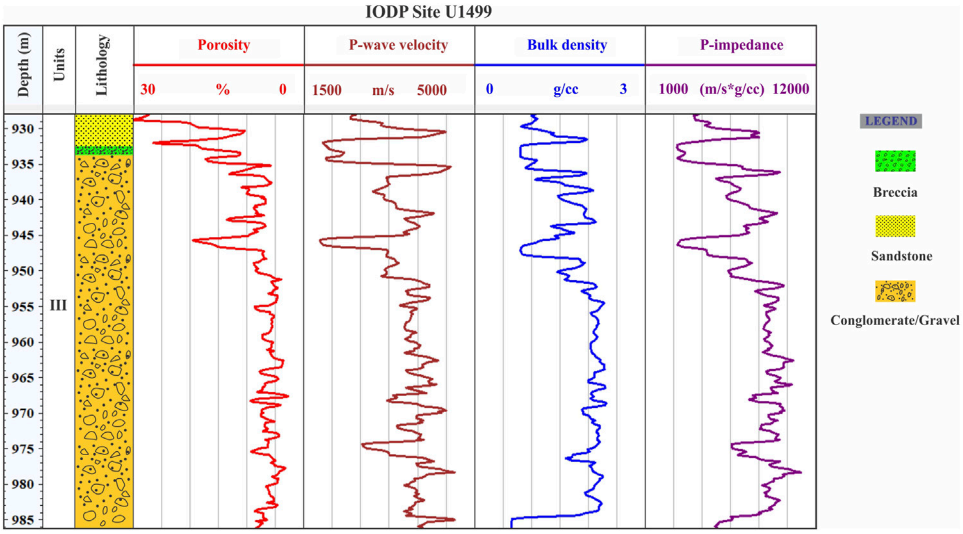

FIGURE 6
Logging curves of the pre-Oligocene interval of IODP Site U1499.

from 1.5 to 2.6 g/cc, and P-impedance from 3190 to 10600 m/s*g/cc while the porosity displays very low values from 29% to 3% (Figures 4B, 6). This variation indicates that the sandstone is quite different from Unit II to Unit III in terms of the physical properties (color, degree of lithification, and composition of clastic components, as shown in (Figure 3B). Therefore, we believethat Unit III was established not far from e littoral-terrestrial environment with an important erosional hiatus that formed in the late Mesozoic or possibly the beginning of the early Cenozoic period. By contrast, unit III at IODP Sites U1431 and U1433 represents the claystone layer recovered directly

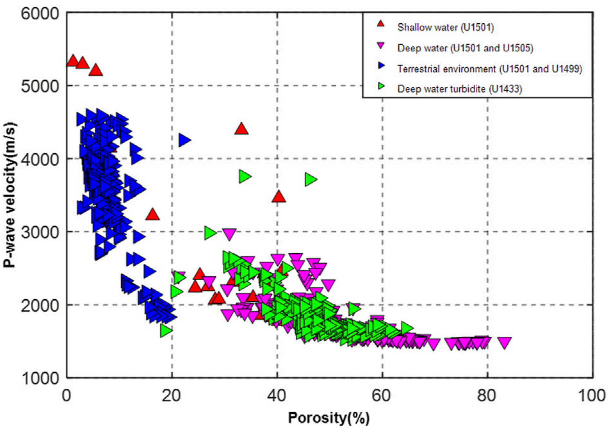

FIGURE 7
Cross plot of P-wave velocity versus porosity for IODP core data of sites U1501, U1505C, U1499, and U1433. Data points are color-coded by different depositional environments.

over the igneous basement. The rock physical characteristics exhibit a trend of decreasing density, from2.13 to 1.86 g/cc and P-wave velocity, from 2100 to 1800 m/s. While the porosity increases to 50%, mainly due to the substantial increase in clay content, which indicatesthat the site is located much closer to continental sediment sources (Figures 5A,B).

The lowermost lithologic Unit IV consists primarily of massive basalt lava flows that display a significant difference in the physical properties of the rocks. It is supported by an increase in both P-wave velocity and density, ranging from 3000 to 6300 m/s and from 2.6 to 2.9 g/cc, respectively, while the porosity is extremely low ranging from 1% to 14% (Figures 5A,B). Furthermore, the presence of a thin layer of clay within the basalt layer at both Sites U1431 and U1433 resulted in changes in physical properties, i.e., decreased velocity and bulk density and increased porosity values. This can be representing non-depositional hiatus between two basaltic flows.

Comparison of depositional environments at different sites on elastic characteristics

Figure 7 illustrates the influences of different depositional environments on the Vp-porosity relationship based on the IODP core data analysis. It is evident that different depositional environments exhibit distinct rock physics characteristics. In general, deep-water turbidite sediments show high porosity and low-velocity signatures. Most of the sediments fall along with the typical suspension trend (Han and Batzle, 2004), where the velocity is almost constantas porosity is smaller than critical porosity (the transition porosity from deposition status to diagenesis). It is also interesting to note that the critical porosity for deep-water turbidite sediments is around 40%, representing a typical value for clastic sediments, whereas the critical porosity for deep-water sediments is around 50%, representing a typical value for calcareous-rich sediment and ooze (Keys and Xu, 2002). Therefore, the Vp-porosity cross-plot as well as the characteristics of critical porosity can provide a clue for the lithofacies of different depositional environments. After crossing the critical porosity, the deep-water turbidite and sediments start to slightly increase as porosity decreases, suggesting the loosely compacted status and early diagenesis. It is necessary to point out that some high-velocity zone in the deep-water turbidite depositional environment corresponds to some carbonate layers which have gone through compaction and diagenesis (Li et al., 2015a).

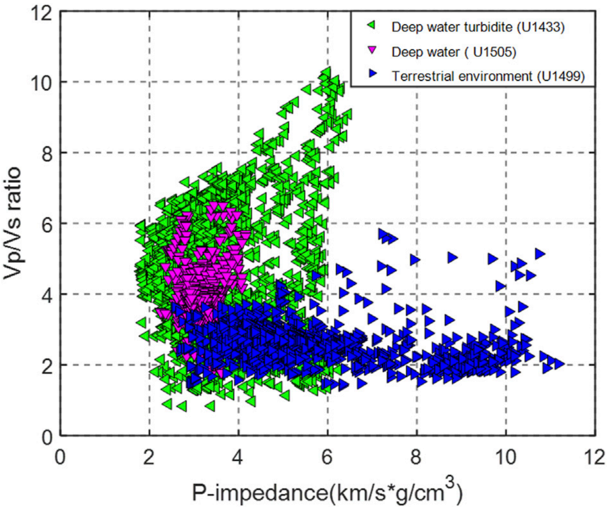

FIGURE 8
Cross plot of P-impedance versus Vp/Vs ratio for IODP logging data of sites U1505C, U1499, and U1433. Data points are color-coded by different depositional environments.

Nevertheless, the shallow water and terrestrial environment overall show low porosity and high-velocity signatures. In particular, the steep velocity-porosity trend for the terrestrial environment suggests that those rocks are strongly affected by post-depositional diagenesis. For example, the clastic facies occurring in Unit II at the U1501 site contain coarse sand intervals, which indicates a terrigenous origin. In addition, the lowermost section (Unit III) from IODP sites U1499 and U1501 has coarse sand intervals that reach pebble-sized clasts, where the extensive diagenetic alteration makes those rocks exhibit higher velocities and lower porosity characteristics.

P-impedance and Vp/Vs ratio are two critical elastic parameters controlling seismic responses. Figure 8 shows the

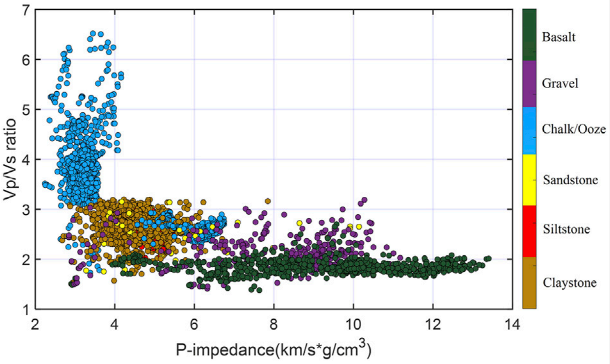

FIGURE 9
Cross plot of P-impedance versus Vp/Vs ratio based on the IODP logging data. Data points are color-coded by different lithofacies including- basalt, gravel, chalk/ooze, sandstone, siltstone, and claystone from different IODP Sites U1499,U1502, and U1505.

cross plot of the P-impedance versus Vp/Vs ratio corresponding to three different depositional environments. Generally, terrestrial environments have a higher P-impedance than deep-water and deep-water turbidite environments. The distinct elastic features mainly come from the different mineralogical content and porosity, which are also associated with the diagenetic features. The Vp/Vs ratio of sediments within the depositional environment of deep-water turbidite is very high. The chaotic and catastrophic depositional environment also makes the P-impedance (2–6 km/s *g/cc) and Vp/Vs ratio vary significantly in a wide range between 1.5 and 10, also reflecting the occurrence of complex lithofacies. The decreasing trend of P-impedance and Vp/Vs ratio within the depositional environment of deep-water turbidite is due to the increase of organic matter because the water depth in this stratum was deeper and thus more favorable for the accumulation of organic matter. It is also interesting to note that the Vp/Vs ratio of calcareous-rich sediment and ooze in the deep-water depositional environment also spans a relatively wide range from 2 to 6, whereas the P-impedance stays at a narrow range.

The influences of lithofacies and compaction on the elastic properties

The lithofacies of sediment sequences have a significant effect on the interrelationships of physical properties. Figure 9 shows the cross plot of the P-impedance and Vp/Vs ratio corresponding to the different lithofacies from the logging data of IODP Sites U1499, U1502, and U1505. Based on the IODP logging data analysis, the SCS can be subdivided into four types of lithofacies namely, 1) calcareous-rich sediment and ooze, 2) argillaceous clay, silt, and sand, 3) coarse sand intervals with up to pebble-sized clasts, 4) volcanic ash interlayer. The different lithofacies exhibit distinct rock physics characteristics.

As illustrated in Figure 9, for the nannofossil ooze/chalk lithofacies, which are exclusively developed in a marine water environment of the study area, the Vp/Vs ratio is significantly high and the P-impedance shows a typical lower value. The abundance of nannofossil ooze within these lithofacies indicated the existence of open ocean water with higher carbonate productivity and less terrestrial input. However, a few data points still exhibit high-impedance characteristics. Presumably, the heterogeneities prevailing in the thin layers with low porosity and high carbonate content are responsible for those outliers, which may be causedby variations in the environment of deposition or diagenesis (e.g., enhanced cementation).

Conversely, the lithofacies of coarse sand intervals show relatively high P-impedance and lower Vp/Vs ratio (Figure 9). Such types of lithofacies is exclusively developed in the terrestrial environment of the study area at IODP Sites U1499 of possible Eocene age. It is featured by sub-angular to angular pebbles and cobbles embedded in the rock body and represents sandstones of different sizes and textures. Finally, the lithofacies of the basaltic layer have high P-impedance ranging from 4 to 14 km/s *g/cc (mainly from IODP site of U1502). It is necessary to point out that the wide range of P-impedance is mainly because the basaltic layers are divided into two distinct zones: the upper brecciated zone shows low P-wave impedance values, while the lower massive basalt lava flows zone is characterized by a gradual increase of P-wave impedance (Planke et al., 1999). In contrast, the Vp/Vs ratio (<2) is confined in a narrow range (Figure 9).

Figure 10 illustrates the influences of physical compaction on the elastic characteristics of P-impedance and Vp/Vs ratio, which are color-coded by depth. It is apparent that physical compaction is also the primary factor controlling the P-impedance and Vp/Vs ratio, the two most important elastic parameters for quantitative seismic interpretation. As the depth increases, except for the igneous rocks, the Vp/Vs ratio gradually decreases and P-impedance gradually increases. This is of no surprise, as shear wave velocity is extremely sensitive to the consolidation degree of marine sediments, and hence the Vp/Vs ratio can decrease from 6 for the poorly consolidated sediments to 1.6 for the siltstone with considerable physical compaction. Note that the quite large range of Vp/Vs ratio for chalk/ooze (3–6) is mainly due to the compaction trend. The calcite content might also slightly contribute to the scattering of the Vp/Vs ratio in such a big range. In addition, the logging measurement of shear wave velocity in the very shallow depth is still challenging, which might also cause uncertainty and scatter in the data.

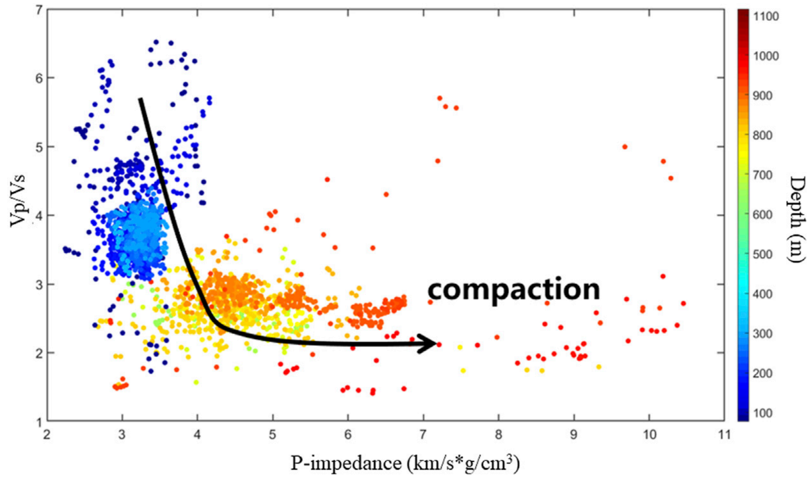

FIGURE 10
Influences of compaction on the elastic characteristics of P-impedance and Vp/Vs ratio. The data points are color coded by depth.

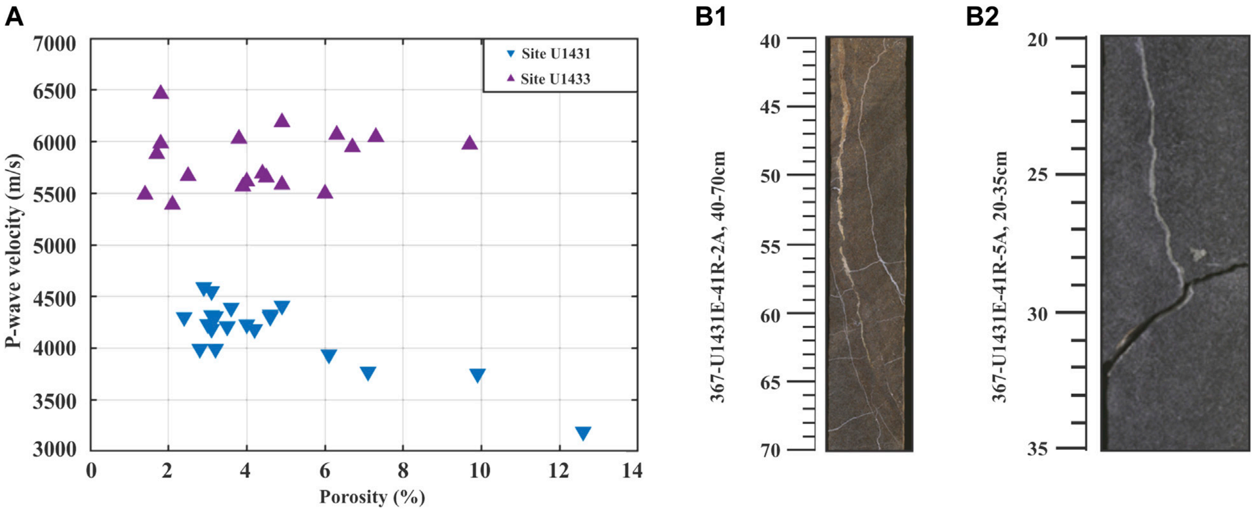

FIGURE 11
(A) Cross plots of P-wave velocity against porosity for basalt data of Sites U1431E and U1433B; **(B1)** Core photo showing the fracture in U1431E-41R-2A; **(B2)** Core photo showing the fracture in U1431E-41R-5A.

Effect of tectonic activity

The data from Sites U1431 and U1433 illustrate the effects of tectonic activity on the physical properties. In 2014, Expedition 349 Scientists found notable changes in the sedimentary facies between the U1431 and U1433 sites and hence a change in physical properties (Li et al., 2015a). It was evident that there were well-defined differences across the fossil ridge as well as the Zhongnan Fault/Ridge between the Southwest and East Sub-basins. This suggests that such structures served as significant sediment barriers, and there was long-term tectonic activity adjacent to this fault.

The main difference between Sites U1431 from the Northern East sub-basin and U1433 from the Southwest Sub-basin is the presence of massive carbonate deposition at Site U1433 from the Lower Pleistocene to the upper Miocene (Figure 2). This difference can be explained by the fact that the Southwest Sub-basin is nearby to the southern blocks that were capped with carbonates such as Reed Bank, Palawan, or Dangerous Grounds (Yao et al.,

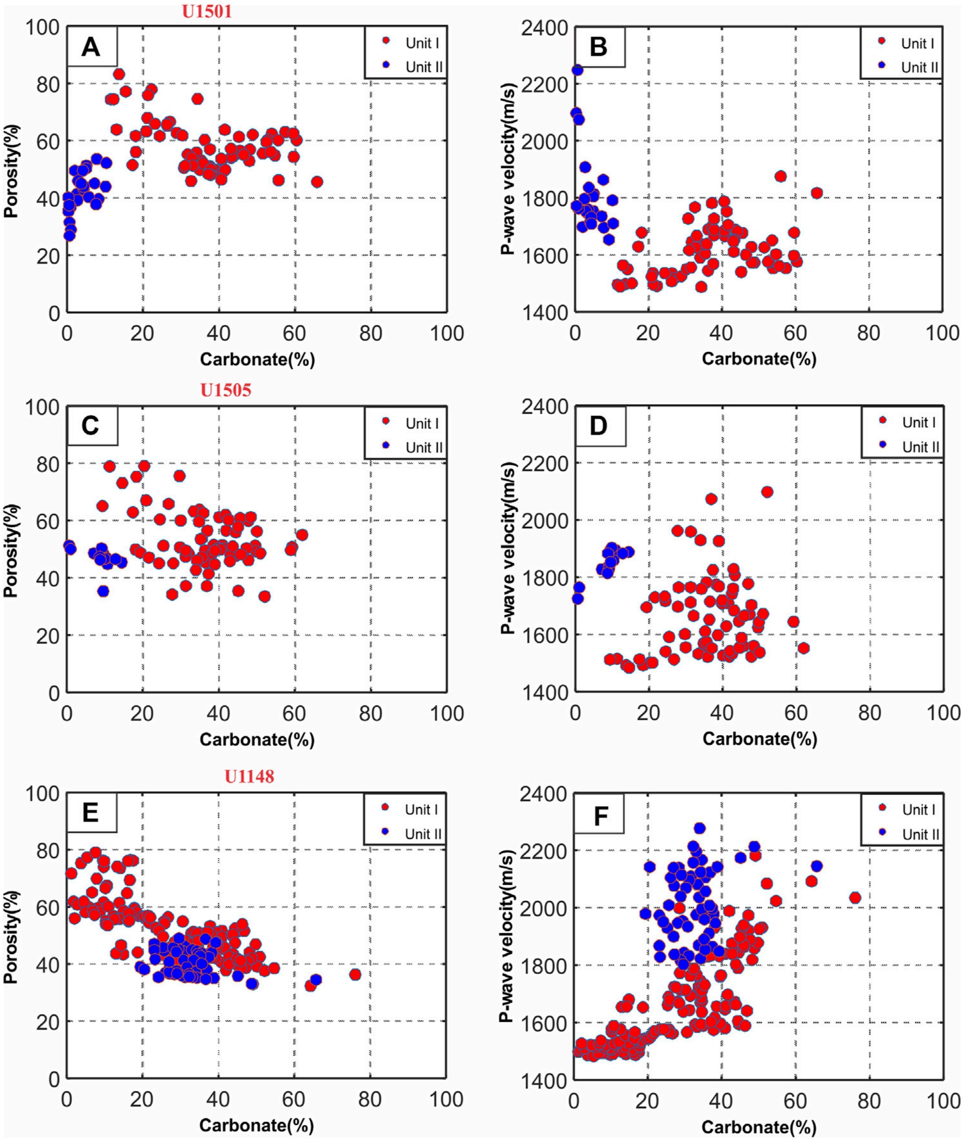

FIGURE 12
Porosity and P-wave velocity versus carbonate based on the ODP/IODP sites; **(A,B)** IODP U1501; **(C,D)** IODP U1505; **(E,F)** ODP site U1148. Data points are color-coded by different depositional units.

2012; Ding et al., 2013), and were carried into the central basin by turbidity currents (Li et al., 2015b). Conversely, the Northeast Sub-basin gained sediments with slightly less production of Miocene carbonate, mostly from the north. As a result, the upper Miocene sequence in the Southwest Sub-basin, which is dominated by deep water carbonate turbidite deposition, displays increasing trends of density and P-wave velocity while the porosity exhibits a decreasing trend (Figure 5).

In addition, as indicated in Figure 11A, the limited velocity measurement of basaltic core samples from Site U1431E show significant differences in P-wave velocity. This is mainly attributed to the higher frequency of fractures occuring at site U1431 compared to Site U1433, reflec a higher degree of alteration of the basalt. The comparatively reduced P-wave velocity approximated from the basaltic layers at Site U1431E could be related to the increased presence of cracks (Figures 11b1,b2) (Walsh, 1965; Toksöz et al., 1976), where the most active faulting currently occur much closer to site U1431 in the East Sub-basin, due to active subduction of the southern part of the Manila Trench, as well as the collision of the Luzon arc with the Northeast Palawan (Li et al., 2015b).

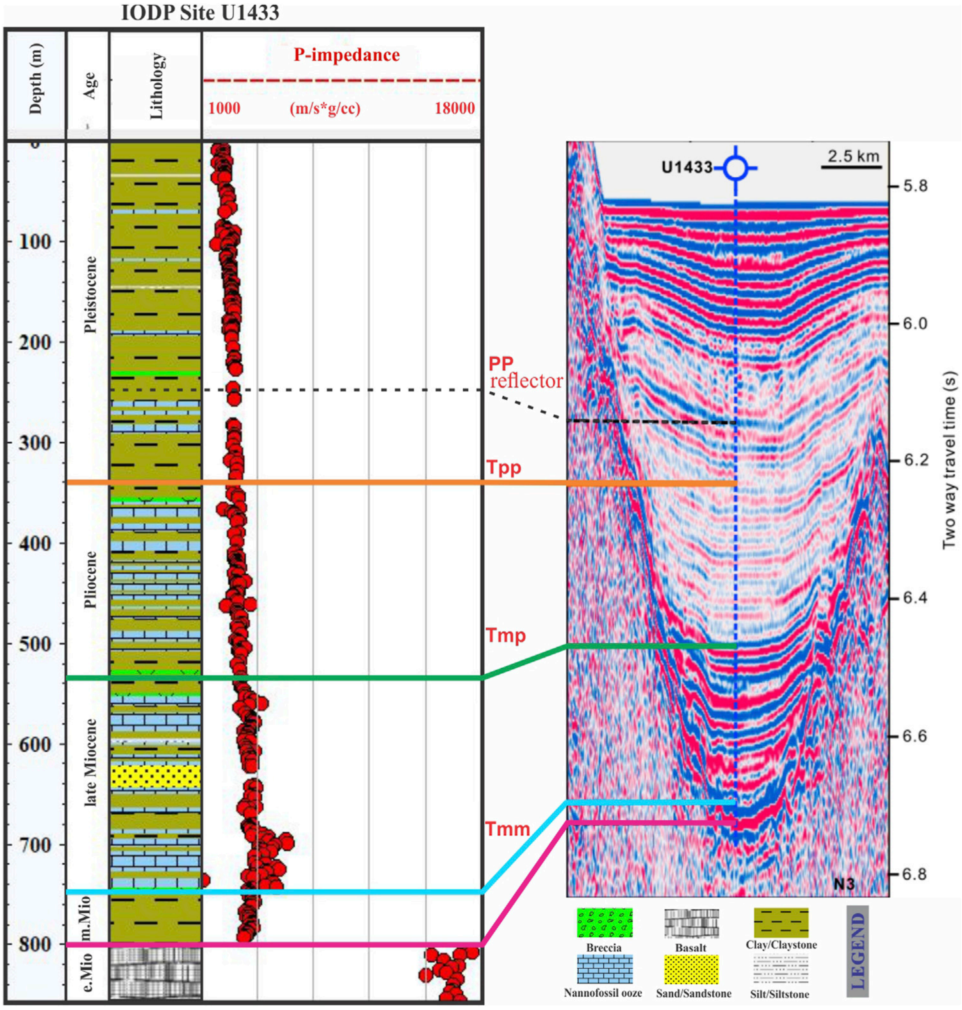

FIGURE 13
Seismic horizons at IODP Site U1433 in the Southwest sub-basin. Modified after (Li et al., 2015a).

Discussion

The effect of carbonate content on the rock physics characteristics

We can compare the relative effects of carbonate contents on rock physical properties by examining the data from Sites U1148, U1501, and U1505 at SCS. The CaCO3 contents of the study area samples varied between 0 and 80 wt% (Figures 12A–F). The low range of carbonate content comprised samples of terrigenous sediments, whereas the high carbonate samples mainly consisted of nannofossil ooze.

Figure 12 shows the cross plot of porosity and P-wave velocity versus carbonate content corresponding to different depositional units. Unit I is dominated by calcareous nannofossils and is distinguished by significantly higher carbonate content (an average of 47 wt%). This indicates a much more stable environment with a low supply of terrigenous material, which may be related to rising sea levels during this interval. The porosity overall decreases with the increase of carbonate content. This is mainly because the carbonate content increases with the increase of depth due to the enhanced carbonate productivity, and hence the porosity gradually increases with the mitigated compaction effects. It is also interesting to notice that different sites have different carbonate contents, which reflect decreasing carbonate productivity as well as increasing clastic input from Site U1501 to Site U1148. Nevertheless, the relationship of P-wave velocity-carbonate content becomes complicated. At Site U1501, the velocity is almost insensitive to the variation of carbonate content, since the porosity is over critical

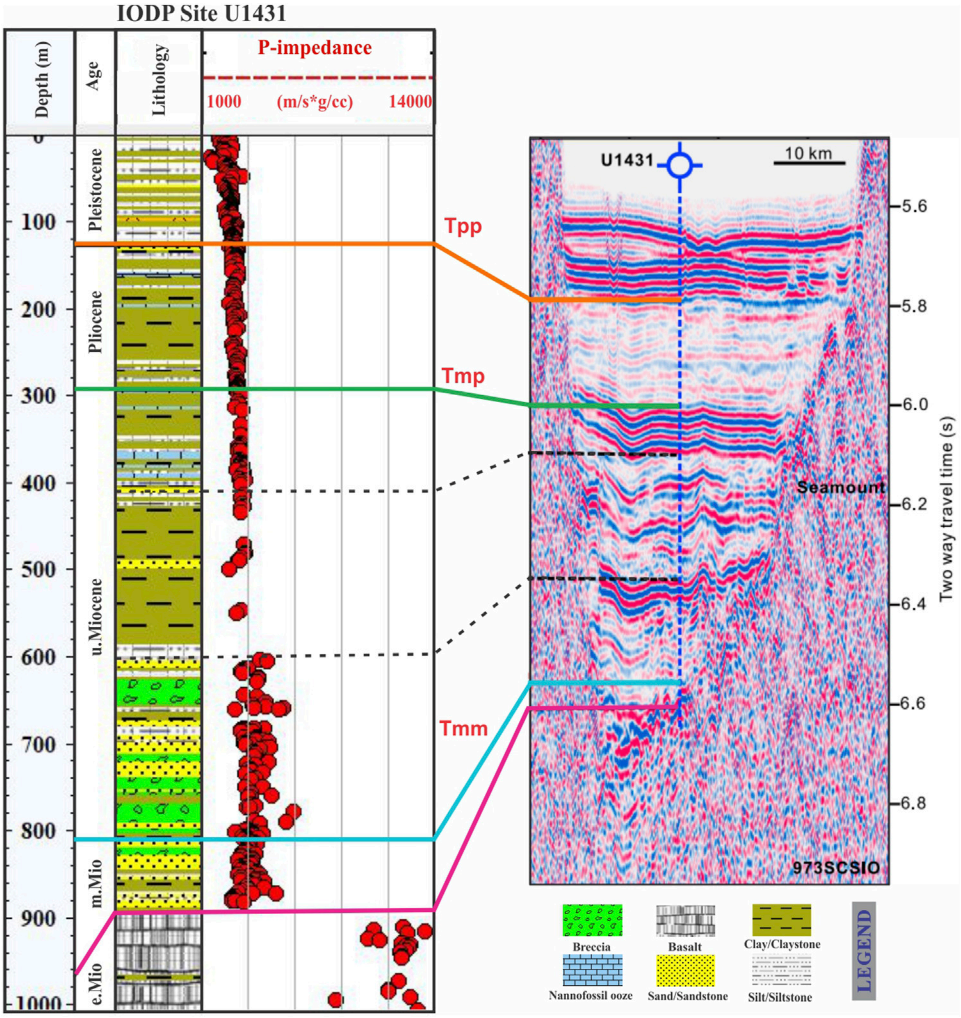

FIGURE 14
Seismic horizons at IODP Site U1431 in the East sub basin. Modified after (Li et al., 2015a).

porosity (~50%) and the marine sediments are in the suspension status. At Site U1148, the velocity exhibits an increasing trend with the increase of carbonate content, which is mainly because the porosity sharply decreases with increased carbonate content.

Unit II has low carbonate contents compared to Unit I indicating a high proportion of aquatic organic matter, but overall contains 8–10 wt% carbonate content at both IODP Sites U1501 and U1505. This is also linked to the change in depositional environment from shallow to deep water as the rate of clastic sedimentation increases, resulting in the accumulation of more detrital minerals. However, even within Unit II at IODP Site U1501, there are still some data points showing an increasing trend of porosity and carbonate content (Figure 12A), which are probably caused by the overall fining of clastic material indicating deepening basin conditions.

In contrast, Unit II at ODP Site U1148 shows a distinct increase in carbonate content compared to other sites ranging between 20–40 wt% and marked by a sharp increase in P-wave velocity, and a decrease in porosity (Figures 12E,F), reflecting a high biogenic silica accumulation during this unit.

Implications for seismic stratigraphy interpretation

Investigating the physical characteristics of rocks lay the groundwork for future seismic interpretation. The changes in sedimentary facies between Sites U1431 and U1433 were revealed by changes in the seismic reflection and thus in rock physical properties. In the Southwest Sub-basin, the upper parts of the Pleistocene sequence are mainly composed of clay and nannofossil oozes by turbidite deposition. Although the P-impedance is very low, there exists significant impedance contrasts. Therefore, as shown in Figure 13, there arestrong seismic reflection. Nevertheless, the lower parts of the Pleistocene sequence are composed of mostly clays interbedded with carbonates, exhibiting uniform impedance variation and weaker seismic reflections (Figure 13).

The IODP cores show that the Pliocene sequences in the East Sub-basin consist primarily of clays whereas in the Southwest Sub-basin consist primarily of interbedded clays and carbonates; As shown in Figures 12, 13, they generally have very weak P-impedance contrast. As a consequence, Pliocene sequences are characterized by weaker seismic reflection at both Sites U1431 and U1433 in the East and Southwest Sub-basin, respectively.

In the East Sub-basin, the alteration between clay, silt, and carbonate in the upper part of the late Miocene sequence, and sand interbedded with volcanoclastic breccia in the lower part of it, characterized by a decrease in porosity and increases in density, P-wave velocity, and P-impedance. These observations explain the strong seismic reflection interface of strata in the upper and lower parts of the late Miocene sequence at IODP Site U1431 (Figure 14). Nevertheless, the middle part of the late Miocene sequences mainly composed of clay corresponds to weak P-impedance contrast, yielding a weaker seismic reflection interface (Figure 14).

In the Southwest Sub-basin, the lithologic interface between clays and massive carbonate in the late Miocene sequence show much higher velocity and P-impedance contrast. This explains the strong seismic reflection of strata in the late Miocene sequence at IODP Site U1433.

Conclusion

This study focuses on the analysis of the elastic properties of marine sediments in the SCS and their influencing factors based on the ODP/IODP sites. The main conclusions are given as follows:

1) The different depositional environments exhibit distinct rock physics characteristics. The sediments deposited in the shallow water and terrestrial environment exhibit higher velocities in comparison with the deep water and deep-water turbidite sediments
2) Across the boundary between the Oligocene-Miocene age, there are sharp decreases in velocities and densities, and an increase in porosity, indicating non-depositional hiatus formed in the sedimentary record at this boundary. This is also associated with a decrease in carbonate content from 65 to 10 wt%.
3) The lithofacies and compaction effects are mainly responsible for the variation of P-impedance and Vp/Vs ratio. With the enhanced compaction effects, the P-impedance exhibits an increasing trend while Vp/Vs ratio significantly decreases from 6 to less than 2.
4) The basalt samples at IODP Site U1433 having a P-wave velocity of 5500–6500 m/s differ significantly from basalt samples at IODP Site U1431 having a lower velocity of 3000–4500 m/s, which might be caused by more fractures occurred at Site U1431, suggesting the distinct tectonic activities along Fossils Spreading Ridge and Zhongnan Ridge/Faults.

Data availability statement

Publicly available datasets were analyzed in this study. This data can be found here: All the data analyzed in this study can be found at https://www.iodp.org/resources/access-data-and-samples.

Author contributions

All authors listed have made a substantial, direct, and intellectual contribution to the work and approved it for publication.

Funding

This work was supported by the National Key R&D Program of China (2018YFC0310105), Shanghai Rising-Star Program (21QA1409200), and Fundamental Research Funds for the Central Universities.

Conflict of interest

The authors declare that the research was conducted in the absence of any commercial or financial relationships that could be construed as a potential conflict of interest.

Publisher's note

References

Ayoub, V., Delenne, C., Chini, M., Finaud-Guyot, P., Mason, D., Matgen, P., et al. (2022). A porosity-based flood inundation modelling approach for enabling faster large scale simulations. *Adv. Water Resour.* 162, 104141. doi:10.1016/j.advwatres.2022.104141

Ba, J., Xu, W., Fu, L. Y., Carcione, J. M., and Zhang, L. (2017). Rock anelasticity due to patchy saturation and fabric heterogeneity: A double double-porosity model of wave propagation. *J. Geophys. Res. Solid Earth* 122 (3), 1949–1976. doi:10.1002/2016jb013882

Bassinot, F., Marsters, J. C., Mayer, L. A., and Wilkens, R. H. (1993). *Variations of porosity in calcareous sediments from the ontong java plateau.*Texas, TX, USA: Ocean Drilling Program College Station TX

Breitzke, M. (2000). Acoustic and elastic characterization of marine sediments by analysis, modeling, and inversion of ultrasonic P wave transmission seismograms. *J. Geophys. Res.* 105 (B9), 21411–21430. doi:10.1029/2000jb900153

Cai, W., Dou, L., Gong, S., Li, Z., and Yuan, S. (2015). Quantitative analysis of seismic velocity tomography in rock burst hazard assessment. *Nat. Hazards (Dordr).* 75 (3), 2453–2465. doi:10.1007/s11069-014-1443-6

Christeson, G. L., Gulick, S. P., Morgan, J. V., Gebhardt, C., Kring, D. A., Le Ber, E., et al. (2018). Extraordinary rocks from the peak ring of the chicxulub impact crater: P-Wave velocity, density, and porosity measurements from IODP/ICDP expedition 364. *Earth Planet. Sci. Lett.* 495, 1–11. doi:10.1016/j.epsl.2018.05.013

Courville, Z., Albert, M., Fahnestock, M., Cathles IV, L., and Shuman, C. (2007). Impacts of an accumulation hiatus on the physical properties of firn at a low-accumulation polar site. *J. Geophys. Res.* 112 (F2), F02030. doi:10.1029/2005jf000429

David, C., Menéndez, B., and Darot, M. (1999). Influence of stress-induced and thermal cracking on physical properties and microstructure of La Peyratte granite. *Int. J. Rock Mech. Min. Sci.* 36 (4), 433–448. doi:10.1016/s0148-9062(99)00010-8

Ding, W., Franke, D., Li, J., and Steuer, S. (2013). Seismic stratigraphy and tectonic structure from a composite multi-channel seismic profile across the entire Dangerous Grounds, South China Sea. *Tectonophysics* 582, 162–176. doi:10.1016/j.tecto.2012.09.026

Eberli, G. P., Baechle, G. T., Anselmetti, F. S., and Incze, M. L. (2003). Factors controlling elastic properties in carbonate sediments and rocks. *Lead. Edge* 22 (7), 654–660. doi:10.1190/1.1599691

Fabricius, I. L. (2014). Burial stress and elastic strain of carbonate rocks. *Geophys. Prospect.* 62 (6), 1327–1336. doi:10.1111/1365-2478.12184

Fabricius, I. L. (2007). Chalk: Composition, diagenesis and physical properties. *bgsd.* 55, 97–128. doi:10.37570/bgsd-2007-55-08

Franke, D., Barckhausen, U., Baristeas, N., Engels, M., Ladage, S., Lutz, R., et al. (2011). The continent-ocean transition at the southeastern margin of the South China Sea. *Mar. petroleum Geol.* 28 (6), 1187–1204. doi:10.1016/j.marpetgeo.2011.01.004

Gatter, R., Clare, M., Kuhlmann, J., and Huhn, K. (2021). Characterisation of weak layers, physical controls on their global distribution and their role in submarine landslide formation. *Earth-Science Rev.* 223, 103845. doi:10.1016/j.earscirev.2021.103845

Graw, J., Wood, W., and Phrampus, B. (2020). Predicting global marine sediment density using the random forest regressor machine learning algorithm. *J. Geophys. Res. Solid Earth* 126, e2020JB020135. doi:10.1029/2020jb020135

Hamilton, E. L., Bachman, R. T., Berger, W. H., Johnson, T. C., and Mayer, L. A. (1982). Acoustic and related properties of calcareous deep-sea sediments. *J. Sediment. Res.* 52 (3), 733–753.

Hamilton, E. L. (1972). Compressional-wave attenuation in marine sediments. *Geophysics* 37 (4), 620–646. doi:10.1190/1.1440287

Hamilton, E. L. (1980). Geoacoustic modeling of the sea floor. *J. Acoust. Soc. Am.* 68 (5), 1313–1340. doi:10.1121/1.385100

Hamilton, E. L. (1974). Prediction of deep-sea sediment properties: State-of-the-art. *Deep-Sea Sediments*, 1–43. doi:10.1007/978-1-4684-2754-7_1

Hamilton, E. L. (1976). Variations of density and porosity with depth in deep-sea sediments. *J. Sediment. Res.* 46 (2), 280–300.

Han, D.-h., and Batzle, M. L. (2004). Gassmann's equation and fluid-saturation effects on seismic velocities. *Geophysics* 69 (2), 398–405. doi:10.1190/1.1707059

Hou, Z., Chen, Z., Wang, J., Zheng, X., Yan, W., Tian, Y., et al. (2018). Acoustic impedance properties of seafloor sediments off the coast of Southeastern Hainan, South China Sea. *J. Asian Earth Sci.* 154, 1–7. doi:10.1016/j.jseaes.2017.12.003

Hughes, T. J., Henstock, T. J., Pilgrim, J. A., Dix, J. K., Gernon, T. M., and Thompson, C. E. (2015). Effect of sediment properties on the thermal performance of submarine HV cables. *IEEE Trans. Power Deliv.* 30 (6), 2443–2450. doi:10.1109/tpwrd.2015.2398351

Hutchison, C. S., and Vijayan, V. (2010). What are the Spratly islands? *J. Asian Earth Sci.* 39 (5), 371–385. doi:10.1016/j.jseaes.2010.04.013

Jian, Z., Jin, H., Kaminski, M. A., Ferreira, F., Li, B., and Yu, P.-S. (2019). Discovery of the marine Eocene in the northern South China sea. *Natl. Sci. Rev.* 6 (5), 881–885. doi:10.1093/nsr/nwz084

Kenter, J., Anselmetti, F., Kramer, P., Westphal, H., and Vandamme, M. (2002). Acoustic properties of" young" carbonate rocks, ODP leg 166 and boreholes Clino and Unda, weWesternreat Bahama Bank. *J. Sediment. Res.* 72 (1), 129–137. doi:10.1306/041101720129

Keys, R. G., and Xu, S. (2002). An approximation for the Xu-White velocity model. *Geophysics* 67 (5), 1406–1414. doi:10.1190/1.1512786

Kim, G.-Y., and Kim, D.-C. (2005). Sediment physical and acoustic properties at ODP sites 1150 and 1151, Japan Trench. *Mar. Georesources Geotechnol.* 23 (1-2), 1–11. doi:10.1080/10641190590944908

Larsen, H. C., Jian, Z., Alvarez Zarikian, C. A., Sun, Z., Stock, J. M., Klaus, A., et al. (2018). *Site U1501.* U S A: IODP. doi:10.14379/iodp.proc.367368.105.2018

Lee, E. Y., Tejada, M. L. G., Song, I., Chun, S. S., Gier, S., Riquier, L., et al. (2021). Petrophysical property modifications by alteration in a volcanic sequence at IODP Site U1513, Naturaliste Plateau. *JGR. Solid Earth* 126 (10), e2020JB021061. doi:10.1029/2020jb021061

Li, A. C., Huang, J., Jiang, H. Y., and Wan, S. M. (2011). Sedimentary evolution in the northern slope of the South China Sea since the Oligocene and its response to tectonics. *Chin. J. Geophys.* 54 (6), 1084–1096. doi:10.1002/cjg2.1686

Li, C.-F., Li, J., Ding, W., Franke, D., Yao, Y., Shi, H., et al. (2015a). Seismic stratigraphy of the central South China Sea basin and implications for neotectonics. *J. Geophys. Res. Solid Earth* 120 (3), 1377–1399. doi:10.1002/2014jb011686

Li, C.-F., Lin, J., Kulhanek, D., Williams, T., Bao, R., Briais, A., et al. (2015b). *Expedition 349 summary.* U S A: IODP.

Li, C. F., Lin, J., Kulhanek, D. K., Williams, T., Bao, R., Briais, A., et al. (2014). Opening of the south China sea and its implications for southeast asian tectonics, climates, and deep mantle processes since the late mesozoic. *Integr. Ocean. Drill. Program Prelim. Rep.* 349, 1.

Lyu, C., Park, J., and Carlos Santamarina, J. (2021). Depth-dependent seabed properties: Geoacoustic assessment. *J. Geotech. Geoenviron. Eng.* 147 (1), 4020151. doi:10.1061/(asce)gt.1943-5606.0002426

Ma, R., Liu, C., Li, Q., and Jin, X. (2019). Calcareous nannofossil changes in response to the spreading of the South China Sea basin during Eocene-Oligocene. *J. Asian Earth Sci.* 184, 103963. doi:10.1016/j.jseaes.2019.103963

Martin, K. M., Wood, W. T., and Becker, J. J. (2015). A global prediction of seafloor sediment porosity using machine learning. *Geophys. Res. Lett.* 42 (24), 10,640–610,646. doi:10.1002/2015gl065279

Nobes, D., Mienert, J., and Dirksen, G. (1991). *Lithologc control of physical-property interrelationships.* Boulder, CO, USA: The Geological Society of America, 35.

Planke, S., Cerney, B., Bücker, C. J., and Nilsen, O. "Alteration effects on petrophysical properties of subaerial flood basalts: Site 990, Southeast Greenland margin," in *Proceedings of the ocean drilling Program scientific results* (Texas, TX, USA: Ocean Drilling Program College Station TX), 17–28.(Year)

Pola, A., Crosta, G., Fusi, N., Barberini, V., and Norini, G. (2012). Influence of alteration on physical properties of volcanic rocks. *Tectonophysics* 566, 67–86. doi:10.1016/j.tecto.2012.07.017

Richardson, M., Lavoie, D., and Briggs, K. (1997). Geoacoustic and physical properties of carbonate sediments of the Lower Florida Keys. *Geo-Marine Lett.* 17 (4), 316–324. doi:10.1007/s003670050043

Stewart, D., Studds, P., and Cousens, T. (2003). The factors controlling the engineering properties of bentonite-enhanced sand. *Appl. Clay Sci.* 23 (1-4), 97–110. doi:10.1016/s0169-1317(03)00092-9

Sun, Z., Jian, Z., Stock, J., Larsen, H., Klaus, A., and Alvarez Zarikian, C. (2018). The expedition 367/368 Scientists. 2018. South China sea rifted margin. *Proc. Int. Ocean Discov. Program* 367, 368.

Toksöz, M. N., Cheng, C., and Timur, A. (1976). Velocities of seismic waves in porous rocks. *Geophysics* 41 (4), 621–645. doi:10.1190/1.1440639

Urmos, J. (1994). *Diagenetic and physical properties of pelagic carbonate sediments: ODP leg 130, ontong java plateau.* Manoa, Hawai: University of Hawai'i at Manoa.

Van der Lingen, G., and Packham, G. (1975). Relationships between diagenesis and physical properties of biogenic sediments of the ontong-java plateau (sites 288 and 289, deep sea drilling project). *Init. Rep. DSDP* 30, 443–481.

Walsh, J. (1965). The effect of cracks on the compressibility of rock. *J. Geophys. Res.* 70 (2), 381–389. doi:10.1029/jz070i002p00381

Wang, Y., Han, D.-H., Zhao, L., Li, H., Long, T., and Hamutoko, J. (2021). Static and dynamic bulk moduli of deepwater reservoir sands: Influence of pressure and fluid saturation. *Lithosphere* 2021 (3). (Special). doi:10.2113/2022/4266697

Xie, Y., Wu, T., Sun, J., Zhang, H., Wang, J., Gao, J., et al. (2018). Sediment compaction and pore pressure prediction in deepwater basin of the South China Sea: Estimation from ODP and IODP drilling well data. *J. Ocean. Univ. China* 17 (1), 25–34. doi:10.1007/s11802-018-3449-2

Yan, Q., Shi, X., and Castillo, P. R. (2014). The late mesozoic–cenozoic tectonic evolution of the south China sea: A petrologic perspective. *J. Asian Earth Sci.* 85, 178–201. doi:10.1016/j.jseaes.2014.02.005

Yao, Y., Liu, H., Yang, C., Han, B., Tian, J., Yin, Z., et al. (2012). Characteristics and evolution of cenozoic sediments in the liyue basin, SE South China sea. *J. Asian Earth Sci.* 60, 114–129. doi:10.1016/j.jseaes.2012.08.003

Ymd, T. (1973). Factors controlling maximum and minimum densities of sands. *Eval. Relat. density its role geotechnical Proj. Involv. cohesionless soils* 523, 98.

Zhang, L., Ba, J., Carcione, J. M., and Fu, L.-y. (2020). Differential poroelasticity model for wave dissipation in self-similar rocks. *Int. J. Rock Mech. Min. Sci.* 128, 104281. doi:10.1016/j.ijrmms.2020.104281

Zhang, L., Ba, J., and Carcione, J. M. (2021). Wave propagation in infinituple-porosity media. *J. Geophys. Res. Solid Earth* 126 (4), e2020JB021266. doi:10.1029/2020jb021266

Zhao, L., Wang, Y., Liu, X., Zhang, J., Liu, Y., Qin, X., et al. (2020). Depositional impact on the elastic characteristics of the organic shale reservoir and its seismic application: A case study of the longmaxi-wufeng shale in the fuling gas field, sichuan basin. *Geophysics* 85 (2), B23–B33. doi:10.1190/geo2019-0326.1

Zhou, X., Lyu, X., Liu, C., Liu, Z., Li, Q., Jin, X., et al. (2019). Depositional mechanisms for upper Miocene sediments in the South China Sea central basin: Evidence from calcareous nannofossils. *Mar. Micropaleontol.* 151, 101768. doi:10.1016/j.marmicro.2019.101768

frontiers | Frontiers in Earth Science

TYPE Original Research
PUBLISHED 17 January 2023
DOI 10.3389/feart.2022.1035735

OPEN ACCESS

EDITED BY
Yuqi Wu,
China University of Petroleum (East China), China

REVIEWED BY
Jing Ba,
Hohai University, China
Yichuan Wang,
University of Calgary, Canada

*CORRESPONDENCE
Li-Yun Fu,
lfu@upc.edu.cn

SPECIALTY SECTION
This article was submitted to Solid Earth Geophysics,
a section of the journal
Frontiers in Earth Science

RECEIVED 03 September 2022
ACCEPTED 31 October 2022
PUBLISHED 17 January 2023

CITATION
Wang Z, Fu L-Y, Jian S and Deng W (2023), Application of a model-driven simultaneous prestack inversion of rock physical properties in ultra-deep Ordovician carbonate reservoirs in the Shunbei area.
Front. Earth Sci. 10:1035735.
doi: 10.3389/feart.2022.1035735

Application of a model-driven simultaneous prestack inversion of rock physical properties in ultra-deep Ordovician carbonate reservoirs in the Shunbei area

Zhiwei Wang[1,2], Li-Yun Fu[1,2,3]*, Shikai Jian[4] and Wubing Deng[1,2]

[1]Shandong Provincial Key Laboratory of Deep Oil and Gas, China University of Petroleum (East China), Qingdao, China, [2]School of Geosciences, China University of Petroleum (East China), Qingdao, China, [3]Laboratory for Marine Mineral Resources, Qingdao National Laboratory for Marine Science and Technology, Qingdao, China, [4]Petroleum Exploration and Development Research Institute of Petrochina Tarim Oil Field Company, Korla, China

Synchronous prestack inversion technology has been widely used to predict the fluid and lithological properties of reservoirs. Its prediction accuracy depends on the seismic data quality. Ultra-deep carbonate reservoirs in the Shunbei area of the Tarim Basin were used as research objects. Based on the shear wave (S-wave) prediction method, petrophysical logging analysis was carried out to select the physical property-sensitive elastic parameters. A physical property indicator with porosity as the target curve was constructed to quantitatively characterize the differences in physical properties in this area. The signal-to-noise ratio (SNR) and resolution of the dataset were improved by preprocessing the seismic and logging data. P- and S-wave impedances and densities obtained from prestack synchronous inversion, which integrate the physical property indicator model. Spatial distribution and transverse variation of the physical parameters of the Ordovician carbonate reservoirs are described. The planar distribution of reservoirs can be effectively predicted.

KEYWORDS

shear wave prediction, physical property indicator model, simultaneous prestack inversion, Shunbei ultra-deep reservoirs, rock physical analysis

1 Introduction

The Shunbei Oilfield is located in the northwest of the Shuntuoguole Low Uplift, which is in the transitional zone between the central and northern regions of the Tarim Basin. Under the influence of multi-stage tectonic movements, two sets of main strike–slip faults and several secondary faults have been formed. The cave-fracture system developed in the Ordovician carbonate rocks at depths below 7,000 m is characterized by strong heterogeneity and local connectivity, which creates favorable conditions for hydrocarbon migration and accumulation. This study aims to present a method for predicting the spatial distribution of favorable reservoirs by incorporating logging, petrophysics, and seismic methods, which is of great significance for oil and gas exploration in this area.

Petrophysics is vital for helping quantitative interpretation by using seismic data; it links core sample, logging, and seismic information to reservoir properties. Rock physics allows for direct observation of the internal structure of the subsurface material by using CT and SEM (Wu et al., 2019a; b, 2020) and allows for various *in situ* measurements of the elastic properties of rocks and the corresponding seismic responses to establish a theoretical model that can help in reservoir characterization (Ba et al., 2017; Zhang et al., 2021, 2022). We determined the sensitive parameters related to physical properties using a crossplot of multiple elastic parameters of rock physics (e.g., Wang and Morozov, 2019), with the porosity curve as the target curve for constructing the indicator factors of physical properties, and quantitatively characterized the physical properties in this area.

The complexity of the deep Cambrian–Ordovician oil and gas transport systems makes geophysical predictions challenging (Ding et al., 2020; Wang et al., 2020; Mu et al., 2021). Prestack synchronous inversion can simultaneously obtain the P-wave impedance, S-wave impedance, and density from the CRP gather. Due to the complexity of the Zoeppritz equation, Aki and Richards (1980) proposed the Zoeppritz approximation. Yin et al. (2014) established a statistical petrophysical model to characterize the relationship between elastic impedance and reservoir physical parameters and determined the inversion of reservoir physical parameters through the Bayesian method. Lang and Grana (2018) developed a prediction method for seismic AVO physical parameters based on Bayesian linear inversion using the first-order approximation model of the Gassmann equation. At present, most of these methods are aimed at clastic reservoirs.

In this study, based on the physical indicator factors of the carbonate reservoir, a model-driven prestack synchronous inversion method is proposed to quantitatively characterize the reservoir's physical properties. The geological background of the Shunbei Oilfield is summarized, and the complex structural characteristics of fault-karst gas reservoirs are pointed out. Second, shear wave prediction was carried out *via* preprocessing and analysis of logging data. A multiple elastic parameter crossplot was created, and the physical property-sensitive elastic parameters were optimized, in order to construct a physical property indicator. Finally, using the prestack synchronous inversion data of P-wave velocity, S-wave velocity, and density, combined with the constructed indicator of physical properties, we predicted the spatial and planar distribution

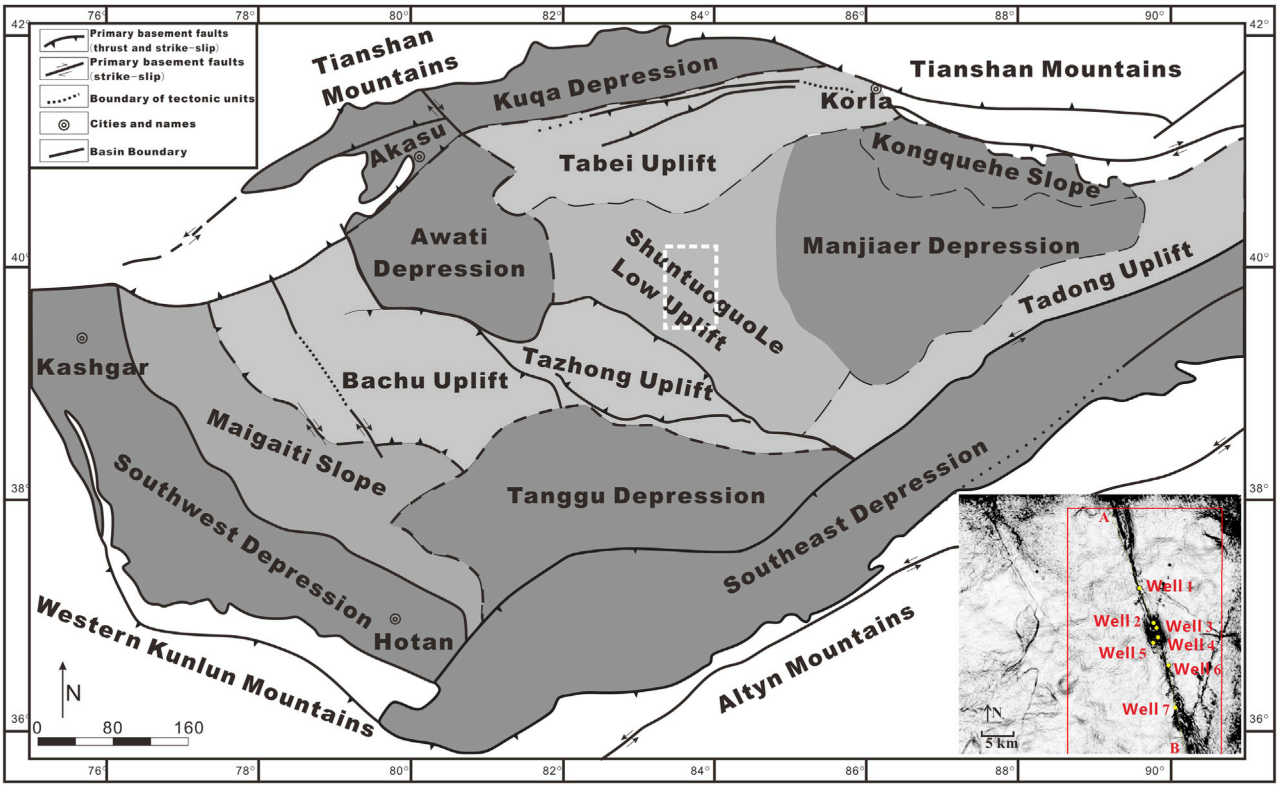

FIGURE 1
Map showing the location of the Shunbei oil field and main tectonic units in the Tarim Basin (modified by Deng et al., 2019). The inset (lower right) corresponds to the location of the white dotted box, showing the distribution of strike–slip fault zones and wells in the study area.

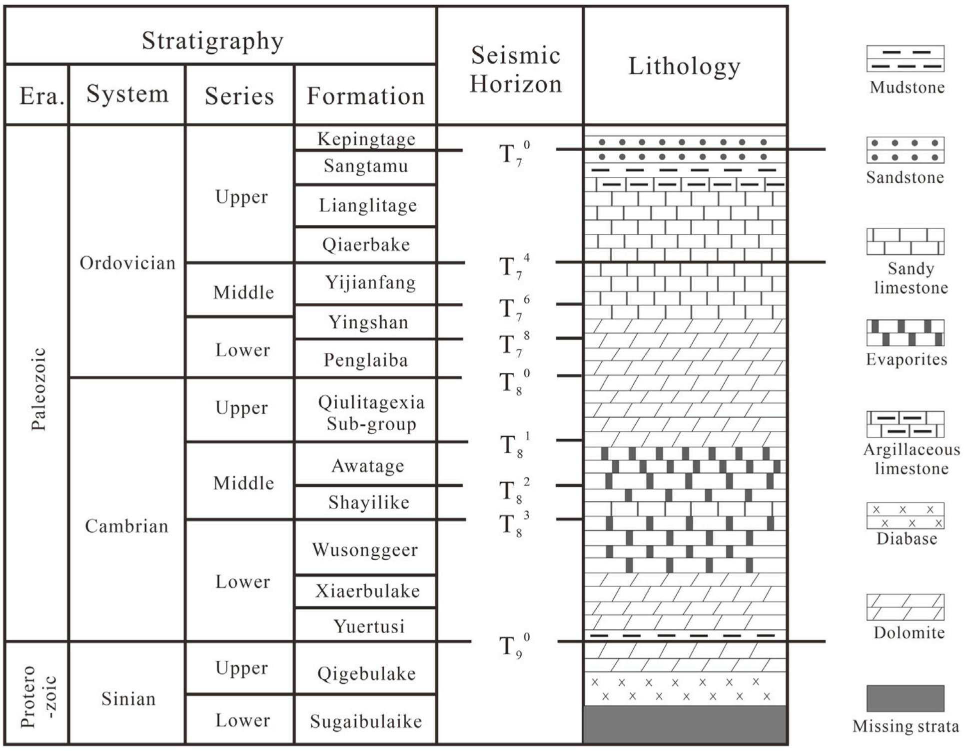

FIGURE 2
Stratigraphic, seismic horizon, and lithologic information of the Shunbei Oilfield (slightly modified from Deng et al., 2019).

of the 405 km^2 Ordovician Yijianfang–Yingshan Formation reservoir near the Shunbei No. 5 fault zone.

2 Geological setting

As shown in Figure 1, the Shuntoguele Low Uplift is connected to the Tabei Uplift in the north, the Tazhong Uplift in the south, the Manjiaer Depression in the east, and the Awati Depression in the west, and it extends to the Shunnan Slope of the Guchengxu Uplift in the southeast (Liu et al., 2020; Lu et al., 2020; Li, 2022; Li et al., 2022). The study area comprises the dotted white box of Figure 1, covering 405 km^2, and is magnified in the lower right inset. The study area contains seven wells along the Shunbei No. 5 strike–slip fault zone in the A–B section in the NW direction.

Recent exploration has shown that carbonate reservoirs in the Shuntuoguole area developed mainly in the upper section of the Ordovician Yijianfang–Yingshan Formation. Figure 2 shows this area's stratigraphic, seismic horizon, and lithographic information. Due to tectonic activity, the pore geometry in these reservoirs is very complex and exhibits significant diversity in shape and size, high-angle and steep fault-related dissolution caves, high-angle structural fractures, pore-expansion dissolution fractures, partially filled fractures, dissolution pores, inter-crystalline pores, and micro-fractures. These fractures and pores are commonly unevenly distributed. Dissolution caves, secondary fractures, and solution pores along fractures are the dominant types of spaces in these reservoirs (Yu et al., 2016; Lu et al., 2017; Yuan et al., 2021).

3 Rock physics analysis

High-quality well log data are a prerequisite for seismic inversion and reservoir property prediction (Jiang et al., 2014). Thus, abnormal data on well logs must be identified to allow for correction of environmental effects before using such data alongside seismic data. In addition, virtual porosity and error fusion technology (Wang et al., 2011) can be introduced to predict shear wave velocity, which provides the basic data for prestack synchronous inversion.

3.1 Crossplots of elastic parameters

The petrophysical analysis is the basis for prestack inversion and enables the linking of seismic, well log, and reservoir property data. Through petrophysical analysis, crossplots of elastic parameters can be drawn to understand

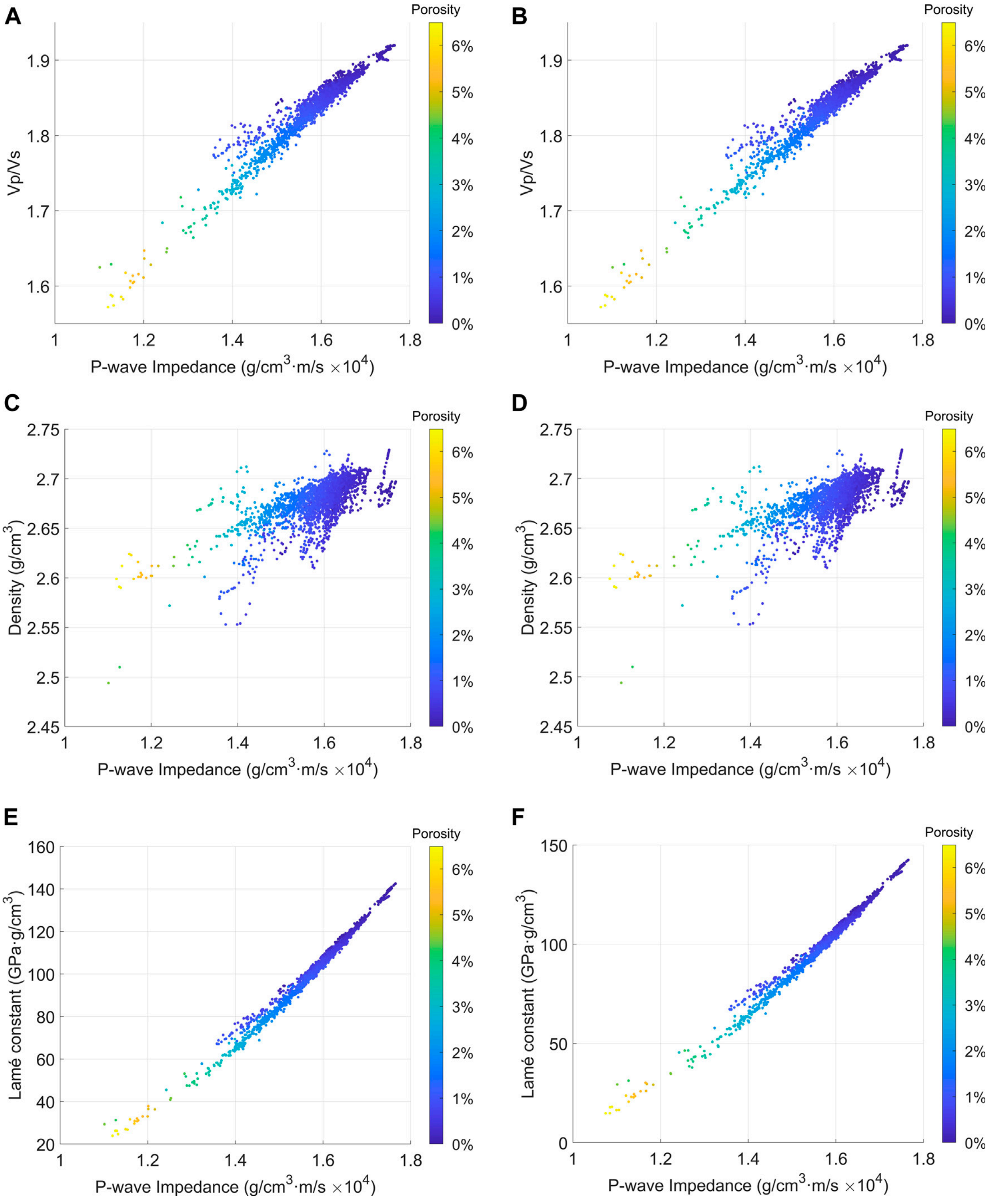

FIGURE 3
Crossplots of P-wave impedance, P-to-S-wave velocity ratio, and porosity **(A)** before and **(B)** after fluid substitution. Crossplots of P-wave impedance, density, and porosity **(C)** before and **(D)** after fluid substitution. Crossplots of P-wave impedance, Lamé constant, and porosity **(E)** before and **(F)** after fluid substitution.

the seismic and logging response characteristics of oil and gas layers and aquifers. It can also help identify elastic parameters that are sensitive to lithology, physical properties, and fluid in the respective area (Ma et al., 2021; Tan et al., 2021; Figure 3).

This analysis is valuable for predicting the physical property distribution of a reservoir and for detecting fluids. Therefore, data from core samples and well logs were analyzed to identify carbonate reservoirs and surrounding rocks with good physical properties (e.g., high

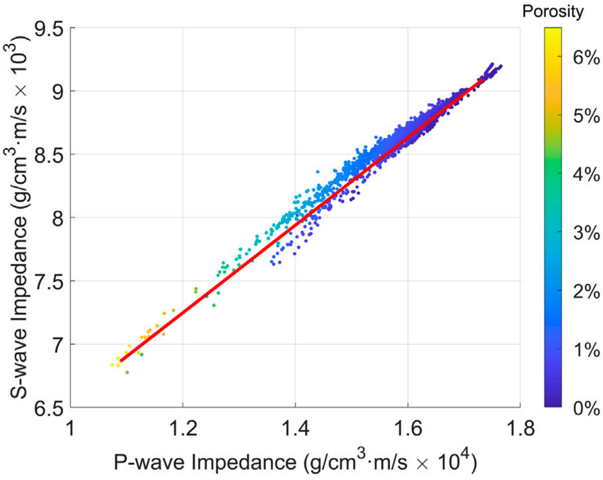

FIGURE 4
Crossplots of P-wave impedance, S-wave impedance, and porosity.

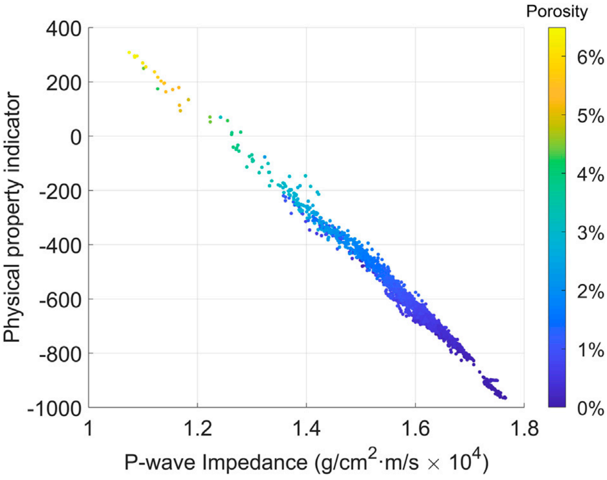

FIGURE 6
Crossplot of the PI and physical property indicator vs. porosity for Well 4.

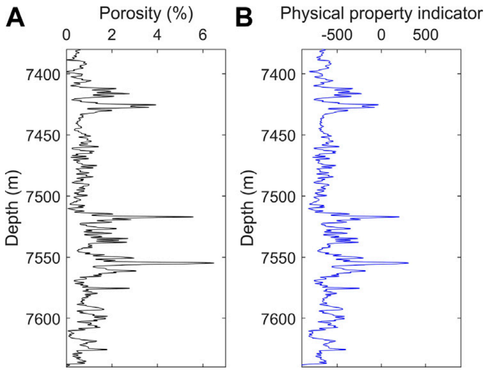

FIGURE 5
(A) Porosity and **(B)** the physical property indicator varied with depth in Well 4.

porosity). These data were then used to further distinguish the physical properties of oil-containing layers from those of aquifers. Crossplots of the P-to-S-wave velocity ratio (Vp/Vs) and P-wave impedance (PI) vs. porosity, density and PI vs. porosity, and Lamé constant and PI vs. porosity before fluid substitution are shown in Figures 3A,C,E, respectively. Carbonate reservoirs associated with good physical properties are characterized by a low P-wave impedance, S-wave impedance (SI), density, and Lamé constant.

In the process of drilling Well 1 in the study area, no effective logging curve was generated. Therefore, it is difficult to analyze fluid-sensitive elastic parameters using the measured logging curve. Due to this, Well 4 with a relatively complete curve is selected, and the aquifer is replaced by an oil layer using fluid replacement technology in a region, and the elastic parameters of the oil layer were obtained. Subsequently, a petrophysical analysis was conducted to identify elastic parameters that are sensitive to fluid properties. Crossplots of Vp/Vs and PI vs. porosity, density and PI vs. porosity, and Lamé constant and PI vs. porosity after fluid substitution are shown in Figures 3B,D,F, respectively. The Vp/Vs, density, and Lamé constant of the reservoir decreased after the fluid substitution.

3.2 Establishment of the physical property indicator

A reservoir with high porosity is a good reservoir in the study area. It is difficult to determine the physical characteristics of carbonate using PI or SI alone. Therefore, PI and SI are required to conduct crossdrawing (Figure 4).

In order to better visually distinguish between good and poor reservoirs, a new physical property indicator (PPI) is proposed in this study:

$$\mathrm{PPI} = \mathrm{PI}\cos\phi + \mathrm{SI}\sin\phi,$$

where ϕ is the rotation angle (the clockwise rotation angle ϕ based on the red line in Figure 4). By changing the angle, the relationship between the porosity and the largest angle can be determined so that the physical property indicator can be determined. As an example, for Well 4, we chose a target porosity curve and a correlation curve to identify property-indicating factors and quantitatively characterize the physical

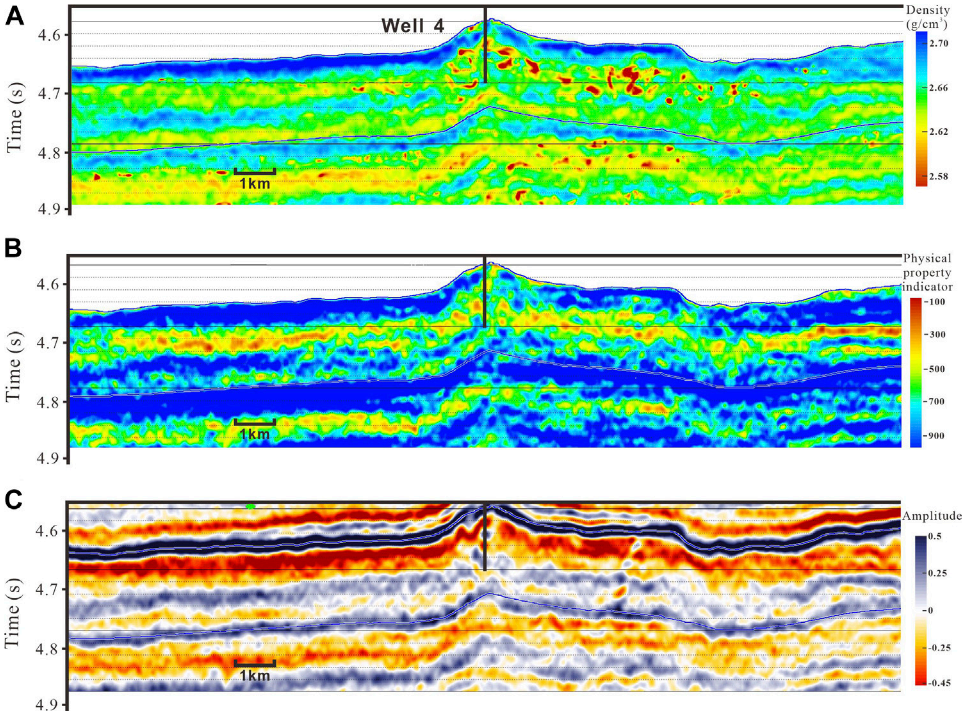

FIGURE 7
Profiles along the N–S direction of Well 4 of **(A)** density, **(B)** the physical property indicator, and **(C)** stack seismic traces.

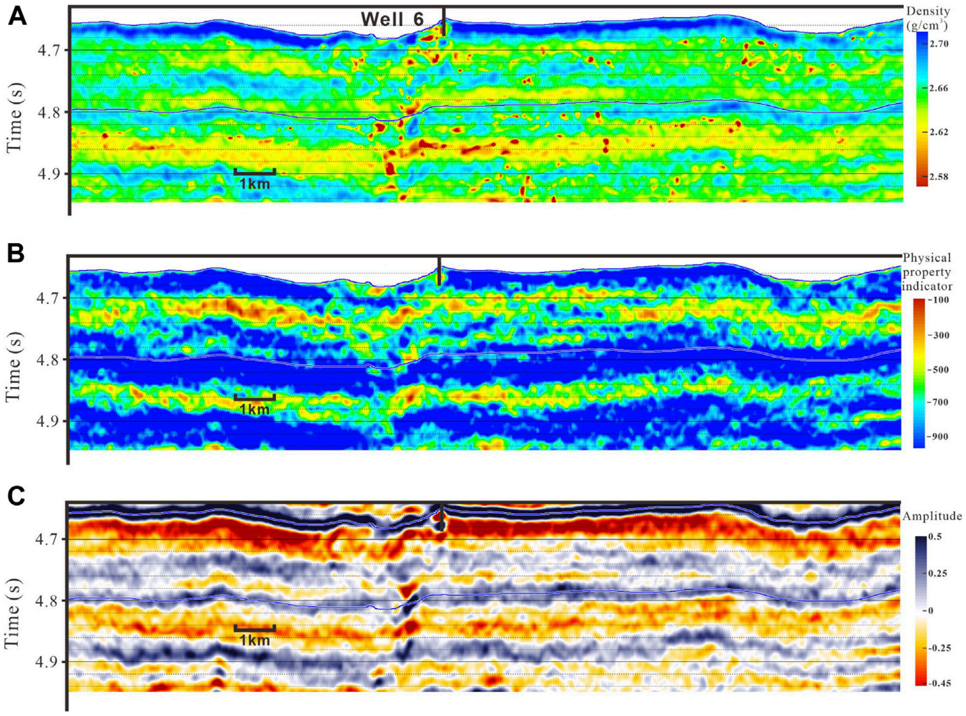

FIGURE 8
Profiles along the N–S direction of Well 6. **(A)** Density, **(B)** the physical property indicator, and **(C)** stack seismic traces.

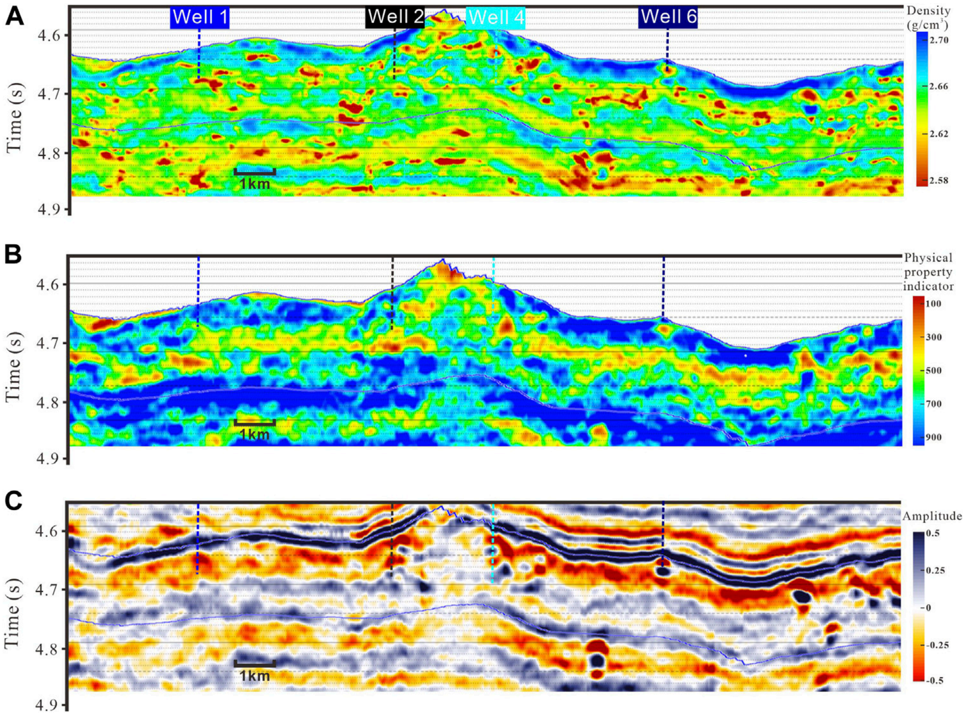

FIGURE 9
Profiles along the main fault zone based on **(A)** density, **(B)** the physical property indicator, and **(C)** stack seismic traces.

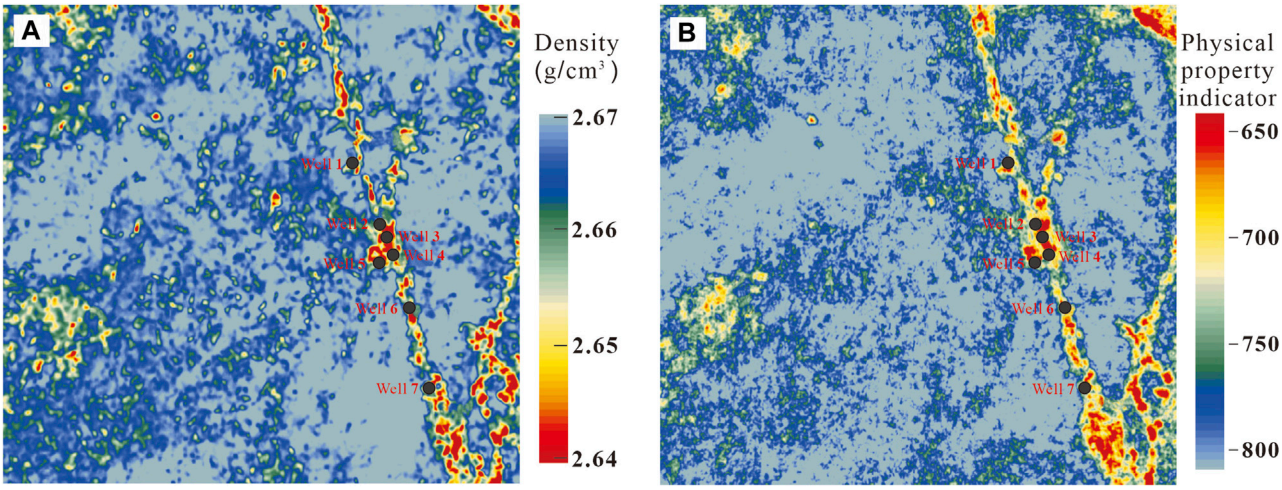

FIGURE 10
Profile of the average parameter values for the T_7^4–T_7^6 formation, including the **(A)** inversion-derived density and **(B)** the physical property indicator.

properties of this area. As shown in Figure 5, the curve of the variation of the physical property indicator with depth agrees with the variation of porosity with depth.

The crossplot of the PI, physical property indicator, and porosity curve after rotating the coordinates by a certain angle is shown in Figure 6. It can be seen that the physical property indicator is a sensitive elastic parameter that can distinguish between good and poor physical properties.

4 Model-driven simultaneous prestack inversion

The seismic gathers of ultra-deep layers in the Shunbei area contain multiple reflections and random noise interferences, which leads to a low SNR. We use the prestack gather optimization to eliminate most multiples to increase the SNR, align events, and increase the dominant frequency, thereby providing high-quality seismic data for subsequent prestack inversion for various physical properties. Simultaneous prestack inversion can derive P- and S-wave velocity, as well as density. These parameters enable the establishment of a physical property indicator according to Section 3.2.

Figure 7 exhibits the inversion results along the N–S direction of Well 4. Well 4 had small-scale leakages, but no large-scale reservoirs were found. The physical property indicator and density inversion results indicate that only relatively weak anomalies occurred at Well 4, which is consistent with the drilling data.

Figure 8 shows the inversion results along the N–S direction of Well 6. Drilling of Well 6 resulted in large-scale leakages. From the profile of the physical property indicator and density, significant anomalies are observed near Well 6, which is consistent with the drilling data.

Profiles of the density, physical property indicator, and stack seismic profile along the main fault zone are shown in Figure 9. Wells 1, 2, 4, and 6 were aligned in an NW–NE direction. Well 1 was partially affected by leakage in the wellbore and the profiles of the physical property indicator and density highlight severe anomalies. In Well 2, the wellbore was unaffected, and thus, profiles of the physical property indicator and density display weak anomalies. Well 4 was impacted by a minor leak in the wellbore, and no major reservoirs were found during drilling. The weak anomalies shown in the profiles of the physical property indicator and density were confirmed by the results from drilling. In Well 6, the wellbore was affected by severe leakage during drilling, and prominent anomalies were observed in the profiles of the physical property indicator and density. Overall, the inversion results are consistent with those from drilling.

An average density profile for the T_7^4–T_7^6 formation is shown in Figure 10A. Anomalies are concentrated near the main fault zone and consistent with the geology setting of the area. A petrophysical analysis confirmed that low-density values indicate the reservoir with high-quality physical properties and the presence of oil-bearing layers, and these findings are consistent with results from drilling in the area. Figure 10B displays a physical property indicator profile for the T_7^4–T_7^6 formation. Sites in red represent those characterized by good physical properties. Reservoirs with good physical properties are concentrated near the main fault zone, which is also consistent with the area's geology setting.

5 Conclusion

Petrophysical analysis of crossplots demonstrated that reservoirs with good physical properties (high porosity) have the following characteristics: low P-wave impedance, low S-wave impedance, low density, low P-to-S-wave velocity ratio, and low Lamé constant. These characteristics are sensitive indicators of the physical properties of reservoirs. Following the substitution of oil with water, the P-to-S-wave velocity ratio, density, and Lamé constant decreased. The porosity curve is selected as the target curve to construct a physical property indicator for quantification of physical properties in the study area. A petrophysical analysis confirmed that the physical property indicator is suitable for distinguishing between good and poor physical properties. The P-wave velocity, S-wave velocity, and density were obtained by using simultaneous prestack inversion. The density near the main fault zone is small. It showed that low density is indicative of a high-quality reservoir and the presence of oil-bearing layers based on the petrophysical analysis. These observations are consistent with results from drilling in the study area.

Data availability statement

The original contributions presented in the study are included in the article/Supplementary Material; further inquiries can be directed to the corresponding author.

Author contributions

ZW and L-YF presented the idea and design of the research. ZW wrote the original draft manuscript; WD and SJ led the data analysis. All authors contributed to the original article revision and approved it for publication.

Funding

The research was supported by the Strategic Priority Research Program of the Chinese Academy of Sciences (Grant

No. XDA14010303), the National Natural Science Foundation of China (Grant No. 42104112), 111 project "Deep-Superdeep Oil & Gas Geophysical Exploration" (B18055), the Major projects during the 14th Five-year Plan period (Grant No. 2021QNLM020001), and the Fundamental Research Funds for the Central Universities (Grant No.20CX06087A).

Conflict of interest

Author SJ was employed by Petroleum Exploration and Development Research Institute of PetroChina Tarim Oil Field Company.

The remaining authors declare that the research was conducted in the absence of any commercial or financial relationships that could be construed as a potential conflict of interest.

Publisher's note

References

Aki, K., and Richards, P. G. (1980). *Quantitative seismology: Theory and methods*. San Francisco: Cambridge University Press.

Ba, J., Xu, W. H., Fu, L. Y., Carcione, J. M., and Zhang, L. (2017). Rock anelasticity due to patchy saturation and fabric heterogeneity: A double double-porosity model of wave propagation. *J. Geophys. Res. Solid Earth* 122 (3), 1949–1976. doi:10.1002/2016JB013882

Deng, S., Li, H. L., Zhang, Z. P., Zhang, J. B., and Yang, X. (2019). Structural characterization of intracratonic strike-slip faults in the central Tarim Basin. *Am. Assoc. Pet. Geol. Bull.* 103 (1), 109–137. doi:10.1306/06071817354

Ding, Y., Du, Q. Z., Fu, L. Y., and Jian, S. K. (2020). Reliability analysis of seismic attribute in the detection of fault-karst. *Interpretation* 8 (4), SP61–SP70. doi:10.1190/INT-2019-0299.1

Jiang, R., Zeng, Q. C., Huang, J. Q., Gan, L., and He, P. (2014). Application of rock physics analysis in pre-stack seismic reservoir prediction. *Oil Geophys. Prospect.* 49 (2), 322. doi:10.13810/j.cnki.issn.1000-7210.2014.02.016

Lang, X., and Grana, D. (2018). Bayesian linearized petrophysical AVO inversion. *Geophysics* 83, M1–M13. doi:10.1190/geo2017-0364.1

Li, H. (2022). Development characteristics of silurian strike-slip faults and fractures and their effects on drilling leakage in Shunbei area of Tarim Basin. *Front. Earth Sci. (Lausanne).* 10, 938765. doi:10.3389/feart.2022.938765

Li, Z. J., Fu, L. Y., Liu, J., Wang, Z. W., and Jian, S. K. (2022). Azimuthal P-P prestack seismic prediction of fractures for superdeep carbonate reservoirs in northwest China. *Mar. Petroleum Geol.* 137, 105485. doi:10.1016/j.marpetgeo.2021.105485

Liu, Y. C., Qiu, N. S., Chang, J., Jia, J. K., Li, H. L., and Ma, A. L. (2020). Application of clumped isotope thermometry to thermal evolution of sedimentary basins: A case study of Shuntuoguole area in Tarim Basin. *Chin. J. Geophys.* 63 (2), 597–611. doi:10.6038/cjg2020N0152

Lu, X., Wang, Y., Tian, F., Li, X. H., Yang, D. B., Li, T., et al. (2017). New insights into the carbonate karstic fault system and reservoir formation in the southern Tahe area of the Tarim Basin. *Mar. Petroleum Geol.* 86, 587–605. doi:10.1016/j.marpetgeo.2017.06.023

Lu, X., Wang, Y., Yang, D. B., and Wang, X. (2020). Characterization of paleo-karst reservoir and faulted karst reservoir in Tahe Oileld, Tarim Basin, China. *Adv. Geo-Energy Res.* 4 (3), 339–348. doi:10.46690/ager.2020.03.11

Ma, R., Ba, J., Carcione, J., Lebedev, M., and Wang, C. (2021). Experimental study on petrophysical properties as a tool to identify pore fluids in tight-rock reservoirs. *Front. Earth Sci. (Lausanne).* 9, 652344. doi:10.3389/feart.2021.652344

Mu, X. R., Huang, J. P., Fu, L. Y., Jian, S. K., Liu, B., and Wang, Z. Y. (2021). Diffraction imaging for the fault-karst structure by least-squares reverse time migration. *Interpretation* 9 (2), T385–T394. doi:10.1190/INT-2020-0146.1

Tan, W. H., Ba, J., Fu, L. Y., Carcione, J. M., and Zhou, X. (2021). 3D rock physics template analysis and "sweet spot" prediction of Longmaxi-Wufeng organic-rich shale. *Chin. J. Geophys.* 64 (8), 2900–2915. doi:10.6038/cjg2021O0380

Wang, J. W., Zhang, E. H., and Xie, C. L. (2011). Prediction of shear wave velocity with optimized Xu-White Model based on virtual porosity. *Fault-Block Oil Gas Field* 18 (4), 445

Wang, Y., and Morozov, I. B. (2019). Time-lapse acoustic impedance variations during CO_2 injection in Weyburn oilfield, Canada. *Geophysics* 85 (1), 1–M13. doi:10.1190/GEO2019-0221.1

Wang, Z. Y., Huang, J. P., Li, Z. C., Fu, L. Y., Luo, W., and Mu, X. (2020). Velocity model estimation of karstic fault reservoirs using full-waveform inversion accelerated on graphics processing unit. *Interpretation* 8 (4), SP191–SP203. doi:10.1190/INT-2019-0304.1

Wu, Y., Lin, C., Yan, W., Liu, Q., Zhao, P., and Ren, L. (2020). Pore-scale simulations of electrical and elastic properties of shale samples based on multicomponent and multiscale digital rocks. *Mar. Petroleum Geol.* 117, 104369. doi:10.1016/j.marpetgeo.2020.104369

Wu, Y., Tahmasebi, P., Lin, C., Munawar, M. J., and Cnudde, V. (2019a). Effects of micropores on geometric, topological and transport properties of pore systems for low-permeability porous media. *J. Hydrology* 575, 327–342. doi:10.1016/j.jhydrol.2019.05.014

Wu, Y., Tahmasebi, P., Lin, C., Zahid, M. A., Dong, C., Golab, A. N., et al. (2019b). A comprehensive study on geometric, topological and fractal characterizations of pore systems in low-permeability reservoirs based on SEM, MICP, NMR, AND X-ray CT experiments. *Mar. Petroleum Geol.* 103, 12–28. doi:10.1016/j.marpetgeo.2019.02.003

Yin, X., Cui, W., Zong, Z., and Liu, X. (2014). Petrophysical property inversion of reservoirs based on elastic impedance. *Chin. J. Geophys.* 57 (12), 4132–4140. doi:10.6038/ejg20141224

Yu, J., Li, Z., and Yang, L. (2016). Fault system impact on paleokarst distribution in the Ordovician Yingshan formation in the central Tarim Basin, northwest China. *Mar. Petroleum Geol.* 71, 105–118. doi:10.1016/j.marpetgeo.2015.12.016

Yuan, H., Chen, S., Neng, Y., Zhao, H., Xu, S., Wang, X., et al. (2021). Composite strike-slip deformation belts and their control on oil and gas reservoirs: A case study of the northern part of the Shunbei 5 strike-slip deformation belt in Tarim Basin, northwestern China. *Front. Earth Sci. (Lausanne).* 9, 755050. doi:10.3389/feart.2021.755050

Zhang, L., Ba, J., and Carcione, J. M. (2021). Wave propagation in infinituple-porosity media. *J. Geophys. Res. Solid Earth* 126 (4), e2020JB021266. doi:10.1029/2020JB021266

Zhang, L., Ba, J., Carcione, J. M., and Wu, C. F. (2022). Seismic wave propagation in partially saturated rocks with a fractal distribution of fluid-patch size. *JGR. Solid Earth* 127, e2021JB023809. doi:10.1029/2021JB023809

frontiers | Frontiers in Earth Science

TYPE Original Research
PUBLISHED 17 January 2023
DOI 10.3389/feart.2022.1046927

EDITED BY
Yuqi Wu,
China University of Petroleum (East China), China

REVIEWED BY
Muhammad Jawad Munawar,
University of the Punjab, Pakistan
Yong Ma,
China University of Petroleum, Beijing, China
Qiming Wang,
University of Texas at Arlington, United States

*CORRESPONDENCE
Liu Keyu,
liukeyu@upc.edu.cn

SPECIALTY SECTION
This article was submitted to Solid Earth Geophysics, a section of the journal Frontiers in Earth Science

RECEIVED 17 September 2022
ACCEPTED 25 October 2022
PUBLISHED 17 January 2023

CITATION
Yuchen F and Keyu L (2023), Large-volume FIB-SEM 3D reconstruction: An effective method for characterizing pore space of lacustrine shales. *Front. Earth Sci.* 10:1046927.
doi: 10.3389/feart.2022.1046927

Large-volume FIB-SEM 3D reconstruction: An effective method for characterizing pore space of lacustrine shales

Fan Yuchen[1] and Liu Keyu[1,2]*

[1]Shandong Provincial Key Laboratory of Deep Oil and Gas, Qingdao, China, [2]Laboratory for Marine Mineral Resources, Qingdao National Laboratory for Marine Science and Technology, Qingdao, China

Focused ion beam scanning electron microscopy (FIB-SEM) is a commonly used three-dimensional (3D) pore-network reconstruction method for shales due to its unique capability in imaging nano-scale pores. However, it has been found that for pore space of lacustrine shales with strongly heterogeneous pore structures, the conventional FIB-SEM 3D models usually with dimensions of 10 μm × 10 μm × 10 μm cannot adequately characterize the pore structures as the representative element volume required is much larger than the FIB models. Here, we propose to utilize large volume FIB-SEM (LV-FIB-SEM) 3D models to resolve this challenge. The LV-FIB-SEM model has a significant enhancement in the model size compared with the commonly used conventional FIB-SEM models and a much higher spatial resolution than non-synchrotron nano X-ray CT models for similar imaging sample sizes. With 75 μm × 65 μm × 60 μm as predesigned reconsruction size, after image processing two LV-FIB-SEM 3D models with sizes of 73.56 μm × 38.13 μm × 52.59 μm and 74.01 μm × 43.05 μm × 42.00 μm and model resolution of 30 nm were reconstructed and quantitatively analyzed. When use the conventional FIB-SEM models of 10 μm × 10 μm × 10 μm, the relative deviations between the porosities derived from 100 stochastic models and the average porosity for the two samples studied are −41.13% ~ +87.31% and −51.66% ~ +56.05%, respectively, indicating that such small models are not representative of the actual pore structure of the shales investigated. When the model sizes have been increased by 96 times volumetrically, the probabilities of matching average porosities for the two samples increase from 13% to 86% and from 12% to 100%, respectively. This research demonstrates that the upsizing of the FIB-SEM models enables an effective improvement on the representativeness of shale pore structures characterized. It is recommended that LV-FIB-SEM 3D reconstruction be employed to study pore space of lacustrine shales with strongly heterogeneous pore structures, which would enable a more accurate characterization and evaluation of reservoirs for shale oil exploration and development.

KEYWORDS

lacustrine shales, digital rock, 3D pore structure, FIB-SEM tomography, upsizing, heterogeneity

Introduction

Nano scale pores are extensively developed in shale reservoirs (Curtis et al., 2012; Loucks et al., 2012; Clarkson et al., 2013). Adequately characterizing nanopore 3D structures of shales is essential for recognizing favorable shale reservoirs (Iglauer and Lebedev, 2018; Wu et al., 2019). FIB-SEM has been routinely used to characterize the 3D distribution of nanopores in shales. Lemmens et al. (2011) used the FIB-SEM 3D reconstruction for the first time to obtain a digital rock (DR) model of shale with dimensions of 15 μm × 15 μm × 1.3 μm, and demonstrated that the FIB-SEM tomography technology is a quite promising new method for characterizing shale pore network, because it has the spatial resolution required to describe the size and geometric features of nanopores. The FIB-SEM 3D reconstruction technique has since been widely used in studying shales worldwide. Dewers et al. (2012) systematically studied the pore-throat diameter distribution, pore connectivity and pore tortuosity of a shale using a 6.6 μm × 3.1 μm × 7.1 μm FIB-SEM 3D model. Yoon and Dewers (2013) investigated the impact of pore structures on fluid transport properties using a 16 μm × 10 μm × 15 μm FIB-SEM 3D model. Shabro et al. (2014) studied the resistivity and permeability at the nanopore scale using a 4.4 μm × 4.4 μm × 4.4 μm organic-rich mudstone model reconstructed by FIB-SEM. Ma et al. (2015) analyzed the preservation mode of shale gas according to the pore geometry characteristics derived from a FIB-SEM 3D model of 7.3 μm × 7.3 μm × 5 μm. Bai et al. (2016) investigated the pore network model of shales in Quebec, Canada segmented from the FIB-SEM 3D model with dimensions of 9.9 μm × 9.1 μm × 10 μm.

However, with increasing application of FIB-SEM 3D reconstruction in characterizing shales, it has been realized that the FIB-SEM model commonly in dimensions of around 10 μm × 10 μm × 10 μm can no longer be representative for most heterogeneous shales. Affected by a strong heterogeneous pore distribution, the conventional-sized FIB-SEM 3D model is insufficient to represent the real pore structure characteristics in shales (Liu et al., 2009; Wu et al., 2020; Wu et al., 2022). Various attempts have been made to address this issue by various researchers using other approaches. Hemes et al. (2015) combined FIB-SEM 3D models and micron X-ray CT 3D models to calculate representative multi-scale pore size distributions and pore throat distributions. Peng et al. (2015) proposed a theoretical model based on data of FIB-SEM reconstruction, micron X-ray CT imaging and high-pressure mercury injection experiment to predict representative permeabilities of shales. Yang et al. (2015) used the multi-point geostatistics method to reconstruct and superimpose digital rock models of different scales to obtain representative shale pore structures. Kelly et al. (2016) proposed to randomly reconstruct the FIB-SEM 3D models at different locations of the same sample and then unify the pore structure features extracted from several models to improve the representativeness of the characterizing results. Gholinia et al. (2020) employed broad ion beam-scanning electron microscopy (BIB-SEM) and obtained a shale digital rock model with a size of 500 μm × 500 μm × 5.3 μm. This technique is good at making 3D models with large length and width. However, the thickness of the reconstructed models is generally quite limited because it would take about up to 30 min for milling and imaging per slice. The voxel size of the BIB-SEM models is 240 nm × 240 nm × 20 nm, insufficient for characterizing shale pores. Fan et al. (2022) developed a fractal method to compute representative pore size distribution curves based on both FIB-SEM models and micron X-ray CT models.

At present, most of methods proposed to enhance the representativeness of digital rock characterizing results are based on prediction models or multiple experiments. There lacks a unified solution to effectively acquire representative data *via* a single experiment credibly. How to effectively overcome the heterogeneity of pore distribution to obtain real and credible shale pore structure features remains unresolved. This paper proposes to break the previously routine model size of approximately 10 μm × 10 μm × 10 μm reconstructed by FIB-SEM. A large-volume FIB-SEM (LV-FIB-SEM) 3D reconstruction technique was employed to characterize 3D pore structures of shales. LV-FIB-SEM models generally refer to digital rock models with size larger than or equal to 50 μm × 50 μm × 50 μm, because this size is more than 100 times larger than the conventional size of 10 μm × 10 μm × 10 μm, and approaches the upper limit of 3D reconstruction size by FIB-SEM.

Samples

The two shale samples used in this study were selected from the second member of the Palaeogene Kongdian Formation (Ek_2) in the Cangdong Sag, Bohai Bay Basin, China. The Ek_2 formation is a typical continental shale characterized by mixed sedimentation and strong heterogeneities (Pu et al., 2016; Zhao et al., 2018). The mineral compositions and lithofacies type of the samples are shown in Table 1. The felsic mineral contents of both samples are over 50%, typical of felsic shales. The main difference between the two samples is the clay mineral content. The clay mineral content of sample G1 is 3.33%, while that of sample G2 is 11.22%. The contents of total organic carbon (TOC) for samples G1 and G2 are 4.82% and 5.53%, respectively. The vitrinite reflectance (R_o %) values of the samples are 0.7%–1.0%, within an oil generation window (Ma et al., 2020; Xin et al., 2021). The organic matter in the samples are primarily oil (bitumen) migrated from the adjacent source rock (Li et al., 2020). The storage space is dominated by nano- and micron-scale inter-grain pores. Microfractures such as interlayer fractures and diagenetic shrinkage fractures are also relatively well developed (Guan et al., 2020; Xin et al., 2022).

TABLE 1 Summary of mineral compositions and lithofacies of investigated samples.

Sample	Depth (m)	Albite (%)	Orthoclase (%)	Quartz (%)	Dolomite (%)	Calcite (%)	Illite (%)	Chlorite (%)	Others (%)	TOC (%)	Lithofacies
G1	4,137.78	67.07	8.42	8.59	7.32	3.19	1.89	1.44	2.08	4.82	Felsic shale
G2	4,105.68	52.44	14.72	8.76	4.33	5.04	9.16	2.06	3.49	5.53	Felsic shale

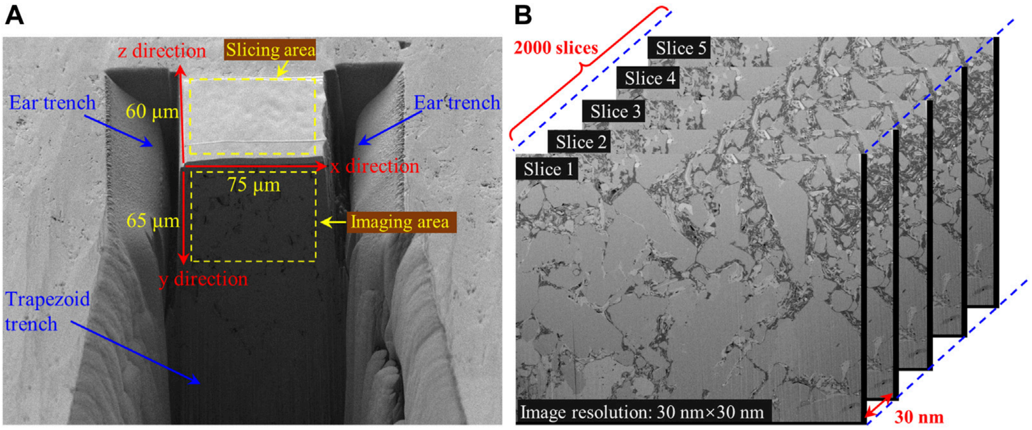

FIGURE 1
Schematic diagram of large-volume 3D reconstruction using FIB-SEM. **(A)** Pre-treatment of the sample for 3D reconstruction showing the positions of the trapezoidal and ear trenches and the imaging area; and **(B)** stacked SEM slices illustrating the consecutive slicing process.

Methods

Shale sample blocks of 5–10 mm long and wide, and a thickness of 5 mm were prepared for FIB-SEM imaging. The surface of the rock block was polished with argon ion beam to obtain a flat surface for SEM imaging. Conductive silver paste was coated on the four sides and the bottom of the polished block samples to reduce charge accumulation on the sample surface and improve the imaging quality.

A Zeiss crossbeam 550 focused ion beam scanning electron microscope was used to reconstruct 3D models. The pre-designed models have sizes of 75 μm × 65 μm × 60 μm, approximately 293 times larger than the conventional FIB-SEM models of 10 μm × 10 μm × 10 μm. After rotating the sample stage by 54° and focusing the electron beam and ion beam, a trapezoidal trench was cut with the gallium ion beam of 30 kV and 65 nA, and two ear trenches were cut with the gallium ion beam of 30 kV and 30 nA. The trapezoidal trench and ear trenches define the 3D reconstruction area (Figure 1A). Rough polishing and fine polishing are then performed on the cross section of the sample using ion beam with a low voltage and current (Figure 1A). Slices with thickness of 30 nm were consecutively cut by ion beam of 30 kV and 7 nA, with each new-exposed surface being imaged using an electron beam of 1 kV and 500 pA (Figure 1B). The image resolution (pixel size) of the sliced SEM image is 30 nm × 30 nm. Both the sample pre-treatment and image acquisition are quite time-consuming. The whole 3D reconstructing process was thus divided into two steps. First, complete the sample pre-treatment including trapezoidal and ear trenching, rough and fine polishing (Figure 1A), which would usually take about 19 h. Consecutive slicing and imaging were then performed on the pre-treated sample, which usually requires 45 h (Figure 1B).

Compared with the conventional FIB-SEM 3D model, the process for making a LV-FIB-SEM model is quite lengthy. The FIB-SEM has a limitation on the continuous operating time. Interruptions may occur during the consecutive slicing and imaging process if the operating time exceeds the limitation. Therefore, one should choose an appropriate SEM imaging resolution according to the sample characteristics (median pore size) to minimize the time required for imaging. The time save from a short SEM imaging process can be used to construct larger volume 3D models. For example, the maximum continuous working time for consecutive slicing and imaging by the Zeiss Crossbeam 550 FIB-SEM in this research is 48 h. Under this time frame, we have set 30 nm as our detection resolution during the image acquisition, so a complete set of 2,000 SEM

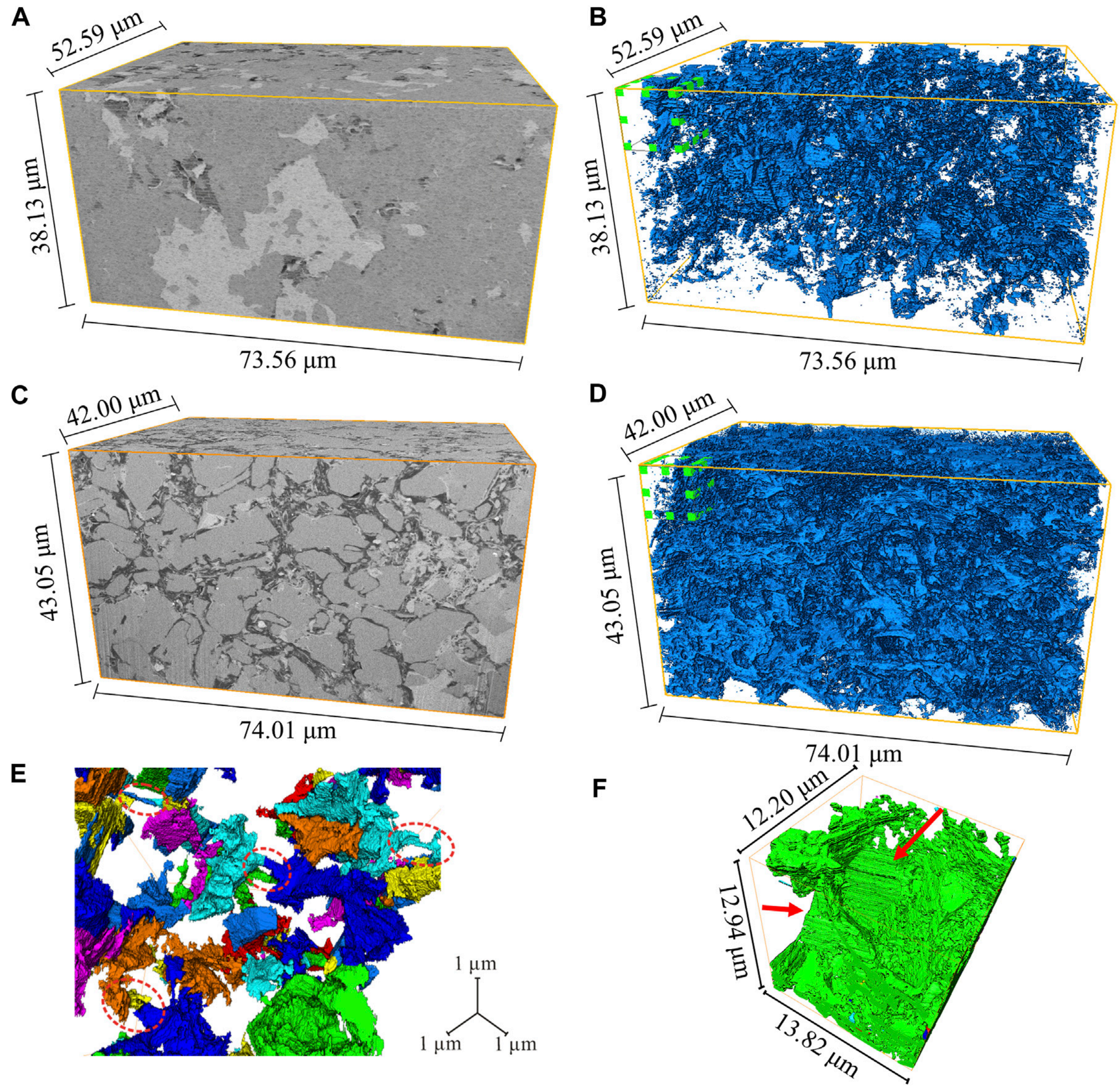

FIGURE 2
Digital rock models of samples G1 and G2 derived from LV-FIB-SEM 3D reconstruction. **(A–D)** Digital rock models and pore network models of samples G1 and G2, respectively; **(E,F)** close-up view of the structure of granular pores and slit-like pores in samples G1 and G2, respectively.

images can be sliced and imaged continuously without interruption. We have finally obtained a LV-FIB-SEM 3D model with lengths of 75 μm in *x* direction, 65 μm in *y* direction and 60 μm in *z* direction (Figure 1). In contrast, if the detection resolution of SEM imaging is set too high, e.g., 5 nm, only the conventional FIB-SEM 3D model (10 μm × 10 μm × 10 μm) can be obtained within the operating time limit. In our case a 30 nm detection resolution is quite adequate for characterizing the shale oil reservoir samples, because it has been shown that oil can only migrate into or produced from pores larger than 50 nm (Li et al., 2019; Liu, 2021).

Results of large volume focused ion beam scanning electron microscopy 3D reconstruction

LV- FIB-SEM 3D reconstruction was used to obtain digital rock models with pre-designed sizes of 75 μm × 65 μm × 60 μm for shale samples G1 and G2. After necessary image cropping for alignment and artifact removing, digital rock models of 73.56 μm × 38.13 μm × 52.59 μm and 74.01 μm × 43.05 μm × 42.00 μm were finally obtained (Figure 2). The pore space of Sample G1 consists primarily of some inter-grain granular

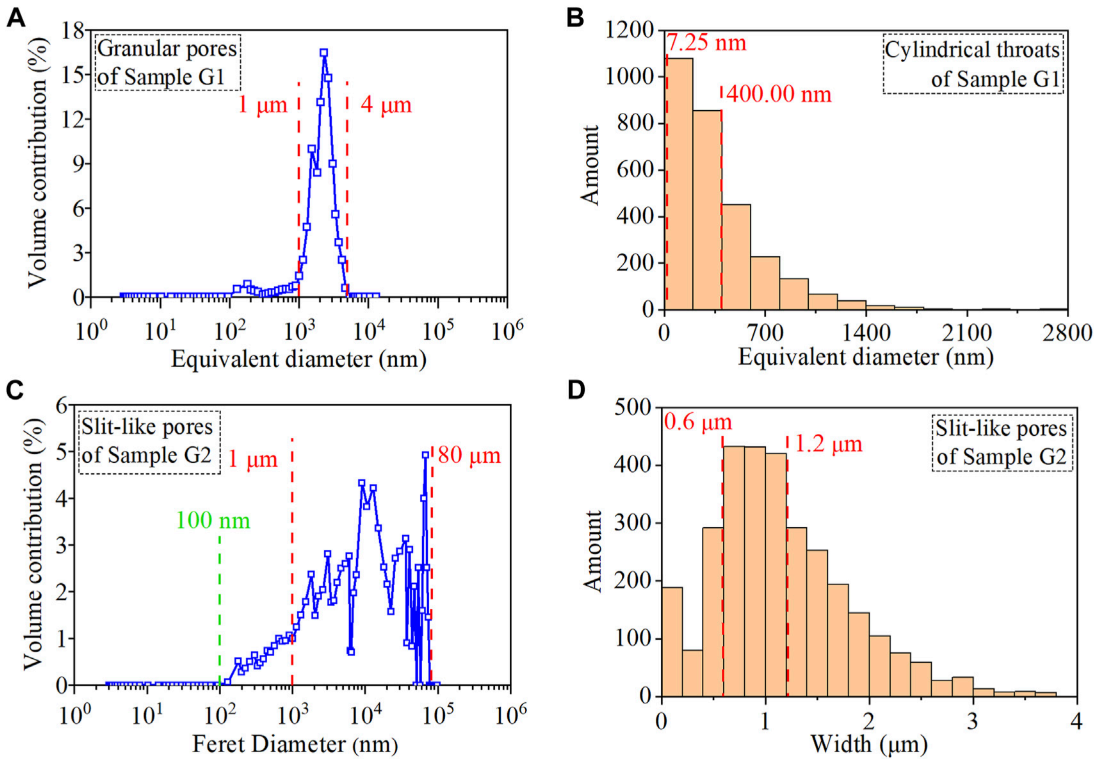

FIGURE 3
Quantitative analysis of LV-FIB-SEM 3D pore-network models. **(A)** Volume contribution distribution of granular pores and **(B)** diameter distribution of cylindrical pore throats of Sample G1; **(C)** volume contribution distribution of slit-pores and **(D)** width distribution of slit-pores of Sample G2.

pores with bitumen filling in (Figure 2A). The 3D pore-network model of Sample G1 was generated by segmenting the void pores and bitumen-bearing pores from the original digital rock model according to the gray-scale (Figure 2B). The storage space of Sample G2 is dominated by some inter-grain slit-pores, which are also filled with bitumen (Figure 2C). Inter-grain slit-pores are interconnected, forming a large interconnected percolation network (Figure 2D). The conventional FIB-SEM 3D models with sizes of 10 μm × 10 μm × 10 μm are also marked by green cubes in Figures 2B,D, which are much smaller than LV-FIB-SEM 3D models. The close-up view of the pore-network model shows that pores in Sample G1 are irregular and connected by cylindrical throats (Figure 2E). The close-up view of percolation network of Sample G2 is shown in Figure 2F, in which the hollow regions (red arrow indicating area) are the distributing locations of mineral particles wrapped by inter-grain slit-pores.

The LV-FIB-SEM model of sample G1 has a porosity of 3.85%. The predominant pore volume is provided by granular pores with equivalent diameters of 1–4 μm shown by the pore size distribution curve (Figure 3A). The equivalent diameter of pore throats is mainly range in 7.25–400.00 nm (Figure 3B). The coordination number of granular pores ranges from 1 to 20, with an average of 3.18, indicating the presence of numerous connecting channels between pores. The volume fraction of the largest interconnected pore cluster is 4.41%, accounting for 47.31% of the total pore space. This indicate that pores are interconnected over a large domain.

The LV-FIB-SEM model porosity of Sample G2 is 8.33%. The storage space for this sample is provided by slit-pores with Feret diameters of 100 nm–80 μm, of which the largest contribution is made by slit-pores of 1–80 μm (Figure 3C). The Feret diameter represents the length of slit-pores in their largest extension direction. Since the storage space of Sample G2 is dominated by slit pores, the width of these slit-pores were counted statistically, which shows a dominant range of 0.6–1.2 μm (Figure 3D). The volume fraction of the largest interconnected pore clusters is 11.46%, accounting for 96.14% of the total pore volume. This indicates slit-pores can interconnect over an extremely large domain.

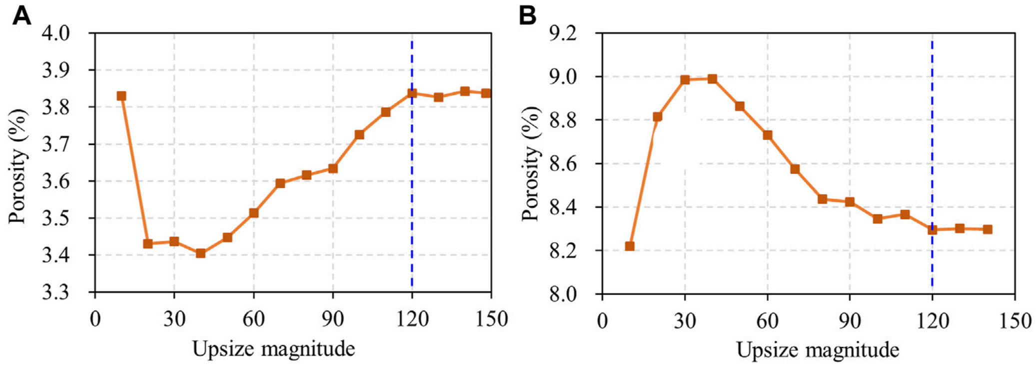

FIGURE 4
Porosity evolution with the increasing model size, showing the size of the representative volume element (REV) of Sample G1 **(A)** and Sample G2 **(B)** at an upsizing of 120 times.

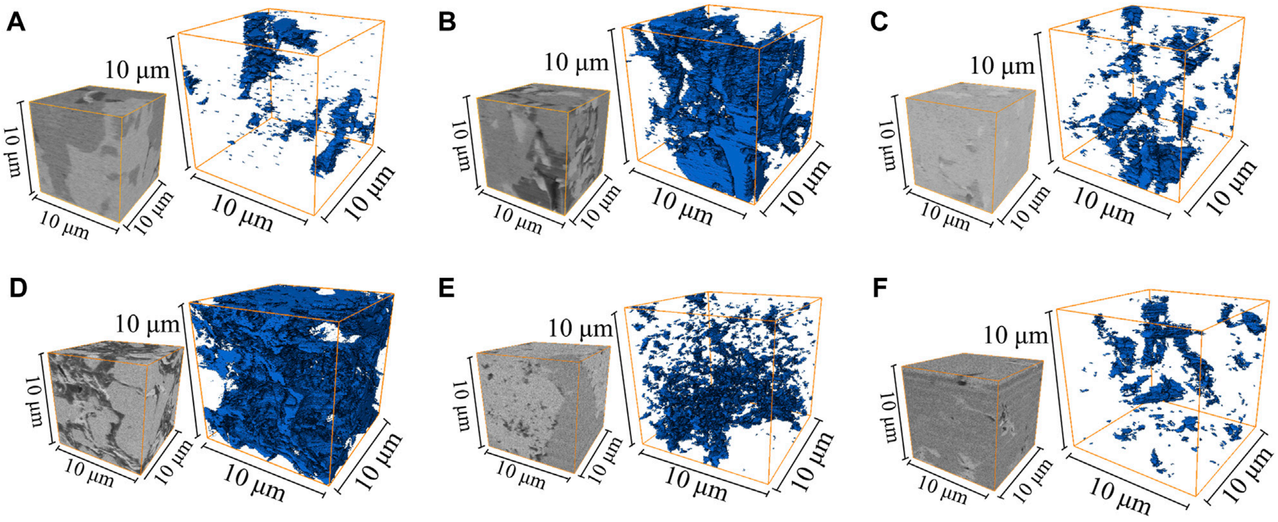

FIGURE 5
Random 10 μm × 10 μm × 10 μm FIB-SEM digital rock models reconstructed from Sample G1 **(A,B,C)** and Sample G2 **(D,E,F)**, showing distinct variability.

Verification of large volume focused ion beam scanning electron microscopy models

What is the specific difference between the LV-FIB-SEM model and the conventional (10 μm × 10 μm × 10 μm) FIB-SEM model? Would the upscaling in model size improve the representativeness and accuracy of the pore structure characterizing results? We compared the porosity of FIB-SEM models of different sizes to analyze the effect of FIB-SEM model sizes on the pore structure characterizing results.

Representative element volume of focused ion beam scanning electron microscopy models

The porosity of the digital rock models would change regularly with a gradual increasing model size. Generally, porosity would go through a period of instability firstly and then become stable gradually. When the porosity begins to stabilize, the corresponding model size is then referred to the representative element volume (Bear and Braester, 1972; Baveye and Sposito, 1984). The 3D pore structure

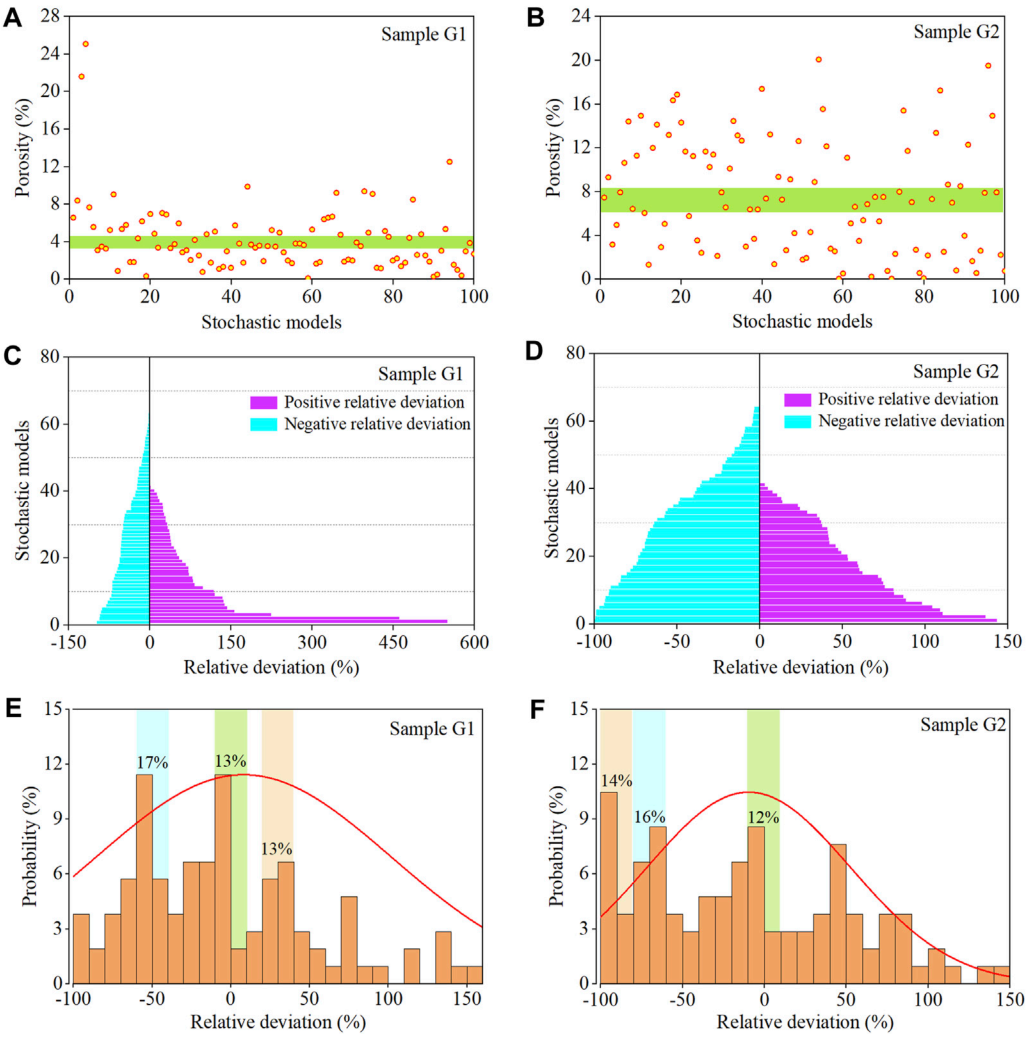

FIGURE 6
(A,B), the porosity distribution of random small-volume models of samples G1 and G2; **(C,D)**, the relative deviations to the average porosity of samples G1 and G2; **(E,F)**, probability distribution of relative deviations of samples G1 and G2.

characterizing results would become representative and credible only when the analyzed model has a size larger than REV (Costanza-Robinson et al., 2011; Adeleye and Akanji, 2017).

The conventional FIB-SEM model size of 10 μm × 10 μm × 10 μm is used as a base model size. When the model is increased by 10 times by volume, the measured model porosity of Sample G1 is 3.83% (Figure 4A). The model porosity would decrease from 3.83% to 3.40% gradually in the process of increasing model size by 40 times. Then, the porosity gradually increases until the model size increased to 120 times. Afterwards the model porosity reaches a stable level around 3.85% (Figure 4A). Therefore, the model size of 68 μm × 50 μm × 36 μm corresponding to the 120-times upscaling can be determined to be the REV size for the pore space of Sample G1.

The porosity of Sample G2 increases from 8.32% to 8.99% with the upsizing of model, and then decreases gradually. Coincidentally, the model porosity also begins to stabilize around 8.30% when the model size is increased by 120 times from the base model (Figure 4B). The corresponding model size of 71 μm × 42 μm × 41 μm is thus determined to be the REV size for the pore space of Sample G2. The digital rock models of samples G1 and G2 obtained *via* the LV-FIB-SEM 3D reconstruction are of 73.56 μm × 38.13 μm × 52.59 μm and 74.01 μm × 43.05 μm × 42.00 μm, respectively. The LV-FIB-SEM model sizes of the two samples are larger than their respective REV sizes, indicating that the pore structure information extracted from these two LV-FIB-SEM models would be credible and representative.

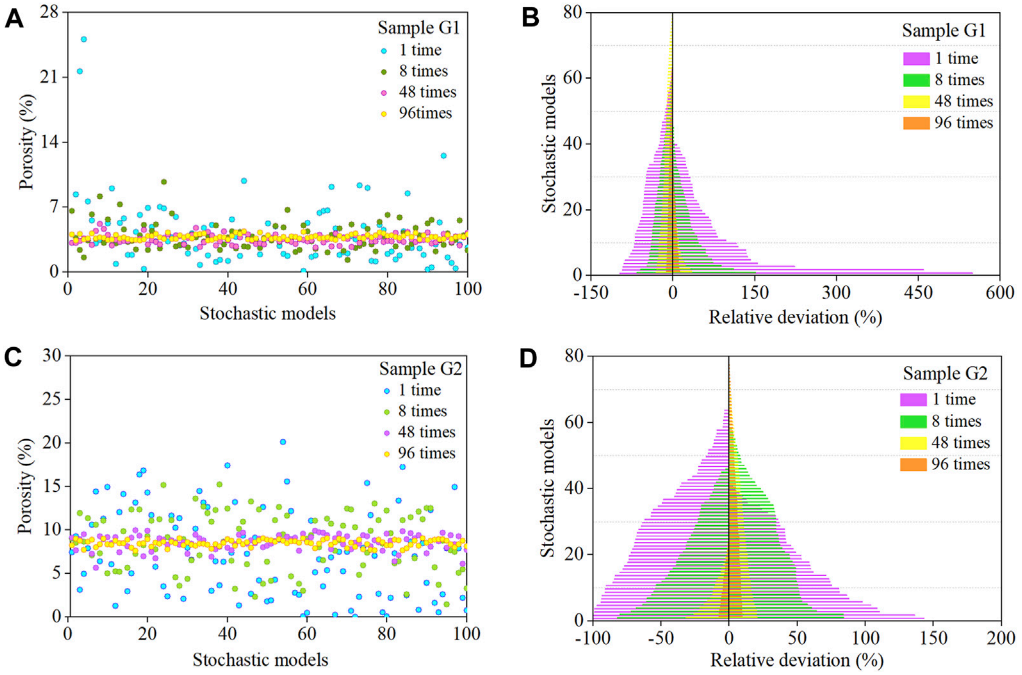

FIGURE 7
(A) Porosity distribution and **(B)** porosity relative deviation distribution of the conventional small-size FIB-SEM (10 μm × 10 μm × 10 μm) stochastic models (1x) and 8x, 48x, and 96x upsized stochastic models for Sample G1. **(C,D)** porosity distribution and the porosity relative deviation distribution plots for Sample G2.

Stochastic analysis of conventional focused ion beam scanning electron microscopy models

The conventional small-volume model refers to the digital core model of 10 μm × 10 μm × 10 μm. One hundred small-volume models were selected at random positions in samples G1 and G2. Figures 5A–C shows the random small-volume models of Sample G1. The pore structures of the random models displayed in Figures 5A,C are relatively similar, both showing relatively discrete pore distribution. However, they are quite different from the pore structure of the random model shown in Figure 5B, which displays an extensively connected pore-network. Figures 5D–F shows the random small-volume models of Sample G2. The pore structures of the three random models are quite different between each other. The pores space shown in Figure 5D has a large interconnected network. Figure 5E exhibits a discrete distribution of small isolated pores. However, the model shown in Figure 5F has fewer pores but a relatively good local connectivity. Qualitative observation demonstrates that affected by the pore distribution heterogeneity, the pore structure characteristics displayed in the 10 μm × 10 μm × 10 μm digital core models can be quite variable. The true and representative pore structure characteristics cannot be extracted from such individual small-size models.

The porosities of 100 random small-volume models of Sample G1 distribute in the range of 0.26%–25.06%, with an average of 4.17% (Figure 6A). The average porosity is regarded as the “true” porosity of the sample investigated. The range −10% ~ +10% to the average porosity is considered as a reasonable error range for the sample porosity. Therefore, the statistically acceptable porosity range of Sample G1 is 3.75%–4.58%, which is marked by a green rectangular area in Figure 6A. It can be seen that only a few porosity values fall within the green rectangular area. The majority of porosities of the random small-volume models fall outside the statistically acceptable porosity range. In addition, the relative deviations of the small-volume model porosities to their average porosity (4.17%) have also been calculated. The maximum positive relative deviation is +549.45%, and the maximum negative relative deviation is −93.04% (Figure 6C). The average positive relative deviation is +87.31%, and the average negative relative deviation is −41.13%. These high relative deviations indicate large differences between porosities of random small-volume models and the true porosity. There is only 13% probability that the porosities of the random small-volume models are within relative deviation of −10% ~ +10% (Figure 6E), which is corresponding to the

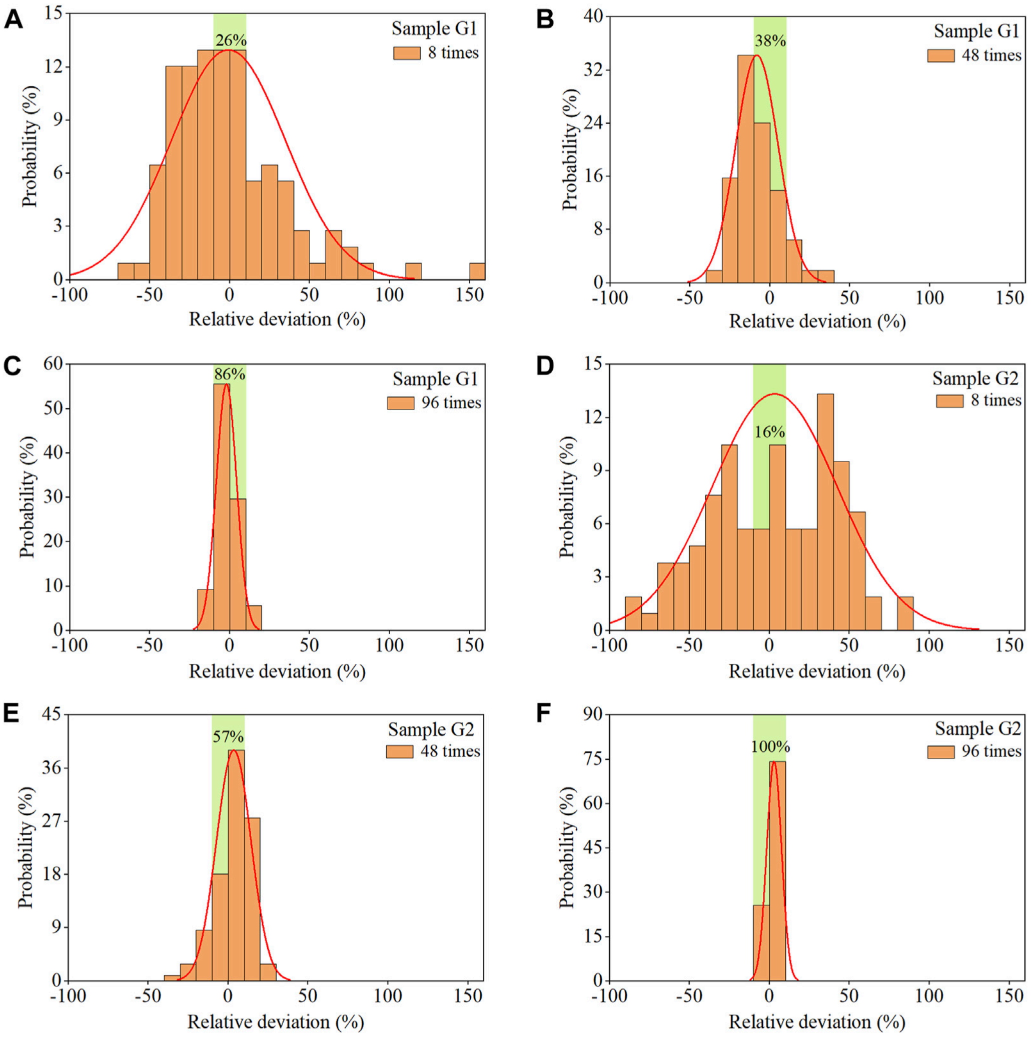

FIGURE 8
Probability distribution of relative deviations to the average porosity, for models upsized by 8 times **(A,D)**, 48 times **(B,E)** and 96 times **(C,F)** of samples G1 and G2, respectively.

porosity range of 3.75%–4.58%. The probability of obtaining a statistically unacceptable porosity value is up to 87%. Among them, there is a 17% probability of porosities being in the relative deviation range of −40% ~ −60%, and a 13% probability of porosities being in the range of +20% ~ +40% (Figure 6E).

The porosities of 100 random small-volume models of Sample G2 are in the range of 0.03%–20.07%, with an average porosity of 7.45%. The statistically acceptable porosity range of Sample G1 is 3.75%–4.58%. Similar to the Sample G1, only a few random models have porosities within the statistically acceptable range (Figure 6B). The maximum positive relative deviation to the average porosity is +143.29%, whereas the maximum negative relative deviation is −99.68% (Figure 6D). The average positive relative deviation is +56.05%, and the average negative relative deviation is −51.66%. There is only 12% probability that the random model porosities fall within the statistically acceptable deviation range (6.71%–8.19%), while there is an extremely high probability (88%) that the model porosities are unrealistic (Figure 6F). The probability of porosity within the deviation range of −60% ~ −80% is up to 16%, while the probability within the deviation range of −80% ~ −100% is 14% (Figure 6F).

Stochastic analysis demonstrates that the pore structure information extracted from the small-volume digital rock models would vary greatly. There is a high probability that the true pore structure information cannot be obtained. The conventional FIB-SEM models of 10 μm × 10 μm × 10 μm are not large enough to provide representative pore structure characteristics.

Stochastic analysis of upsized focused ion beam scanning electron microscopy models

The small-volume FIB-SEM models (10 μm × 10 μm × 10 μm) are upsized by 8 times, 48 times and 96 times to study the impact of upscaling on the pore-network model representativeness, with corresponding model sizes of 20 μm × 20 μm × 20 μm, 40 μm × 40 μm × 30 μm and 60 μm × 45 μm × 35.5 μm, respectively. When the small-volume models of Sample G1 are upsized by 8 times, the porosity distribution ranges of the 100 random models narrow from 0.26%–25.06% to 1.31%–9.71%. After the upsizing of 48 and 96 times, the porosity distribution ranges further converge to 2.67%–5.21% and 3.41%–4.35%, respectively (Figure 7A), which gradually approach the statistically acceptable porosity distribution range (3.75%–4.58%) shown by the green rectangular area in Figure 6A. The relative deviations to the average porosity are still up to −65.99% ~ +151.48% after an upsize of 8 times. At an upsize of 48 times the relative deviation narrows to −30.67% ~ +34.85% and finally converge to −11.78% ~ +12.79% after an upsize of 96 times (Figure 7B). The gradual decreased relative deviations indicate that the obtained pore structure characteristics slowly approach their true occurrence.

Similarly, when the small-volume models of Sample G2 are upsized by 8 times, the porosity distribution ranges of 100 random models narrow from 0.02%–20.07% to 2.31%–15.19%. As the size is gradually upsized to 96 times, the porosity distribution range is further converged to 7.62%–9.06% (Figure 7C), which is quite close to the statistically acceptable porosity distribution range of 6.71%–8.19% (Figure 6B). When the small-volume models are upsized by 8 times, the relative deviations to the average porosity narrow from −99.68% ~ +143.29% to −72.00% ~ +84.23%, and finally converge to −6.3% ~ +9.81% after 96-time upsizing (Figure 7D).

When the small-volume models of Sample G1 are upsized by 8 times, the probability of the relative deviation falling within −10% ~ +10% (statistically acceptable range of porosity) is 26% (Figure 8A). When the model size is upsized by 48 times and 96 times, the probability increases markedly to 58% and 86%, respectively (Figures 8B,C). The gradual increased probability of acceptable relative deviation can also be reflected by their normal fitting curves, which transform from a relatively broad pattern to a relatively concentrated pattern during the upsizing process of 8 times to 96 times. For Sample G2, the probability of the relative deviation falling in the acceptable deviation range is 16% at 8-time upsizing (Figure 8D). When the model is upsized by 48 times, the probability increases significantly to 67% (Figure 8E). After the model is upsized to 96 times, the probability of the random models falling within the statistically acceptable porosity range reach 100% (Figure 8F).

As the size of the digital rock model is upsized from 10 μm × 10 μm × 10 μm (1x) to 60 μm × 45 μm × 35.5 μm (96x), the model porosity distribution of samples G1 and G2 rapidly approaches to the reasonable error range of the true porosity. The probability of obtaining a true porosity value increases from 13% to 86% and from 12% to 100%, respectively. The stochastic analyses demonstrate that the size increase of the FIB-SEM models can effectively improve the accuracy and representativeness of pore structure characterizing results.

Conclusion

As we have demonstrated, LV-FIB-SEM 3D reconstruction is able to achieve adequate pore space characterization of lacustrine shales with heterogeneous pore structures by using a relatively large volume. The LV-FIB-SEM 3D models we have obtained in this study are at least two orders of magnitude of the conventional FIB-SEM models with sizes of 10 μm × 10 μm × 10 μm. The detection resolution of LV-FIB-SEM model is much higher than that from nano X-ray CT imaging, enabling an effective differentiation of minerals, bitumen and pores. Due to the significant increase in the 3D reconstruction volume, the quantitative results of the LV-FIB-SEM models are much more representative than that of the conventional FIB-SEM models. This allows us to obtain realistic pore structure features more accurately. The LV-FIB-SEM 3D reconstruction technique is an effective method for studying pore structures of strongly heterogeneous lacustrine shales.

Data availability statement

The original contributions presented in the study are included in the article/supplementary material, further inquiries can be directed to the corresponding author.

Author contributions

All authors listed have made a substantial, direct, and intellectual contribution to the work and approved it for publication.

Funding

This research was financially supported by the Major Research Project on the Tethys Geodynamic System from the

National Science Foundation of China (No. 92055204), the Shandong Provincial Government on “Continental shale oil accumulation mechanisms and prediction techniques in the Jiyang Depression” (No. 2020ZLYS08), the 14th Five-Year Plan Major Project of the National Laboratory for Marine Science and Technology (2021QNLM020001).

Acknowledgments

Ms. Chunyu Li, the Laboratory manager of Shandong Provincial Key Laboratory of Deep Oil and Gas, China University of Petroleum, Qingdao, China is thanked for her help in acquiring the FIB-SEM images.

Conflict of interest

The authors declare that the research was conducted in the absence of any commercial or financial relationships that could be construed as a potential conflict of interest.

Publisher’s note

References

Adeleye, J. O., and Akanji, L. T. (2017). Pore-scale analyses of heterogeneity and representative elementary volume for unconventional shale rocks using statistical tools. *J. Pet. Explor. Prod. Technol.* 8 (3), 753–765. doi:10.1007/s13202-017-0377-4

Bai, B., Sun, Y., and Liu, L. (2016). Petrophysical properties characterization of Ordovician Utica gas shale in Quebec, Canada. *Petroleum Explor. Dev.* 43 (1), 74–81. doi:10.1016/S1876-3804(16)30008-8

Baveye, P., and Sposito, G. (1984). Reply [to “comment on ‘the operational significance of the continuum hypothesis in the theory of water movement through soils and aquifers’ by P. Baveye and G. Sposito”]. *Water Resour. Res.* 20 (5), 1295–1296. doi:10.1029/wr021i008p01295

Bear, J., and Braester, C. (1972). On the flow of two immscible fluids in fractured porous media. *Dev. Soil Sci.* 2, 177–202. doi:10.1016/S0166-2481(08)70538-5

Clarkson, C. R., Solano, N., Bustin, R. M., Bustin, A. M. M., Chalmers, G. R. L., He, L., et al. (2013). Pore structure characterization of North American shale gas reservoirs using USANS/SANS, gas adsorption, and mercury intrusion. *Fuel* 103, 606–616. doi:10.1016/j.fuel.2012.06.119

Costanza-Robinson, M. S., Estabrook, B. D., and Fouhey, D. F. (2011). Representative elementary volume estimation for porosity, moisture saturation, and air-water interfacial areas in unsaturated porous media: Data quality implications. *Water Resour. Res.* 47 (7), W07513. doi:10.1029/2010WR009655

Curtis, M. E., Cardott, B. J., Sondergeld, C. H., and Rai, C. S. (2012). Development of organic porosity in the Woodford Shale with increasing thermal maturity. *Int. J. Coal Geol.* 103, 26–31. doi:10.1016/j.coal.2012.08.004

Dewers, T. A., Health, J., Ewy, R., and Duranti, L. (2012). Three-dimensional pore networks and transport properties of a shale gas formation determined from focused ion beam serial imaging. *Int. J. Oil Gas. Coal Trans.* 5 (2-3), 229–248. doi:10.1504/IJOGCT.2012.046322

Fan, Y., Liu, K., Yu, L., Liu, J., and Regenauer-Lieb, K. (2022). Assessment of multi-scale pore structures and pore connectivity domains of marine shales by fractal dimensions and correlation lengths. *Fuel* 330, 125463. doi:10.1016/j.fuel.2022.125463

Gholinia, A., Curd, M. E., Bousser, E., Taylor, K., Hosman, T., Coyle, S., et al. (2020). Coupled broad ion beam–scanning electron microscopy (BIB–SEM) for polishing and three dimensional (3D) serial section tomography (SST). *Ultramicroscopy* 214, 112989. doi:10.1016/j.ultramic.2020.112989

Guan, M., Liu, X., Jin, Z., and Lai, J. (2020). The heterogeneity of pore structure in lacustrine shales: Insights from multifractal analysis using N2 adsorption and mercury intrusion. *Mar. Pet. Geol.* 114, 104150. doi:10.1016/j.marpetgeo.2019.104150

Hemes, S., Desbois, G., Urai, J., Schroppel, B., and Schwarz, J. (2015). Multi-scale characterization of porosity in Boom Clay (HADES-level, Mol, Belgium) using a combination of X-ray μ-CT, 2D BIB-SEM and FIB-SEM tomography. *Microporous Mesoporous Mat.* 208, 1–20. doi:10.1016/j.micromeso.2015.01.022

Iglauer, S., and Lebedev, M. (2018). High pressure-elevated temperature x-ray micro-computed tomography for subsurface applications. *Adv. Colloid Interface Sci.* 256, 393–410. doi:10.1016/j.cis.2017.12.009

Kelly, S., Ei-Sobky, H., Torres-Verdin, C., and Balhoff, M. T. (2016). Assessing the utility of FIB-SEM images for shale digital rock physics. *Adv. Water Resour.* 95, 302–316. doi:10.1016/j.advwatres.2015.06.010

Lemmens, H. J., Butcher, A. R., and Botha, P. W. S. K. (2010). FIB/SEM and SEM/EDX: A new dawn for the SEM in the core lab? *Petrophysics* 52 (06), 452–456. doi:10.1007/s12182-011-0169-2

Li, M., Chen, Z., Ma, X., Cao, T., Qian, G., Jiang, Q., et al. (2019). Shale oil resource potential and oil mobility characteristics of the eocene-oligocene shahejie formation, Jiyang super-depression, Bohai Bay Basin of China. *Int. J. Coal Geol.* 204, 130–143. doi:10.1016/j.coal.2019.01.013

Li, Y., Liu, K., Pu, X., Chen, S., Han, W., Zhang, W., et al. (2020). Lithofacies characteristics and formation environments of mixed fine grained sedimentary rocks in second member of Kongdian Formation in Cangdong depression, Bohai Bay Basin. *J. Earth Sci-China* 45 (10), 3779–3796. doi:10.3799/dqkx.2020.167

Liu, H. (2021). Geological particularity and exploration practice of paleogene shale oil in Jiyang depression: A case study of the upper submember of member 4 to the lower submember of member 3 of shahejie formation. *Acta Pet. Sin.* 43 (5), 581–591. doi:10.7623/syxb202205001

Liu, J., Regenauer-Lieb, K., Hines, C., Liu, K., Gaede, O., and Squelch, A. (2009). Improved estimates of percolation and anisotropic permeability from 3-D X-ray microtomography using stochastic analyses and visualization. *Geochem. Geophys. Geosyst.* 10, Q05010. doi:10.1029/2008GC002358

Loucks, R. G., Reed, R. M., Ruppel, S. C., and Hammes, U. (2012). Spectrum of pore types and networks in mudrocks and a descriptive classification for matrix-related mudrock pores. *Am. Assoc. Pet. Geol. Bull.* 96 (6), 1071–1098. doi:10.1306/08171111061

Ma, B., Hu, Q., Yang, S., Zhang, T., Qiao, H., Meng, M., et al. (2020). Pore structure typing and fractal characteristics of lacustrine shale from Kongdian Formation in East China. *J. Nat. Gas. Sci. Eng.* 85, 103709. doi:10.1016/j.jngse.2020.103709

Ma, Y., Zhong, N., Li, D., Pan, Z., Cheng, L., and Liu, K. (2015). Organic matter/clay mineral intergranular pores in the lower cambrian lujiaping shale in the north-eastern part of the upper yangtze area, China: A possible microscopic mechanism for gas preservation. *Int. J. Coal Geol.* 137, 38–54. doi:10.1016/j.coal.2014.11.001

Peng, S., Yang, J., Xiao, X., Bob, L., Stephen, C. R., and Zhang, T. (2015). An integrated method for upscaling pore-network characterization and permeability estimation: Example from the mississippian barnett shale. *Transp. Porous Med.* 109, 359–376. doi:10.1007/s11242-015-0523-8

Pu, X., Zhou, L., Han, W., Zhou, J., Wang, W., Zhang, W., et al. (2016). Geologic features of fine-grained facies sedimentation and tight oil exploration: A case from the second member of paleogene Kongdian Formation of Cangdong sag, Bohai Bay Basin. *Petroleum Explor. Dev.* 43 (1), 26–35. doi:10.1016/s1876-3804(16)30003-9

Shabro, V., Kelly, S., Torres-Verdin, C., Sepehrnoori, K., and Revil, A. (2014). Pore-scale modeling of electrical resistivity and permeability in FIB-SEM images of organic mudrock. *Geophysics* 79 (5), 289–299. doi:10.1190/GEO2014-0141.1

Wu, S., Yang, Z., Pan, S., Cui, J., Lin, S., Su, L., et al. (2020). Three-dimensional imaging of fracture propagation in tight sandstones of the upper triassic chang 7 member, ordos basin, northern China. *Mar. Pet. Geol.* 120 (3–4), 104501. doi:10.1016/j.marpetgeo.2020.104501

Wu, Y., Tahmasebi, P., Lin, C., Zahid, M. A., Dong, C., Golab, A. N., et al. (2019). A comprehensive study on geometric, topological and fractal characterizations of pore systems in low-permeability reservoirs based on SEM, MICP, NMR, and X-ray CT experiments. *Mar. Pet. Geol.* 103, 12–28. doi:10.1016/j.marpetgeo.2019.02.003

Wu, Y., Tahmasebi, P., Liu, K., Fagbemi, S., Lin, C., An, S., et al. (2022). Two-phase flow in heterogeneous porous media: A multiscale digital model approach. *Int. J. Heat. Mass Transf.* 194, 123080. doi:10.1016/j.ijheatmasstransfer.2022.123080

Xin, B., Hao, F., Han, W., Xu, Q., Zhang, B., and Tian, T. (2021). Paleoenvironment evolution of the lacustrine organic-rich shales in the second member of Kongdian Formation of Cangdong Sag, Bohai Bay Basin, China: Implications for organic matter accumulation. *Mar. Pet. Geol.* 133, 105244. doi:10.1016/j.marpetgeo.2021.105244

Xin, B., Zhao, X., Hao, F., Jin, F., Pu, X., Han, W., et al. (2022). Laminae characteristics of lacustrine shales from the Paleogene Kongdian Formation in the Cangdong Sag, Bohai Bay Basin, China: Why do laminated shales have better reservoir physical properties? *Int. J. Coal Geol.* 260, 104056. doi:10.1016/j.coal.2022.104056

Yang, Y., Yao, J., Wang, C., Gao, Y., Zhang, Q., An, S., et al. (2015). New pore space characterization method of shale matrix formation by considering organic and inorganic pores. *J. Nat. Gas. Sci. Eng.* 27, 496–503. doi:10.1016/j.jngse.2015.08.017

Yoon, H., and Dewers, T. A. (2013). Nanopore structures, statistically representative elementary volumes, and transport properties of chalk. *Geophys. Res. Lett.* 40, 4294–4298. doi:10.1002/grl.50803

Zhao, X., Zhou, L., Pu, X., Jin, F., Jiang, W., Xiao, D., et al. (2018). Development and exploration practice of the concept of hydrocarbon accumulation in rifted-basin troughs: A case study of paleogene Kongdian Formation in Cangdong sag, Bohai Bay Basin. *Petroleum Explor. Dev.* 45 (6), 1166–1176. doi:10.1016/S1876-3804(18)30120-4

Frontiers in
Earth Science

Investigates the processes operating within the major spheres of our planet

Advances our understanding across the earth sciences, providing a theoretical background for better use of our planet's resources and equipping us to face major environmental challenges.

Discover the latest Research Topics

See more →

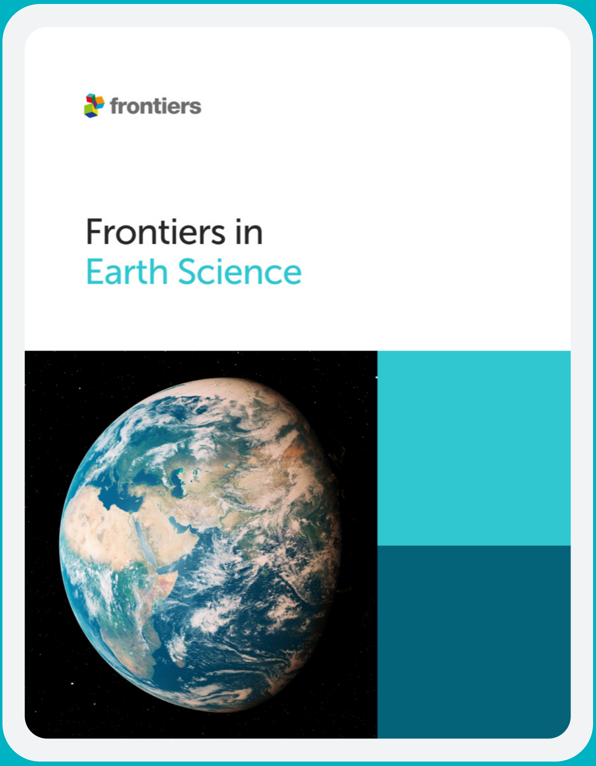

frontiers

Frontiers in
Earth Science

Frontiers

Avenue du Tribunal-Fédéral 34
1005 Lausanne, Switzerland
frontiersin.org

Contact us

+41 (0)21 510 17 00
frontiersin.org/about/contact